

# **Order from Disorder**

---

**Cover:** Configuration of a simulation of an antagonistic salt solution, using the model introduced in chapter 4. An external field attracting negative ions (red) was added to form the letters of the title and author's name. The choice of colors is inspired by the art of Dutch artist Piet Mondriaan and the Dutch artistic movement 'De Stijl', which is celebrating its 100th birthday, this year.

PhD thesis, Utrecht University, the Netherlands, June 2017.

ISBN: 978-90-393-6796-4

Printed by Gildeprint.

A digital version of this thesis is available at <http://www.colloid.nl>

# **Order from Disorder**

---

Orde uit Wanorde

(met een samenvatting in het Nederlands)

Proefschrift

ter verkrijging van de graad van doctor aan de Universiteit Utrecht op gezag van de rector magnificus, prof.dr. G.J. van der Zwaan, ingevolge het besluit van het college voor promoties in het openbaar te verdedigen op woensdag 28 juni 2017 des middags te 2.30 uur

door

Nikos Tasios

geboren op 27 mei 1987 te Rhodos, Griekenland.

**Promotor:** Prof. dr. ir. M. Dijkstra

This research was supported by an NWO-ECHO grant.

# Contents

|          |                                                                                                                                              |           |
|----------|----------------------------------------------------------------------------------------------------------------------------------------------|-----------|
| <b>1</b> | <b>Introduction</b>                                                                                                                          | <b>1</b>  |
| 1.1      | Computer Simulations                                                                                                                         | 2         |
| 1.2      | Statistical Mechanics                                                                                                                        | 2         |
| 1.3      | Phase Transitions and Critical Phenomena                                                                                                     | 5         |
| 1.4      | Colloids, Nanoparticles, and Suspensions Thereof                                                                                             | 7         |
| 1.5      | Salt and Electrostatic Interactions in Solutions                                                                                             | 8         |
| 1.6      | Liquid Crystals                                                                                                                              | 9         |
| 1.7      | Hard-Particle Model                                                                                                                          | 10        |
| 1.8      | The Monte Carlo Simulation Method                                                                                                            | 12        |
| <b>2</b> | <b>Critical Casimir Interactions and Colloidal Self-Assembly in Near-Critical Solvents</b>                                                   | <b>15</b> |
| 2.1      | Introduction                                                                                                                                 | 16        |
| 2.2      | Model                                                                                                                                        | 20        |
| 2.3      | Methods                                                                                                                                      | 22        |
| 2.3.1    | Direct Coexistence Simulations                                                                                                               | 23        |
| 2.3.2    | Grand Canonical Staged-Insertion Method                                                                                                      | 23        |
| 2.3.3    | Transition Matrix Monte Carlo Technique                                                                                                      | 26        |
| 2.3.4    | Two-Point Correlation Function and Structure Factor                                                                                          | 27        |
| 2.4      | Results                                                                                                                                      | 28        |
| 2.4.1    | Phase Diagram of Solvent                                                                                                                     | 28        |
| 2.4.2    | Adsorption at a Single Wall                                                                                                                  | 29        |
| 2.4.3    | Neutral vs. Attractive Colloids                                                                                                              | 30        |
| 2.4.4    | Phase Behaviour and Structure                                                                                                                | 32        |
| 2.4.5    | The Effective Two-Body Potential                                                                                                             | 37        |
| 2.5      | Conclusion                                                                                                                                   | 41        |
| <b>3</b> | <b>Scaling of the 2D Critical Casimir Potential and Phase Behavior of Colloids in Near Critical Solvents in 3D Using a Cluster Algorithm</b> | <b>47</b> |
| 3.1      | Introduction                                                                                                                                 | 48        |
| 3.2      | Cluster Algorithm                                                                                                                            | 49        |
| 3.3      | The Derjaguin Approximation and the Small-Sphere Expansion                                                                                   | 51        |
| 3.4      | Results                                                                                                                                      | 53        |
| 3.4.1    | Scaling of the Critical Casimir Potential in 2D                                                                                              | 53        |
| 3.4.2    | 3D Model Phase Diagram                                                                                                                       | 54        |
| 3.5      | Conclusion                                                                                                                                   | 57        |

|                                                                                           |            |
|-------------------------------------------------------------------------------------------|------------|
| <b>4 Are Antagonistic Salt Solutions Block Copolymers? No, but they behave similarly.</b> | <b>59</b>  |
| 4.1 Introduction                                                                          | 60         |
| 4.2 Model                                                                                 | 61         |
| 4.3 Methods                                                                               | 65         |
| 4.4 Results                                                                               | 67         |
| 4.4.1 Model Verification: Comparison with Poisson-Boltzmann Theory                        | 67         |
| 4.4.2 Pure Solvent Phase Diagram                                                          | 68         |
| 4.4.3 Mesophase Behavior of an Antagonistic Salt Solution                                 | 70         |
| 4.4.4 Structure of Lamellae and Mean-Field Model                                          | 72         |
| 4.5 Conclusion                                                                            | 75         |
| <b>5 A Simulation Study on the Phase Behavior of Hard Rhombic Platelets</b>               | <b>79</b>  |
| 5.1 Introduction                                                                          | 80         |
| 5.2 Model                                                                                 | 81         |
| 5.3 Methods                                                                               | 82         |
| 5.3.1 NPT Cluster algorithm                                                               | 82         |
| 5.3.2 Order Parameters                                                                    | 83         |
| 5.4 Results                                                                               | 84         |
| 5.4.1 Phase Behavior Characterization                                                     | 84         |
| 5.4.2 Structure                                                                           | 85         |
| 5.4.3 Phase Diagram                                                                       | 85         |
| 5.5 Conclusion                                                                            | 89         |
| <b>6 Investigating the Presence of a Biaxial Nematic Phase in Hard Rhombic Particles</b>  | <b>91</b>  |
| 6.1 Introduction                                                                          | 92         |
| 6.2 Model                                                                                 | 93         |
| 6.3 Methods                                                                               | 93         |
| 6.3.1 Event-Driven Molecular Dynamics                                                     | 94         |
| 6.3.2 Order Parameters                                                                    | 100        |
| 6.4 Results                                                                               | 101        |
| 6.4.1 Phase Behavior and Structure                                                        | 101        |
| 6.4.2 Phase Diagram                                                                       | 108        |
| 6.4.3 Phase Behavior as a Function of the Particle Width                                  | 109        |
| 6.5 Conclusion                                                                            | 110        |
| <b>7 Spherical Confinement of Hard Convex-Shaped Particles</b>                            | <b>113</b> |
| 7.1 Introduction                                                                          | 114        |
| 7.2 Models                                                                                | 116        |
| 7.3 Methods                                                                               | 117        |
| 7.3.1 Detecting Particle Overlap with a Spherical Boundary                                | 117        |
| 7.3.2 Monte Carlo Stack Rotation Move                                                     | 118        |
| 7.3.3 Cluster and Surface Layer Identification                                            | 118        |
| 7.3.4 Calculating the Twist                                                               | 119        |

|                             |                                                           |            |
|-----------------------------|-----------------------------------------------------------|------------|
| 7.4                         | Results                                                   | 120        |
| 7.4.1                       | Crystallization of Hard Cubes Under Spherical Confinement | 120        |
| 7.4.2                       | Chiral Twist in Spherically Confined Hard Round Platelets | 124        |
| 7.5                         | Conclusion                                                | 127        |
| <b>References</b>           |                                                           | <b>129</b> |
| <b>Summary</b>              |                                                           | <b>146</b> |
| <b>Samenvatting</b>         |                                                           | <b>149</b> |
| <b>Acknowledgements</b>     |                                                           | <b>152</b> |
| <b>List of Publications</b> |                                                           | <b>155</b> |
| <b>About the Author</b>     |                                                           | <b>156</b> |



# 1

---

## Introduction

---

In this chapter, we introduce various topics and basic concepts that are used throughout this thesis. We make the description of these concepts as approachable as possible so that later chapters can be followed more easily. The Introduction should be seen as a guide for ‘further reading’. We introduce the concept of computer simulations, present the necessary statistical mechanics, and discuss concepts such as colloids and suspensions thereof, states of matter, phase transitions, and hard particles.

## 1.1 Computer Simulations

Since the early days of civilization, science was based solely on observation and the power of deduction. Although we can say science has now matured greatly, its two pillars, theory and experiments, have remained since the very beginning. Experiments are performed, observations are made and confirmed, and a theory is deduced. With the invention of computers, science has substantially evolved along with our everyday lives which demonstrates the power of this invention. Along the two aforementioned pillars, a third one is added, making the foundations of science ever sturdier. This third pillar is known as *computer simulations*.

Before we discuss what exactly computer simulations are and their role in modern science, we first need to explain what a scientific model is. Generally, a scientific model tries to simplify phenomena, and physical processes, to only the parts that are needed to understand the phenomenon or process. A scientific model needs to be testable, and the most successful ones can also make predictions. As an example, weather is very complex, and is affected by many parameters which are impossible to keep track of. Instead, meteorologists might first identify the most important parameters that affect weather in an isolated area, such as wind, humidity, barometric pressure, etc. At first instance, the meteorologist might consider the clouds being spherical, and the velocity of the wind to be uniform in space, thereby constructing a simple model that can be easily solved by either humans, or computers.

Scientific models are used both in theory and in computer simulations. In computer simulations, a model is used to reproduce the behavior of the system of interest, by computing the outcome for a given set of input parameters (e.g. wind velocity, pressure, etc. in the above example). One could say that a computer simulation is trying to virtually imitate the physics of a system. At this point, the differences between simulations, experiments, and theory, might get muddled, and that is understandable. Theory and simulations are similar in the sense that they use scientific models to make predictions. On the other hand, given enough computational power and understanding of the underlying physics, computer simulations could very accurately simulate a physical process, and even make observations beyond what is experimentally possible by our measuring devices. Ever since the first large-scale deployment of a computer simulation to model the process of nuclear detonation during the Manhattan Project in World War II, the field of computer simulations has evolved hand-in-hand with the rapid development of computers. In 2013, the Nobel prize was awarded for the first time for work done using computer simulations [1], marking the point in history where simulations are now considered a viable alternative to theory and experiments.

## 1.2 Statistical Mechanics

Statistical mechanics, is a framework for relating microscopic properties of the individual constituents, typically atoms and molecules, to the macroscopic or bulk properties of materials that can be observed in everyday life, therefore explaining thermodynamics as a natural result of statistics, classical mechanics, and quantum mechanics at the microscopic

level. These constituents are usually all the same, but interact with each other. The sheer number of these constituents that is contained in typical systems (i.e. one liter of oxygen at room temperature and pressure consists of about  $3 \times 10^{22}$  oxygen molecules), makes it impossible to predict how they will evolve in time. Even if these constituents were e.g. perfect spheres bouncing off each other elastically, like idealized billiard balls, we can not solve this system analytically for three spheres or more. Clearly, though, looking at thermodynamic quantities, such as temperature, pressure, etc., we see that they obey simple relations, indicating there is some way to average out the multiple degrees of freedom. Statistical mechanics does just that, by looking at the system as having a certain probability of being in a certain macroscopic state.

Swiss physicist Daniel Bernoulli, in 1738, was the first that posited the argument, still used today, that gases consist of large numbers of molecules moving in all directions, that their impact on a surface causes the gas pressure that we feel, and that what we experience as heat is simply the kinetic energy of their motion. In 1859, after reading a paper on the diffusion of molecules by Rudolf Clausius, Scottish physicist James Clerk Maxwell formulated the Maxwell distribution of molecular velocities, which gave the fraction of molecules having a certain velocity, within a specific range. This was the first statistical law in physics. Five years later, in 1864, Ludwig Boltzmann, a young student in Vienna, came across Maxwell's paper and spent much of his life developing the subject further. Modern statistical mechanics came about in the 1870s with the work of Boltzmann.

We now delve into slightly greater detail in the inner workings of statistical mechanics. Suppose a system is in some state  $\mu$ . We define the probability for the system to transition to state  $\nu$  after some time  $dt$  as  $R(\mu \rightarrow \nu)dt$ , where  $R(\mu \rightarrow \nu)$  denotes the rate at which the system transitions from state  $\mu$  to state  $\nu$ . We additionally define the probability the system will be in a state  $\mu$  at time  $t$  as  $w_\mu(t)$ . The probability weights,  $w_\mu(t)$ , should obey the normalization condition

$$\sum_{\mu} w_{\mu}(t) = 1, \quad (1.1)$$

i.e. the system should always be in some state  $\mu$ . We can then define the expectation of some observable  $Q$  (i.e. average kinetic energy of the molecules in a gas) at a time  $t$  as the sum,

$$\langle Q(t) \rangle = \sum_{\mu} Q_{\mu} w_{\mu}(t), \quad (1.2)$$

where  $Q_{\mu}$  is the value of the observable when the system is in state  $\mu$ . The above equation is simply a weighted average of the observable quantities,  $Q_{\mu}$ . If a scientist is to measure the quantity  $Q$  at time  $t$ , for a large number of independent systems, the average of these values should converge to  $\langle Q(t) \rangle$ . This collection of systems is known as an *ensemble* in statistical mechanics. Clearly, in real experiments, or even in continuous-time simulations, performing a measurement at an exact point in time is impossible. Instead, a scientist conducting an experiment would wait for the system to reach equilibrium, and take the average measurement of  $Q$  at different times,  $t$ . At equilibrium, by definition the probability weights,  $w_{\mu}(t)$ , should be independent of time  $t$ , i.e. the stationary probability of a system being in state  $\mu$  remains the same as time passes. We can thus write,

$$p_{\mu} = \lim_{t \rightarrow \infty} w_{\mu}(t), \quad (1.3)$$

where  $p_\mu$  is the equilibrium probability of finding a system in state  $\mu$ . Here we take the limit of infinite time, but realistic systems ‘equilibrate’ in a finite span of time. Gibbs, in 1902, showed that a system in thermal equilibrium with a reservoir, i.e. a system in which the temperature,  $T$ , volume,  $V$ , and number of particles,  $N$ , do not change (also known as ‘canonical ensemble’), has equilibrium occupation probabilities given by,

$$p_\mu = \frac{1}{Z} e^{-\beta E_\mu}, \quad (1.4)$$

where  $\beta = 1/k_B T$ , with  $k_B$  being the Boltzmann factor,  $E_\mu$  is the energy associated with state  $\mu$ , and  $Z$  is known as the *canonical partition function*. The probability distribution in eq. (1.4) is known as the *Boltzmann distribution*, after Ludwig Boltzmann. The probabilities  $p_\mu$  should also obey the normalization condition, eq. (1.1), so that the partition function can be written as,

$$Z = \sum_\mu e^{-\beta E_\mu}. \quad (1.5)$$

Knowledge of the canonical partition function,  $Z$ , for different values of the parameters  $N$ ,  $V$ , and  $T$ , contains all the information needed to predict the macroscopic behavior of a system. In this ensemble, using eqs. (1.4) and (1.2), the expectation of the observable,  $Q$ , for a system in thermal equilibrium with a reservoir is given by

$$\langle Q \rangle = \frac{1}{Z} \sum_\mu Q_\mu e^{-\beta E_\mu}. \quad (1.6)$$

From thermodynamics it can be shown that the Helmholtz free energy,  $F$ , which is a measure of the ‘useful’ work obtainable from a thermodynamic system at a constant temperature, volume, and number of particles, can be written as,

$$F = U - TS = -k_B T \ln Z, \quad (1.7)$$

where  $U = \langle E \rangle$  is the total energy of the system,  $T$  is the temperature, and  $S$  is the entropy. Entropy is a measure of the number of microscopic configurations available to a system in a certain state. The last statement was first written formally by Max Planck around 1900 [2] as,

$$S = k_B \ln W. \quad (1.8)$$

although it was already formulated by Ludwig Boltzmann between 1872 and 1875. Here,  $W$  is the number of microscopic configurations of a system in a certain thermodynamic state. As the free energy is directly related to the partition function,  $Z$ , it is evident that it is a very important quantity, and indeed its measurement is the objective of many research projects, especially in simulations [3, 4]. A thermodynamic system reaches equilibrium by minimizing its (Helmholtz) free energy. From eq. (1.7), we see that this can be achieved by e.g. minimizing the total energy,  $U$ ; the energy  $U$  is associated with interactions between constituents, and, thus, a system can minimize its total energy by minimizing the distance between particles that attract, or maximize it for particles that repel each other. An alternative, is to maximize the entropy,  $S$ , which from eq. (1.8), we see that this can be achieved by increasing the number of configurations available to the system. This is also the reason it is easy to break eggs but not to put the pieces back together; the broken pieces can be arranged in more configurations than the egg itself.

## 1.3 Phase Transitions and Critical Phenomena

Having discussed the meaning of equilibrium, we proceed by discussing the classification of an equilibrium state of a system in what is generally known as phases. Often, the term ‘phase’ is used to denote a *state of matter*, i.e. one of the four distinct (basic) forms that matter can take: solid, liquid, gas, and plasma. A state of matter, though, such as a solid, can be in one of several different phases. Thus, the equilibrium states of a system are usually classified according to the microscopic order of its constituents, which can be positional and orientational, and either short- or long-ranged. The type of symmetries present in a certain phase has important implications for the properties of that phase. As an example, a substance in the solid state, will show long-range order of its constituents, in all three dimensions. The presence of long-range order can be determined by e.g. scattering light off of the material. The scattered light ought to show Bragg peaks ordered in patterns representative of the type of order in the system. A certain type of phase that is pertinent to this thesis, is the so-called *mesophase*. A mesophase is a state of matter that sits in between the crystalline and liquid phases. It possesses long-range positional order in less than the three spatial dimensions. Examples of mesophases include liquid crystals, which are used in displays, and lipid bilayers in cell membranes of living organisms.

We mentioned that the equilibrium state of a system is classified as a certain phase based on its inherent symmetries. Under certain conditions, the stable (equilibrium) state of a system might be a coexistence between phases. This can happen when a system transitions between two different phases. An example of phase coexistence from everyday life is when water reaches its boiling point temperature. When this happens, the water (liquid) coexists with steam (gas). Phase transitions may fall into two basic categories: first-order, and second-order or continuous phase transitions, where at transitions of the first category we encounter phase coexistence. Paul Ehrenfest classified phase transitions according to the behavior of the free energy, introduced in section 1.2. According to Ehrenfest, in first-order phase transitions, the first derivative of the free energy exhibits a discontinuity. The first derivative of the free energy are thermodynamic observables such as the density. On the other hand, in continuous phase transitions, the first derivative does not show a discontinuity. We should take the opportunity, here, to mention once more how important the free energy is. Knowledge of the free energy of a system not only allows us to calculate the order of phase transitions, but also the range of occurrence of these phases. The discontinuities in physical behavior which occur when a system undergoes a phase transition has always been a heated research topic for many scientists. Phenomena associated with the approach of a critical point (also known as critical phenomena), such as the liquid-vapor critical point, or the critical point of ferromagnetic materials, have been especially interesting for reasons we will discuss.

A historically important model in the study of phase transitions is the well known Ising model, named after physicist Ernst Ising. The Ising model was actually invented by physicist Wilhelm Lenz in 1920 who gave it as a problem to his student, Ernst Ising. The model consists of a lattice where each site,  $i$ , can take the value  $s_i \in \{+1, -1\}$ , which represents the direction of spins in a ferromagnet. Here,  $i$  denotes the coordinate of the site. Each lattice site may interact with adjacent lattice sites, which we simply call its

*nearest neighbors.* Given a certain lattice configuration, the energy of the *standard* Ising model is given by the Hamiltonian function,

$$\mathcal{H} = -J \sum_{\langle i,j \rangle} s_i s_j - \mu \sum_i s_i, \quad (1.9)$$

where the sum is over nearest-neighbor pairs  $\langle i,j \rangle$ ,  $J > 0$  is the ferromagnetic coupling constant, and  $\mu$  is an external field. From eq. (1.9), we see that nearest-neighbor pairs having the same lattice value, corresponds to an energy  $-J$ , leading to attraction, while when their lattice values are opposite, the energy is  $J$ , leading to repulsion. This is a simplified view of how a ferromagnet works. The two-dimensional square lattice model with vanishing external field,  $\mu = 0$ , was first solved exactly by Lars Onsager in 1942 and was published in 1944 [5]. The model exhibits a continuous phase transition at critical temperature  $k_B T_C = 2J / \ln(1 + \sqrt{2})$ , between an ordered and a disordered phase. At high temperatures,  $T \gg T_C$ , the interactions between the nearest-neighbor pairs become negligible, and thus the spins of the lattice will be randomly oriented. The magnetization of the ferromagnet in this case, will vanish,  $M = \sum_i s_i = 0$ . While approaching the critical point at  $T_C$ , the nearest-neighbor interactions become increasingly important, leading to a first-order phase transition to a state where most spins are aligned in either the positive,  $M > 0$ , or the negative,  $M < 0$ , direction. Typical configurations above and below the critical temperature are shown in figure 1.1.

If we make the substitution  $s_i \rightarrow (s_i + 1)/2$ , lattice sites may now take the values  $s_i \in \{0, 1\}$ , which could represent the presence of an atom. Note that the substitution results in an additional term to the Hamiltonian, which is irrelevant, as only the energy differences of different states are important. Nearest-neighbor atoms, then, attract each other with strength  $J/4$ . This is essentially a square-well interaction, which is a very coarse-grained approximation of a typical interatomic interaction potential between neutral atoms, see figure 1.1. The two phases with  $M < 0$  and  $M > 0$  described in the previous paragraph can then be interpreted as a gas and a liquid phase. This interpretation of the Ising model is also known as a lattice gas. We will use the Ising model as a model for a binary solvent mixture in chapters 2, and 3.

As we mentioned earlier, phenomena of significant scientific importance occur close to the critical point of a phase transition. Critical phenomena take place when the phase transition is continuous, although not exclusively (at a first-order phase transition between an ordered and a disordered phase, the interface between the two phases can undergo a continuous phase transition [6]). An important quantity, here, is the correlation length,  $\xi$ , which becomes system size dependent upon approach of the critical point, and diverges in the thermodynamic limit, i.e. at the limit of infinite system size. The correlation length signifies the characteristic size of regions in a system that behave similarly. As an example, in the Ising model, it is the characteristic size of clusters of lattice sites with the same value,  $s_i$ , as shown in figure 1.1(b). This ‘clustering’, which is enhanced as the critical point is approached, is also known as critical fluctuations. In the Ising model, the correlation length diverges as,  $\xi \sim |T - T_C|^\nu$ , where  $\nu$  is a so-called critical exponent. The divergence of the correlation length renders the microscopic details of the system irrelevant – diverging observables behave as  $Q(T) \propto (T - T_C)^\alpha$  for some critical exponent  $\alpha$ . These critical exponents are characteristic of the universality class of the system. The

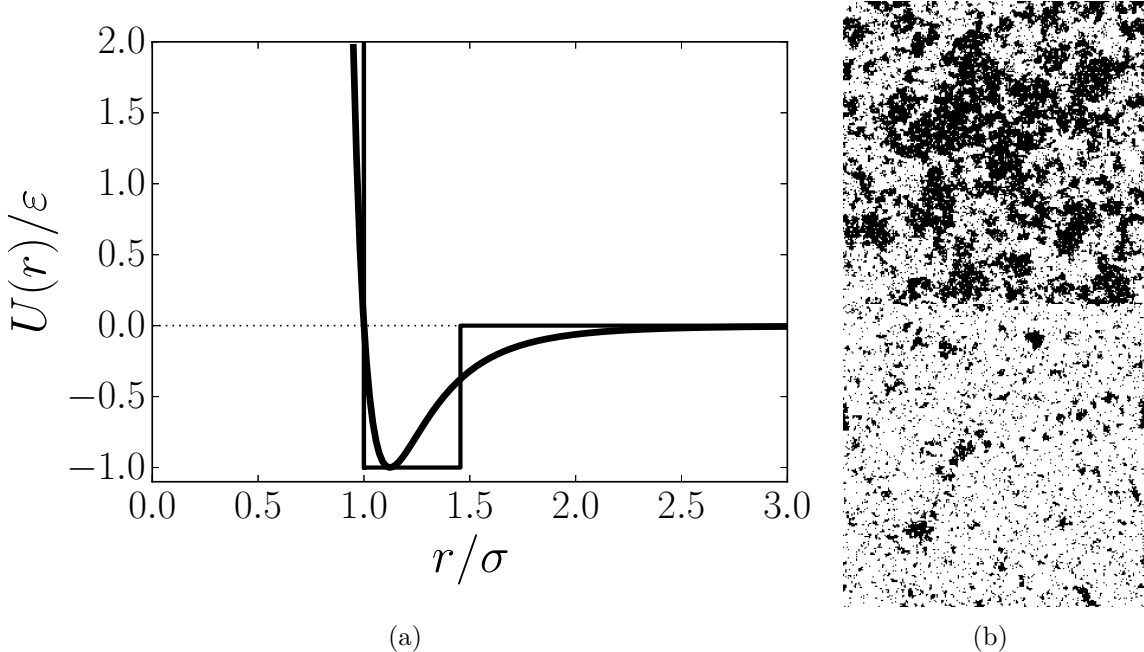


**Figure 1.1:** (a) Lennard-Jones potential,  $U(r) = 4\epsilon [(\frac{r}{\sigma})^{12} - (\frac{r}{\sigma})^6]$ , which is an approximation of the typical interaction between a pair of neutral atoms or molecules of diameter  $\sigma$ . (b) Typical configurations from Ising model simulations at  $\tau = 0.05$  (top) and  $\tau = -0.025$  (bottom), where  $\tau = (T - T_C)/T_C$ , is the reduced temperature. The top configuration is above the critical temperature, i.e. in the mixed state, while the bottom one is in the one-phase state. The temperatures are chosen such that the bulk correlation lengths are equal.

universality class, is a class of systems that behave in the same way at the critical point. Fluids typically fall in the 3D Ising universality class.

## 1.4 Colloids, Nanoparticles, and Suspensions Thereof

With the huge technological leaps of the last century, we were able to ‘minify’ virtually everything. We are now able to synthesize particles of various shapes at the nano and micrometer scale [7–26]. In 1861 Thomas Graham coined the term colloid (from the Greek  $\chiόλλα$  (/kóla/) which means “glue”) to describe Francesco Selmi’s “pseudosolutions”. The term emphasizes their low rate of diffusion and lack of crystallinity. Graham deduced that the low rate of diffusion implied that the particles were fairly large — at least 1 nm in diameter. On the other hand, the failure of particle sedimentation implied an upper size limit of 1 μm. Graham’s definition of the range of particle sizes that characterize the colloidal domain is still widely used today. The term nanoparticle is usually reserved for particles between 1 and 100 nanometers in size. Nanoparticles and colloids are of great scientific interest as they are, in effect, a bridge between bulk materials and atomic or molecular structures. A bulk material should have constant physical properties regardless of its size, but at the nano-scale size-dependent properties are often observed. Thus, the properties of materials change as their size approaches the nanoscale and as the percentage

of the surface in relation to the percentage of the volume of a material becomes significant.

Today colloid science is the study of systems involving small particles of one substance suspended in another. Suspensions in liquids form the basis of a wide variety of systems of scientific and technological importance, including paints, ceramics, cosmetics, agricultural sprays, detergents, soils, biological cells, and many food preparations. As a result of their surface chemistry, colloids suspended in a fluid with a gas-liquid phase transition, usually have a preference for the liquid phase, or one of the two components of a binary solvent mixture. We say then, that the colloid ‘prefers’ one of the components. Due to this preference a film of the preferred component gets adsorbed at the colloid surface. The existence and size of this adsorbed film, depends strongly on the state of the solvent and the bulk correlation length [27, 28] – as we mentioned in section 1.3, as the critical point is approached, the bulk correlation length diverges, which leads to what is known as critical adsorption. When two such colloids are then brought together, the adsorbed films are expected to interact with each other in a non-trivial manner, inducing an effective interaction between the colloids, with a characteristic length proportional to the film thickness [27, 29–31]. For high enough colloid concentrations, the effective interaction leads to aggregation of the colloids [32]. Other well-known examples of effective interactions include depletion, arising from the presence of additional, smaller components (depletants), and the Derjaguin-Landau-Verwey-Overbeek (DLVO) interaction arising from screening by counterions in the case of a charge-stabilised colloidal suspension. We will delve deeper in adsorption-induced effective interactions between colloidal particles in chapters 2 and 3.

Colloids suspended in liquids, are small enough to be affected by random collisions with the smaller solvent atoms. The random motion generated by these collisions is known as *Brownian motion*, after the botanist Robert Brown who, in 1827, while looking through a microscope at particles trapped in cavities inside pollen grains in water, observed the particles moving through the water but was not able to determine the mechanisms causing this motion [33]. Although the idea that matter is made up of discrete units dates back to ancient Greece, it was not until Dalton, in 1803, proposed his atomic theory [34]. Thus, it took some time to develop a theory explaining the observed motion. In 1905, Albert Einstein published his theory explaining in detail the way water molecules caused the apparent Brownian motion. Jean Baptiste Perrin was awarded the Nobel prize in 1926 for the experimental verification of Einstein’s theory, which was published in 1908 [35]. In colloidal systems, Brownian motion ensures that the colloids explore the surrounding space so that the system quickly finds its equilibrium state. As we shall discuss, certain computer simulation methods exploit this fact to efficiently sample the space of possible configurations. Additionally, as we will show in this thesis, and as the title reveals, order can arise from the chaotic Brownian motion and random fluctuations.

## 1.5 Salt and Electrostatic Interactions in Solutions

In everyday life, salt refers to the mineral composed mainly of sodium chloride ( $\text{NaCl}$ ), and is commonly used to add taste to food. In chemistry, a salt is a more general term which describes an ionic compound composed of cations and anions such that it is overall

electrically neutral. When a salt is dissolved in a solvent, it dissociates into its ionic constituents. This solution is commonly known as an electrolyte solution. Most natural systems contain some amount of salt which allows for important effects, such as osmosis which is vital for biological systems. Examples of charged systems are suspensions of sulfonated latex spheres, gold colloids, clay sheets, DNA and polyelectrolytes (charged polymers).

In colloidal suspensions, the preference of the colloids for certain solvent species, creates interfaces, which may be diffuse depending on the thermodynamic state of the mixture. Furthermore, the dissolved ions may also have a certain preference for a solvent species, leading to complex phenomena. It is well known that the addition of salt in a solvent mixture changes its interfacial tension; decreasing the surface tension allows the two solvent phases to mix more easily, which is also the reason that the addition of a surfactant, such as soap, in water, helps remove oil and grime. In a colloidal suspension where the colloids are aggregated, this results in reversing the colloidal aggregation by decreasing the strength of the effective solvent-mediated interactions due to the adsorbed solvent films [36]. The addition of salt also has the effect of screening the Coulombic interactions between charged colloids. In some cases, the effective interaction between like-charged colloids may even, unintuitively, become attractive [37].

Electrolytes, being ubiquitous as alluded to above, have been studied for a long time, but due to the long range of the Coulombic interactions and the big number of different types of components, progress has been difficult. An important development has been the calculation of ion distributions around charged surfaces. The traditional approach towards charged systems has been the Poisson-Boltzmann (PB) formalism, which uses a mean-field approach to calculate ion distributions from the Poisson-Boltzmann equation [38]. The PB method becomes asymptotically exact in the limit of weak surface charges, low ion valency, and high temperature, at least in the absence of other interactions. In all other cases, fluctuations become important, and a mean-field description can not provide an accurate picture, but improved theories have been developed recently [39, 40]. Another important development, is the DLVO theory [41–43]. The theory quantitatively explains the aggregation in colloidal suspensions, and describes the force between charged surfaces interacting through a liquid medium. It combines the effects of the van der Waals attraction and the electrostatic repulsion due to the way ions distribute themselves close to charged interfaces. The ‘van der Waals’ force, is a short-ranged weak intermolecular force, attributed mainly to the dipole fluctuations of other molecules.

In this thesis, in chapter 4 specifically, we will look into antagonistic salt solutions. An antagonistic salt is a salt in which the positive and negative ions have a preference for different solvent species when dissolved in a binary solvent mixture. This system was predicted to exhibit mesophases as a result of the coupling of the fluctuations of the solvent mixture and the ions [44].

## 1.6 Liquid Crystals

In section 1.3, we mentioned a specific class of mesophases known as liquid crystals. The two words, *liquid* and *crystal*, are incompatible, but instead, they reflect the fact that

liquid crystals are in a state in between liquids and crystals; they possess long-range orientational order and some or no degree of long-range positional order [45]. There are only a few types of liquid crystals, and they all possess remarkable optical properties. Due to these properties, liquid crystals are easily recognizable under a microscope with a polarizing filter.

We now review the various types of liquid crystals that have been discovered, in increasing positional order. The liquid crystal with the lesser degrees of long-range positional order, is the *nematic* phase. The word nematic comes from the Greek νήμα (/nima/), which means “thread”. This term is associated with the thread-like structures typically seen under the microscope. In a nematic phase, the particles are usually rod-shaped and align their long axes, but their center of mass positions are randomly distributed as in a liquid. In some cases the particles also align a secondary axis [46]. This is known as a biaxial nematic liquid crystal. Another possibility is that the particle orientations twist along the average direction of the system. This variant of the nematic phase is called *chiral* from the Greek word for hand, χείρ (/cir/), because the winding is either left- or right-handed. Moving up a dimension, the *smectic* liquid crystals show long-range positional order along one dimension in a layered structure. The layers themselves are positionally disordered, but possess various degrees of inter- and intra-molecular long-range orientational order. The particles may simply be aligned along a common director, twist between layers, etc. The various smectic phases are labelled with a letter of the alphabet, with the different smectic phases ranging from smectic-A, to smectic-L [47]. Finally, if a system shows long-range positional order along two dimensions, it is known to be in the *columnar* liquid crystal phase. These can again be distinguished on the basis of their inter- and intra-columnar order, as well as the particle orientations. The liquid crystals described above, can be divided into *thermotropic* and *lyotropic* liquid crystals. Thermotropic liquid crystals consist mainly of organic molecules and occur in a certain temperature range. If the temperature is too high, thermal motion will destroy the delicate cooperative ordering, pushing the material into a conventional isotropic liquid phase. At too low temperatures, most materials will form a standard crystalline structure. Examples of *lyotropic* liquid crystal are colloids, viruses, proteins, and detergents, which show liquid crystalline behavior in certain concentration ranges.

In chapter 4, we will show a binary solvent mixture with added antagonistic salt, exhibiting of different lyotropic liquid crystalline phases. In chapters 5,6, we will instead investigate hard-particle systems exhibiting a range of thermotropic liquid crystalline phases.

## 1.7 Hard-Particle Model

In section 1.2 we mentioned that one way to minimize the free energy, is by maximizing the entropy. It is, then, scientifically instructive to envision a model where the total energy of the system is fixed. This way we can study the isolated effect of entropy. Such models have existed in the scientific literature since around 1924, and were first used to model a simple gas [48]. The particles in the model are called ‘hard’ because they behave as macroscopic rigid bodies, interacting solely through the exclusion of their volumes.

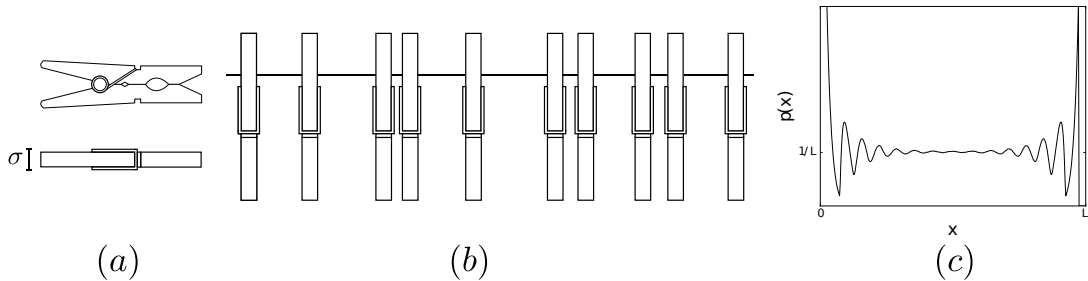


**Figure 1.2:** (a) Diagram of a clothespin of width  $\sigma$ . (b) Example of a random configuration of  $N = 10$  clothespins on a washline of length  $L = 20\sigma$ . (c) Probability,  $p(x)$ , of finding a clothespin at position  $x$  of the washline. The plot is the result of a simulation of  $N = 15$  pins, on a washline of length  $L = 20\sigma$ . The probability shows oscillatory behavior, with increased probability of finding a pin close to the end-points of the line.

This type of interaction for e.g. a pair of hard spheres with diameter  $\sigma$  at a distance  $r$ , is formally written as,

$$\beta V(r) = \begin{cases} 0, & r > \sigma \\ \infty, & r \leq \sigma \end{cases} \quad (1.10)$$

Hard-particle models were only used to model fluids until 1949, when Onsager was the first to show that a discontinuous phase transition could take place by means of shape only [49]. The system he studied was a system of infinitely thin rods, which showed a transition from an isotropic liquid to a nematic liquid crystal. It was not until Kirkwood in 1951 [50] showed that a system of hard spherical particles could crystallize, that we knew that such entropy-driven phase transitions were as rich as standard phase transitions. Only three years later, in 1954, Rosenbluth and Rosenbluth performed the first Monte Carlo (see section 1.8) simulation of 256 hard spheres, qualitatively confirming Kirkwood's results [51]. The simulations took around 150 hours on MANIAC in Los Alamos. A few years later, in 1957, Alder and Wainwright performed a computer simulation of hard spheres using the ‘Molecular Dynamics’ simulation method [52], and confirmed the freezing transition of hard spheres, but found quantitative disagreement with the Rosenbluths. Alder and Wainwright found that even 32 hard spheres were enough to get accurate results. Wood and Jacobson, the same year, confirmed Alder and Wainwright’s results simulating only 32 hard spheres using the Monte Carlo method. They attributed the discrepancies to the fact that the Rosenbluths used a larger number of particles, making it harder for the simulations to reach equilibrium in a timely fashion.

The simplest hard-particle model that showcases the unintuitive effects of entropy, is the so-called random clothespin model [53], which can be alternatively viewed as a one-dimensional hard-sphere model, and is also known as a Tonks gas, due to Lewi Tonks who studied the model in 1936 [54]. In this model, clothespins of width  $\sigma$  (see figure 1.2 (a)), are attached to a washing line of length  $L$  at random positions. An example of a random configuration is seen in figure 1.2 (b). The clothespins, being ‘hard’, are not allowed to overlap each other. In figure 1.2 (c), we have plotted the probability,  $p(x)$  of finding a pin at position  $x$ , for 15 clothespins of width  $\sigma$ , and a washing line of length  $L = 20\sigma$ . We see that the probability is oscillatory and, on average, higher close to the line ends. This is a rather mysterious result, showcasing the ramifications of entropy.

## 1.8 The Monte Carlo Simulation Method

As both theory and experiments have various tools at their disposal, so do computer simulations. One such tool which will be used throughout this thesis, is the so-called Monte Carlo method. The Monte Carlo method stems from the same roots as statistical physics itself, and relies on random sampling to solve problems that might even be deterministic. It is very useful for simulating systems with many degrees of freedom, where calculating all possible outcomes would otherwise be impossible, and is an especially important tool in statistical physics. A standard example of the use of the Monte Carlo method, is estimating the value of  $\pi$ , by generating random points within a square, and calculating the ratio of points that lie within the inscribed circle. Here, each generated point is generated independently from the previous ones. This is called direct sampling. A different sampling method used often in Monte Carlo simulations, is called Markov-chain sampling. In Markov-chain sampling, each subsequent sample is generated by modifying the previous one.

The modern version of the Markov-chain Monte Carlo method was invented in the late 1940s by Stanislaw Ulam, while he was working on nuclear weapons projects at the Los Alamos National Laboratory. Immediately after Ulam's breakthrough, John von Neumann understood its importance and programmed the ENIAC computer to carry out Monte Carlo calculations. Being secret, the work of von Neumann and Ulam required a code name. A colleague of von Neumann and Ulam, Nicholas Metropolis, suggested using the name Monte Carlo, which refers to the Monte Carlo Casino in Monaco where Ulam's uncle would borrow money from relatives to gamble. Monte Carlo methods were central to the simulations required for the Manhattan Project, though severely limited by the computational power at the time. The scientific community quickly realized the power of the Monte Carlo method [51, 55].

The Monte Carlo method is not very specific in what way states should be sampled. It is compelling to sample the states of our model, based on their importance. This is called *importance sampling*. From statistical mechanics, we know that at equilibrium, a state,  $\mu$ , has probability,  $p_\mu$ , equal to the Boltzmann distribution (eq. (1.4)). If states are selected with this probability, then our estimate of the observable  $Q$  is,

$$Q_M = \frac{1}{M} \sum_{i=1}^M Q_{\mu_i}, \quad (1.11)$$

where the sum is over the  $M$  states,  $\mu_i$ , chosen with probability equal to the Boltzmann distribution. Note that the estimate,  $Q_M$  is independent of the partition function,  $Z$ . This flexibility of choosing the probability distribution allows for some efficient simulation algorithms.

In the Markov chain Monte Carlo method, a new state,  $\nu$ , is generated from the current state,  $\mu$ , with a probability  $P(\mu \rightarrow \nu)$ , which is also called a transition probability. As the system needs to transition to a new state, or stay in the same state, the transition probability should be normalized,

$$\sum_{\nu} P(\mu \rightarrow \nu) = 1 \quad (1.12)$$

where the sum is over all states, including state  $\mu$ . An important point here, is the ergodic hypothesis of physics (or ergodicity), which states that, given enough time, a system in a certain state, should be able to access all other states. Ergodicity allows one to set arbitrary transition probabilities, as long as there is always a path from each state to each other state. Lastly, one more condition is imposed to ensure that our choice of transition probabilities will lead to the correct Boltzmann distribution when equilibrium is reached. The condition is widely known as detailed balance [56] and is sufficient, but not necessary, to ensure the correct distribution is sampled. Detailed balance is written as,

$$p_\mu P(\mu \rightarrow \nu) = p_\nu P(\nu \rightarrow \mu) \quad (1.13)$$

which says that the probability flux from a state  $\mu$  to a state  $\nu$  should be equal to the probability flux from state  $\nu$  to state  $\mu$ . As we mentioned, this condition is sufficient but not necessary. A less strict condition exists, called *global balance*, which is less intuitive, but can be used to create very efficient sampling algorithms [57]. For generating the Boltzmann distribution, the condition, eq. (1.13) becomes,

$$\frac{P(\mu \rightarrow \nu)}{P(\nu \rightarrow \mu)} = \frac{p_\nu}{p_\mu} = e^{-\beta(E_\nu - E_\mu)}. \quad (1.14)$$

A useful technique from statistics is the *rejection sampling* technique. It allows one to easily sample a probability distribution by generating a simpler one and rejecting the samples that are unwanted. As a simple geometric example, suppose we would like to generate a random point within the unit circle. This can be done by generating random points  $x, y$  in the unit square and rejecting points for which  $x^2 + y^2 > 1$ . This concept can be applied to the transition probabilities, by writing it as the product of the probability of selecting a certain transition,  $g(\mu \rightarrow \nu)$ , and the probability of accepting the transition,  $a(\mu \rightarrow \nu)$ ,

$$P(\mu \rightarrow \nu) = g(\mu \rightarrow \nu)a(\mu \rightarrow \nu). \quad (1.15)$$

A frequently used prescription for choosing the acceptance probabilities, is the *Metropolis criterion*, which was introduced by Nicolas Metropolis *et al.* in 1953 and is based on equation 1.14 so that detailed balance is ensured and the Boltzmann distribution is correctly generated. Given a chosen set of selection probabilities, the Metropolis criterion is written as,

$$a(\mu \rightarrow \nu) = \min \left[ 1, \frac{p_\nu g(\nu \rightarrow \mu)}{p_\mu g(\mu \rightarrow \nu)} \right], \quad (1.16)$$

The Metropolis criterion will be used in all Monte Carlo simulations presented in this thesis.



## 2

---

# Critical Casimir Interactions and Colloidal Self-Assembly in Near-Critical Solvents

---

A binary solvent mixture close to critical demixing experiences fluctuations whose correlation length,  $\xi$ , diverges as the critical point is approached. The solvent-mediated (SM) interaction that arises between a pair of colloids immersed in such a near-critical solvent can be long-ranged and this so-called critical Casimir interaction is well-studied. How a (dense) suspension of colloids will self-assemble under these conditions is poorly understood. Using a two-dimensional lattice model for the solvent and hard disks to represent the colloids, we perform extensive Monte Carlo simulations to investigate the phase behaviour of this model colloidal suspension as a function of colloid size and wettability under conditions where the solvent reservoir is supercritical. Unlike most other approaches, where the solvent is modelled as an implicit background, our model employs an explicit solvent and treats the suspension as a ternary mixture. This enables us to capture important features, including the pronounced fractionation of the solvent in the coexisting colloidal phases, of this complex system. We also present results for the partial structure factors; these shed light on the critical behaviour in the ternary mixture. The degree to which an effective two-body pair potential description can describe the phase behaviour and structure of the colloidal suspension is discussed briefly.

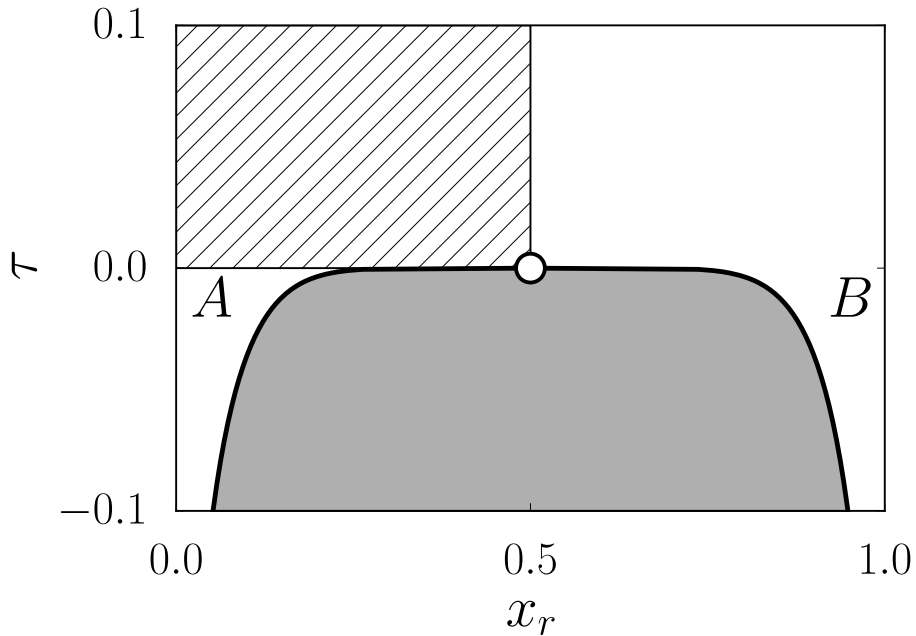


**Figure 2.1:** Phase diagram of a binary  $AB$  solvent mixture in the reduced temperature,  $\tau = (T - T_c)/T_c$ , versus composition,  $x_r$ , representation. The grey area denotes the two-phase region, where the solvent mixture demixes in an  $A$ -rich and a  $B$ -rich phase. The phases coexist on the binodal (solid line) and the critical point is indicated by the white circle. The hatched box indicates the (supercritical,  $A$ -rich) region investigated in this study.

## 2.1 Introduction

Colloidal particles suspended in a solvent can display a rich variety of effective interactions. Well-known examples include depletion, arising from the presence of additional, smaller components (depletants), and the Derjaguin-Landau-Verwey-Overbeek (DLVO) interaction arising from screening by counter-ions in the case of a charge-stabilised colloidal suspension. Theoretical treatments of effective interactions between colloids usually proceed by tracing out the degrees of freedom of the smaller components, i.e. depletants and ions, assuming that the underlying molecular solvent is merely an ‘inert’ structureless background. However, there are several situations where the thermodynamic state of the solvent plays a key role leading to characteristic solvent-mediated (SM) interactions between colloids. In particular, for certain colloidal suspensions long-ranged SM interactions can arise due to the local fluctuations of the solvent composition. An important situation occurs when the solvent is close to its (demixing) critical point. Then the SM interaction between two colloidal particles becomes long-ranged; the range is set by the (diverging) correlation length,  $\xi$ , of the solvent mixture. This is the situation we consider in the present chapter where we investigate the properties of a model of a ternary mixture that mimics colloidal particles suspended in an explicit binary solvent near its critical point. Here we describe the Monte Carlo (MC) simulation methods and present a comprehensive set of results for the phase behaviour and structural properties of the (lattice) model.

We motivate our study by recalling first the properties of a binary  $AB$  solvent mixture near its demixing critical point. Figure 2.1 shows a schematic phase diagram of such a mixture in the reduced temperature,  $\tau = (T - T_c)/T_c$ , versus composition,  $x_r = N_B/(N_A + N_B)$ , representation, with  $T$  the temperature,  $T_c$  the critical temperature, and  $N_{A(B)}$  the number of particles of solvent  $A(B)$ . The solvent has an upper critical solution temperature, denoted by the white circle. The critical point occurs at  $\tau = 0$  and at critical composition,  $x_{r,c} = 1/2$ . For  $\tau < 0$  the phase diagram exhibits a two-phase region, where the solvent mixture demixes into an  $A$ -rich and a  $B$ -rich phase. The binodal in figure 2.1 is symmetric about  $x_r = 1/2$  as the solvent model employed here has Ising or lattice gas symmetry. The approach to criticality is signalled by the presence of fluctuations in the order parameter, in this case composition, occurring on increasing length scales, up to the bulk correlation length of the solvent,  $\xi$ . Sufficiently close to the critical point,  $\xi \sim |\tau|^{-\nu}$ , where  $\nu$  is a critical exponent characteristic of the particular universality class of the system.

Suppose now the solvent comes into contact with a substrate (plate), or a large colloidal particle, that prefers one of the solvent species, say  $B$ . The local composition of the solvent close to the surface will be enriched with that species. If the solvent is close to its critical point, the white circle in figure 2.1, the length scale over which the composition profile approaches the bulk composition is set by the correlation length,  $\xi$ . This is the well-known phenomenon of critical adsorption, see e.g. Ref. [28]. When the near-critical fluid is confined between two plates, or two large colloids, one expects that the critical adsorption at each surface will lead to interesting SM interactions. Indeed Fisher and de Gennes showed in 1978 [27] that when two plates, at a separation  $L \sim \xi$ , are immersed in such a solvent mixture these will experience a long-ranged SM interaction. Exactly at the critical point, the SM force between plates decays algebraically, i.e. as  $L^{-D}$ , where  $D$  is the bulk spatial dimension. The interaction is attractive if the two plates are identical or preferentially adsorb the same solvent species, but can be repulsive if they adsorb opposite species. In recent times this effect has been termed the *critical Casimir effect* [58–60], due to the similarities it shares with the celebrated Casimir effect. In the latter, an algebraically decaying force is induced between two conducting macroscopic bodies as a consequence of confining quantum fluctuations of the electromagnetic field [61]. Theoretical and simulation studies of critical Casimir interactions in planar wall confinement are numerous; see for example Refs. [58–60, 62, 63]. The scaling behaviour of the SM force, i.e. how it depends on  $L/\xi$ , has been determined for various universality classes and various choices of boundary conditions. Results for two parallel plates can be extended to a sphere near a plate and to a pair of large spherical colloids using the Derjaguin approximation [64]. Accepting concepts of universality, and that real fluid mixtures lie in the 3D Ising universality class, we can argue that from theory and simulation we now have a rather good description of the effective pair interaction, at large inter-particle separations, between an isolated pair of identical colloidal particles suspended in a solvent at its critical composition  $x_{r,c}$ . For off-critical compositions the scaling behaviour of the critical Casimir interaction is more complicated but there has been recent progress in ascertaining this; see Refs. [65–67] and references therein. Moreover, the results of direct experimental measurements of the critical Casimir force between a colloid and a planar substrate, using total internal reflection microscopy [37, 68], confirm the form of the pre-

dicted scaling functions. A forthcoming review [69] provides a comprehensive account of this subject.

Suppose now we move up in complexity and enquire what is the phase behaviour and structure of a dense suspension of identical colloids in the same near-critical solvent. The critical Casimir effect might well be expected to play an important role in colloidal aggregation and phase behaviour; long-ranged SM interactions should be present close to the critical point of the solvent. The history is interesting. Probably the first experimental observation of colloidal aggregation in a near-critical solvent goes back to Beysens and Estève [32] in 1985. In this experiment, silica spheres, with diameter 160 nm, preferentially adsorbing lutidine, were suspended in a water-lutidine mixture. Beysens and Estève measured the temperature at which the silica particles began to form aggregates upon heating the ternary mixture, which allowed them to determine an ‘aggregation line’ in the composition-temperature diagram. This aggregation line resided on the water-rich side of the phase diagram and the authors first associated this with the prewetting line that might be linked with preferential adsorption of lutidine at a single macroscopic substrate. However, the line extended to temperatures in the one-phase region below the demixing critical point, which is not found for prewetting lines at a planar substrate. Note that the water-lutidine mixture exhibits a demixing phase transition above a lower critical temperature rather than demixing below an upper critical temperature, as shown in figure 2.1. Transcribing to our present model, the observed aggregation line extended to the region  $\tau > 0$ , on the A-rich side of the phase diagram supposing species B to be preferentially adsorbed on the colloids, indicated by the hatched region in figure 2.1. Several other experimental studies followed, using different solvents and colloids [70–76]. In addition the effect of adding salt was investigated [77] and it was found that adding sufficient  $Mg^{2+}$  ions resulted in the aggregation line flipping from the lutidine-rich phase to the water-rich phase. The phenomenon of reversible colloidal aggregation in near-critical solvents appears to be quite general. A brief review [78] summarizes the state of play up to 1999. Although the precise location of the aggregation line depends on a complex interplay of van der Waals (dispersion), screened Coulomb, and adsorption-induced long-ranged effective interactions, reversible aggregation appears to occur generally in near-critical binary solvents at compositions, near the binodal, that are poor in the species preferentially adsorbed by the colloidal particle. Note that this is the region of the solvent phase diagram where the critical Casimir attraction between two identical colloids is expected to be strongest [65, 79, 80].

Pertinent to our present study is the experimental work of Kaler *et al.* [73, 74] who argued that the system of colloids in a binary solvent mixture should be viewed as a true ternary mixture including full fractionation of the components of the solvent. On the theoretical side, Sluckin [81] had argued already in 1990 that colloidal aggregation should be regarded as phase separation in a ternary system. Löwen [82], Netz [83] and Gil *et al.* [84] followed this line, but focused on the subcritical,  $\tau < 0$ , region of the pure solvent reservoir, where capillary bridging between colloids brought about by wetting is likely to be the dominant mechanism in driving the colloidal aggregation. The view that reversible aggregation is a manifestation of colloidal phase transitions was reinforced strongly by experimental studies in 2008 by Guo *et al.* [85] who carried out SAXS studies on density-matched polystyrene particles in a solvent of water, heavy-water and picoline.

The measured structure factors revealed colloidal gas, liquid and fcc crystalline phases as the temperature was increased towards the solvent binodal at an off-critical composition. Maciolek and Dietrich [69] provide a valuable overview of early experimental and theoretical work.

The same article reviews recent studies, e.g. Refs. [65–67], which construct an effective pair potential between the colloids, incorporating the long-ranged critical Casimir attraction and some empirically determined short-ranged repulsion, that is then used to investigate the properties of a dense near-critical suspension. Specifically, by extracting the attractive part of the effective pair potential from MC simulations and using liquid state theories, Mohry *et al.* investigated the phase behaviour, structure and aggregation of an effective one-component model of a colloid-solvent mixture near the solvent’s critical point. The papers of Nguyen *et al.* and Dang *et al.* adopt a similar philosophy to Mohry *et al.* but use instead an effective pair potential extracted from experimental measurements of the colloid-colloid pair correlation function [86, 87]. The results are summarized in another topical review [88], more experimentally focussed, which outlines important and exciting possibilities for reversible colloidal particle assembly brought about by tuning the temperature and composition of an appropriate host solvent. The title of this review: ‘Critical Casimir Forces for Colloidal Assembly’ is revealing. Indeed the authors argue strongly that an effective pair potential description, which incorporates critical Casimir attraction, should be sufficient to capture most of the physics relevant for colloidal phase behaviour.

The extent to which a one-component description, incorporating only pairwise effective interactions between the colloids, might be accurate for a dense suspension is not at all obvious. Very close to solvent criticality, where the solvent correlation length  $\xi$  can be several times the colloid radius, the inter-particle forces are long-ranged, and one must expect that many-body effects are important. Consequently, in this regime, an effective pair potential description should break down — perhaps not in the qualitative description of colloidal phase behaviour but certainly in a quantitative description. At off-critical compositions, further from criticality, where  $\xi$  is considerably smaller than the colloid radius, one might hope that the effective pair potential description is better founded and this is the viewpoint taken in both recent reviews [69, 88].

In order to address such issues it is necessary to investigate in detail the phase behaviour of a ternary colloid-AB solvent mixture. Our present study is also motivated partly by work of Edison *et al.* who developed a mean-field theory, based on free-volume arguments [89], that describes the phase behaviour of the model we are presenting here; we shall allude to this later. We provide results for the effects of temperature, colloid size and wettability (strength of the preferential adsorption) on the phase behaviour of the ternary mixture and, in addition, we present some results for the effective pair interactions between colloids under different conditions of the solvent reservoir, that is in diffusive (osmotic) equilibrium with the suspension. Moreover, details on the computational methods are provided; these were not given in Ref. [90]. We focus on the supercritical,  $\tau > 0$ , region of the pure solvent mixture phase diagram, where wetting-induced interactions such as capillary bridging are absent. The latter can be very strong and could potentially mask the subtle effects of the critical Casimir interactions. This chapter is organized as follows: We describe our lattice model in Sec. 2.2. Sec. 2.3 provides information about

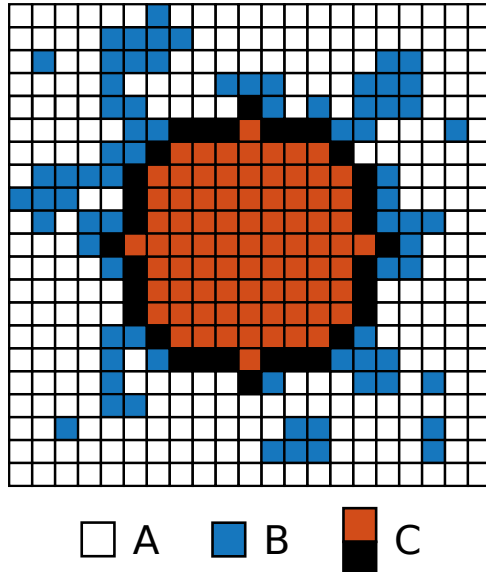


**Figure 2.2:** A schematic representation of the colloid-solvent model with the grid representing the lattice sites. White cells are occupied by solvent species  $A$  and blue cells by solvent species  $B$ . The brown (interior) and black cells belong to a single colloidal particle,  $C$ , of radius  $R = 6$ . Particles of species  $B$  adjoining the black cells experience an attractive interaction of strength  $\alpha\epsilon$ .

the simulation and analysis methods. This Section is aimed at readers who are interested in the important but more technical details of our MC study and might be skipped by those readers interested only in the results, which we present in Sec. 2.4. Finally, in Sec. 2.5, we summarize and make some concluding remarks.

## 2.2 Model

The aim of this chapter is to investigate, by means of computer simulations, the phase behaviour of colloids immersed in a near-critical binary solvent. However, simulations of colloids in a molecular solvent with a bulk correlation length that diverges upon approaching the critical point pose major challenges from a computational point of view, as very different length- and time-scales are involved. Moreover two steps precede our investigations of the colloid-solvent model, i) determining the phase diagram (binodal) and the critical point of the pure solvent and ii) obtaining a good understanding of the behaviour of the solvent adsorbed on the surface of a single model colloidal particle (interfacial properties). It is therefore highly advantageous to choose a model for which the bulk phase diagram and interfacial properties have been established already or can be carefully investigated. To describe the solvent, we choose an incompressible nearest-neighbour  $AB$  lattice model which is isomorphic to the well known lattice-gas model of fluids. From a computational standpoint, lattice-based models are highly favourable since they are easy to parallelize and are computationally highly efficient. The lattice-gas model has been used extensively to study wetting and capillary phenomena, and the effects of confinement between planar walls [91, 92]. By drawing analogies directly between a binary

solvent mixture and a one-component gas-liquid system with regard to phenomena such as complete wetting, capillary condensation, critical adsorption etc. [93] we are provided with a wealth of information on interfacial properties pertinent to our solvent mixture.

Upon approaching the critical point of the solvent, it is important to simulate sufficiently large systems to accommodate the diverging correlation length [56]. A direct consequence of the diverging correlation length is the critical slowing down of the dynamics. It thus becomes increasingly difficult to simulate fluids as their critical point is approached, although algorithms exist which try to alleviate these problems by operating on correlated clusters [94, 95]. The size asymmetry (big colloid versus small solvent molecule) in our system is also a serious computational challenge. These complications forced us to restrict the present study to two-dimensional systems, but a cluster algorithm is presented in chapter 3, which is able to overcome these challenges.

Thus, in our model of the solvent-colloid mixture, colloids are modelled as hard disks whose centres can undergo translational motion restricted to an underlying (solvent) lattice. The solvent and colloids also interact via nearest-neighbour interactions. Essentially, our model is an incompressible *ABC* mixture on a 2D square lattice, and shares many similarities with the lattice model used by Rabani *et al.*, to simulate the drying-mediated self-assembly of nanoparticles [96]. Our model also derives inspiration from the ‘finely discretized’ lattice model of Panagiotopoulos [97, 98]. To elaborate, colloids *C* are discretized hard disks (HD) with a radius *R*, measured in number of lattice sites, and occupy a set of sites  $S_C = \{r_i \mid d(r_i, r_C) \leq R\}$ , where  $r_C$  are the lattice coordinates of the disk,  $r_i$  are the coordinates of lattice site *i*, and the function  $d(a, b)$  calculates the absolute distance between *a* and *b* using the minimum image convention. The disks have only translational degrees of freedom, and their Hamiltonian  $H_C$  (in the absence of the solvent mixture) is zero for non-overlapping configurations, and is infinite if any pair of colloids overlap, or if a colloid and solvent site overlap. We assign to every lattice site *i* an occupancy number  $n_i \in \{0, 1\}$ . A lattice site *i* is occupied by a colloidal disk, and thus not available for a solvent species *A* or *B*, in the case  $n_i = 1$ . For occupancy number  $n_i = 0$ , lattice site *i* is not occupied by a colloidal disk and we assign an occupancy number  $s_i \in -1, 1$  which indicates if it is occupied by solvent species *A* or *B*, respectively. We consider only nearest neighbour interactions, and assign an energy penalty  $\epsilon/2 > 0$  for every nearest neighbour *AB* pair, to drive *AB* demixing at sufficiently low temperatures, and an energy gain of  $-\alpha\epsilon/2$  with  $\alpha \geq 0$  for every *BC* pair, to mimic preferential adsorption of solvent *B* on the colloid surfaces. The parameter  $\alpha$  measures the wettability of the colloidal disk. figure 2.2 illustrates the model. The total Hamiltonian reads

$$\begin{aligned} H = & H_C + \frac{\epsilon}{4} \sum_{\langle i,j \rangle} (1 - s_i s_j)(1 - n_i)(1 - n_j) \\ & - \frac{\alpha\epsilon}{4} \sum_{\langle i,j \rangle} n_i(1 + s_j)(1 - n_j) \end{aligned} \quad (2.1)$$

where the summation runs over the set of distinct nearest neighbour pairs  $\langle i, j \rangle$ . In the absence of colloids, the *ABC* model reduces to the simple lattice-gas, or *AB* model.

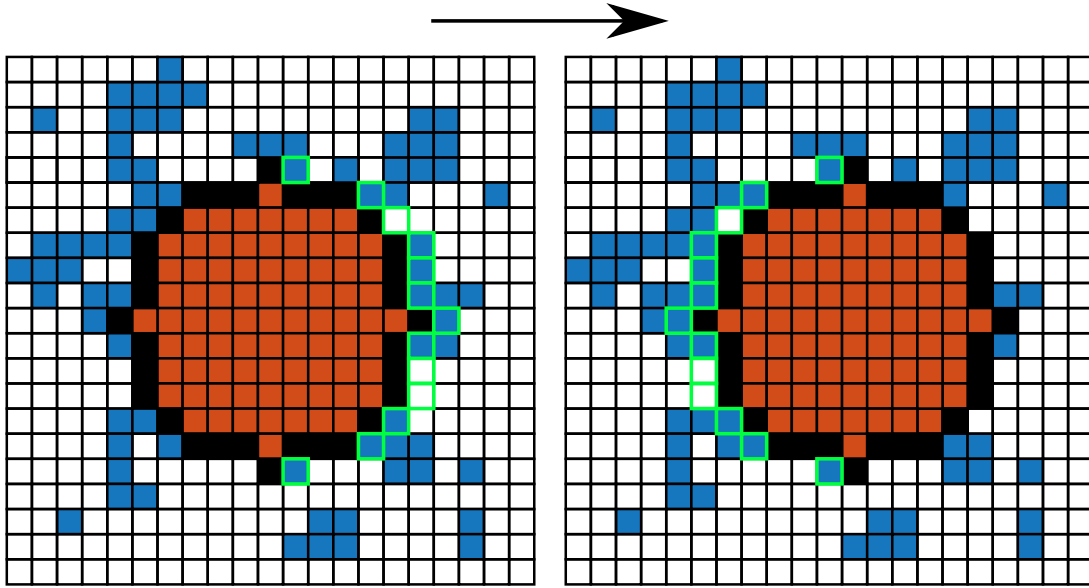


**Figure 2.3:** Illustration of the translation of a colloid. Here we attempt to move the disk by one lattice site to the right. Any sites that are occupied by solvent species  $B$  (blue outlined with green colour), are reflected with respect to the new disk position, resulting in the new configuration seen in the right figure.

## 2.3 Methods

In order to study the structure and phase behaviour of the  $ABC$  model of a binary solvent-colloid mixture, just described, we choose to use Monte Carlo simulations. To this end, the following Monte Carlo moves are employed:

- An attempt to flip the solvent occupancy  $s_i$  of every site, i.e. sites which have  $n_i = 0$ .
- An attempt to translate every colloidal particle in the system, along either the  $x$  or  $y$  axis.

The occupancy flip moves are accepted using the standard Metropolis criterion for changing the number,  $N_B$ , of sites occupied by  $B$ :

$$a(N_B \rightarrow N_B \pm 1) = \min \left[ 1, e^{-\beta(\Delta E \mp \epsilon \Delta \mu_s)} \right], \quad (2.2)$$

with  $\Delta E$  the difference in potential energy (Hamiltonian Eq. (2.1)) of the new and old configuration. The dimensionless quantity  $\Delta \mu_s = (\mu_B - \mu_A)/\epsilon$  denotes the chemical potential difference of solvent species  $A$  and  $B$ , and  $\beta = 1/k_B T$  is the inverse temperature, with  $k_B$  Boltzmann's constant. Note that the acceptance rule (2.2) depends on the chemical potential difference  $\Delta \mu_s$  as the total number of solvent species  $N_s = N_A + N_B$  is fixed, and thus  $N_B \rightarrow N_B + 1$  simultaneously means that  $N_A \rightarrow N_A - 1$ . Disk translations are handled using symmetry operations [94] to remove any disk-solvent overlaps. An attempt is made to move a disk in a random direction  $x$  or  $y$  by one lattice site. If no overlaps with other disks occur, the disk is translated and the sites outlined with a green colour in

figure 2.3, are reflected with respect to the new disk position. The move is then accepted using the Metropolis algorithm.

To determine the phase behaviour, we use the direct interfacial or coexistence simulation method [99] in combination with the grand-canonical staged-insertion (GCSI) Monte Carlo technique [100–102]. In spite of the simplicity of our model, a considerable amount of computational time is needed to collect data with sufficiently high accuracy. Below, we describe these techniques, tailored for the *ABC* model, in more detail.

### 2.3.1 Direct Coexistence Simulations

In the direct coexistence method, simulations are performed in the canonical ensemble at a thermodynamic state point that lies well inside the two-phase coexistence region of the ternary mixture. The system will therefore phase separate according to the lever rule. To facilitate the formation and subsequent stabilization of the interfaces between the two phases, an elongated simulation box with a typical aspect ratio of 2:1 is chosen. The densities of the coexisting phases can then be computed from the density profiles of the system. The direct interfacial simulation is computationally the least expensive method for determining phase coexistence when compared to alternative techniques. However, the method has several disadvantages: for finite-sized systems a significant fraction of particles are at or near the interface, and when a critical point is approached, the interface becomes very broad as the surface tension approaches zero. Therefore the simulations become inaccurate close to the critical point of the ternary *ABC* mixture. For our *ABC* model, we utilize this technique to determine gas-solid coexistence since alternative techniques that involve particle insertions, e.g., grand canonical or Gibbs ensemble Monte Carlo simulations, are not feasible in the case of crystal phases. In our direct coexistence simulations we treat the colloids canonically while the solvent is treated grand canonically, i.e. we fix the number of colloids  $N_C$ , the solvent chemical potential difference  $\Delta\mu_s$ , the volume  $V$  (or area, in the present case) of the system, and the temperature  $T$ . At fixed  $\Delta\mu_s$  and reduced temperature  $\tau$ , we run simulations at a series of colloid packing fractions,  $\eta$ . If the value of  $\eta$  lies between two bulk coexisting density values, phase coexistence is observed directly in the simulations. We can then estimate the densities of the coexisting phases from the average density profiles of the system in the direction perpendicular to the interface.

### 2.3.2 Grand Canonical Staged-Insertion Method

In order to get accurate estimates of the colloidal gas-liquid coexistence region of the phase diagram we perform grand canonical simulations, i.e. we fix  $\Delta\mu_s, V, T$ , and the colloid chemical potential difference,  $\Delta\mu_c = (\mu_c - \mu_A v_c)/\epsilon$ , with  $\mu_c$  the chemical potential of the colloids and  $v_c$  the number of lattice sites occupied by a single colloidal particle. Simulations in the grand canonical ensemble involve additional Monte Carlo moves which attempt to either insert or remove colloidal hard disks from the system. Due to the size asymmetry between the colloids ( $C$ ) and the solvent species, and the hard-core repulsion between the hard disks, the acceptance of such moves becomes prohibitively low. Recently, a technique which deals effectively with this issue was introduced by Ashton and Wilding

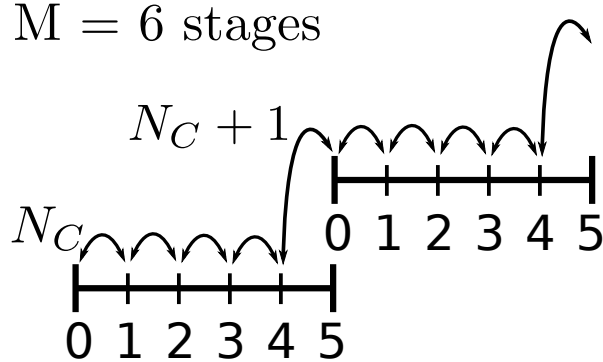


**Figure 2.4:** Allowable transitions for a ghost particle with  $M = 6$  stages. Note that a system with  $N_C$  colloids and a ghost at stage index  $m = M - 1$  (5 in the diagram), the stage at which the ghost becomes fully coupled, is equivalent to a system with  $N_C + 1$  colloids and a ghost at stage index  $m = 0$ , where the ghost is fully decoupled.

[100]. This is based on the expanded ensemble simulation technique, see Refs. [101, 102] for more details. Next, we describe the implementation of this method, called grand canonical staged-insertion (GCSI), for our *ABC* model.

The grand canonical partition function of the ternary system can be written as

$$\Xi = \sum_{\{\Omega\}} e^{-\beta(H - \epsilon\Delta\mu_s N_B - \epsilon\Delta\mu_c N_C)}, \quad (2.3)$$

where  $\{\Omega\}$  is the set of all allowed configurations of the lattice,  $N_C$  is the number of colloids. Due to the symmetries present in our model, the ternary *ABC* system is equivalent to a binary system where the amount of species *B* and *C* is controlled by fields  $\Delta\mu_s$  and  $\Delta\mu_c$ , respectively. The staged insertion method involves inserting the colloidal (large) particle in stages. That is, one could insert a small particle and grow it to the desired size, or insert an ideal-gas particle of the desired size and couple it to the system energetically in a series of stages. We use the latter method, and refer to the particle inserted in stages as the ghost particle. In principle there is no restriction on the number of ghost particles in the system, however, we employ a maximum of one ghost particle at any instant of the simulation.

A ghost particle can transition between  $M$  different stages, where stage  $m = 0$  is equivalent to a system of  $N_C$  colloidal particles and  $m = M - 1$  is equivalent to a system with  $N_C + 1$  colloidal particles. The ghost particle at a particular stage  $m$  interacts with the solvent particle in the following fashion: at stage  $m = 0$  the ghost particle is merely an ideal gas particle, with no interaction with the solvent particles, and at  $m = M - 1$ , the solvent particles at the surface of the colloid interact with an attractive interaction of strength  $\alpha$ , and solvent particles existing within the hard core experience an infinite repulsion. Following Ashton and Wilding [100] we introduce a stepwise potential for the intermediate stages. The ghost particle has an  $m$ -dependent field strength  $\alpha_m$  and an additional field, with strength  $\sigma_m$ , associated with the excluded-volume interaction of the ghost particle with the solvent sites. A typical set of stage-dependent fields used in our

simulations is

$$\alpha_m = \alpha \frac{m}{M - 1} \quad (2.4)$$

$$\sigma_m = \frac{m}{M - 1 - m}, \quad (2.5)$$

where we typically employ  $M = 6$  stages. Depending on the simulated state point, different forms of the fields  $\alpha_m$  and  $\sigma_m$  can provide better acceptance rates. The method increases slowly the coupling of the ghost particle to the system by interpolating the two fields, between the fully coupled and fully decoupled state.

The partition function of the system with the inclusion of a ghost particle is given by,

$$\Xi_m = \sum_{\{\Omega_m\}} e^{-\beta(H + H_m^G - \epsilon\Delta\mu_s N_B - \epsilon\Delta\mu_c N_C)} \quad (2.6)$$

where  $\{\Omega_m\}$  is the set of all allowed configurations including a ghost particle at stage  $m$ , and  $H_m^G$  is the interaction Hamiltonian of the ghost particle at stage  $m$ ,

$$H_m^G = -\frac{\alpha_m \epsilon}{4} \sum_{\langle i,j \rangle} g_i(1+s_j)(1-g_j) \quad (2.7)$$

$$+ \frac{\sigma_m \epsilon}{2} \sum_i g_i(1+s_i), \quad (2.8)$$

where  $g_i \in \{0, 1\}$ , denotes the presence of a ghost particle at lattice site  $i$ . Note that the grand canonical ensemble is a subset of the above ensemble. More specifically, this is the subset for which the stage index  $m = 0$ . The expanded ensemble partition function, is then simply defined as the sum of  $\Xi_m$  over the different stages,  $m$ ,

$$\Xi_E = \sum_{m=0}^{M-2} \Xi_m. \quad (2.9)$$

To simulate the system in the expanded ensemble, a Monte Carlo move is introduced which attempts to change the stage index, as shown in figure 2.4. The move is accepted using the Metropolis criterion with a probability given by,

$$a(\{N_C, M-2\} \rightarrow \{N_C + 1, 0\}) = \min \left[ 1, e^{-\beta(U_0^G - U_{M-2}^G) + \beta\epsilon\Delta\mu_c - \ln(N_C + 1)} \right] \quad (2.10)$$

$$a(\{N_C, 0\} \rightarrow \{N_C - 1, M-2\}) = \min \left[ 1, e^{-\beta(U_{M-2}^G - U_0^G) - \beta\epsilon\Delta\mu_c + \ln N_C} \right] \quad (2.11)$$

$$a(\{N_C, m\} \rightarrow \{N_C, m \pm 1\}) = \min \left[ 1, e^{-\beta(U_{m \pm 1}^G - U_m^G)} \right], \quad (2.12)$$

where  $U_m^G$  is the potential energy due to the interactions with the ghost at stage  $m$ , given by equation (2.7). During each sweep we perform  $k$  such moves. After every move, we equilibrate locally the solvent sites in a square of size  $(2R + 3) \times (2R + 3)$  centred around the position of the ghost particle, to facilitate the transition between stages.

### 2.3.3 Transition Matrix Monte Carlo Technique

As we mentioned earlier, the interface of the ternary mixture in the two-phase region becomes too diffuse for us to make reliable measurements close to the critical point using direct coexistence simulations. In order to determine the accurate phase coexistence in this case, we use the transition matrix Monte Carlo (TMMC) technique to calculate the particle number probability distribution  $P(N_C)$  in a grand canonical Monte Carlo simulation. The objective of the TMMC technique is to estimate the probability of observing the system at a certain value of a chosen macrostate variable,  $Y$ , i.e. energy, volume, density, etc. We employ this technique to determine phase coexistence but also the probability distribution of the distance between two colloids,  $P(\mathbf{r})$ , from which the effective colloid-colloid potential can be calculated. The TMMC technique is also used to determine the probability distribution of the number of  $BC$  surface interactions,  $m_B$ , around a colloid,  $P(m_B; \alpha)$ . This enables us to calculate the saturation point for the colloid wettability,  $\alpha$ , i.e. the value at which the colloid has essentially only species  $B$  solvent neighbours.

A TMMC simulation involves a regular simulation of the system with a few additional bookkeeping steps. After every move which attempts to change the macrostate,  $Y$ , of the system, regardless of whether the move is accepted, we update a collection matrix in the following fashion:

$$\begin{aligned} C(Y \rightarrow Y') &= C(Y \rightarrow Y') + a(y \rightarrow y') \\ C(Y \rightarrow Y) &= C(Y \rightarrow Y) + 1 - a(y \rightarrow y'), \end{aligned} \quad (2.13)$$

where the lower-case  $y$  denotes the microstate variable corresponding to the observed macrostate variable,  $Y$ . Periodically during the simulation the macrostate transition probability  $\pi(Y \rightarrow Y')$  is estimated as follows

$$\pi(Y \rightarrow Y') = \frac{C(Y \rightarrow Y')}{\sum_W C(Y \rightarrow W)}. \quad (2.14)$$

If we restrict transitions such that any macrostate has only two neighbouring macrostates, and provided the transition probabilities are estimated, the macrostate probabilities  $P(Y)$  can be calculated simply using the detailed balance condition

$$P(Y)\pi(Y \rightarrow Y') = P(Y')\pi(Y' \rightarrow Y). \quad (2.15)$$

In order to sample efficiently all macrostates, the acceptance probabilities are biased according to the multicanonical approach in the following fashion,

$$a_b(y \rightarrow y') = \min \left( 1, e^{\eta(Y') - \eta(Y)} a(y \rightarrow y') \right), \quad (2.16)$$

where  $\eta(Y) = -\ln P(Y)$ . We begin initially with a flat distribution for  $\eta(Y)$ . Then routinely as  $P(Y)$  is estimated, we update the biasing function and the simulations are continued until the distribution  $P(Y)$  converges within a certain acceptable tolerance.

In the grand canonical ensemble, knowledge of the particle number probability distribution,  $P(N)$ , allows one to calculate easily the densities of the two coexisting phases using histogram reweighting techniques [103]. For the GCSI simulations, we associate

the macrostate variable  $Y$ , with the pair  $\{N_C, m\}$ . The dimension of the collection matrix is  $(N_C^{max} \times M - 1) \times (N_C^{max} \times M - 1)$ . In order to improve the efficiency of the method we split the range  $[0, N_C^{max}] \times [0, M - 1]$  into several overlapping windows of size  $[N_C^i, N_C^{i+1}] \times [0, M - 1]$ , and simulate the windows in parallel. The macrostate probabilities,  $P(Y)$ , are then estimated by combining the probabilities from each window in the following manner,

$$\log P(Y_i) = \log P(Y_{I(i)}^{W(i)}) + \sum_{j=0}^{W(i)-1} \log P(Y_{n_j}^j), \quad (2.17)$$

where  $Y_i$  is the  $i$ th macrostate,  $Y_i^j$  is the  $i$ th macrostate of window  $j$ , and the functions  $W(i)$  and  $I(i)$  give the window, and index inside the window of macrostate  $i$ , respectively.  $Y_{n_i}^i$  is the last macrostate of window  $i$ , and  $Y_{n_i}^i = Y_0^{i+1}$ . Note that when  $Y_i = Y_{n_j}^j = Y_0^{j+1}$ , then  $W(i) = j + 1$ , and  $I(i) = 0$ . The particle number probability distribution,  $P(N_C)$ , then follows directly from  $P(\{N_C, m\})$ , by setting  $m = 0$ .

In calculating the two-body effective interaction,  $U(\mathbf{r})$ , one particle is kept immobile at position  $\mathbf{r} = (0, 0)$ , while the position of the second is used as the macrostate variable for the transition matrix. This allows us to calculate the effective interaction between a pair of colloids as,  $\beta U(\mathbf{r}) = -\ln[P(\mathbf{r})/P(\mathbf{r} \rightarrow \infty)]$ . As the particle is only allowed to translate to the nearest lattice sites, the problem of calculating the macrostate probabilities can be described as a quasi-birth-death process [104, 105]. In order to calculate the probabilities  $P(\mathbf{r})$ , instead of equation (2.14), we solve the global balance equation which in matrix notation can be written as,

$$\mathbf{P} = \boldsymbol{\pi} \mathbf{P} \quad (2.18)$$

The above equation can be solved easily using an iterative solver such as successive over-relaxation, if we rewrite it as,

$$\mathbf{P}^{i+1} = \boldsymbol{\pi} \mathbf{P}^i \quad (2.19)$$

with the index  $i$  denoting the  $i$ th iteration of the algorithm.

Using the simulation methods described above, we study the phase behaviour and structure of a 2D lattice model of discretized colloidal hard disks in a near-critical binary solvent mixture. In addition, we investigate systematically the effects of wettability,  $\alpha$ , and the colloid radius,  $R$ , on the phase behaviour of the model colloidal suspension.

### 2.3.4 Two-Point Correlation Function and Structure Factor

An important quantity that tells us how two points in space are correlated, is the two-point connected correlation function, which for a multi-component system, is defined [106] as,

$$x_\mu x_\nu \rho g_{\mu\nu}(\mathbf{r}) = \left\langle \frac{1}{N} \sum_{i=1}^{N_\nu} \sum_{j=1}^{N_\mu} \delta(\mathbf{r} + \mathbf{r}_j - \mathbf{r}_i) \right\rangle \quad (2.20)$$

where in the Grand-Canonical ensemble,  $\rho = \langle N \rangle / V$ ,  $x_\mu = \langle N_\mu \rangle / \langle N \rangle$  and  $N = \sum_\mu N_\mu$ , with  $N_\mu$  being the number of particles of the  $\mu$  component of our system. For a discretized

lattice, we use the following mapping,

$$\begin{aligned} \sum_{i=1}^{N_\mu} \delta(\mathbf{r} - \mathbf{r}_i) &\rightarrow n_i^\mu \\ \sum_{i=1}^{N_\mu} \sum_{j=1}^{N_\nu} \delta(\mathbf{r} - \mathbf{r}_i + \mathbf{r}_j) &\rightarrow \sum_{\{\{i,j|\mathbf{r}_i-\mathbf{r}_j=\mathbf{r}\}} n_i^\mu n_j^\nu \end{aligned} \quad (2.21)$$

where  $n_i^\mu$  is the occupancy of site  $i$  for species  $\mu$ . Integrating over the whole volume of the system, one can confirm that the top equation will give the number of particles and the bottom one, the number of particles with a distance  $\mathbf{r}$  in the bottom one. Using this map, we get for eq. 2.20,

$$x_\nu x_\mu \rho g_{\nu\mu}(\mathbf{r}) = \frac{1}{\langle N \rangle} \left\langle \sum_{\{\{i,j|\mathbf{r}_i-\mathbf{r}_j=\mathbf{r}\}} n_i^\mu n_j^\nu \right\rangle. \quad (2.22)$$

Solving for  $g_{\nu\mu}$ , we finally find,

$$g_{\nu\mu}(\mathbf{r}) = \frac{V}{\langle N_\mu \rangle \langle N_\nu \rangle} \left\langle \sum_{\{\{i,j|\mathbf{r}_i-\mathbf{r}_j=\mathbf{r}\}} n_i^\mu n_j^\nu \right\rangle. \quad (2.23)$$

We can use Fast Fourier transforms to calculate these correlation functions very efficiently [56]. The static structure factor for a multi-component system, is defined [106] as,

$$S_{\mu\nu}(\mathbf{k}) = \left\langle \frac{1}{N} \rho_{\mathbf{k}}^\mu \rho_{-\mathbf{k}}^\nu \right\rangle, \quad (2.24)$$

as a function of Fourier components of the density. For a lattice, we can write these as,

$$\rho_{\mathbf{k}}^\mu = \sum_{i=0}^V n_i^\mu e^{-i\mathbf{k}\cdot\mathbf{r}_i} \quad (2.25)$$

which is simply the discrete Fourier transform of the occupancy of species  $\nu$ . With this definition it is easy to calculate the static structure factor  $S_{\mu\nu}(\mathbf{k})$  directly from eq. 2.24.

## 2.4 Results

### 2.4.1 Phase Diagram of Solvent

In the absence of colloids, the  $AB$  solvent is isomorphic to the Ising model and in 2D the exact phase diagram is known analytically from Onsager [5]. In figure 2.1 we represent the phase diagram of the solvent in  $\tau$  vs.  $x_r$  representation, where  $\tau = (T - T_c)/T_c$  is the reduced temperature, with  $T_c$  the critical temperature of the pure solvent, and  $x_r$ , the composition. The critical temperature is given by  $k_B T_c = 0.567\epsilon$ . We use the subscript  $r$  to denote the solvent reservoir. Due to the Ising symmetry inherent to the  $AB$  lattice model, the critical composition  $x_{r,c} = 1/2$  and the chemical potential corresponding to the binodal, at which saturation occurs, is at  $\Delta\mu_s = 0$ , for  $\tau < 0$ . For  $\Delta\mu_s < 0$  ( $\Delta\mu_s > 0$ )

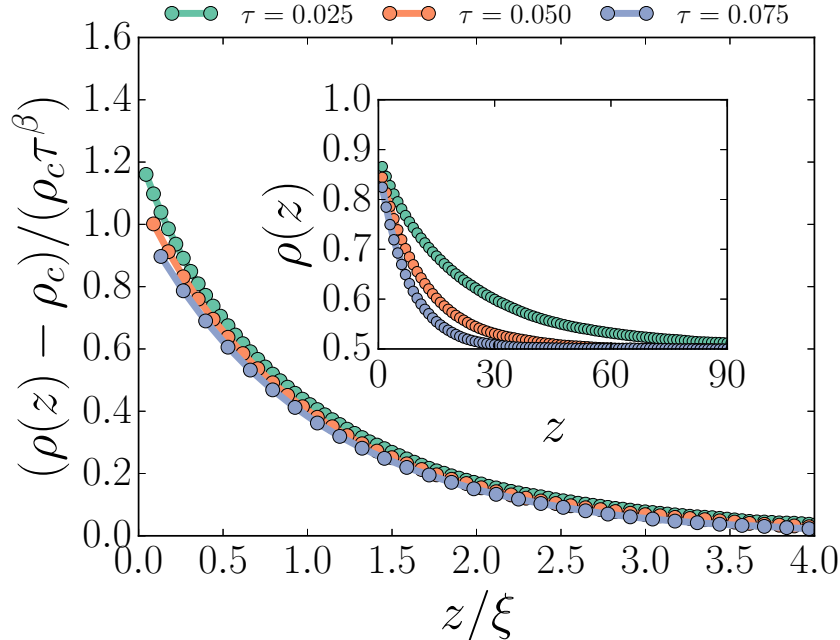


**Figure 2.5:** Density profiles of species  $B$  adsorbed on a planar wall with wettability  $\alpha = 0.6$ , for  $\Delta\mu_s = 0$ , and three reduced temperatures  $\tau$ . In the main figure, the distance from the wall  $z$  is scaled with the correlation length of the pure solvent  $\xi = 0.567\tau^{-1}$ . The inset shows the unscaled profiles.  $\rho_c$  is the critical density.

the bulk solvent mixture is rich in solvent species  $A(B)$ . In this chapter we show results for colloids which prefer the  $B$  species of the supercritical solvent.

It is important to comment on the choice of our model. Had we chosen a different model, lattice or off-lattice, to describe the solvent, we would have needed to compute and identify with great accuracy the solvent phase diagram. Moreover, given that a grand canonical treatment of the solvent is the most accurate way to study the phase behaviour of the  $ABC$  model, lattice models offer computational advantages over off-lattice models.

#### 2.4.2 Adsorption at a Single Wall

Before we present our results on the phase behaviour of colloids, we study first the adsorption behaviour of the solvent mixture at a flat planar wall, which can be regarded as an infinitely large colloid. We consider only nearest neighbour interactions between solvent species  $B$  and the wall. As described in section 2.2, the wettability parameter,  $\alpha$ , is a measure of the preference of the substrate for solvent species  $B$ . For  $\alpha = 0$ , the planar wall prefers neither solvent species and is termed neutral. For such a wall, and  $\Delta\mu_s = 0$ , there is no ordering at the surface [107], due to the perfect AB (Ising) symmetry.

In this work we consider only states where the solvent is super-critical, i.e.  $\tau > 0$ , and surfaces with wettability  $\alpha > 0$ . In the limit  $\tau \rightarrow 0^+$ , the solvent exhibits critical adsorption, i.e. the thickness of the adsorbed film is determined by  $\xi$ , the bulk correlation length of the solvent [28]. Thus, as the critical point is approached, the presence of a wall can be felt at very large distances, set by the diverging  $\xi$ . In figure 2.5 we present

the density profiles of species  $B$  adsorbed on a planar wall with  $\alpha = 0.6$ , at reduced temperatures,  $\tau = 0.025, 0.05$ , and  $0.075$ , for  $\Delta\mu_s = 0$ , i.e. at fixed critical composition.  $\rho(z)$  is simply the local composition at distance  $z$  from the planar wall, with  $z$  measured in lattice spacings. The critical density,  $\rho_c = \rho(\infty)$ , is the critical composition, i.e.  $\rho_c = x_{r,c} = 1/2$ . We choose to use the term density profile since this makes clear the connection with studies of real (off-lattice) mixtures. The scaling in figure 2.5 is motivated by general considerations [28]. Distances from the wall are scaled with  $\xi$ , the bulk correlation length, and the deviation from the critical density is scaled by  $\tau^{-\beta}$ , where the order parameter critical exponent  $\beta = 1/8$  in  $D = 2$ . The plot demonstrates excellent data collapse to the universal scaling prediction and confirms that the simulations can tackle efficaciously near-critical adsorption phenomena. Note that the scaling described in figure 2.5 is applicable only for  $\Delta\mu_s = 0$ . For non-zero values of  $\Delta\mu_s$  a field (chemical-potential) -dependent variable enters the scaling relation.

The thickness of adsorbed films is highly sensitive to the thermodynamic state of the solvent reservoir. Thick adsorbed films are also observed far from the critical point of the solvent. In particular, these can arise for  $\tau < 0$  when wetting films develop. We refer to adsorption far from the critical scaling regime as preferential adsorption; this is a non-universal phenomenon. Here the detailed nature of the wall-fluid interactions plays a key role in determining the film thickness, and hence the effective interactions between colloidal particles suspended in the solvent.

### 2.4.3 Neutral vs. Attractive Colloids

We now turn our attention to a system of many colloids immersed in a supercritical binary solvent mixture,  $\tau > 0$ , and relatively poor in the colloid-preferred species  $B$ ,  $\Delta\mu_s \leq 0$ , i.e. we consider states corresponding to those in the hatched region in figure 2.1. This choice precludes solvent-mediated colloidal aggregation arising from complete wetting and capillary condensation, i.e. formation of capillary bridges [108]. To this end, we consider a colloidal suspension at a fixed packing fraction  $\eta$  (the fraction of lattice sites occupied by colloids), and we treat the solvent grand-canonically, i.e. we view our system as being in thermal and diffusive contact with an  $AB$  solvent reservoir with composition  $x_r$  that fixes  $\tau$  and  $\Delta\mu_s$ . Generally, the  $ABC$  mixture has composition  $x \neq x_r$ . Here  $x$  denotes the fraction of sites occupied by  $B$  when the colloids are present. Note that the variable  $\tau$  merely sets the temperature of the reservoir, and is not a measure of distance from criticality of the ternary mixture. We consider first the case of neutral colloids of radius  $R = 6$ , which have no preference for species  $A$  or  $B$  ( $\alpha = 0$ ). In figure 2.6 (Top) we show a system of these colloids (right) at  $\tau = 0.005$  and  $\Delta\mu_s = 0$  in equilibrium with the solvent reservoir (left). The visualization reveals the tendency of the colloids to preferentially adsorb at the 'interfaces' between the instantaneous (*supercritical*)  $A$  and  $B$  domains. This feature, which resembles the binding of colloids to static air-liquid or liquid-liquid interfaces by a Pieranski potential [109], is captured here owing to the Brownian character of the colloids. figure 2.6 (Bottom) shows a visualization for the same parameter set, except now the colloids strongly prefer solvent  $B$  ( $\alpha = 19$ ). The strong  $B$ -adsorption on the colloids and the unfavourable  $AB$  interaction lead to an overall excess of  $B$ , thereby driving the  $ABC$  mixture far away from criticality; the solvent correlation

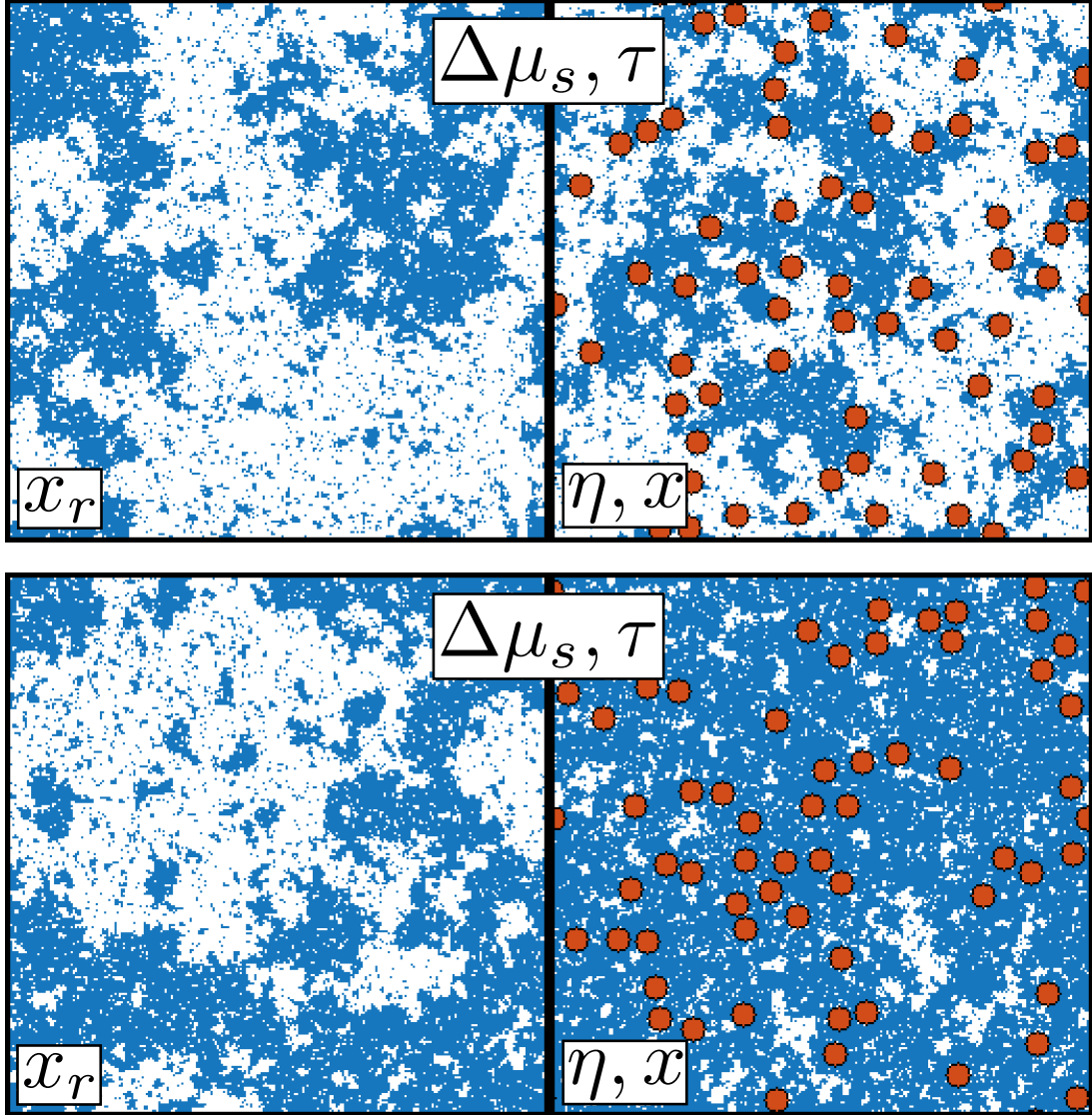


**Figure 2.6:** **Top:** Typical configurations of a ternary *ABC* mixture (right) with neutral colloids with no preference for *A* or *B* (radius  $R = 6$ ,  $\alpha = 0$ ) at colloid packing fraction  $\eta = 0.11$  and solvent composition  $x = (1 - \eta)/2$  in equilibrium with a solvent reservoir (left) with  $\eta = 0$ ,  $\Delta\mu_s = 0$ ,  $x_r = 1/2$ ,  $\tau = 0.005$ , and bulk correlation length  $\xi \approx 19R$ . **Bottom:** Typical configurations of a ternary *ABC* mixture (right) with colloids strongly preferring solvent *B* ( $R = 6$ ,  $\alpha = 19.0$ ) at packing fraction  $\eta = 0.11$  and solvent composition  $x > (1 - \eta)/2$  in equilibrium with the same solvent reservoir (left) as in **Top**. The system consists of  $512 \times 512$  lattice sites and in both the **Top**, and **Bottom**, the number of colloids is  $N_C = 64$ .

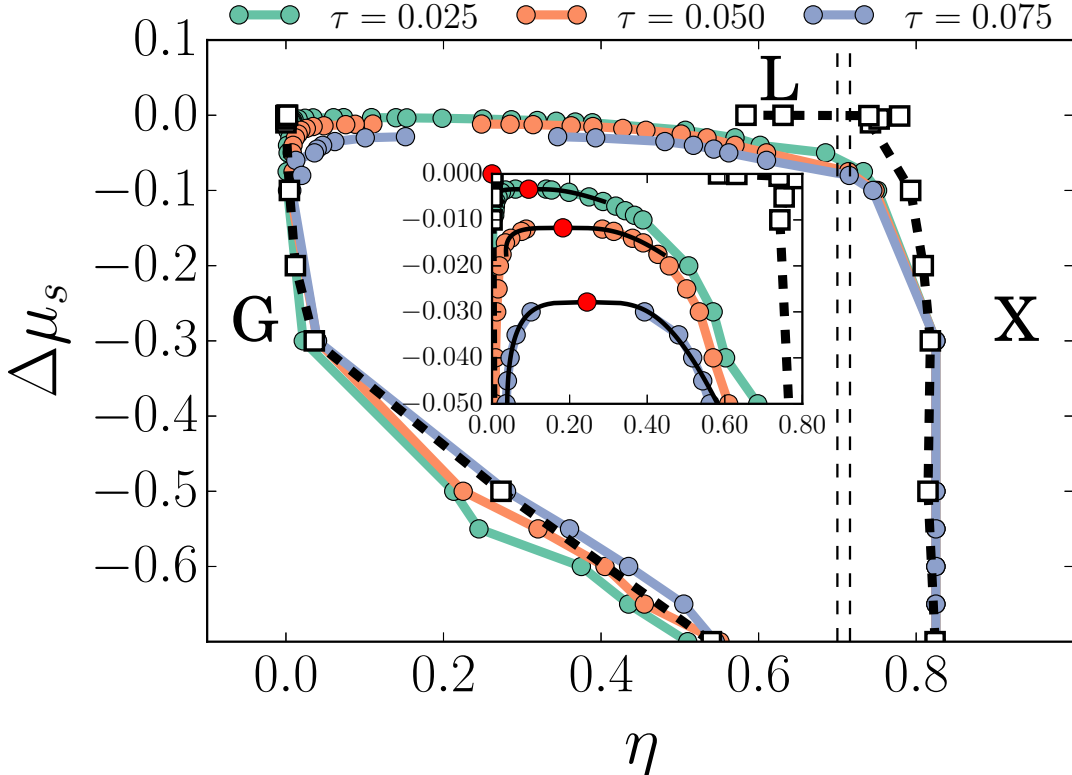


**Figure 2.7:** Binodals of the *ABC* ternary mixture, computed using a combination of the GCSI-TMMC method for near-critical  $\Delta\mu_s$ , and the direct coexistence method for the remaining points, for three fixed temperatures  $\tau = 0.025$  (green),  $\tau = 0.05$  (orange), and  $\tau = 0.075$  (blue) with  $R = 6$  and  $\alpha = 0.6$ . The square symbols, correspond to coexistence packing fractions, computed from simulations using the measured effective two-body potential at  $\tau = 0.025$ . In this solvent chemical potential,  $\Delta\mu_s$ , vs. colloid packing fraction,  $\eta$ , representation, the tie lines are horizontal. The red circles and black lines in the inset are the critical points and binodals obtained by least-squares fitting of equation (2.26). Note that the vertical dashed lines denote fluid-solid coexistence for pure hard disks..

length is observed to be smaller than the particle size. This is in sharp contrast to figure 2.6 (Top) where the correlation length of the solvent is hardly altered by the presence of neutral colloids.

#### 2.4.4 Phase Behaviour and Structure

The results in the previous subsection refer to  $\Delta\mu_s = 0$ . Here we focus on  $\Delta\mu_s < 0$  where colloidal phase transitions occur. As mentioned earlier, due to the symmetries inherent in our model, the ternary *ABC* mixture is equivalent to a binary mixture and therefore any binodals are a two-dimensional manifold in the three-dimensional  $\eta$  vs.  $\Delta\mu_s$  vs.  $\tau$  space. We determine cuts of this manifold at certain fixed temperatures. Here, we expand upon key results from our earlier work on the *ABC* model [90].

Once again, we fix the parameters  $R = 6$  and  $\alpha = 0.6$ , and determine the binodals

at three different fixed temperatures  $\tau = 0.025, 0.05$ , and  $0.075$ , as shown in figure 2.7. We choose these temperatures as the bulk correlation length,  $\xi = 0.567/\tau$ , of the solvent reservoir evaluated at  $\Delta\mu_s = 0$ , is then comparable to the size of the colloid. We plot the binodals in the  $\eta$  vs.  $\Delta\mu_s$  representation. In this representation the tie-lines are horizontal. We observed stable colloidal gas (G), liquid (L) and crystal (X) phases [90]. There is broad G-X coexistence for  $\Delta\mu_s < -0.1$ . The vertical dashed lines in figure 2.7 correspond to the (discretized) hard-disk phase behaviour that is recovered in the limit  $\Delta\mu_s = \pm\infty$  [89, 90]. In the inset to figure 2.7 we have also plotted estimates of the critical points, obtained by a least-squares fit to the equation: [110–113]

$$\eta_{\pm} - \eta_c = A |\Delta\mu_s - \Delta\mu_s^c| \pm \frac{1}{2} B |\Delta\mu_s - \Delta\mu_s^c|^{\beta} \quad (2.26)$$

where  $\eta_{\pm}$  stands for colloidal liquid/gas packing fraction, with  $\eta_c$  its critical value, and  $A, B$ , as well as the exponent,  $\beta$ , are fit parameters. Note that we have substituted temperature with the solvent chemical potential,  $\Delta\mu_s$ , with  $\Delta\mu_s^c$  being the solvent chemical potential at the critical point of the ternary mixture. It is important to realize that equation (2.26) is not an exact relation, and under this understanding, we fit it to our results mostly as a guide to the eye.

In figure 2.8 we show a visualization of a supercritical sample, and G-X and G-L coexistence for  $\tau = 0.05$  using the direct coexistence method. In the middle and right panels of figure 2.8, we note the presence of two interfaces and that the composition of the solvent in the coexisting phases is very different. The liquid and crystal phases, dense in colloids (orange disks), is extremely dilute in species  $A$  (white). By contrast, the gas phase,  $G$ , dilute in colloids, is rich in  $A$ . Indeed, we find that the solvent composition in  $G$  is close to that of the reservoir:  $x \approx x_r$ . This is important to note as several theoretical approaches that study the phase behaviour of a colloid solvent mixture treat the solvent as a uniform background with a fixed composition in both the coexisting phases [65–67, 88]. In the remainder of this work we shall focus on the G-L coexistence.

The G-L coexistence shown in figure 2.7 terminates at a critical point (see red circles) that shifts to lower  $\Delta\mu_s$  and higher packing fraction,  $\eta$ , with increasing  $\tau$ . A signature of criticality is the divergence of the partial structure factors,  $S_{ab}(k)$ , in the low  $k$  limit. We note that in any mixture, the solvent-solvent ( $ab = BB$ ), colloid-colloid ( $ab = CC$ ), and solvent-colloid ( $ab = BC$ ) pair correlation functions should all decay with the same true correlation length [114]. Calculations of  $S_{BB}(k \rightarrow 0)$  vs.  $\eta$ , yield a rough estimate of the G-L critical point. In figure 2.9(a) we show the  $BB$  structure factor defined as  $S_{BB}(k) = (1/N) \langle n_{\mathbf{k}}^B n_{-\mathbf{k}}^B \rangle$ , where  $n_{\mathbf{k}}^B$  is the Fourier transform of the solvent species  $B$  occupancy profile [115]. We compute  $S_{BB}(k)$  at  $\tau = 0.025$  and  $\Delta\mu_s = -0.00315$  and five values of  $\eta$ , i.e. the state points indicated by dots in the phase diagram shown in the inset of figure 2.9(a). In figure 2.9(b) we plot the limit  $S_{BB}(k = 0)$ , obtained from a linear extrapolation to  $k = 0$  of the simulation data, vs.  $\eta$ . This shows a maximum corresponding to the state closest to the G-L critical point. figure 2.9(a) displays data for two values of  $\eta$  (0.1724 and 0.3276) for which  $S_{BB}(k)$  exhibits pronounced oscillations. The period of these is about  $\Delta k \approx 0.54/a$ , with  $a$  the lattice spacing, which implies that the wavelength of oscillations in  $g_{BB}(r)$  is about  $12a$ , the diameter of the colloidal hard disks. Examination of plots of  $g_{ab}(r)$  (see figure 2.9(c)) shows that all three oscillate with

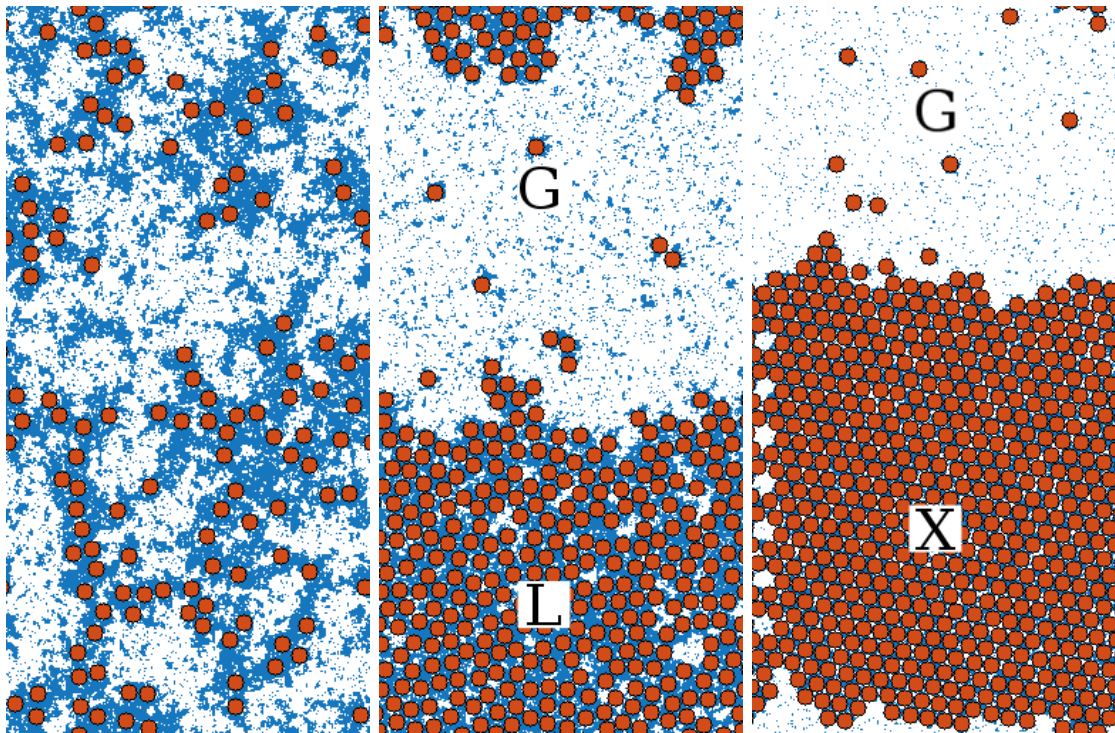


**Figure 2.8:** Simulation snapshots of a system of  $256 \times 512$  lattice sites at  $\tau = 0.05$  and  $\alpha = 0.6$ , showing (**Left**) a supercritical colloidal phase at  $\Delta\mu_s = -0.005$  of 128 colloids, (**Middle**) gas-liquid (G-L) coexistence at  $\Delta\mu_s = -0.04$  of 348 colloids, and (**Right**) gas-crystal (G-X) coexistence at  $\Delta\mu_s = -0.3$  of 580 colloids.

roughly this wavelength. In other words, the (large) colloidal length scale determines the form of  $BB$  and  $BC$  correlations, as well as  $CC$  correlations, at sufficiently large packing fraction  $\eta$ .

### Phase behaviour: Dependence on $\alpha$

Here we discuss how the phase behaviour of the model depends on the wettability  $\alpha$  of the colloids  $C$ . Recall that values of  $\alpha > 0$  cause species  $B$  to preferentially adsorb on the surface of colloid  $C$ . We have shown that phase separation into colloidal gas, liquid, or crystal phases then occurs for  $\Delta\mu_s < 0$ , i.e. where the bulk solvent reservoir is rich in species  $A$ . Clearly, the phase separation is driven by a competition between bulk, favouring  $A$ , and colloid adsorption, favouring  $B$ . When  $\Delta\mu_s > 0$ , so that the bulk reservoir is rich in species  $B$ , there is no phase separation. By the same argument, if we set  $\alpha < 0$ , then phase separation will be observed for states where the bulk prefers species  $B$ , i.e.  $\Delta\mu_s > 0$ .

The role of  $\alpha$  in our model is to promote the formation of an adsorption layer around each colloidal particle. This extends, due to solvent-solvent correlations, up to a distance given by the solvent correlation length  $\xi$ . Above a certain value of  $\alpha$  the surface of the colloid remains saturated with particles of species  $B$ . In figure 2.10 we show  $m_B$ , the fraction of  $BC$  interactions on a single colloidal particle, as a function of the wettability,  $\alpha$ , for reduced temperature  $\tau = 0.025$ , and  $\Delta\mu_s = 0$  and  $-0.1$ . As expected, for  $\Delta\mu_s = 0$ ,

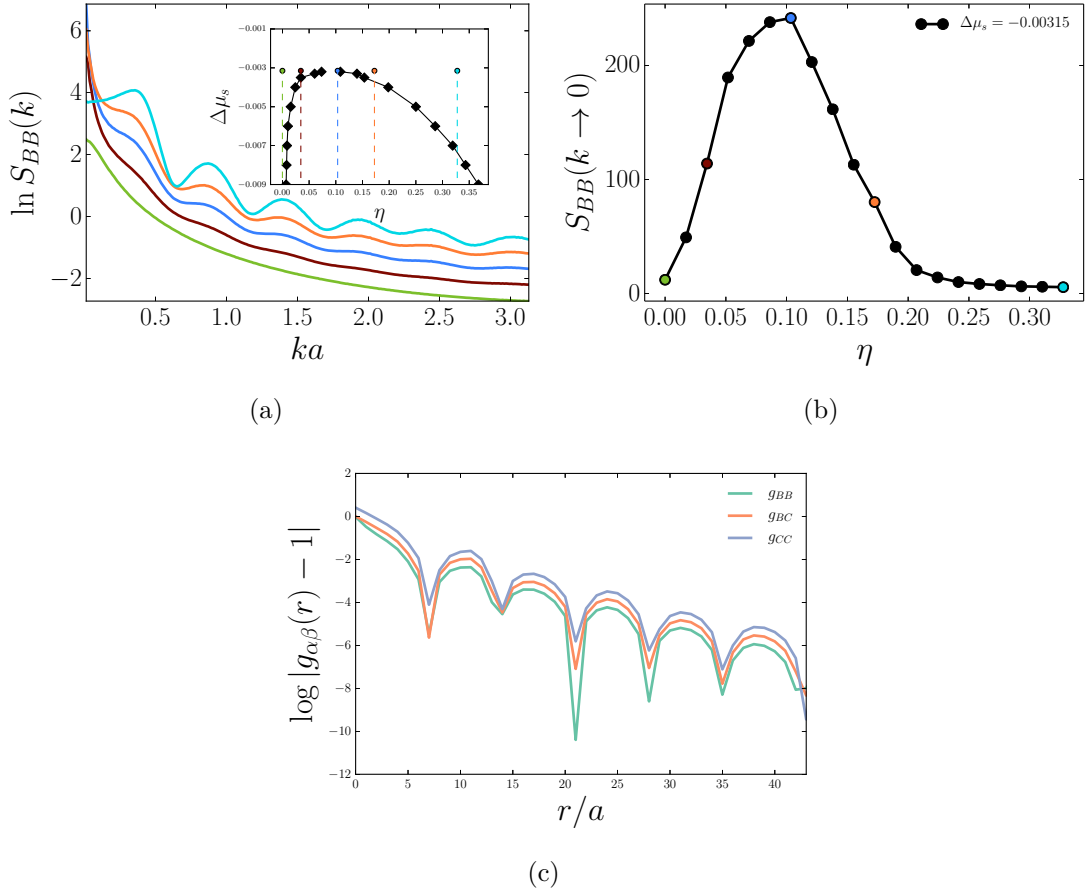


**Figure 2.9:** (a) Partial structure factor,  $S_{BB}(k)$ , of the solvent computed at  $\tau = 0.025$ ,  $\Delta\mu_s = -0.00315$ ,  $R = 6$ , at different values of colloid packing fraction:  $\eta = 0.0$  (green),  $\eta = 0.0345$  (brown),  $\eta = 0.1035$  (blue),  $\eta = 0.1724$  (orange), and  $\eta = 0.3276$  (cyan). For clarity, the curves were shifted by 0.5 on the log-scale. The inset shows the G-L binodal for  $\tau = 0.025$  (black diamond symbols). (b) The value of the structure factor linearly interpolated to  $k = 0$ ,  $S_{BB}(k \rightarrow 0)$  vs.  $\eta$ , at  $\Delta\mu_s = -0.00315$ . (c) The partial pair correlation functions plotted as  $\log |g_{\alpha\beta}(r) - 1|$  vs distance, normalized by the lattice spacing  $a$ , at temperature  $\tau = 0.025$ , colloid packing fraction  $\eta = 0.4$  and chemical potential  $\Delta\mu_s = -0.005$ . All three correlation functions exhibit the same decay length and period, as predicted by [114].

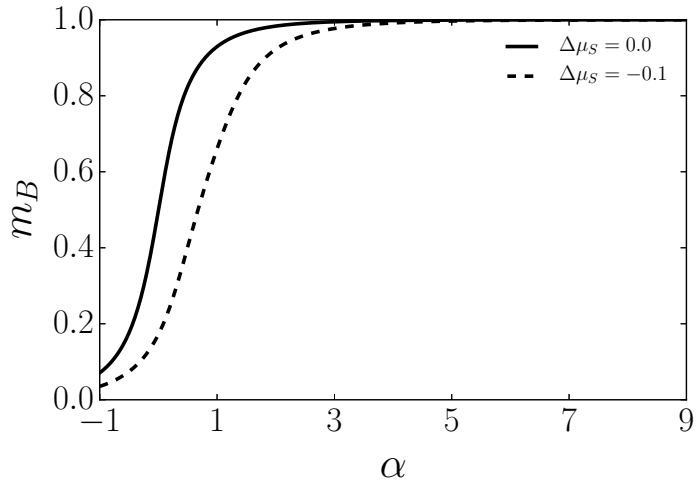


**Figure 2.10:** Fraction of  $BC$  interactions,  $m_B$ , for a colloid of  $R = 6$ , as a function of the wettability,  $\alpha$ , at temperature  $\tau = 0.025$ , for solvent chemical potential,  $\Delta\mu_s = 0.0$  (solid line), and  $\Delta\mu_s = -0.1$  (dashed line).

$m_B = 1/2$  for the neutral case  $\alpha = 0$ . These results are obtained by calculating the probability  $P(m_B; \alpha)$  using TMMC (see section 2.3.3), and subsequently using histogram reweighting in the wettability,  $\alpha$ . This procedure is similar to that described in Ref. [116]. From figure 2.10 we see that the surface layer is saturated at  $\alpha \simeq 3$ .

In figure 2.11(a) we plot the G-L coexistence region of the phase diagram for four different values of the wettability  $\alpha$  at a fixed temperature  $\tau = 0.025$  and colloid radius  $R = 6$ . The binodals are computed from probability distributions using the TMMC technique (see section 2.3.3) for a system size  $L = 256$ , and broaden upon increasing the wettability. However, for  $\alpha$  beyond a saturation value of about 4.0, the binodals are unchanged. Provided  $\alpha$  is sufficiently large that the surface layer around the colloid is occupied fully by  $B$ , i.e.  $m_B = 1$  in figure 2.10, G-L coexistence remains unaffected by stronger wettability. Note that for  $\alpha = 0.6$ , the value chosen for the majority of our studies,  $m_B$  is typically about  $0.8 - 0.9$  for states close to the colloidal critical points.

The results in figure 2.11(a) correspond to a much narrower range of  $\Delta\mu_s$  than in figure 2.7. In addition to broadening the binodals, increasing  $\alpha$  shifts the colloidal critical point to smaller values of  $\eta$  and to smaller values of  $|\Delta\mu_s|$ . This trend is similar to that found in the mean-field treatment of Edison *et al.* – see figure 7 of Ref. [89].

For  $\Delta\mu_s < -0.1$ , we observed broad G-X coexistence (not shown in figure 2.11(a)) similar to that shown in figure 2.7. In this regime lattice effects become important and below we explain this in more detail.

### Phase behaviour: Dependence on $R$

Next we discuss the dependence of the phase behaviour on the radius of the colloids,  $R$ . We computed the phase diagrams of three systems where the colloids have radii  $R = 6$ ,  $R = 9$  and  $R = 12$ . Ideally we would like to investigate colloid sizes which are much larger  $\sim O(100)$ . However, determining the phase behaviour of these systems using the

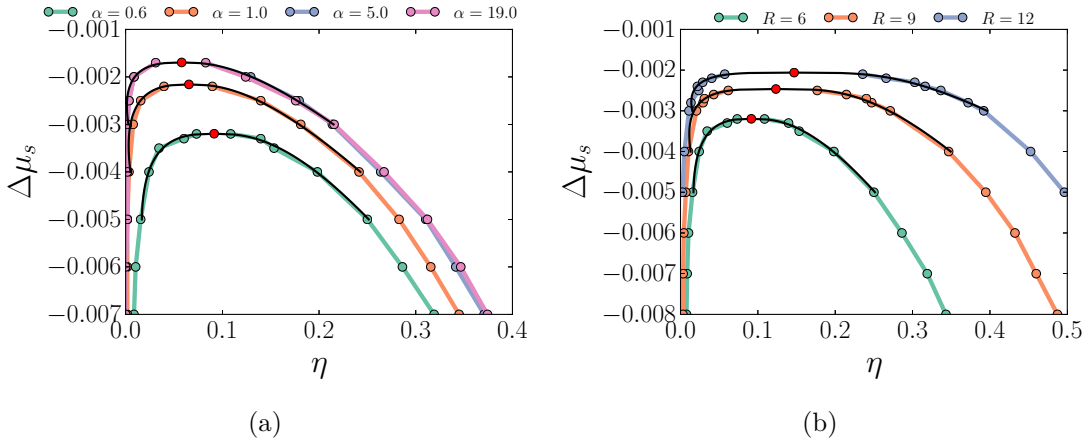


**Figure 2.11:** G-L binodals for the full *ABC* ternary mixture plotted as hard-disk packing fraction  $\eta$  vs. solvent chemical potential  $\Delta\mu_s$ , at temperature  $\tau = 0.025$ . **(a)** The particle radius is fixed at  $R = 6$  and the wettability is varied,  $\alpha = 0.6$  (green),  $\alpha = 1.0$  (orange),  $\alpha = 5.0$  (blue), and  $\alpha = 19.0$  (pink). Note that for  $\alpha = 5.0$  and 19.0, the binodals are extremely close. **(b)** The wettability is fixed at  $\alpha = 0.6$  and the particle radius is varied,  $R = 6$  (green),  $R = 9$  (orange), and  $R = 12$  (blue). The red circles and black lines are the critical points and binodals obtained by least-squares fitting of equation (2.26).

aforementioned techniques is not computationally feasible. The sizes we investigate are more representative of nanoparticles in solvents than micron-sized colloids. The G-L binodals are computed from probability distributions using the TMMC technique (see section 2.3.3). We used system sizes of  $L = 256$ , 384, and 512 for colloid radii  $R = 6$ , 9, and 12, respectively. In figure 2.11(b) we show the G-L binodals at a fixed temperature  $\tau = 0.025$ . We set the wettability  $\alpha = 0.6$  for all three cases. Increasing the radius broadens the binodal and shifts the colloidal critical point to larger values of  $\eta$  and smaller values of  $|\Delta\mu_s|$ . The same trend is found in figure 8 of Ref. [89]. Note that for  $R = 12$ , the binodal is extremely flat in the neighbourhood of the critical point.

As a remark concerning the critical behaviour of the ternary mixture, we note that although the various liquid-gas coexistence curves in Figs. 2.11(a) and 2.11(b) appear to show different degrees of ‘flatness’ in the vicinity of their critical points, all the ternary mixtures must lie in the 2D Ising universality class. In other words, were we able to perform simulations for increasing system sizes at states sufficiently close to criticality, and employ finite-size scaling arguments, we would find the critical exponent in Eq. (2.26) is  $\beta = 1/8$ . Current resources do not permit such an analysis.

#### 2.4.5 The Effective Two-Body Potential

In this subsection we present some results for the effective pair potential,  $U(x, y)$ , obtained from our MC simulations, using the method described in Section 2.3C.

As mentioned earlier, there have been several attempts to ascertain the phase behavior of colloids in a near-critical solvent based solely on effective two-body interactions, e.g., Refs. [66, 86]. In order to assess the validity of this approach for the present model system,

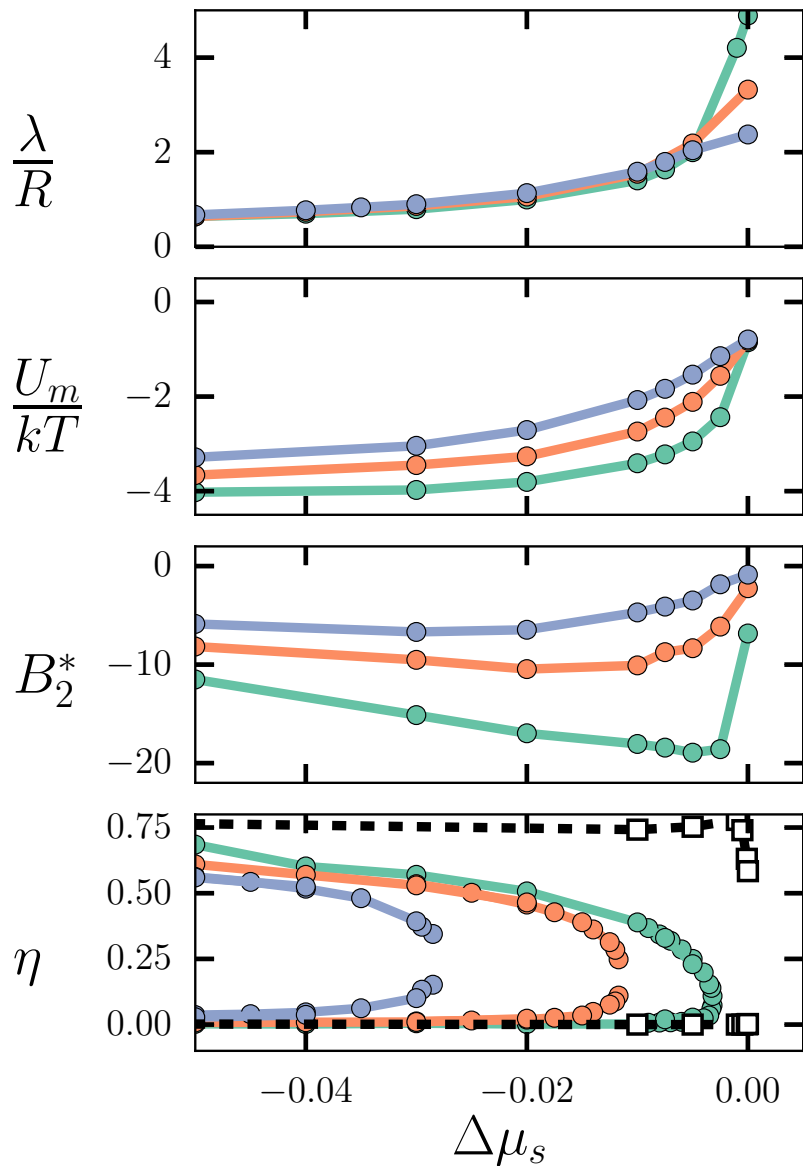


**Figure 2.12:** (a) Thickness  $\lambda$  of the  $B$ -rich film adsorbed on a single colloid. (b) The minimum well depth of the effective two-body SM potential. (c) The reduced second virial coefficient  $B_2$ . (d) To facilitate comparison, the phase boundaries of the ternary  $ABC$  mixture of figure 2.7 are replotted in the  $\eta$  vs  $\Delta\mu_s$  representation. The square symbols (d) correspond to packing fractions of coexisting phases computed from simulations of colloids interacting via the measured two-body interaction at  $\tau = 0.025$ . Black, red, and blue symbols refer to reduced temperatures  $\tau = 0.025, 0.05$ , and  $0.075$ , respectively ( $R = 6, \alpha = 0.6$ ).

we calculated several one- and two-colloid properties for the range of thermodynamic state points studied in figure 2.7. For the three temperatures investigated, we show in figure 2.12 the dependence on  $\Delta\mu_s$  of (a) the thickness  $\lambda$  of the adsorbed *B*-rich film on a single disk, (b) the minimum  $U_m$  of the effective pair potential  $U(x, y)$ , and (c) the reduced second virial coefficient

$$B_2^* = \frac{2}{L^2} \int_0^{L/2} \int_0^{L/2} dx dy (1 - e^{-\beta U(x, y)}), \quad (2.27)$$

To facilitate comparison, we replot the phase diagrams of figure 2.7 in the  $\eta$  vs  $\Delta\mu_s$  representation in figure 2.12(d). The film thickness  $\lambda$  and the well depth  $U_m$  are measures of the range and strength of  $U(x, y)$ , respectively. The quantity  $B_2$  is a well-established (dimensionless) measure of combined strength and range. This must be sufficiently negative in order for gas-to-liquid condensation to occur in systems described by pairwise additive interactions [117, 118].

Figure 2.12(a) shows a monotonic increase of the film thickness from  $\lambda \ll R$  to  $\lambda \gg R$ , reflecting the growth of the correlation length, as the isochoric composition is approached ( $\Delta\mu_s \rightarrow 0$ ). In the same range,  $U_m$  varies nonmonotonically, being strongest at slightly negative  $\Delta\mu_s$ , reaffirming earlier theoretical predictions [65, 79, 80]. At  $\Delta\mu_s \approx 0$ , the effective pair potential is long ranged; however, it is only weakly attractive ( $\beta|U_m| < 1$ ). Upon decreasing  $\Delta\mu_s$ ,  $U(x, y)$  does become more attractive, although the adsorbed film thickness  $\lambda$  and thereby the range of  $U(x, y)$  decrease.  $B_2^*$  also becomes more negative. This is more clearly seen in figure 2.13, which shows the radially average effective potential,  $U(s)$ , as a function of the contact distance,  $s$ , for  $R = 6$  and  $\alpha = 0.6$ , calculated at the solvent state points given in the inset, i.e.  $\tau = 0.025$  and three different values of  $\Delta\mu_s$ . For the state at the critical composition,  $\Delta\mu_s = 0$ , the potential is slowly decaying. Recall that the correlation length,  $\xi \sim 23$  lattice spacings at this state point. For  $\Delta\mu_s = -0.01$ , slightly off the critical composition, the potential decays faster but the range is comparable with  $\xi$ . However, the minimum of  $U(s)$ , which occurs at contact between the disks,  $s = 0$ , is about 5 times deeper than for  $\Delta\mu_s = 0$ . Moving further into the *A*-rich phase,  $\Delta\mu_s = -0.2$ , the strength of the attraction is reduced. More strikingly, the range is dramatically reduced and the potential becomes ‘sticky’. This variation of  $U(s)$  with  $\Delta\mu_s$  leads to a characteristic variation in the reduced second virial coefficient,  $B_2^*$  seen in figure 2.12.

As we model the colloid-fluid interactions via nearest neighbour interactions, and the surface perimeter of our colloid is discretized, the effective two-body potential between colloids is not smooth. Therefore certain solvent sites right next to the colloid can have more than one colloid site as its neighbour, as is clear from figure 2.2. The surface field induced by the colloid is not homogeneous and under certain conditions this heterogeneity plays an important role. In figure 2.14 we plot the effective two-body potential between colloids of radius  $R = 6$  with  $\alpha = 0.6$ , determined at  $\Delta\mu_s = -0.01$  and  $\Delta\mu_s = -0.5$ , for temperature  $\tau = 0.05$ . The effective potential close to the surface of the colloid is heterogeneous for both chemical potentials, i.e.  $U(x, y) \neq U(x^2 + y^2)$ . It turns out that these lattice effects can have a pronounced effect on phase coexistence. The lattice effects play no role in G-L coexistence where typically a solvent film spanning several lattice sites is found preferentially adsorbed on the surface of a colloid and the range of the

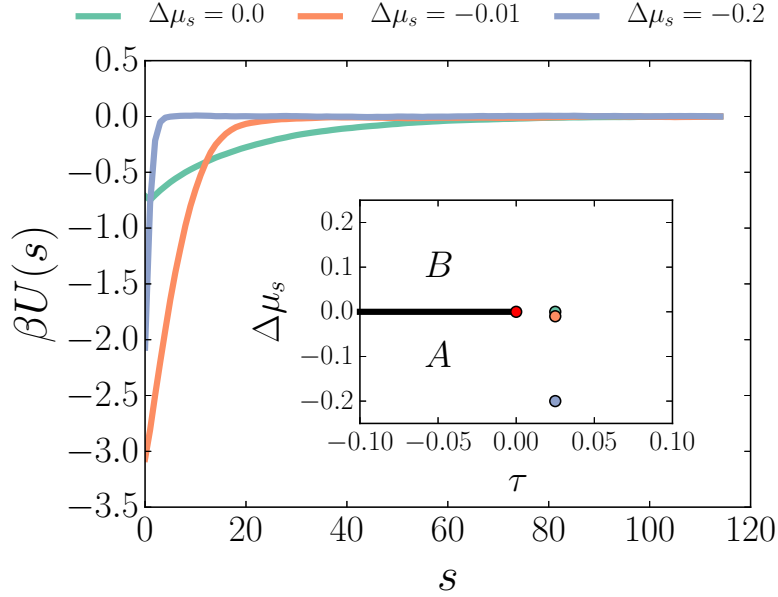


**Figure 2.13:** Effective two-body potentials,  $U(s)$ , between two colloids of radius  $R = 6$  and  $\alpha = 0.6$ , suspended in a solvent at  $\tau = 0.05$ , for  $\Delta\mu_s = 0$  (green),  $\Delta\mu_s = -0.01$  (orange), and  $\Delta\mu_s = -0.2$  (blue). Here,  $s$  is the surface to surface distance,  $s = |\vec{r}| - (2R + 1)$ . The inset shows the phase diagram of the  $AB$  solvent in the  $\Delta\mu_s$  vs.  $\tau$  representation. The red dot denotes the solvent critical point. The other dots show the state points at which the effective potential is calculated.

effective interaction is many lattice sites, as in figure 2.14(a). However, they do play a significant role in G-X coexistence, i.e. the crystal phase is facilitated by the colloids aligning along the more energetically favourable directions. Recall that the crystal phase typically becomes stable for  $\Delta\mu_s \lesssim -0.1$  (see figure 2.7) where for  $\alpha = 0.6$ ,  $m_B$ , the fraction of  $BC$  surface interactions, is  $\lesssim 0.5$  (see figure 2.10). In this regime it is the relatively low surface occupancy that determines the short-range of the effective potential: this is only 1-3 lattice sites in figure 2.14(b).

We performed simulations of the effective system, with the colloid-colloid pair interaction determined by the measured effective potential, which is shown in Figs. 2.7, and 2.12(d). Whilst the effective system does exhibit G-L and G-X coexistence, the G-L binodals are not close to those computed for the full ternary mixture with  $R = 6$  and  $\alpha = 0.6$  — see the inset of figure 2.7 in the supercritical region where simulations performed with the effective two-body potential predict G-L coexistence. This along with the  $B_2$  and  $\beta U_m$  curves indicates that the approaches employing only effective pair potentials as obtained from, e.g., planar slit studies and the Derjaguin approximation overestimate the extent of G-L coexistence and underestimate the shift in critical point of the ternary mixture with respect to that of the solvent reservoir. We return to this point later. Once more, we note that lattice effects are not important for G-L coexistence. On the other hand, the effective pair-potential treatment provides a rather good account of G-X coexistence, i.e. the binodals for  $\Delta\mu_s < -0.1$  in figure 2.7, provided lattice effects are incorporated properly. From our present study we conclude that an effective-pair potential treatment

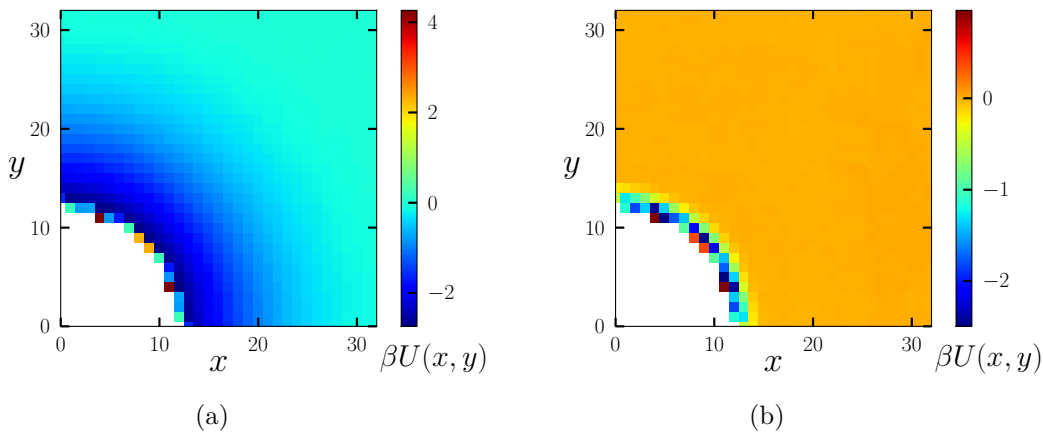


**Figure 2.14:** Effective two-body potential,  $U(x,y)$ , between two colloids of radius  $R = 6$  and  $\alpha = 0.6$  suspended in a solvent at  $\tau = 0.025$  for (a)  $\Delta\mu_s = -0.01$  and (b)  $\Delta\mu_s = -0.5$ . The area in white is inaccessible due to the hard-core repulsion. For  $(x^2 + y^2)^{1/2} \approx 2R$ , the potential displays lattice-induced heterogeneity.

can capture the gross features of the phase behaviour but is very unlikely to provide a quantitative description. It would be instructive to perform detailed comparisons for other radii and wettability strength.

## 2.5 Conclusion

Using a simple lattice model we have investigated the phase behaviour of colloidal particles immersed in near-critical solvents. Our model is a minimal one for treating colloidal self-assembly mediated by the long-ranged effective interactions that arise from long-ranged correlations in an explicit solvent. The choice of model was motivated in Sec. 2.2. The size asymmetry between the (big) colloid and the (small) solvent particles and the requirement to treat a dense solvent grand canonically set severe computational demands. In addition, having accurate estimates of the binodal of the colloid-free solvent and knowledge of the solvent's adsorption (wetting) properties at the surface of a single (very large) colloid are important prerequisites. Such considerations led us to treat a 2D lattice model for the AB solvent, incorporating hard disks representing the colloids (C), that was introduced in a recent Letter [90]. There we presented results for the phase behaviour of the ABC model for colloids of a particular radius  $R = 6$  and colloid-solvent adsorption strength (wettability)  $\alpha = 0.6$ . In the present work we have provided details of the computer simulation methods employed and extended our earlier study by i) investigating systematically the phase behaviour of our model as a function of  $R$  and  $\alpha$ , and ii) by determining the structure of the ternary liquid mixture.

In Ref. [90] we found that the critical point of the ternary colloid-solvent mixture shifts significantly from that of the colloid-free solvent upon adding a small volume fraction  $\eta$  of colloids. Here we show that on increasing  $\alpha$ , i.e. the preference of colloid C for species B, at a fixed reduced temperature  $\tau$  and radius  $R = 6$ , the G-L binodals broaden and the G-L critical point shifts towards the critical point of the solvent. However, there is a

saturation value of  $\alpha$  above which the phase coexistence is unchanged. For the data shown in figure 2.11(a), the saturation value of  $\alpha$  is  $\simeq 5.0$ . The phase behaviour with respect to the size of the colloid  $R$  is arguably more important than that w.r.t.  $\alpha$ . Upon increasing  $R$  at fixed  $\tau$  and  $\alpha$ , the G-L binodal becomes much flatter, and the critical point shifts to larger colloid fraction  $\eta$  (see figure 2.11(b)). Unfortunately, investigating larger values of  $R$  pertinent to the regime of real colloidal systems is constrained by computational resources. It is significant that the trends found by increasing both  $\alpha$  and  $R$  are similar to those found in the mean-field treatment of Ref. [89] for the same model. This observation suggests that excluded volume considerations, incorporated in the mean-field treatment, are important in determining G-L coexistence and, indeed, the overall phase behaviour of our model.

One of the key advantages of our ternary mixture model is that it enables us to investigate fractionation of the solvent; the composition  $x$  of the solvent is generally different from that of the solvent reservoir  $x_r$ . This is illustrated (see figure 2.8) for coexisting colloidal liquid and gas phases. In the dense liquid phase, L, the solvent is very rich in the solvent species  $B$  favoured by the colloids. In principle we could calculate the values of  $x$  from our simulation results for the two coexisting phases. That would allow us to make further contact with the mean-field treatment of Ref. [89]. Note that unlike the results for  $\Delta\mu_s$  versus  $\eta$  shown here and those for  $x_r$  versus  $\eta$  given in figure 3c of Ref. [90], the tie-lines are not horizontal in the  $x$  versus  $\eta$  representation—see figure 3 of Ref. [89]. Fractionation arises naturally in our approach that treats a full ternary mixture. By contrast, approaches such as those of Mohry *et al.* [65–67] and Nguyen *et al.* [88] that treat the solvent as an implicit background, whose role is merely to induce an effective pairwise colloid-colloid interaction, struggle to incorporate this important element of the physics of the phase behaviour.

Results for the partial structure factors shed further light on the nature of criticality in our model ternary mixture. Sufficiently close to a critical point, all the partial structure factors  $S_{ab}(k)$  exhibit Ornstein-Zernike-like (OZ) behaviour at small wavenumbers  $k$  characterized by a single (OZ) correlation length. We chose to focus on  $S_{BB}(k)$ , i.e. on solvent species  $BB$  correlations. However, we could equally well have measured the  $BC$  or  $CC$  partial structure factors. Although these are quite different from  $S_{BB}(k)$  plotted in figure 2.9(a), the modulus of each  $S_{ab}(0)$  should exhibit the same dependence on  $\eta$  as that shown in figure 2.9(b). That is, proximity to the critical point is signalled by a diverging  $S_{ab}(0)$  for any  $ab$  pair. This phenomenon of ‘critical point infection’ is manifest more directly in real space. The quantity  $r^{(D-1)/2}(g_{ab}(r) - 1)$ , as  $r \rightarrow \infty$ , decays exponentially with a common correlation length  $\xi$  [114]. Here,  $g_{ab}(r)$  is the pair correlation function for species  $ab$  and, as before,  $D$  is the spatial dimension. As the critical point is approached,  $\xi$  diverges.

Now consider an extremely dilute colloidal suspension, that may or may not be close to criticality of the solvent, where the colloid volume fraction  $\eta \rightarrow 0$ . Then, for mixtures where all species interact with short-ranged potentials,  $r^{(D-1)/2}(g_{CC}(r) - 1)$  decays as  $e^{-r/\xi}$  where, in the dilute colloid limit,  $\xi$  is determined by correlations in the pure solvent. In this limit,  $g_{CC}(r) = \exp(-\beta\phi_{\text{eff}}(r))$ , and it follows that the effective colloid-colloid pair potential  $\phi_{\text{eff}}(r)$  must decay as  $e^{-r/\xi}/r^{(D-1)/2}$  as  $r \rightarrow \infty$ . Suppose now the solvent is only very slightly removed from its criticality. The solvent correlation length  $\xi$  is long and

sets the length scale determining the range of  $\phi_{\text{eff}}(r)$ . This simple argument describes the origin of the tail of the critical Casimir interaction between two identical colloids in the framework of liquid mixtures. Suppose now we have a more concentrated suspension of colloids. Measuring  $S_{CC}(k)$  or  $g_{CC}(r)$  at given  $\eta$ ,  $\tau$  and  $x_r$  will yield the correlation length of the concentrated ternary mixture, not that of the pure solvent, under the given conditions. This observation is relevant for experimental work [86, 87] that attempts to extract a reliable  $\phi_{\text{eff}}(r)$ , characteristic of the pure solvent, from measurements of  $g_{CC}(r)$ . Performing an experiment that extracts reliable data in the dilute limit is not straightforward. Given that the critical point shifts rapidly with  $\eta$ , values extracted for  $\xi$ , and hence  $\phi_{\text{eff}}(r)$ , are likely to be very sensitive to  $\eta$ .

We have focused on the supercritical regime of the solvent phase diagram —the box in figure 2.1. The same *ABC* model and computational techniques could be used to investigate the sub-critical region of the solvent reservoir. In this regime ( $\tau < 0$ ,  $\Delta\mu_s < 0$ ) strong preferential adsorption can lead to a bridging transition [119] between two identical colloidal particles. This is equivalent to rounding the well-known capillary condensation transition of a binary mixture confined between two identical planar substrates [108]. Once again it is important that the bulk solvent prefers species *A*, while the colloids prefer the phase rich in *B*, leading to a capillary bridge of the latter phase. The resulting SM interaction can be strongly attractive [29, 31, 120–122]. Unlike the critical Casimir SM interactions, these non-critical interactions are non-universal and are dependent on the precise nature of the local interactions between a colloid and the binary solvent at the given state point. Our model can incorporate these. Indeed we have observed bridging phenomena in our simulations under subcritical conditions.

The results presented here are relevant to experimentally realisable quasi-2D systems such as protein assembly in plasma membranes of living cells where it is argued critical Casimir forces might arise between macromolecules embedded in a biomembrane [123, 124], an observation that has spurred careful density matrix renormalization group calculations of the scaled Casimir force between disks [125]. In our earlier discussion we implied that our results should also be relevant to 3D systems. The results of a mean-field theory presented in Ref. [89] suggest that the fine details of solvent criticality, specifically the precise nature of two-body critical Casimir forces, are not too important in determining the main features of the observed phase coexistence. Thus, we speculate that the phase behaviour in 3D will be qualitatively similar to the currently investigated 2D case. These speculations will be investigated in the next chapter.

Equipped with this insight, we conclude by returning to two pertinent experimental studies of near-critical colloidal aggregation. We focus first on the pioneering study of Beysens and Estève [32], mentioned in Section 2.1, who used light scattering to investigate silica colloids suspended in a water-lutidine mixture. Recall this solvent exhibits a lower demixing critical point with  $T_c = 34^\circ\text{C}$  and lutidine mass fraction of  $x_c = 0.286$ . The colloids prefer lutidine over water and in figure 2 of Ref. [32], the authors plot the thickness of the lutidine layer adsorbed on a silica colloid. At fixed solvent concentrations  $x_{\text{Lu}}$  lying slightly below  $x_c$ , the thickness increases rapidly with increasing temperature until the aggregation line is reached; this lies about  $0.4K$  below the binodal. The observed increase in layer thickness at state points approaching the aggregation line, residing in the water-rich region, is a signature that strong preferential adsorption drives the aggregation

phenomenon. The inset to our figure 2.5 shows that the (excess) adsorption, obtained by integrating the density profiles, increases rapidly with decreasing  $\tau$ , approaching the critical point. figure 4(a) of Ref. [90] shows the thickness of the  $B$ -rich film increasing with decreasing  $\tau$ , for  $\Delta\mu_s$  slightly negative, corresponding to solvent compositions slightly below  $x_{r,c}$ . Clearly our model system incorporates correctly the preferential adsorption at a single colloid. It also incorporates the crucial competition between the bulk solvent preferring a certain species ( $A$ ) and the colloid preferring another ( $B$ ), that drives the aggregation. In a typical experiment a fixed number of colloids is suspended in a solvent at fixed composition,  $x_r$ , and the temperature is changed to induce (reversibly) aggregation. Then, for fixed  $\eta$ , the locus of points in the  $T$  versus  $x_r$  plane, where aggregation is first observed, is termed an aggregation line —see e.g. figure 3 in Ref. [32]. In Ref. [89] aggregation lines were calculated using the mean-field treatment, taking the view that aggregation corresponds to the onset of colloidal phase separation. Results are shown for  $\eta = 0.05$  and  $0.1$  in figure 2.5. The shape of the aggregation lines is similar to that shown in Ref. [32] when we recognize that our model has an upper, rather than a lower, demixing critical point. In principle we could also compute aggregation lines from our simulation results but this would be hugely expensive. Given the mean-field treatment captures the main features of the simulation phase diagrams, we would expect to find the same shapes for aggregation lines from our simulations. Quantitative comparisons with experiment are inappropriate. In Ref. [32] results near aggregation imply the ratio  $\xi/R$  is at most 0.2 which should be contrasted with a typical value of about 3 from theory and simulation [89].

The second experimental study we consider is the confocal microscopy (real-space) investigation [86] of poly-n-isopropyl acrylamide (PNIPAM) colloidal particles suspended in quasi-binary solvent of 3-methyl pyridine, water and heavy water which has a lower critical temperature and a critical methyl pyridine mass fraction  $x_c = 0.31$ . PNIPAM particles swell in the solvent; near the critical point the particle radius was about 250 nm. In the experiments the initial packing fraction was about 0.02 and the mass fraction of methyl pyridine was fixed at 0.25, i.e. substantially below the critical composition. Remarkably, upon increasing the temperature towards that of the solvent binodal, colloidal gas, liquid, and crystal phases were observed. Specifically, condensed, liquid-like aggregates were first observed at 0.3 K below the temperature of the solvent binodal, and upon raising the temperature a further 0.1 K the particles inside the aggregates formed an ordered fcc crystal [86]. Although our model certainly yields stable gas, liquid and crystal phases it is not clear that it can account for the sequence of phases found in Ref. [86]. As observed in Ref. [89], changing the composition of the solvent reservoir does lead to considerable variation in the  $\tau$  versus  $\eta$  phase diagrams of our model. Making direct comparisons is not straightforward. We noted in Ref. [89], that changing the composition of the solvent reservoir does lead to considerable variation in the  $\tau$  versus  $\eta$  phase diagrams of our model. Given the PNIPAM particles are very large and there is substantial deviation from the critical composition, the ratio  $\xi/R$  is very small in these experiments and is typically much smaller than in the regime investigated in the present study. Therefore one should not rule out the possibility that aggregates observed in Ref. [86] arise from specific (non-universal) solvent-mediated interactions. Whether these are captured properly by the ‘Casimir’ pair potentials extracted from measurements of  $g_{CC}(r)$  in the dilute

colloidal gas is open to discussion. Bearing in mind the ratios of length scales, our study is, perhaps, more representative of nanoparticles suspended in a near-critical solvent. In this respect it suggests that such systems might exhibit very rich phase diagrams with the potential for a wide range of colloidal self-assembly controlled by sensitive tuning of temperature and solvent composition.

## Acknowledgements

We thank N. Wilding, D. Ashton, and A. Maciołek, and especially R. Evans, for stimulating discussions. We furthermore thank R. Evans for his literary contributions to this project.



# 3

---

## Scaling of the 2D Critical Casimir Potential and Phase Behavior of Colloids in Near Critical Solvents in 3D Using a Cluster Algorithm

---

Colloids dispersed in a binary solvent mixture experience long-ranged solvent-mediated (SM) interactions (critical Casimir forces) upon approaching the critical demixing point of the solvent mixture. The range of the interaction is set by the bulk correlation length of the solvent mixture, which diverges upon approaching the critical point. The large difference in length scales between the colloid and solvent, and the critical slowing down as the ternary mixture critical point is approached, hampers the performance of simulation studies.

Here, we develop a rejection-free geometric cluster algorithm that enables us to study the scaling of the critical Casimir potentials in a two-dimensional system, and more importantly, the full ternary mixture of colloidal hard spheres suspended in an explicit three-dimensional lattice model for the solvent mixture using extensive Monte Carlo simulations. The effective potentials seem to scale according to the small-sphere limit, suggesting that the colloids in our simulations are closer in size to proteins. The phase diagram of the three-dimensional system displays stable colloidal gas, liquid, and crystal phases, as well as broad gas-liquid and gas-crystal phase coexistence, and pronounced fractionation of the solvent in the coexisting colloid phases. The topology of the phase diagram in our three-dimensional study shows striking resemblance to that of the previous chapter, which was carried out in two dimensions.

## 3.1 Introduction

The critical Casimir interaction has been thoroughly studied, especially in the context of solvent mixtures. For instance, the critical Casimir interaction between two static planar walls has been the subject of numerous theoretical studies [58–60, 62, 63], and has been extended to a pair of spherical particles using the Derjaguin approximation [64] which approximates the spherical surface with a number of planar walls. As the critical Casimir interactions depend directly on the bulk correlation length, these are very sensitive to the temperature and composition of the mixture, and this raises prospects to tune the self-assembly process of e.g. suspended colloids, reversibly and in an *in situ* fashion.

Theoretical and simulation studies on the phase behavior and structure of the full ternary mixture of colloidal particles moving around in an explicit solvent mixture are hampered by the huge differences in length and time scales between the colloids, solvent species, and the diverging bulk correlation length of the solvent mixture. As such, in most theoretical and simulation approaches, such as the work of Mohry *et al.* [65–67], Nguyen *et al.* [86, 88], and Dang *et al.* [87], the binary solvent mixture is taken to be a structureless implicit background. This approach fails to capture important elements such as the fractionation of the solvent in the coexisting colloidal phases. In the previous chapter, we used a model that is able to capture the above-mentioned important elements by using a simple lattice-gas binary solvent model with embedded colloids interacting through first neighbor and excluded volume interactions with the solvent. The model, although simple, contains all the necessary physics to describe the SM interactions between colloids. Since an explicit solvent is used, fractionation and many-body effects arise naturally. Due to the large difference in length scales between the colloid and solvent, and the critical slowing down as the ternary mixture critical point is approached, studying a three-dimensional system using Monte Carlo simulations was deemed computationally unfeasible when starting out our study presented in chapter 2 and in Refs. [90, 126].

Cluster algorithms are known to alleviate problems of critical slowing down and of low acceptance when performing Monte Carlo moves on constituents of very different sizes [94, 127, 128], and would, thus, be pertinent to our study of the critical Casimir interactions. In the current chapter, we develop a cluster algorithm which we describe in section 3.2 — we mention that a geometric cluster algorithm was also developed recently by Hucht *et al.* [95] for a similar lattice model. After first studying the scaling of the critical Casimir interaction between a pair of colloids in 2D, we study the phase behavior of preferentially adsorbing colloidal spheres embedded in a binary solvent mixture in 3D. We once again focus on the supercritical,  $\tau > 0$ , region of the pure solvent mixture reservoir, where we note that the lattice-gas model has an upper critical solution temperature. Here,  $\tau = (T - T_C)/T_C$  is the reduced temperature of the system – it is important to recognize that  $T_C$ , here, refers to the critical temperature of the solvent in the absence of colloids. The motivation behind this choice is to avoid the added complexity of having to deal with subcritical effects such as capillary bridging. Of course, the model can be used in any scenario.

This chapter is organized as follows. In section 3.2, we describe the cluster algorithm which made this study possible. In section 3.3, we briefly derive the form of the effective potential using the Derjaguin approximation and discuss the ‘small-sphere’ expansion. In

section 3.4.1, we present results for the scaling behavior of the critical Casimir interaction between a pair of colloids in a two-dimensional system. In section 3.4.2 we present the phase diagram for a three-dimensional system of colloids in a binary solvent mixture, in the solvent chemical potential difference,  $\Delta\mu_S$ , colloid packing fraction,  $\eta$ , representation, for varying temperatures. In section 3.5, we make some conclusions.

## 3.2 Cluster Algorithm

The model we presented in chapter 2 involves species of significantly different sizes, which is known to cause difficulties when performing Monte Carlo moves, such as translations [100, 128, 129]. This, coupled with the fact that solvent species  $B$  can adsorb strongly to the colloid surface, and that critical slowing-down upon approaching the ternary mixture critical point is encountered, leads to extremely low acceptance rates, and exponentially longer equilibration times as a function of temperature [56]. In addition, we note that colloid translations have a much higher acceptance rate in 2D than in 3D; colloids in 2D have significantly fewer surface sites with which they can interact with solvent species, than colloids of the same radius in 3D. This makes displacements of colloids much more difficult in higher dimensions and with increasing colloid radius.

To overcome the low acceptance of colloid translations and the critical slowing down, we developed a geometric cluster algorithm based on the work by Heringa et al. [94, 127] and Ashton et al. [128]. This exploits the facts that the Hamiltonian is symmetric under reflection of the lattice about an arbitrary pivot point (note that the pivot point can also take half-integer values). In the implementation of our model, a lattice site at index  $i$  is represented by the variable  $t_i$  which takes the values  $t_i \in [0, N_C + 2]$  corresponding to the species that occupies lattice site  $i$ , with  $A \equiv 0$ ,  $B \equiv 1$ , and colloid  $n$ ,  $C_n \equiv n + 2$ . It is also easy to see that  $s_i = t_i - 1$ ,  $n_i = 0$  when  $t_i < 2$ , and  $n_i = 1$  when  $t_i \geq 2$ . In the same spirit as Ref. [94], we use primed identifiers, i.e.  $i'$ , to denote identifiers that are mapped from the original by a symmetry transformation, in this case a point reflection about a random pivot point. As is the case with most cluster algorithm implementations, since the algorithm is rejection free, we can point-reflect lattice sites as they are added to the cluster instead of reflecting the whole cluster at the end of the algorithm. To this end, we keep track of the lattice sites that are added to the cluster by marking them as *added to the cluster*. The geometric cluster algorithm, modified for our model, consists of the following steps,

1. Choose a random colloid and lattice pivot point,  $r$ , about which point reflection is to be performed. The site at the center of the colloid, is denoted  $i$ , and the site reflected about the pivot point  $r$ ,  $i'$ . Figure 3.1 presents a schematic picture.
2. Interchange the species variables  $t_i$  and  $t_{i'}$  of sites  $i$  and  $i'$ , and mark them as *added to the cluster*.
3. For all neighboring sites,  $k$  and  $k'$ , of site  $i$  and corresponding reflected site  $i'$ , that have not been added to the cluster, do the following,

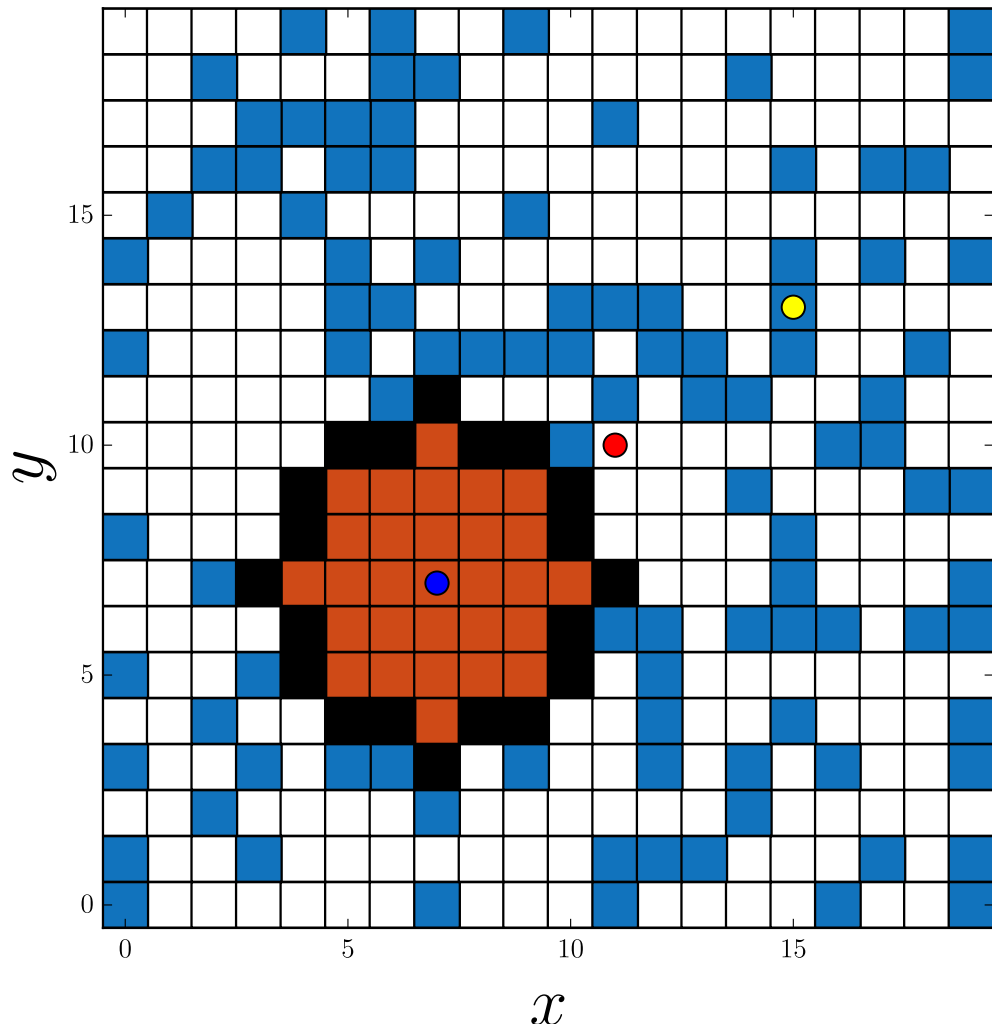


**Figure 3.1:** When performing a cluster move, a random colloid and a random pivot point,  $r$  (red circle at  $(11, 10)$ ), are chosen. Starting with its central site at lattice index  $i$  (blue circle at  $(7, 7)$ ), and the site reflected about the pivot point,  $i'$  (yellow circle at  $(15, 13)$ ), neighboring sites are added to the cluster according to the cluster move rules described in the text.

- 3.1. If  $t_i \geq 2$ , i.e. it belongs to a colloid, and  $t_{k'} = t_i$ , i.e. sites  $i$  and  $k'$  belong to the same colloid, or if site  $t_{i'} \geq 2$  and site  $t_k = t_{i'}$ , interchange the species variables  $t_k$  and  $t_{k'}$ , and mark sites  $k$  and  $k'$  as *added to the cluster*.
- 3.2. Else, calculate the energy difference,  $\Delta H$ , associated with interchanging  $t_k$  and  $t_{k'}$ . If  $\Delta H > 0$ , interchange the species variables  $t_k$  and  $t_{k'}$ , and mark sites  $k$  and  $k'$  as *added to the cluster* with probability  $1 - e^{-\beta\Delta H}$ .
4. For each site that was added to the cluster in step 3, denote these as  $i$ , and repeat steps 3 and 4, or terminate if no sites were added.

Step 3.1 is the equivalent of saying that nearest-neighbor pairs belonging to the same colloid are bonded infinitely strongly, such that  $\Delta H = \infty$ . The geometric cluster algorithm described above, significantly reduces the relaxation time of the system and renders translations rejection free. When a cluster becomes percolating, the cluster move may leave the system unchanged. For this reason, we also attempt standard colloid translations. In our implementation, we found it to be more effective to restrict the random pivot point to a small window centred around the colloid.

### 3.3 The Derjaguin Approximation and the Small-Sphere Expansion

The critical Casimir force for an Ising film of thickness  $L$ , has the following form in  $d$  dimensions [58, 59],

$$F_C = \frac{k_B T}{L^d} \vartheta(x, y, z) \quad (3.1)$$

where  $\vartheta$  is the universal scaling function and its variables are defined as,

$$\begin{aligned} x &= L/\xi_\tau = L |\tau| / \xi_0^\pm \\ y &= L/\xi_h = L |h|^{8/15} / \xi_h^0 \\ z &= L/l_{h_1} = L h_1^2. \end{aligned} \quad (3.2)$$

The  $\pm$  sign in  $\xi_0^\pm$  indicates if we are above or below the critical temperature,  $h$  is the external Ising field and  $h_1$  is the surface field of a wall located at the boundaries of the Ising film. For the LGHD model, these fields would correspond to the distance of the chemical potential from the coexistence value  $\Delta\mu_s$  and the field strength parameter  $\alpha$ , respectively. For a 2D Ising model,  $\xi_0^+ = 1/2 \ln(\sqrt{2} + 1)$ ,  $\xi_0^- = \xi_0^+/2$  and  $\xi_h^0 = 0.233 \pm 0.001$  [130, 131]. For simplicity, we will assume a strong enough surface field  $h_1$  (or  $\alpha$ ) such that the effect of the field reaches saturation. In the LGHD  $\alpha = 19$  is high enough, so that the critical Casimir interaction does not change anymore with an increase of the field strength.

In the Derjaguin approximation in two dimensions, the curved edge of a disk is considered to be made up of infinitely thin stair-steps of length  $dS$ , as seen in figure 3.2. In this approximation, the force acting on a single ‘stair-step’ is,

$$\beta dF_C = \frac{dS(\theta)}{L^2(\theta)} \vartheta(x(\theta), y(\theta)) \quad (3.3)$$

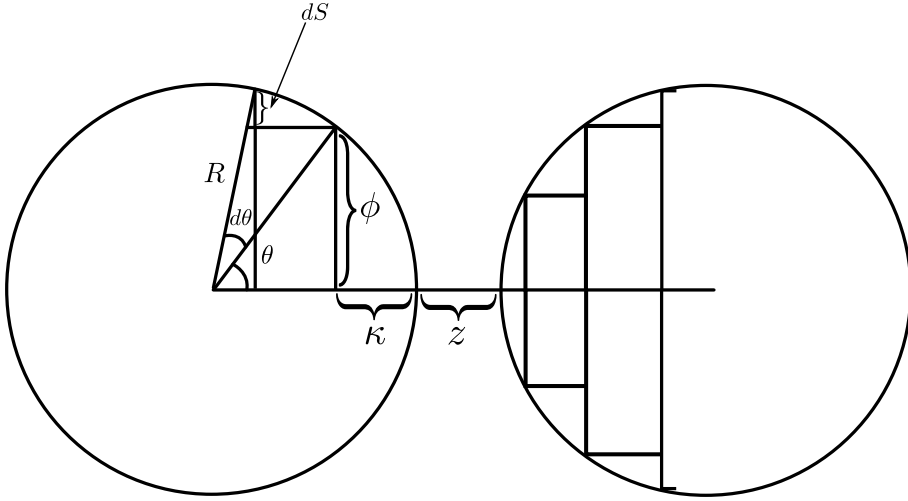


**Figure 3.2:** Geometry of the Derjaguin approximation for 2D disks. Various lengths important to our derivation are annotated.

where  $\theta$  denotes the angle of the stair-step, as shown in figure 3.2. For two disks at a surface-to-surface distance  $z$ , we find from figure 3.2, that  $L = 2\kappa + z$  and  $\kappa = R(1 - \cos \theta)$ , yielding,

$$L(\theta) = z + 2R(1 - \cos \theta). \quad (3.4)$$

Using some basic trigonometry, we obtain,

$$dS(\theta) = R(\sin(\theta + d\theta) - \sin \theta). \quad (3.5)$$

Substituting eq. 3.4 and eq. 3.5 in eq. 3.3 and integrating up to a maximum angle  $\theta_M$ , the critical Casimir force at coexistence ( $\delta\mu/h = 0$ ) reads,

$$\begin{aligned} \beta F_C &= \frac{R}{z^2} \int_0^{\theta_M} \frac{\sin(\theta + d\theta) - \sin \theta}{\left[1 + 2\frac{R}{z}(1 - \cos \theta)\right]^2} \\ &\quad \times \vartheta\left(z \left[1 + 2\frac{R}{z}(1 - \cos \theta)\right] / \xi\right), \end{aligned} \quad (3.6)$$

with  $\xi = \xi_\tau$ , the bulk correlation length. In the Derjaguin approximation,  $R \gg z$ , and as a consequence, the integral is dominated by the small angle contributions, such that  $1 + 2\frac{R}{z}(1 - \cos \theta) \approx 1 + (R/z)\theta^2$ . If we change the integral variable to  $l = 1 + (R/z)\theta^2$ , we find,

$$\beta F_C = \frac{1}{2} R^{1/2} z^{-3/2} \int_1^{l_M} dl \frac{1}{l^2 \sqrt{l-1}} \vartheta(l\xi). \quad (3.7)$$

The critical Casimir potential,  $\Phi_C(z)$  follows from integrating the critical Casimir force,  $\beta F_C$  in eq. 3.7,

$$\begin{aligned} \beta \Phi_C(z) &= \frac{1}{2} R^{1/2} \int_z^\infty d\kappa \int_1^\infty dl \frac{\kappa^{-3/2}}{l^2 \sqrt{l-1}} \vartheta(\kappa l / \xi) \\ &= \frac{1}{2} \left(\frac{R}{z}\right)^{1/2} \int_1^\infty dq \int_1^\infty dl \frac{q^{-3/2}}{l^2 \sqrt{l-1}} \vartheta(l q z / \xi). \end{aligned} \quad (3.8)$$

The integral is over a universal scaling function, and depends only on  $z/\xi$ , which allows us to write,

$$\beta\Phi_C(z) = \frac{1}{2} \left( \frac{R}{z} \right)^{1/2} \Theta(z/\xi), \quad (3.9)$$

where we substituted the integral with  $\Theta(z/\xi)$ .

In the opposite limit of  $\xi \gg z \gg R$ , the critical Casimir potential is derived using the so-called ‘small-sphere’ operator product expansion [132],

$$\beta\Phi_C(z) = -\sqrt{2} \left( \frac{R}{z} \right)^{1/4} \Theta'(z/\xi). \quad (3.10)$$

In section 3.4, we compare the critical Casimir potentials obtained from MC simulations using the cluster algorithm, with the two scaling limits shown above.

## 3.4 Results

### 3.4.1 Scaling of the Critical Casimir Potential in 2D

In section 2.4.5, we saw that knowledge of the effective two-body potential can be used to elucidate the various features of the phase diagram of the LGHD model. The dependence of the effective potentials on the size of the colloids and adsorption strengths can, thus, give us valuable information pertaining the phase behavior of the mixture.

Using the LGHD model, we calculate the effective two-body (critical Casimir) interaction between a pair of colloids. We use the TMMC method to extract the probability distribution of finding a colloid of radius  $R$  at a position  $\mathbf{r}$  with respect to a colloid of equal size. In our simulations, we use square lattices of different sizes, depending on the correlation length and fix the position of one disk at the origin. Due to the periodic boundary conditions we only need to consider positions of the second disk restricted to one quarter of the lattice. See section 2.3.3 for a more in-depth description. After extracting the probability distribution  $P(\mathbf{r})$ , the effective potential is easily calculated as,

$$\beta U(\mathbf{r}) = -\ln \frac{P(\mathbf{r})}{P(\infty)}. \quad (3.11)$$

In figure 3.3 we plot the critical Casimir interaction between a pair of hard disks for a range of radii and temperatures, corresponding to bulk correlation lengths  $7.5 < \xi < 23$ , and for two surface fields,  $\alpha = 19$ , which is well beyond the saturation transition, and for neutrally adsorbing disks,  $\alpha = 0$ , for the two scaling limits in equations (3.9) and (3.10). In figures 3.3(a) and 3.3(c), the two scaling limits are compared for  $\alpha = 19$ . In figure 3.3(a), we show the critical Casimir interactions using the scaling as predicted using the Derjaguin approximation. As the size of the colloids is of the order of the bulk correlation length,  $\xi$ , the Derjaguin approximation is not valid, and indeed we find no collapse of the data, especially at short distances. In figure 3.3(c), we plot the critical Casimir interactions using the scaling in the small-sphere limit. We find a better collapse of the data using the small-sphere scaling limit. At short distances, we find deviations which we attribute to the discretization of the colloids. For neutrally adsorbing colloids,

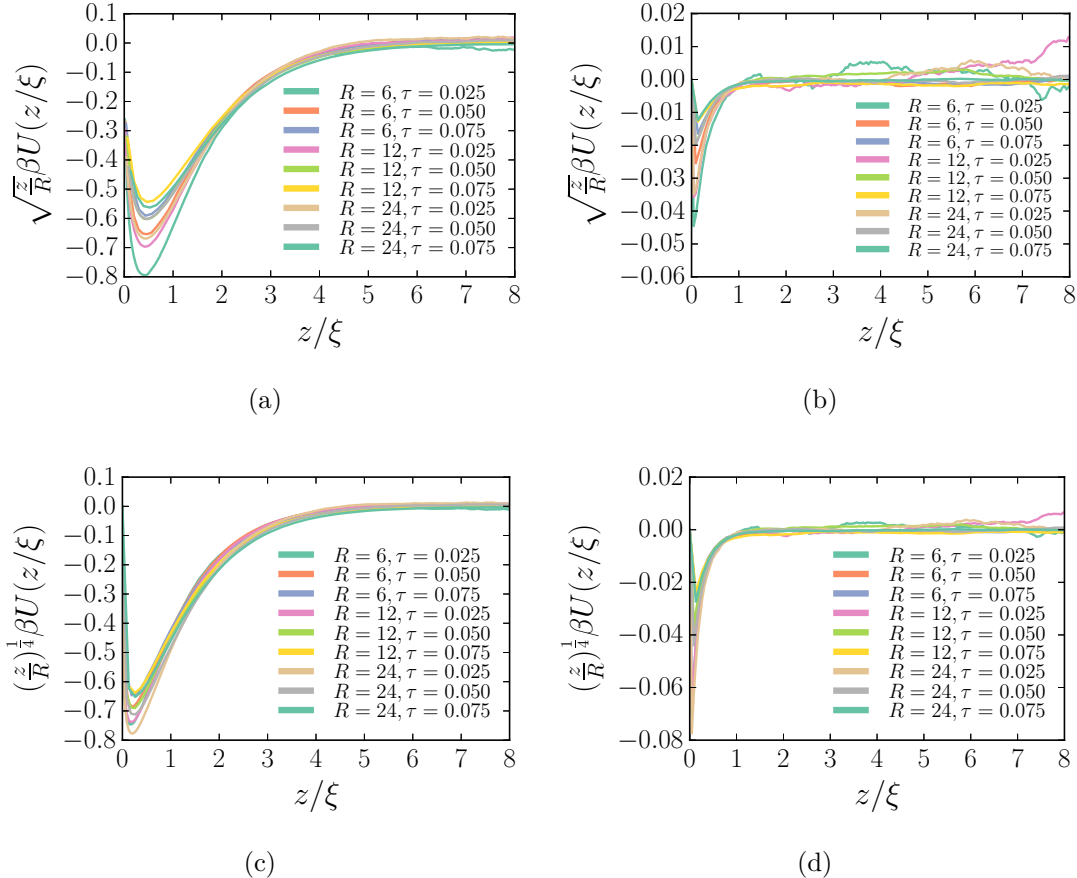


**Figure 3.3:** Critical Casimir interactions of two hard disks as a function of the scaled surface-to-surface distance  $z/\xi$  for different radii, temperatures and surface fields at bulk solvent coexistence ( $\delta\mu = 0$ ). Figures (a) and (c) are for colloids with adsorption strength  $\alpha = 19$ , well beyond the saturation transition, while figures (b) and (d) are for an adsorption strength  $\alpha = 0$ , i.e. for neutrally adsorbing disks. The critical Casimir interactions in figures (a) and (b) are plotted using the Derjaguin scaling limit (eq. 3.9), while figures (c) and (d) are plotted using the small-sphere limit (eq. 3.10).

$\alpha = 0$ , we have a very short-ranged weak attraction. Again, both scaling limits seem to give good scaling results in figures 3.3(b) and 3.3(d), with the small-sphere limit giving slightly better results once more.

The scaling plots in figure 3.3, make it clear that the colloid sizes in our simulations are closer to the small-sphere limit, which is also known as the ‘protein limit’. This makes our results especially useful for studies in e.g. living cells [123, 124].

### 3.4.2 3D Model Phase Diagram

In this section, we demonstrate that the development of our cluster algorithm also enabled us to perform large-scale simulations of a ternary *AB*-solvent-colloid mixture in 3D and in near-critical solvent conditions. We do this by assessing the phase behavior, and compare

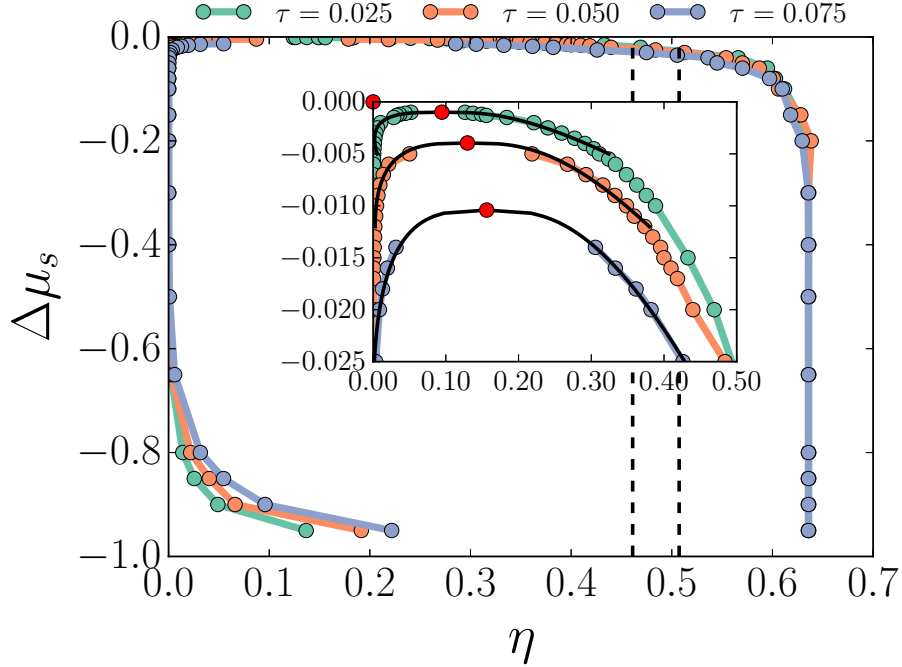


**Figure 3.4:** Phase diagram of the *ABC* ternary mixture, computed using the direct coexistence method, for three fixed temperatures  $\tau = 0.025$  (green),  $\tau = 0.05$  (orange), and  $\tau = 0.075$  (blue) with colloid radius  $R = 6$  and colloid-solvent adsorption strength  $\alpha = 0.6$ . In this solvent chemical potential,  $\Delta\mu_s$ , vs colloid packing fraction,  $\eta$ , representation, the tie lines are horizontal. The red circles and black lines in the inset are the critical points and binodals respectively, obtained by least-squares fitting of equation (3.12). Note that the vertical dashed lines denote fluid-solid coexistence for our lattice representation of the pure hard-sphere system; see text.

the overall topology of the resulting 3D phase diagram with that of the two-dimensional system introduced in chapter 2. This comparison is achieved by calculating the solvent chemical potential difference,  $\Delta\mu_s$ , vs colloid packing fraction,  $\eta$ , phase diagrams of the ternary mixture at different reduced temperatures,  $\tau$ .

To calculate the phase diagrams, we employ the direct coexistence method [126] in which an elongated box is used to facilitate the formation of an interface between two phases. This allows us to calculate density profiles along the direction normal to the interface, from which the colloid coexistence packing fractions,  $\eta$  can be ‘read off’ for a fixed solvent chemical potential,  $\Delta\mu_s$ . We thus treat the colloids in the canonical ensemble, whereas the solvent is treated grand-canonical, similarly to chapter 2. Throughout this section, a simulation box with dimensions of  $128 \times 128 \times 256$  lattice sites is used; this is large enough to avoid significant finite-size effects.

By calculating the density profiles at different chemical potentials,  $\Delta\mu_s$ , we determined the phase diagrams for three different temperatures,  $\tau = 0.025, 0.05$ , and  $0.075$ , as shown in figure 3.4, and for a colloid radius  $R = 6$ , and a fixed value of the adsorption strength used previously in 2D in chapter 2,  $\alpha = 0.6$  — we focus on the supercritical, *B*-rich,  $\Delta\mu_s < 0$  region, where capillary effects are absent. We observe colloidal gas (G), liquid

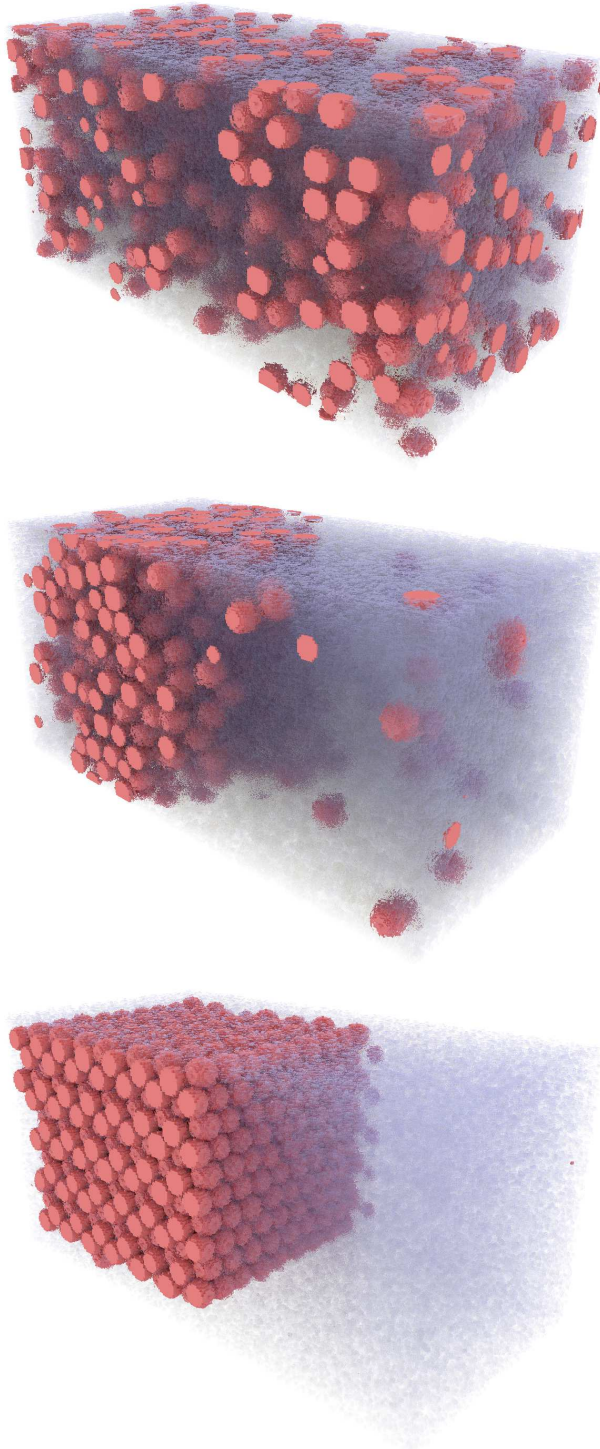


**Figure 3.5:** Representative configurations of our ternary colloid-solvent mixture model at reduced temperature  $\tau = 0.05$ , colloid radius  $R = 6$ , and for different chemical potentials, **Top:**  $\Delta\mu_s = -0.002$  (supercritical), **Middle:**  $\Delta\mu_s = -0.008$  (G-L coexistence), and **Bottom:**  $\Delta\mu_s = -0.3$  (G-X coexistence). The pink-colored particles represent the colloids, while the grey-colored ones, the solvent  $B$  species. The configurations were visualized using a path tracing renderer.

(L), and crystal (X) phases, as well as phase coexistence between colloidal gas and liquid phases, and colloidal gas and crystal phases, with pronounced fractionation of the solvent. In figure 3.5 we show examples of G-L (middle), and G-X (bottom) coexistence, along with a supercritical configuration (top). In the inset of the phase diagram in figure 3.4, we present a close-up of coexistence in the near critical region. We also plot estimates of the critical points, obtained by a least-squares fit to the equation [110–113]

$$\eta_{\pm} - \eta_c = A |\Delta\mu_s - \Delta\mu_s^c| \pm \frac{1}{2} B |\Delta\mu_s - \Delta\mu_s^c|^{\beta} \quad (3.12)$$

where  $\eta_{\pm}$  stands for the coexisting colloidal liquid/gas packing fraction, with  $\eta_c$  its critical value, and  $A, B$ , are fit parameters. The critical exponent,  $\beta$ , was fixed to its value for the three-dimensional Ising universality class,  $\beta = 0.3258$  [133]. Note that we have substituted temperature with the solvent chemical potential,  $\Delta\mu_s$ , with  $\Delta\mu_s^c$  being the solvent chemical potential at the critical point of the ternary mixture. We note that we use equation (3.12) as a fit to our result, only in order to guide the eye. From the phase diagram in figure 3.4, we observe broad G-X coexistence for  $\Delta\mu_s < -0.1$ , and a L-X coexistence region for  $-0.1 < \Delta\mu_s < -0.9$ , which becomes narrower upon decreasing  $\Delta\mu_s$ . In addition, we expect to recover the fluid-crystal transition of pure hard spheres at  $\Delta\mu_s = \pm\infty$ , corresponding to hard spheres in either a pure  $A$  or a pure  $B$  solvent background. We thus find that the G-L binodal ends in a G-L-X triple point at lower  $\Delta\mu_s$ . Assuming the colloidal spheres are sufficiently large that lattice effects are minimal, the system of pure hard spheres should exhibit fluid-crystal coexistence at packing fractions  $\eta = 0.4915$  and  $\eta = 0.5428$  [134]. From our lattice simulations, we find that the actual coexistence packing fractions are  $\eta = 0.4611$  and  $\eta = 0.5073$ , drawn as dashed lines in figure 3.4. This should come as no surprise; the spheres in our model are rather small such that the lattice discretization affects their packing and hence the coexistence packing fractions.

From the phase diagram in figure 3.4 it is clear that the topology is similar to that of the two-dimensional system. The coexistence curves of the three-dimensional system, are broader, mainly due to the fact that the particle surface is proportional to  $R^2$  as opposed to  $R$  in 2D; the colloidal particles in 3D are overall adsorbing more strongly for the same value of  $\alpha$ . The phase diagrams also exhibit the same trends when decreasing the temperature,  $\tau$ ; the two-phase G-L(X) coexistence region broadens, and the critical point of the ternary system shifts towards the critical point of the pure solvent reservoir.

### 3.5 Conclusion

Computer simulations of a suspension of colloidal particles in a near critical solvent mixture in three dimensions were previously prohibited due to slow equilibration arising from large differences in length and time scales between the individual components, the strong adsorption of the solvent on the colloids, and the critical slowing down. In this work, we circumvented these problems by developing a rejection-free geometric cluster algorithm which takes advantage of the point reflection symmetry of the Hamiltonian of our lattice-based model.

Using a cluster-type algorithm for the model of a ternary colloid binary solvent mixture introduced in chapter 2, we calculated the 2D effective interactions of hard disks with very

high precision, which enabled us to test the Derjaguin and ‘small-sphere’ scaling limits. In the Derjaguin approximation, the distance,  $z$  between two spherical particles is assumed to be much smaller than their radius,  $R$ , while in the small-sphere expansion, the opposite is assumed, i.e. that the spheres are much farther apart than the size of their radii. From the scaling limits, we deduced that our disks size corresponds to the typical size of proteins as the effective interactions show a better collapse using the small-sphere scaling.

We further determined the phase behavior of colloidal hard spheres in a near-critical solvent mixture in 3D, using the direct coexistence method. We determined the gas-liquid and gas-solid binodals for three different supercritical reduced temperatures,  $\tau = 0.025, 0.05$ , and  $0.075$ , close to the solvent reservoir’s critical point. We found the same qualitative features as in the two-dimensional case: i) we observe that the upper gas-liquid critical point of the ternary colloid-solvent mixture shifts towards lower solvent chemical potential differences  $\Delta\mu_S$  and higher colloid packing fractions,  $\eta$ , upon adding colloids, and ii) we find broad gas-liquid and gas-solid phase coexistence, with significant fractionation of the solvent species favored by the colloids.

In conclusion, we have developed a rejection-free geometric cluster algorithm which enabled us to investigate the scaling behavior of the critical Casimir pair potentials, and to determine the phase diagram of colloids in a binary solvent mixture in 3D. Moreover we also demonstrated that the key features of our previous results on the phase behavior and structure in two dimensions, in chapter 2, are present in three dimensions.

## Acknowledgements

We thank J. R. Edison, R. Evans, for many stimulating and inspiring discussions.

# 4

---

## Are Antagonistic Salt Solutions Block Copolymers? No, but they behave similarly.

---

Mesophases are phases that lie in between the solid and liquid phase, and are classified by their symmetry. Recent experiments using a binary solvent mixture of deuterium oxide ( $D_2O$ ) and 3-methylpyridine (3MP), showed the presence of a lamellar mesophase, for certain concentrations of sodium tetraphenylborate ( $NaBPh_4$ ), an organic salt. The organic salt used in the experiments consists of an organic group with a small inorganic counterion. The lamellae were found to assemble into micrometer-sized onion-like structures with a lamella spacing on the order of 10 nm. Although theoretical models have been able to describe the experimental results to a certain extent, the degrees of freedom of the solvent mixture are integrated out, and treated on a mean-field level, thereby ignoring fluctuations. Moreover, simulation techniques involving electrostatics are computationally expensive, due to the long range of the Coulomb interaction. Here, we develop an efficient lattice model, and present the first simulation study of an antagonistic salt suspended in a polar binary solvent mixture. In our lattice model, the solvent mixture and electrostatics are treated explicitly, by combining the simplicity of a lattice gas model and the efficiency of the auxiliary field method for treating the electrostatics. In our study of an antagonistic salt solution, we find rich mesophase behavior, including a lamellar phase, for a wide range of temperatures, and solvent and salt compositions, resembling the phase behavior of diblock copolymers. We further analyze the ion distribution, and behavior of the lamellar phase as a function of the salt concentration and temperature and build a simple mean-field theory which is capable of describing our observations.

## 4.1 Introduction

In section 1.5, we gave a brief introduction on the effect of ions on the phase behavior of binary mixtures of water and organic solvent (oil). The dissolved ions interact via Coulombic interactions, and each ionic species may have a preference for a particular solvent species. In chapters 2, and 3, we saw that a simple suspension of neutral solutes in a binary solvent mixture with the solutes preferring one of the two solvent species, leads to rich phase behavior. The fact that electrostatics also come into play leads us to believe that the behavior of electrolyte solutions should be even richer. In 1943 it was already shown that the addition of salt consisting of hydrophilic ion pairs expands the two-phase region of these binary mixtures [135, 136], as the interfacial tension increases. The effect of hydrophilic salt is thus opposite to that of surfactants that decrease the surface tension.

In 2001, Jacob *et al.* detected a novel phase behaviour in aqueous systems of organic solutes [137–139]. They reported the formation of a solid-like third phase forming at the liquid/liquid interface of a 3-methylpyridine-water mixture, and long-lived mesoscopic heterogeneities, with the addition of NaBr salt at near-critical conditions. It was later found that these heterogeneities occurred only when the solution was contaminated by impurities [140–142]. Nonetheless, this sparked interest in the community, leading to the discovery of periodic structures in solutions of antagonistic salts [142–146]. Sadakane *et al.* observed that the addition of small amounts of sodium tetraphenylborate ( $\text{NaBPh}_4$ ), which consists of a hydrophobic cation,  $\text{Na}^+$ , and a hydrophilic anion,  $\text{BPh}_4^-$ , to a mixture of  $\text{D}_2\text{O}$  and 3-methylpyridine (3MP), a mixture with both a lower and upper critical solution temperature, made the phase coexistence region shrink. For high enough salt concentrations, they found that the phase coexistence region completely disappeared, and instead observed, using neutron scattering, lamellar structures within the one-phase region of the pure solvent mixture, even far from criticality [144–146]. Moreover, in some cases they found that the lamellae formed onion-like structures composed of approximately 1000 concentric lamellae with a lamella spacing of  $\sim 18 \text{ nm}$ .

Already in 1980, Nabutovskii theorized, using a mean-field theory, the existence of a phase with a periodic substructure in the vicinity of the critical point of an electrolyte solution [44]. This phase was found to occur due to the interaction of charge-density and order-parameter waves when the solutes adsorbed strongly. This mesophase was not further studied until recently by Onuki *et al.* [147–150], who was motivated by the experimental advances of Sadakane *et al.* [143–146]. Using a mean-field model of a mixture of oil, water and an antagonistic salt with strong adsorption, they were able to find various mesophases, including phases with a bicontinuous and a tube-like pattern of the solvent composition. They also found an onion structure as the one discovered experimentally by Sadakane *et al.* [144–146]. Furthermore, Onuki *et al.* [151] and Pousaneh *et al.* [152] studied the effective interactions between a pair of colloids suspended in such an antagonistic salt solution, and found an oscillatory interaction, as is expected due to the periodic substructure.

The above developments are important for the study of biological systems. These usually contain some amount of salt that allows for important effects, such as osmosis, a vital process for living organisms. The developments by Onuki *et al.* [151] and Pousaneh

*et al.* [152], underline, furthermore, the importance of salt concentration in colloidal suspensions. If an oscillatory interaction between colloids can be realized experimentally, they could potentially self-assemble into quasi-crystals [153–156].

As outlined above, the antagonistic salt solution has been treated theoretically at the mean-field level. Although the theory has been successful in describing the experimental observations, mean-field theories neglect fluctuations, which could be potentially important in describing a near-critical system. Moreover, in the theories developed by Ciach *et al.* and Onuki *et al.*, the mixture constituents are taken to be point-like, neglecting excluded volume interactions. On the other hand current simulation techniques are notoriously slow, due to the long range of the Coulomb interaction. Moreover, in simulating solutions of ions in polar fluids, techniques such as the ‘Ewald sum’ [157], cannot handle dipole-charge interactions — dipoles need to be treated as a pair of charges, adding to the already high complexity of the algorithm. In addition, effects based on the fluctuation of dipoles, or the dielectric inhomogeneity in a medium, are collective effects that can make the equilibration of a model system very difficult. Here, motivated by the intriguing mesophase behavior of a (polar) solution of antagonistic salt, as seen in the experimental work of Sadakane *et al.* [143–146], and the lack of computationally efficient simulation techniques in this area, we develop a lattice model of solutes suspended in an explicit polar binary solvent mixture. The electrostatics are treated explicitly, using a relatively new, highly efficient, simulation technique developed by Maggs [158], in which an auxiliary electrostatic field is evolved using local Monte Carlo moves. Using this model, we not only replicate the experimental results of Sadakane *et al.* but we are able to uncover an even richer behavior, as a function of its solvent composition, temperature, and salt concentration.

This chapter is organized as follows. In section 4.2, we present our lattice model and in section 4.3 we present the Monte Carlo algorithms that we employ to treat the electrostatics. In section 4.4 we present the results of our study on the mesophase behavior of the mixture, after first verifying the validity of our model by comparing it with theoretical predictions of the Poisson-Boltzmann theory. Finally, in section 4.5, we present our concluding remarks.

## 4.2 Model

As alluded to in the Introduction, simulating an explicit solution of ions in a polar solvent, is hampered by the high computational cost of current methods of handling the electrostatics in a model system. This is reflected in the scarcity of simulation-based research literature on this topic. Here, we choose to use a lattice-gas model, coupled with the simulation method developed by Maggs, which we henceforth simply call ‘Maggs’s method’, to treat the electrostatics. A lattice-based model is chosen over a continuum model because of the simplicity, and the coarse-graining and parallelization opportunities these models present. Lattice-gas models have also been used extensively to study wetting and capillary phenomena, and the effects of confinement [91, 92], and we are, thus, provided with a wealth of information pertinent to our solvent mixture. Below, we describe our model, and in section 4.3 we introduce the Monte Carlo algorithms we use to simulate it.

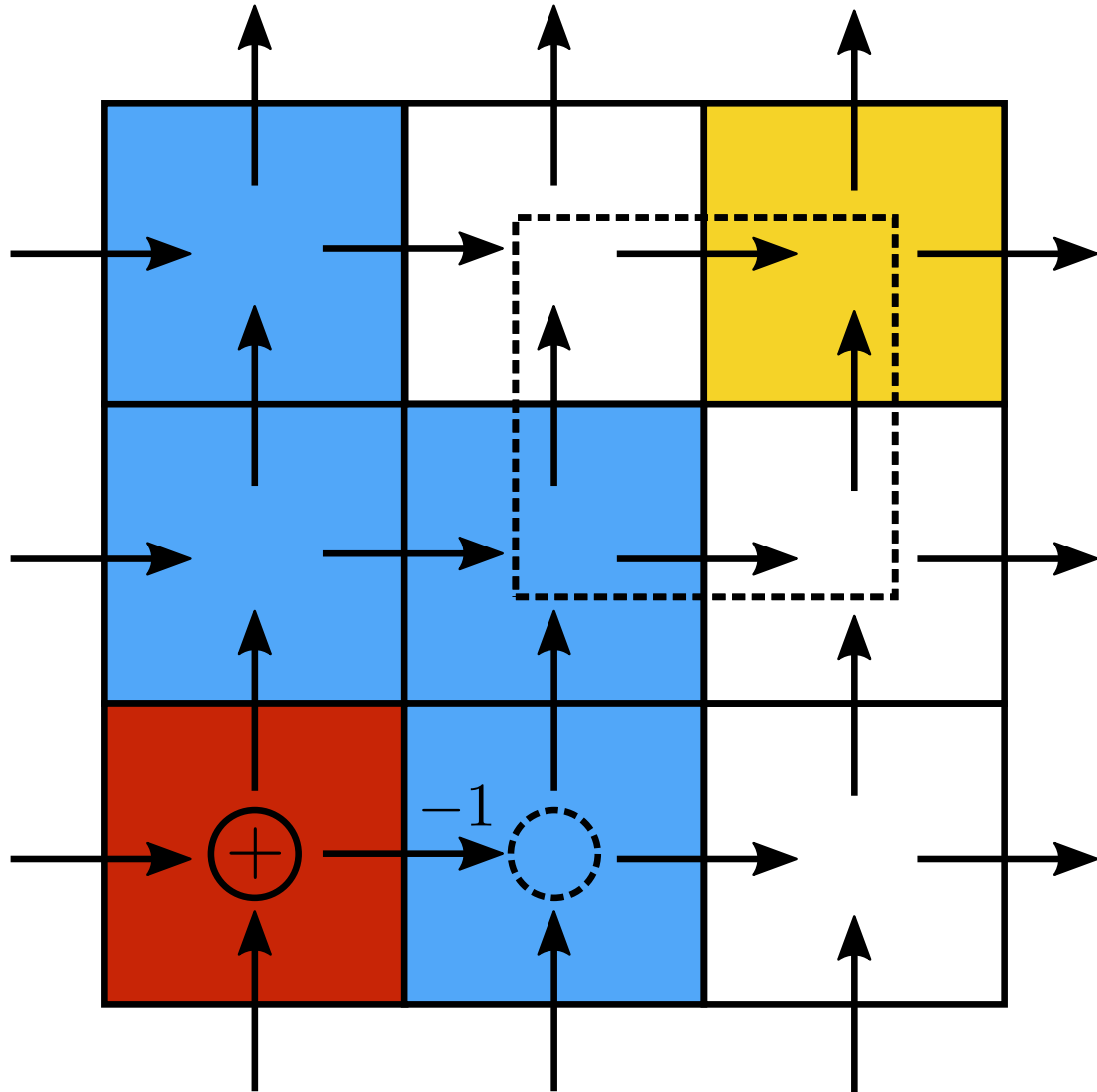


**Figure 4.1:** Schematic representation of the lattice model of an ion-solvent mixture with the grid representing the lattice sites. The different colors represent the different species of the model, with white and blue representing  $A$  and  $B$  solvent species, respectively, and yellow and red representing negative and positive ions. The arrows represent the discretized electric field of Maggs's method – the magnitude of the field is not shown here. The dotted square encloses a field plaquette. In the lower left corner, a positive ion is drawn. To move the ion to the lattice site to the right, the reduced  $\tilde{D}$  field on the link between the two sites needs to be modified by  $-1$ , so that Gauss's law (eq. (4.11)) is satisfied.

We consider a simple cubic lattice consisting of  $N$  sites of size  $\Lambda$ . Each site,  $i$ , of our lattice model can be occupied by one of the following four species: the  $A$  or  $B$  solvent species, and the positive or negative ionic species, as depicted in figure 4.1. We define an occupancy operator,  $o_{i\mu}$ , to take the value 1 if site  $i$  is occupied by species  $\mu$ , and 0 otherwise. Note that we use Greek subscripts to denote lattice species, and Latin to denote the lattice site. We also require excluded volume interactions between all species, i.e.

$$\sum_{\mu} o_{i\mu} = 1 \quad (4.1)$$

where the sum is implied to run over all species. The different species of our model, may interact with each other via a short-ranged nearest-neighbor interaction,

$$\mathcal{H}_{LG} = -\frac{\epsilon}{2} \sum_{\langle i,j \rangle} \sum_{\mu,\nu} J_{\mu\nu} o_{i\mu} o_{j\nu} \quad (4.2)$$

where the first sum runs over all nearest-neighbour pairs  $\langle i,j \rangle$ , and where  $J_{\mu\nu}$ , sets the strength of the interaction between species  $\mu$  and  $\nu$ . It is important to realize that a lattice site does not represent e.g. a single ion or solvent molecule, but a coarse-grained view of a solvated ion, or a ‘blob’ of solvent molecules.

As discussed earlier, we use the method first introduced by Maggs and Rosetto [158], to simulate the electrostatics in our model system. The advantage of Maggs’s method is two-fold; it circumvents the time-consuming computations of the long-ranged Coulombic interactions in charged systems, which is often based on Ewald summation methods, and it can be straightforwardly applied to systems with a spatially varying dielectric permittivity (or polarization), in contrast to conventional methods. It uses constrained updates of an auxiliary electric field instead of the electric potential, which allows the co-evolution of field and charged particles. More specifically, in a Monte Carlo simulation, the electrostatics can be simulated by generating configurations with a probability proportional to the Boltzmann distribution with the following Hamiltonian for the electrostatic energy,

$$\mathcal{H}_D = \frac{1}{2} \int d\mathbf{r} \frac{\mathbf{D}^2(\mathbf{r})}{\epsilon(\mathbf{r})}, \quad (4.3)$$

where  $\epsilon(\mathbf{r})$  is the spatially varying dielectric, and  $\mathbf{D}(\mathbf{r})$  is the electric displacement field, which obeys Gauss’s law,

$$\nabla \cdot \mathbf{D}(\mathbf{r}) - \rho(\mathbf{r}) = 0, \quad (4.4)$$

with  $\rho(\mathbf{r})$  the charge density field. For brevity’s sake we shall drop the explicit dependence on the variable  $\mathbf{r}$ . We can then write the partition function by taking the path integral over all configurations of the electric displacement and charge density fields.

$$\mathcal{Z} = \int \mathcal{D}\rho \int \mathcal{D}\mathbf{D} \delta[\nabla \cdot \mathbf{D} - \rho] e^{-\frac{\beta}{2} \int d\mathbf{r} \frac{\mathbf{D}^2}{\epsilon}}. \quad (4.5)$$

The general solution to Gauss’s law eq. (4.5), is given by  $\mathbf{D} = \mathbf{D}_{\parallel} + \mathbf{D}_{\perp}$ , with  $\mathbf{D}_{\perp} = -\epsilon \nabla \phi$  and  $\mathbf{D}_{\parallel} = \nabla \times \mathbf{Q}$  being the transverse and longitudinal parts, respectively. By doing so, the partition function factorizes,

$$\mathcal{Z} = \int \mathcal{D}\rho e^{-\frac{\beta}{2} \int d\mathbf{r} \epsilon(\nabla \phi)^2} \times \int \mathcal{D}\mathbf{D}_{\perp} \delta[\nabla \cdot \mathbf{D}_{\perp}] e^{-\frac{\beta}{2} \int d\mathbf{r} \frac{\mathbf{D}_{\perp}^2}{\epsilon}} = \mathcal{Z}_{\text{Coulomb}} \times \mathcal{Z}_{\perp}. \quad (4.6)$$

Here,  $\mathcal{Z}_\perp = \text{const.}$ , is independent on the charge positions, and contains only integrations over the transverse field degrees of freedom, while  $\mathcal{Z}_{\text{Coulomb}}$  gives the Coulomb interactions between the charged particles. From the above, it is evident that only the transverse degrees of freedom need to be integrated out, along with the charge positions with the restriction that Gauss's law is preserved. The system is subsequently discretized by defining a lattice of  $N = N_x N_y N_z$  sites with periodic boundary conditions. The electric field is discretized on the links between the lattice sites. This discretization scheme is often also used when solving Poisson's equation using finite difference methods [159] (see also figure 4.1). We denote the field on the link between sites  $i$  and  $j$  as  $D_{ij}$ .

To make the species in our model polar, we further assign a dielectric permittivity,  $\varepsilon_\mu$ , to each of them. For Maggs's method, knowledge of the value of the dielectric constant at the positions of the lattice links is required. We choose to interpolate the dielectric permittivity on the link between sites  $i$  and  $j$  by taking the harmonic mean of the permittivities of the two sites, as follows [160],

$$\frac{1}{\varepsilon_{ij}} = \frac{1}{2} \left( \frac{1}{\varepsilon_i} + \frac{1}{\varepsilon_j} \right) \quad (4.7)$$

where  $\varepsilon_i = \sum_\mu \varepsilon_\mu o_{i\mu}$ , is the dielectric permittivity of the species occupying site  $i$ . In Yee's finite-difference time-domain scheme, effective permittivities are often used to account for offsets of dielectric interfaces from grid nodes [161]. Note that we can also write  $1/\varepsilon_i = \sum_\mu (1/\varepsilon_\mu) o_{i\mu}$ , which leads to the following expression for the dielectric permittivity of link  $\{i, j\}$ ,

$$\frac{1}{\varepsilon_{ij}} = \sum_\mu \frac{1}{2\varepsilon_\mu} (o_{i\mu} + o_{j\mu}). \quad (4.8)$$

With all this, the full Hamiltonian of our model system reads,

$$\mathcal{H} = \mathcal{H}_{LG} + \frac{\Lambda^3}{4} \sum_{\langle i,j \rangle} \sum_\mu \frac{1}{\varepsilon_\mu} D_{ij}^2 (o_{i\mu} + o_{j\mu}). \quad (4.9)$$

$\mathcal{H}_{LG}$ , here, is the nearest-neighbour interaction term defined in eq. (4.2). The second part is the electrostatic energy. Substituting  $D_{ij} \rightarrow (e/\Lambda^2) \widetilde{D}_{ij}$ , where  $e$  is the elementary charge, the Hamiltonian reads,

$$\mathcal{H} = -\frac{\epsilon}{2} \sum_{\langle i,j \rangle} \sum_{\mu,\nu} J_{\mu\nu} o_{i\mu} o_{j\nu} + \frac{\epsilon\Gamma}{4} \sum_{\langle i,j \rangle} \sum_\mu \frac{1}{\tilde{\varepsilon}_\mu} \widetilde{D}_{ij}^2 (o_{i\mu} + o_{j\mu}), \quad (4.10)$$

with  $\Gamma = e^2/\varepsilon_0 \Lambda \epsilon$ , and  $\tilde{\varepsilon}_\mu = \varepsilon_\mu/\varepsilon_0$ , is the value of the dielectric constant. With these definitions, Gauss's law reads simply,

$$\sum_{j \in nnb(i)} \widetilde{D}_{ij} = o_{i+} - o_{i-}. \quad (4.11)$$

Note that the dielectric constants of the different species of our model,  $\tilde{\varepsilon}_\mu$ , can be written as a function of the dielectric constant of one of the species. We thus set  $\tilde{\varepsilon}_A = 1$ , and vary the dielectric constants of the other species in our simulations.

### 4.3 Methods

The solvent and ions in the model introduced above, are simulated in the canonical ensemble using the following Monte Carlo moves,

1. Attempt to translate a solvent site by swapping it with a nearest-neighbour solvent site of the opposite species.
2. Attempt to swap an ion site with a nearest-neighbour solvent site.
3. Attempt to modify the circulation of the electric field  $\widetilde{D}$  in a closed directed loop.
4. Attempt to modify the global field  $\widetilde{D}_g$  in the directions in which metallic boundary conditions are imposed.

and are accepted using the standard Metropolis acceptance,  $a = \min[1, \exp(-\beta\Delta\mathcal{H})]$ , where the energy difference,  $\Delta\mathcal{H}$ , is calculated from eq. (4.10). Site in move 1 are chosen randomly from the lattice, and moves which end up picking a non-solvent site are immediately rejected. For the ion translations in move 2, we keep a list of their positions, so we can randomly pick an ion straightforwardly. In each Monte Carlo cycle, we perform move 1 and 3,  $N$  times, move 2,  $N_{\pm}$  times, and we perform move 4 once.

To simulate the solvent grand-canonically, step 1 is replaced by an attempt to ‘flip’ the species of a solvent site, and is accepted by the Metropolis criterion,

$$a(N_B \rightarrow N_B \pm 1) = \min \left[ 1, e^{-\beta(\Delta\mathcal{H} \mp \epsilon\Delta\mu_s)} \right] \quad (4.12)$$

where  $\Delta\mu_s = (\mu_B - \mu_A)/\epsilon$  is the chemical potential difference between the two solvent species.

When we move an ion from site  $i$ , to its neighbour site,  $j$ , in the case of move 2, the field on the link connecting sites  $i$  and  $j$ ,  $\widetilde{D}_{ij}$ , needs to be modified by  $-(o_{i+} - o_{i-})$  to satisfy Gauss’s law, as shown in figure 4.1. The move is then accepted with the standard Metropolis criterion, based on the change in electrostatic energy, given by the second part in eq. (4.10). Additionally, to increase the acceptance, we use temporary charge spreading, as described in Ref. [162], and later generalized by Maggs *et al.* [160]. The concept of temporary charge spreading is simple; the charge of the ion is temporarily spread to neighbouring sites according to some rule that maximizes the overall acceptance, they are subsequently translated, and pulled back in. The benefit of temporary spreading is that the modification of the electric field is also spread out, leading to an overall higher acceptance based on the spreading range.

To generate configurations of the electric field,  $D$ , with the correct statistical weight, an additional Monte Carlo move is introduced (move 3, above), which integrates over the transverse degrees of freedom,  $\mathbf{D}_{\perp}$ , by modifying the field circulation. This can be achieved by modifying the field along a closed directed path, by some random value, and again, accepted based on the energy change in eq. (4.10). The simplest such path is shown in figure 4.1, and is commonly referred to as a plaquette. As described in Refs. [163, 164], under periodic boundary conditions, the electric field actually decomposes into

$$\mathbf{D} = -\epsilon\nabla\phi + \nabla \times \mathbf{Q} + \mathbf{D}_g, \quad (4.13)$$

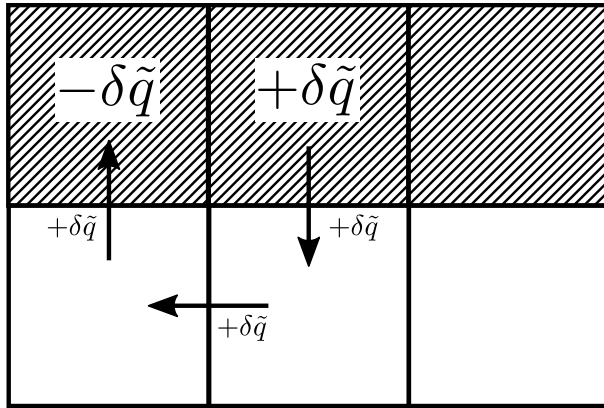


**Figure 4.2:** Local update move for fluctuating the surface charge of a metallic plate (hatched sites). A random reduced charge  $\delta\tilde{q}$  is exchanged between the two sites, and the reduced field,  $\tilde{D}$ , along the arrows shown in the figure are modified by an amount  $\delta\tilde{q}$  so that Gauss's law is satisfied and the field inside the plate remains zero.

where the global electric field,  $\mathbf{D}_g = \text{const}$ , and  $\phi$  is the electrostatic potential. If we wish to simulate tinfoil instead of vacuum boundary conditions, the global electric field,  $\mathbf{D}_g$ , also needs to be relaxed with a Monte Carlo move (move 4, above). Tinfoil boundary conditions set the dielectric constant at infinite distance to  $\tilde{\epsilon}_\infty = \infty$ , while the vacuum boundary conditions set it to  $\tilde{\epsilon}_\infty = 1$ .

In addition to the above moves, we introduce an additional Monte Carlo move for simulating parallel charged plates with a fixed charge density. We need to be able to fluctuate the surface charge of the metallic plates while keeping the total charge fixed. Additionally, the electric field should be zero everywhere inside the metallic plates. Levrel and Maggs [164] introduced a Monte Carlo move in which a random site at the surface of a plate is chosen and a random amount of charge  $\delta q$  is transferred to a neighbouring site. To keep the electric field inside the plates zero, it is modified on a path outside the plates, as shown in figure 4.2. In our simulations, we perform this move  $N_\pm$  times. The surface charge on the plate surface is continuous, unlike the charge of the sites occupied by the ion species. When parallel plates are simulated, vacuum boundary conditions should be imposed in the direction perpendicular to the plates [164].

Before simulating a system, the electric field should be initialized so that it is consistent with Gauss's law. A simple procedure is to initialize the electric field to zero, and then take a Hamiltonian path through the lattice, e.g. a path that visits each site exactly once, and solve Gauss's law for each site visited by modifying the link to the next site in the path. On arriving at site  $p_i$ , i.e. the  $i$ th step of the path  $p$ , holding a charge  $q_{p_i} = o_{p_i+} - o_{p_i-}$ , we have already solved the Gauss constraint for sites  $\{p_1, \dots, p_{i-1}\}$ . The incoming link to the site,  $\{p_i-1, p_i\}$ , thus bears the initialized field  $\tilde{D}_{p_{i-1}, p_i} = \sum_{j=1}^{j=i-1} q_{p_j}$ . The outgoing field  $\tilde{D}_{p_i, p_{i+1}}$  is then set to  $\sum_{j=1}^{j=i} q_{p_j}$  so that  $\tilde{D}_{p_i, p_{i-1}} + \tilde{D}_{p_i, p_{i+1}} = q_{p_i}$ : Gauss's law is now fulfilled on site  $p_i$  and we proceed to site  $p_{i+1}$ . At the end of the path, we reach site  $p_N$  with  $\tilde{D}_{p_{N-1}, p_N} = \sum_{j=1}^{j=N-1} q_{p_j}$ . Imposing periodic boundary conditions in charged systems is only possible if the total charge,  $Q$ , is zero (otherwise the total energy is divergent). Thus  $\tilde{D}_{p_{N-1}, p_N} = Q - q_{p_N} = -q_{p_N}$  and Gauss's law is satisfied everywhere

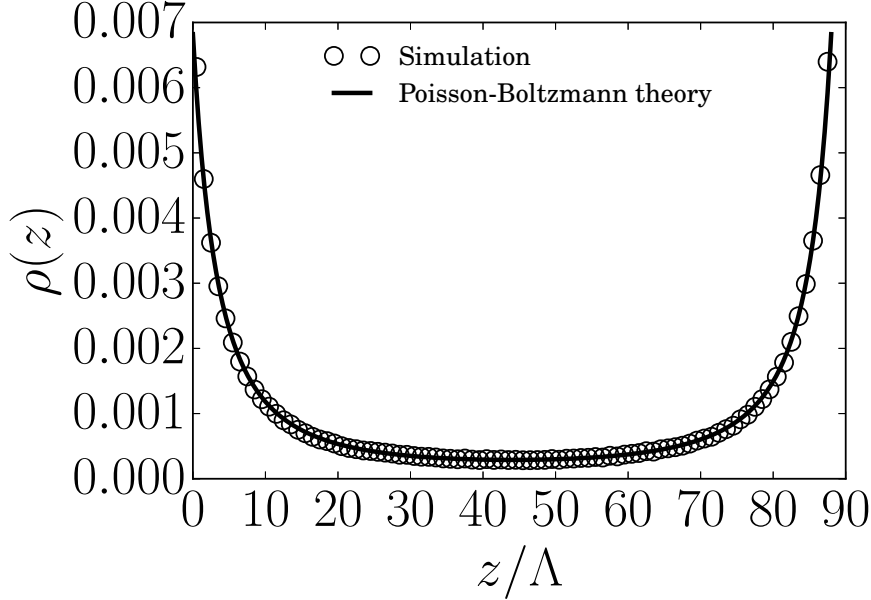


**Figure 4.3:** Ion density profile,  $\rho(z)$ , as a function of the distance to the left wall  $z/\Lambda$ . The simulated system consists of  $N_- = 128$  counter-ions of valency  $q = 1$  using a lattice of dimensions  $38 \times 38 \times 90$ , with a charge density of  $\sigma_s = 0.044e/\Lambda^2$  on each plate, at an inverse temperature  $\beta\epsilon = 13.299$ . The remaining lattice sites are filled by  $B$  solvent species, i.e.  $N_B = N - N_-$ , with permittivity  $\varepsilon_B = 2e^2/\Lambda\epsilon$ . The permittivity of the counter-ions is also set to  $\varepsilon_- = 2e^2/\Lambda\epsilon$ , so that  $\varepsilon = \varepsilon_B = \varepsilon_-$ . This results in a weak coupling,  $\Xi = 0.078$ . The straight line, is the result predicted by Poisson-Boltzmann theory in the weak coupling limit eq. (4.14).

on the lattice.

## 4.4 Results

### 4.4.1 Model Verification: Comparison with Poisson-Boltzmann Theory

A system consisting of two parallel uniformly charged plates inside an electrolyte, exhibits two classical length scales, the Bjerrum length,  $\lambda_B = e^2\beta/4\pi\varepsilon$ , which is defined as the length at which the thermal energy equals the Coulomb energy between two unit charges (elementary charge  $e$ ), and the Gouy-Chapman length,  $\mu = e/2\pi q\sigma_s\lambda_B$ , which measures the distance from the wall at which the potential energy of an isolated ion reaches thermal energy. Here,  $q$  is the charge valency, and  $\sigma_s$  is the charge density of the plates. We also introduce the so called *coupling parameter*,  $\Xi = 2\pi q^3\lambda_B^2\sigma_s/e$ , in line with Refs. [38, 39].

To verify our model, we simulate a system of parallel charged plates, using a lattice of dimensions  $N_x \times N_y \times N_z$ , where  $N_x = N_y = 38$  and  $N_z = 90$ , and lattice site size  $\Lambda$ , with a charge density  $\sigma_s = 0.044e/\Lambda^2$  on each plate, at an inverse temperature  $\beta\epsilon = 13.299$ . To keep the system charge-neutral, we embed  $N_- = 128$  counter-ions of valency  $q = 1$  in a homogeneous background of  $B$  solvent species (i.e.  $N_B = N - N_-$ ), with permittivity

$\varepsilon_B = 2e^2/\Lambda\epsilon$ . The permittivity of the counter-ions is also set to  $\varepsilon_- = 2e^2/\Lambda\epsilon$ , so that  $\varepsilon = \varepsilon_B = \varepsilon_-$ . We can calculate the Bjerrum length,  $\lambda_B = 0.529\Lambda$ , and the Gouy-Chapman length,  $\mu = 6.786\Lambda$ , which results in a weak coupling,  $\Xi = 0.078$  and a reduced plate separation,  $\tilde{d} = N_z\Lambda/\mu = 13.262$ .

In figure 4.3 we present the average density profile of the system, as a function of the distance,  $z$ , from the left charged plate. For comparison, we plot the Poisson-Boltzmann prediction in the weak coupling limit [38, 39],

$$\rho(\tilde{z}) = \frac{2\pi\lambda_B\sigma_s^2\lambda}{\cos^2(\lambda^{1/2}[\tilde{z} - \tilde{d}/2])}, \quad (4.14)$$

where  $\tilde{z} = z/\mu$ . The parameter  $\lambda$ , is determined by the transcendental equation,

$$\lambda^{1/2} \tan(\lambda^{1/2}\tilde{d}/2) = 1. \quad (4.15)$$

Figure 4.3 shows that our simulations agree very well with theory, leading us to the conclusion that the implementation of the simulations is correct. There is a slight deviation, very close to the charged plates which is most probably caused by the lattice resolution.

#### 4.4.2 Pure Solvent Phase Diagram

We now consider a four-component mixture of solvent species  $A$  and  $B$ , and positive and negative ions. We set our simulation parameters close to the experimental parameters of a D<sub>2</sub>O-3MP mixture with NaBPh<sub>4</sub> salt [145]. We start by setting the lattice-gas nearest-neighbor interaction between solvent species  $A$  and  $B$ , to  $J_{AA} = J_{AB} = 0$ , and  $J_{BB} = 1$ , to drive phase separation. From symmetry of the Hamiltonian in eq. (4.2), we know that an adsorption strength  $J_{B\pm} = 1$ , corresponds to neutrally adsorbing ions. To make the salt antagonistic, we set the nearest-neighbor interaction between ions and solvent to,  $J_{B+} = 6$  and  $J_{B-} = -4$ . Hence, the positive ions preferentially adsorb the  $B$  solvent species, whereas the positive ions prefer the  $A$  solvent species. All other nearest-neighbor interactions,  $J_{\mu\nu}$ , are set to 0. Note that the above choice of adsorption strength, leads to a self-energy of  $\pm 15\epsilon$  (which can be calculated from the hamiltonian  $\mathcal{H}_{LG}$  as  $3(J_{B\pm} - 1)\epsilon$ ) in the absence of electrostatics. This is large, but not unreasonable, as seen from the Gibbs transfer energies in tables of Refs. [165, 166], and also used in theoretical models [167]. Although the two ionic species (dis)like solvent species  $B$  equally, the effective Keesom potential generated due to the electrostatics, slightly increases the preference of both ionic species for solvent species  $B$ . Next, we set the dielectric constants of the different species to,  $\varepsilon_A = \varepsilon_+ = \varepsilon_- = 1$ , and  $\varepsilon_B = 3$ . This choice is arbitrary, but as it will become clear, we are still able to tune the simulation parameters to lie close to those of the experimental system. The size of a lattice site is set to  $\Lambda = 10\text{\AA}$ , which is equal to the size of the biggest component of the experimental system, i.e. BPh<sub>4</sub><sup>-</sup>. The Bjerrum length in our model can be written as,

$$\lambda_B = \frac{\Gamma\tilde{\beta}}{4\pi\tilde{\varepsilon}}\Lambda, \quad (4.16)$$

where the bulk dielectric permittivity for e.g. a pure  $AB$  mixture with  $x_B = N_B/(N_A + N_B) = 0.5$ , is  $1/\tilde{\varepsilon} = (1/\varepsilon_A + 1/\varepsilon_B)/2 = 1/1.5$ . We set the Bjerrum length to  $\lambda_B =$

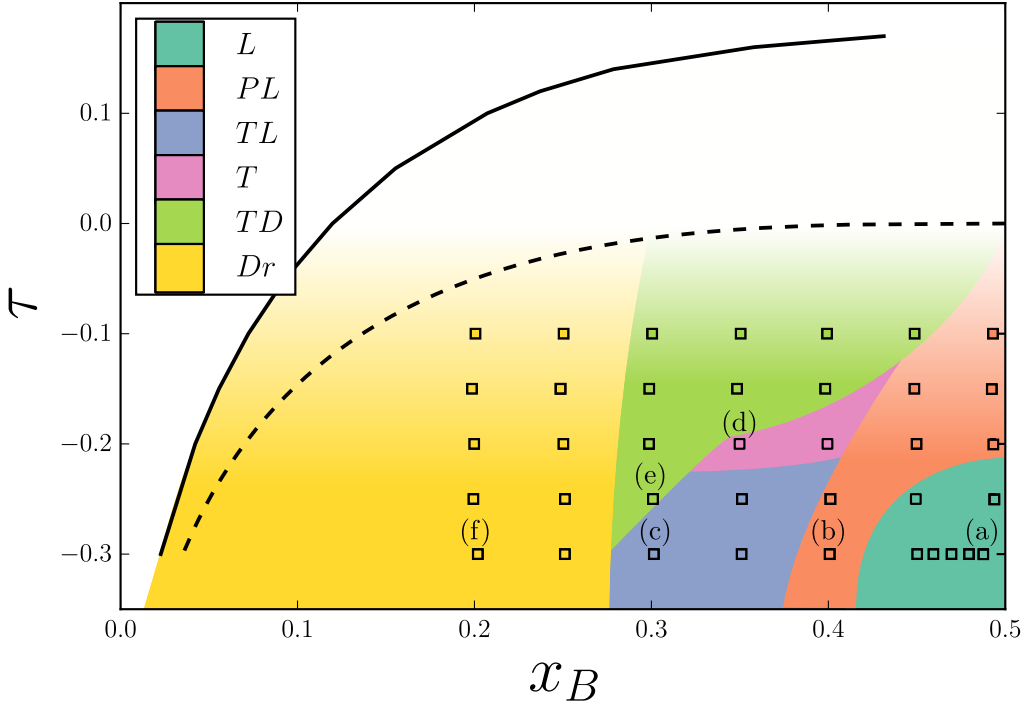


**Figure 4.4:** The phase diagram of the pure  $AB$  solvent mixture, as described by a simple lattice-gas model, in the reduced temperature,  $\tau$ , composition,  $x_B = N_B/N$ , representation as denoted by the dotted line. The solid line represents the phase diagram for the polar solvent mixture with  $\varepsilon_B/\varepsilon_A = 3$ . The colored boxes denote the various phases we observe at the different state points, for a fixed molar concentration of salt,  $C = 51.89$  mmol/L. The phases seen here are the lamellar phase ( $L$ ), the perforated lamellar phase ( $PL$ ), the tubular lamellar phase ( $TL$ ), the tubular phase ( $T$ ), the tubular disordered phase ( $TD$ ), and the droplet phase ( $Dr$ ). Here, we only plot the  $B$ -poor,  $x_B < 0.5$ , part of the phase diagram as it is symmetric around  $x_B = 0.5$ . The colored regions are only guesses of the mesophase boundaries and serve as a guide to the eye. The color gradient represents the uncertainty in the maximum temperature at which these mesophases are observed.

$5.64\text{\AA} = 0.564\Lambda$ . Using equation (4.16) and assuming  $\tilde{\beta} = \beta\epsilon = 0.886618$ , i.e. the critical temperature of the lattice-gas, we find  $\Gamma = 12$ . For reference, the Debye length can be written as,  $\kappa^{-1} = \Lambda^{-1}\sqrt{\tilde{\varepsilon}N/2\tilde{\beta}\Gamma N_{\pm}}$ , where  $N_{\pm} = N_-/2 = N_+/2$ . With this, we have set all system parameters close to the experimental values of a  $\text{D}_2\text{O}$ -3MP solvent mixture with  $\text{BPh}_4$  salt.

Before simulating the full binary solvent-ion mixture it is useful to calculate the phase diagram of the pure  $AB$  solvent mixture for the parameters we set above. To do so, we simulate the solvent in the Grand-Canonical ensemble and monitor the probability  $P(N_B)$  of observing a certain number of  $B$  solvent sites,  $N_B$ , using the transition-matrix Monte Carlo (TMMC) method [168]. In figure 4.8(b), we plot the probability distribution  $\ln P(x_B)$ , as a function of the solvent composition,  $x_B$  at coexistence, for the pure polar solvent with  $\varepsilon_B/\varepsilon_A = 3$ , at a reduced temperature  $\tau = 0.12$ . Using histogram reweighing,

we can determine the coexisting particle numbers,  $N_B$  of the  $A$ -rich and  $B$ -rich phases at a certain temperature, for our system size. See section 2.3.3 for a more in-depth description. We repeat this process for a range of different temperatures, and finally plot the phase diagram of the solvent mixture in figure 4.4. Here, we plot the fraction of  $B$  solvent sites,  $x_B$  at different reduced temperatures  $\tau = (T - T_C^{LG})/T_C^{LG}$ , where  $T_C^{LG} = T_C^I/4 \approx 1.127881964$  [133] is the critical temperature of the simple lattice-gas system, i.e.  $\Gamma = 0$ , with  $T_C^I$  the critical temperature of the Ising model. The phase diagram of the simple lattice-gas model is also plotted using a dotted line for reference. The phase diagrams are fairly symmetric around  $x_B = 0.5$ , so we only plot the  $A$ -rich side,  $x_B < 0.5$ . A lattice with dimensions of  $32 \times 32 \times 32$  was used in all simulations for calculating the phase diagram in figure 4.4. Larger system sizes did not seem to affect the phase diagram significantly. The phase diagram of this polar solvent mixture is broader than that of the simple lattice-gas model. This is expected, since the introduction of electrostatics to the system generates an effective (attractive) Keesom potential between solvent sites [163].

#### 4.4.3 Mesophase Behavior of an Antagonistic Salt Solution

We next focus on the full quaternary mixture by introducing a certain amount of antagonistic salt to the  $AB$  solvent mixture investigated in the previous section. We now simulate the solvent in the canonical ensemble, in line with standard experimental setups. We simulate the system using a cubic lattice consisting of  $N = 64^3$  lattice sites. We first study the behavior of the mixture as a function of reduced temperature,  $\tau$ , and solvent composition,  $x_B$ , for a small number of ions  $N_{\pm} = 8192$ , which corresponds to a molar concentration  $C = N_{\pm}/N_{Av}N\Lambda^3 = 51.89$  mmol/L, where  $N_{Av}$  is Avogadro's number. This value is close to the lower limit at which Sadakane *et al.* observed an ordered-lamellar phase,  $60$  mmol/L  $\leq C \leq 250$  mmol/L [146]. Within the pure solvent binodal, see figure 4.4, we find mesophases with remarkably diverse structures, depending on both the temperature and solvent composition. Isosurfaces at composition  $x_B = 0.5$  are plotted for various conditions in figure 4.5. We categorize the various sub-figures according to their structural characteristics. In figure 4.5(a), we show an ordered lamellar phase (L). Here, the solvent is arranged in lamellae of alternating composition. In figure 4.5(b), we show a perforated lamellar phase (PL). As the name suggests, the lamellae here are perforated. In figure 4.5(c), we find a tubular-lamellar (TL) phase which exhibits lamellar ordering, but each lamella has a tube-like structure. One could argue that this is actually the PL phase. We further find a tubular phase (T) in figure 4.5(d), where the minority solvent species is organized in parallel tubes, a tubular disordered (TD) phase in figure 4.5(e), where the tubes are not parallel, and a droplet or peanut phase (Dr) in figure 4.5(f), where the minority solvent species is organized in disordered droplets. We have plotted the state points within the phase diagram of figure 4.4 indicating the type of mesophase found for that solvent composition,  $x_B$ , and reduced temperature,  $\tau$ . The droplet phase seems to form for a solvent composition  $x_B \leq 0.25$ . For temperatures,  $\tau \leq -0.25$ , we find L, PL, and TL phases, from which, only the PL phase survives at higher temperatures. The system transitions from the lamellar phase to the tubular-lamellar phase by reducing the fraction of  $B$  solvent. For higher temperatures,  $\tau \geq 0.0$ , the system becomes disordered.

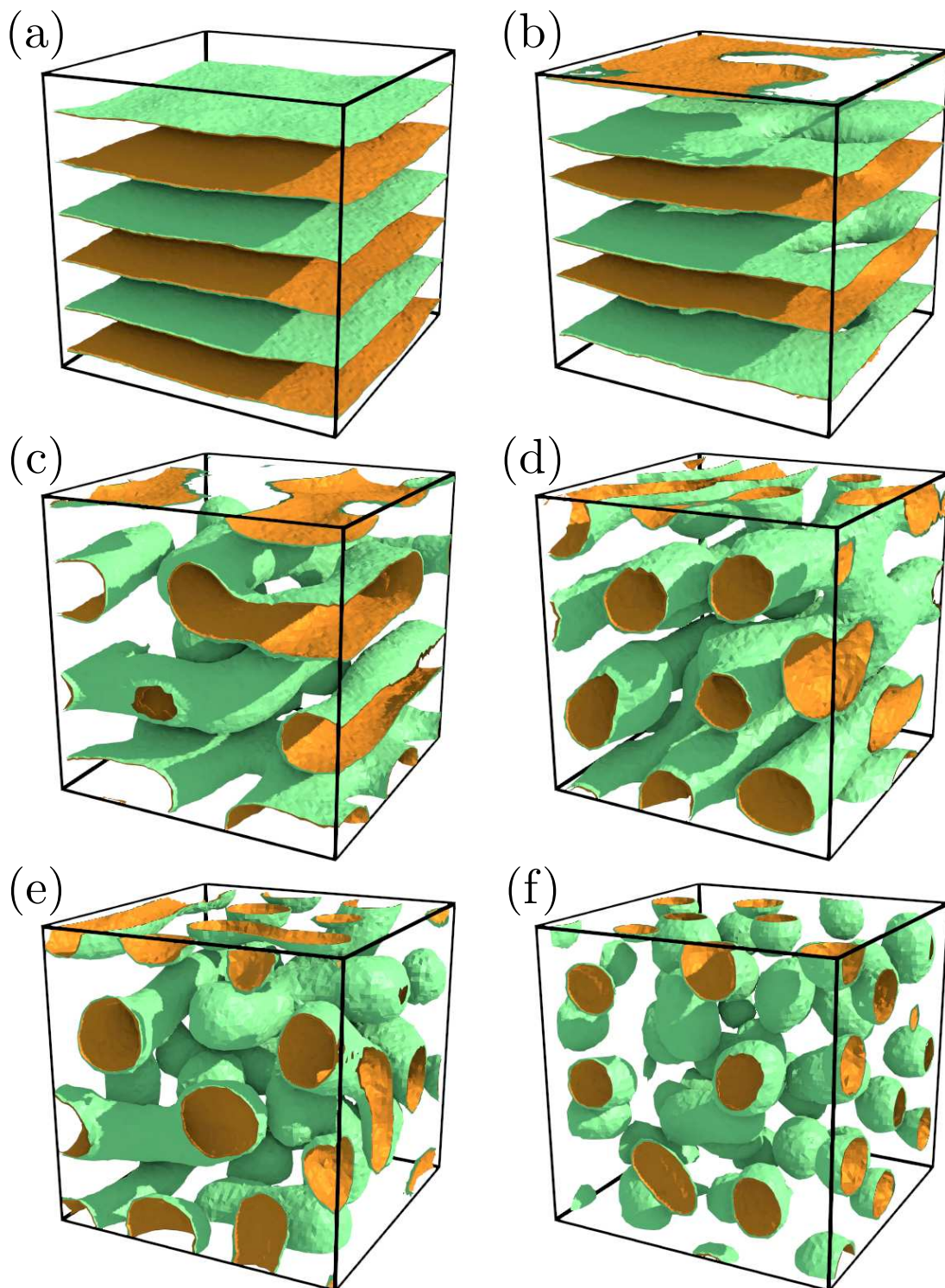


**Figure 4.5:** Representative isosurfaces at the interface between the *A* and *B* solvent micro-phases, for the different observed mesophases. Here, the orange color represents the side of the isosurface of the minority phase. We show six representative configurations, (a) the lamellar (L) phase, (b) the perforate lamellar (PL) phase, (c) the tubular lamellar (TL) phase, (d) the tubular (T) phase, (e) the tubular disordered (TD) phase, and (f) the droplet (Dr) phase.

We should mention here, that these mesophases are also observed for smaller adsorption strengths,  $J_{\pm B}$ , and in some cases, also for an apolar solvent,  $\varepsilon_B = \varepsilon_A = 1$ , but the effects are enhanced for higher values, such as the ones chosen in this study.

Surprisingly, the various mesophases we find in our model system remind us of a completely different system, namely a diblock copolymer system. A diblock copolymer is a polymer consisting of two types of monomers,  $A$  and  $B$ . The two monomers are arranged in two chains that are attached on one end to form the diblock copolymer. Theoretical work [169–171], has shown that these polymers can form various phases, such as a droplet phase where the droplets are arranged in either an face-centered cubic (FCC) or body-centered cubic (BCC) lattice, a tubular phase where the tubes are packed in a hexagonal phase, a gyroid phase which has a sponge-like structure, and a lamellar phase. In experiments [169] and simulations [172], additional phases have been found, including a perforated lamellar, a double-diamond phase, and a droplet phase where the droplets are peanut shaped. We can argue that the present quaternary mixture, because of the strong adsorption and electrostatic interactions, can be seen as a system consisting of bound ion pairs at a distance set by the Bjerrum length and a thick film of the corresponding preferred species adsorbed around each ion. The similarities with the diblock copolymer system become then clear. This, of course, is only a simplified view, which helps us understand why e.g. the interfaces between the two solvent phases become more curved as the fraction of one solvent phase is decreased in favor of the other; the effective adsorbed films around the ions become uneven. The behavior we see here is not unique to either antagonistic salt solutions nor diblock copolymers, but other systems such as surfactants also exhibit similar phase behavior [173, 174].

#### 4.4.4 Structure of Lamellae and Mean-Field Model

We further investigate the lamellar phase by examining the structure of the lamellae. In figure 4.6, we plot the average fraction of sites occupied by  $B$  solvent species, and positive and negative ions, as a function of the position,  $r/\Lambda$ , in the lamella-normal direction, for a system simulated at a reduced temperature  $\tau = -0.2$ , solvent composition  $x_B \approx 0.5$ , and  $N_{\pm} = 8192$  ions. We observe 3  $AB$  lamellae for this system. The fraction of  $B$  solvent sites approaches the pure solvent coexistence compositions in the middle of the  $A$  and  $B$  lamella regions. The ions seem to completely partition between the two  $A$  and  $B$  regions, with the negative ions concentrating in the  $B$ -rich regions, and the positive ions concentrating in the  $A$ -rich regions, as expected from their solvent preferences. We also observe that the ions show higher concentrations at the  $AB$  interfaces, forming electric double layers. There is also a slight asymmetry between the two ion profiles; this is due to the effective Keesom interaction which yields a small preference to  $B$  solvent sites, for both ionic species.

From our observations of figure 4.6, we can build a simple mean-field model. As a first approximation, we assume that both ionic species and the solvent species, partition completely between the two lamella regions, and that their densities are position independent within the regions. We denote the salt concentration,  $c = N_{\pm}/N$ , the dimensionless surface area of an  $AB$  lamella as  $\tilde{A} = A/\Lambda^2$ , and the dimensionless thickness as  $\tilde{\delta} = \delta/\Lambda$ , with the thickness of the  $A$ -rich lamellae being  $x_A \tilde{\delta}$ , and that of  $B$ -rich lamellae,  $x_B \tilde{\delta}$ .

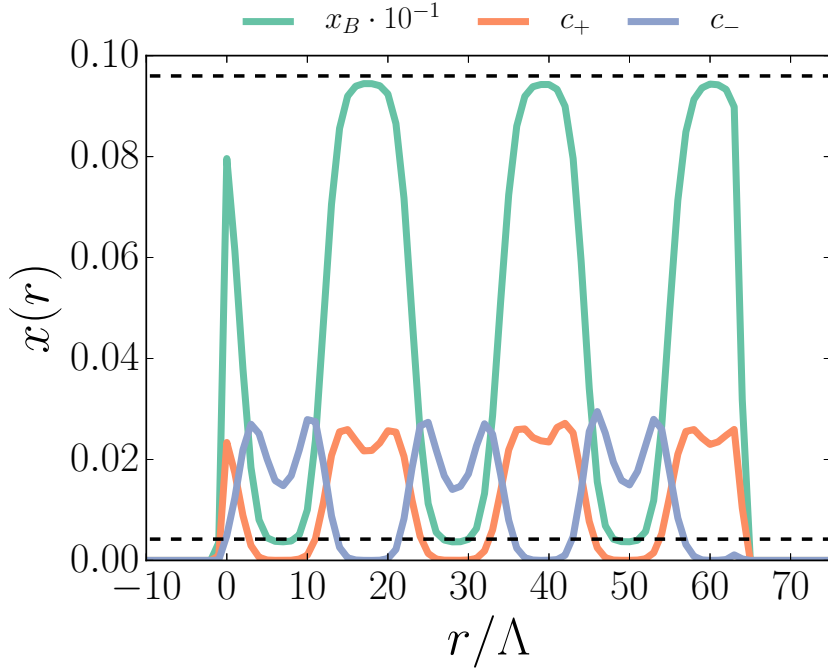


**Figure 4.6:** Average fraction of sites occupied by  $B$  solvent species,  $x_B \cdot 10^{-1}$ , and positive,  $c_+$ , and negative,  $c_-$ , ions, as a function of the distance,  $r/\Lambda$ , in the lamellae-normal direction. The profiles presented here are calculated from simulations at a reduced temperature  $\tau = -0.2$ , solvent composition  $x_B \approx 0.5$ , and inverse salt concentration  $c^{-1} = 32$ . The dashed lines denote the coexistence compositions of the pure solvent.

The number of  $AB$  lamellae,  $k$  in a box of reduced length  $\tilde{L} = L/\Lambda$  is given by  $k = \tilde{L}/\tilde{\delta}$ . Note that  $N = \tilde{L}\tilde{A}$ . Given these assumptions, we can write an expression for the free energy of the ions in this system,

$$\begin{aligned} F_{\text{ion}}/\epsilon\Lambda^3 N &= \frac{x_A c_+^A}{\tilde{\beta}} \ln c_+^A + \frac{x_B c_-^B}{\tilde{\beta}} \ln c_-^B - \frac{cx_B}{2} (J_{B+} - 1) + \frac{2k\tilde{\gamma}\tilde{A}}{N} \\ &+ \frac{\Gamma\tilde{A}k}{2N} \left[ \int_{-\tilde{\delta}x_A/2}^{\tilde{\delta}x_A/2} dr \frac{\tilde{D}_A^2(r)}{\tilde{\varepsilon}_A} + \int_{-\tilde{\delta}x_B/2}^{\tilde{\delta}x_B/2} dr \frac{\tilde{D}_B^2(r)}{\tilde{\varepsilon}_B} \right] \end{aligned} \quad (4.17)$$

The first two terms correspond to the entropy of the two ion species, where the concentration of positive ions in the  $A$ -rich phase is simply  $c_+^A = N_+/N_A = (N_\pm/2)/(x_AN) = c/2x_A$ , and that of the negative ions in the  $B$ -rich phase is  $c_-^B = c/2x_B$ . The third term is the adsorption energy of the ions. An energy penalty is paid for the formation of the  $2k$  interfaces, which is seen in the fourth term, where  $\tilde{\gamma} = \gamma\Lambda^2/\epsilon$  is the dimensionless surface tension. The electric displacement field of an  $A/B$  lamella, due to symmetry, can be calculated to be,  $\tilde{D}_{A/B}(r) = cr/2x_{A/B}$ . With this, we arrive at the final expression for the free energy of the ions in the lamellar phase,

$$\begin{aligned} F_{\text{ion}}/\epsilon\Lambda^3 N &= \frac{c}{\tilde{\beta}} \ln c - \frac{c}{2\tilde{\beta}} \ln [4x_B(x_B - 1)] - \frac{cx_B}{2} (J_{B+} - 1) \\ &+ \frac{2\tilde{\gamma}}{\tilde{\delta}} + \frac{\Gamma c^2 \tilde{\delta}^2}{192} \left[ \frac{1 - x_B}{\tilde{\varepsilon}_A} + \frac{x_B}{\tilde{\varepsilon}_B} \right]. \end{aligned} \quad (4.18)$$

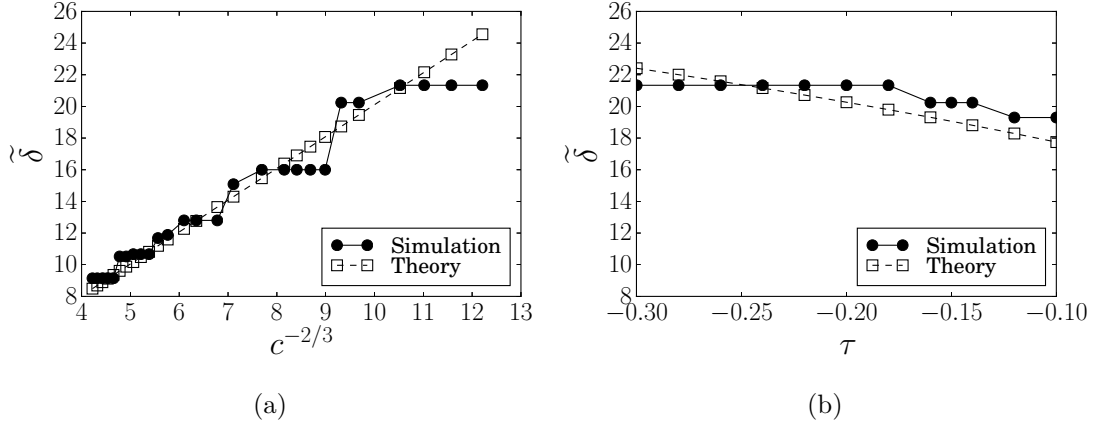


**Figure 4.7:** (a) Lamella thickness,  $\tilde{\delta}$ , as a function of  $c^{-2/3}$ , for a system at reduced temperature,  $\tau = -0.2$ , and solvent composition  $x_B \approx 0.5$ . The thickness is calculated from the radially averaged structure factor,  $S(k)$ . (b) Lamella thickness,  $\tilde{\delta}$ , as a function of the reduced temperature,  $\tau$ , for a system with  $N_{\pm} = 8192$  ions, and solvent composition  $x_B \approx 0.5$ . The thickness is calculated from the radially averaged structure factor,  $S(k)$ .

Finally, we minimize the free energy expression (eq. 4.18) with respect to the lamella thickness,  $\tilde{\delta}$ , to get,

$$\begin{aligned} \frac{1}{\epsilon \Lambda^3 N} \frac{\partial F_{\text{ion}}}{\partial \tilde{\delta}} &= -\frac{2\tilde{\gamma}}{\tilde{\delta}^2} + \frac{\Gamma c^2 \tilde{\delta}}{96} \left[ \frac{1-x_B}{\tilde{\varepsilon}_A} + \frac{x_B}{\tilde{\varepsilon}_B} \right] = 0 \Leftrightarrow \\ &\Leftrightarrow \tilde{\delta} = \left( \frac{192\tilde{\gamma}\tilde{\varepsilon}_B}{\Gamma c^2 [x_B + (1-x_B)\frac{\tilde{\varepsilon}_B}{\tilde{\varepsilon}_A}]} \right)^{1/3}. \end{aligned} \quad (4.19)$$

The lamella thickness  $\tilde{\delta}$  appears to scale with the power  $-2/3$  as a function of the salt concentration. Coincidentally, the lamella thickness in block copolymers is found to scale with the same power law as a function of the copolymer molecular weight [169, 171].

We compare the prediction of our model in eq. (4.19) by studying the thickness of the lamellae as a function of salt concentration,  $c$ . We run simulations for molar concentrations in the range,  $29.189 \text{ mmol/L} \leq C \leq 347.027 \text{ mmol/L}$ , at reduced temperature  $\tau = -0.2$ , and solvent composition  $x_B \approx 0.5$ . In figure 4.7(a), we plot the dimensionless lamella thickness,  $\tilde{\delta}$ , as a function of  $c^{-2/3}$ . The lamella thickness,  $\tilde{\delta}$ , is calculated as  $\tilde{\delta} = 2\pi/\tilde{k}_{\max}$ , where  $\tilde{k}_{\max} = k_{\max}\Lambda$  is the position of the second largest peak of the radially averaged structure factor,  $S_{BB}(k)$ . In figure 4.8(a), we show a typical example of  $S_{BB}(k)$  for the lamellar phase of a quaternary mixture at  $x_B = 0.49$ ,  $\tau = -0.3$ , and  $C = 51.89 \text{ mmol/L}$ . In figure 4.7(a), we also plot the mean-field prediction (eq. (4.19)) by substituting the quantities from our simulations. The surface tension was calculated using the results for the probability density  $P(x_B)$  from the TMMC simulations of the pure solvent mixture as [168],

$$\tilde{\gamma} = \frac{1}{2\tilde{L}^2 \tilde{\beta}} \left[ \frac{1}{2} \left( \max_{x_B < x_B^{\min}} \ln P(x_B) + \max_{x_B > x_B^{\min}} \ln P(x_B) \right) - \ln P(x_B^{\min}) \right], \quad (4.20)$$

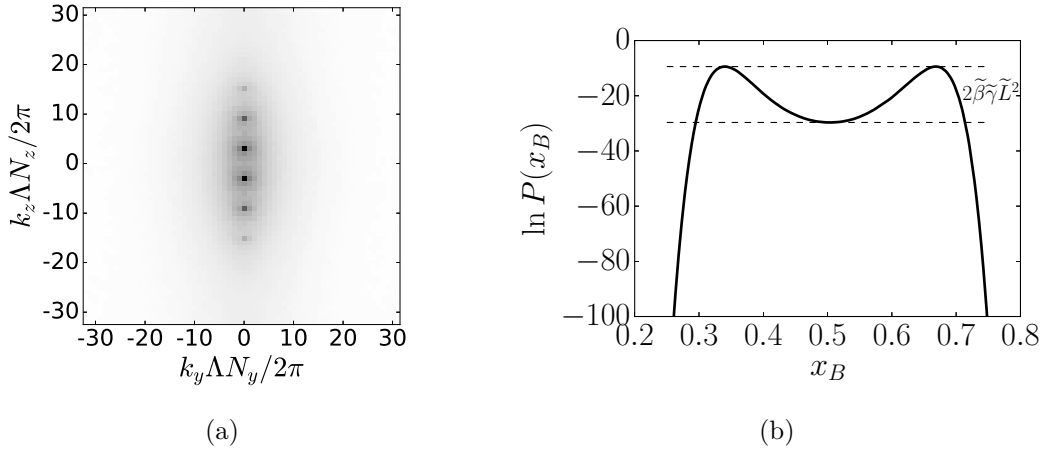


**Figure 4.8:** (a) Structure factor,  $\log S_{BB}(\mathbf{k})$ , averaged in the direction of  $k_x$ , for lamellar phase of a quaternary mixture at  $x_B = 0.49$ ,  $\tau = -0.3$ , and  $C = 51.89$  mmol/L. (b) Probability distribution function  $P(x_B)$  of the pure polar solvent mixture with  $\varepsilon_B/\varepsilon_A = 3$ , calculated using TMMC, as a function of the solvent composition,  $x_B$ , for a system at a reduced temperature  $\tau = 0.12$ .

where  $x_B^{\min}$  is the position at which the probability distribution  $P(x_B)$  is minimized. The first term amounts to an average over the two maxima of  $\ln P(x_B)$ . We show  $\ln P(x_B)$  as a function of  $x_B$  at coexistence, for the pure polar solvent mixture, at  $\tau = 0.12$ , in figure 4.8(b). In figure 4.7(a), we notice that the lamella thickness,  $\tilde{\delta}$ , changes in increasingly larger steps. This happens due to the finite size of the box and because only an integer number of lamellae is allowed. Barring these ‘finite size’ effects, we find that our mean-field model is able to give a very good quantitative estimate of the lamella thickness,  $\delta$ .

In figure 4.7(b) we plot the temperature dependence of the lamella thickness,  $\delta$ , for a system with inverse salt concentration  $c^{-1} = 32$ , and solvent composition  $x_B \approx 0.5$ , along with the corresponding mean-field prediction. The mean-field model seems to give satisfactory results even in this case, although our model fails to include the temperature dependence of the solvent composition of the lamellae. On the other hand, the temperature is low enough such that fluctuation effects are not that important.

## 4.5 Conclusion

In a series of recent experiments, with a mixture of an antagonistic salt ( $BPh_4$ ) and a binary solvent mixture ( $D_2O$  - 3MP), Sadakane *et al.* made some intriguing observations [144–146]: a) the binary solvent mixture exhibits a two-phase region with an upper and lower critical point, which shrinks with increasing salt concentration, and b) the mixture exhibits a structural transition into an ordered lamellar phase for certain salt concentrations and temperatures, which is confirmed from small-angle neutron scattering experiments. Although some theoretical work in explaining these observations was presented by Onuki *et al.* recently [147–150], simulations can often provide more insight.

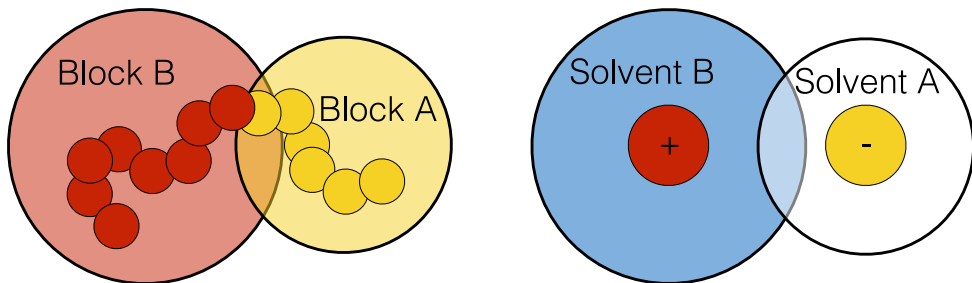


**Figure 4.9:** Schematic helping to draw analogies between a ‘bound’ ion pair in a system of *A* and *B* solvent species, and positive and negative ions (**right**), and a diblock copolymer with a certain number of block *B* monomers and block *A* monomers (**left**). Due to preferential adsorption, a diffuse layer of *B* solvent species and *A* solvent species, drawn as a blue and a white disk, surrounds the positive and negative ions, respectively. Similarly, a diffuse layer of block *B* and block *A* monomers, surrounds the respective diblock copolymer chain. These diffuse layers are drawn as colored discs of the same size as the case of the bound ion pair to facilitate the analogy.

Unfortunately, current simulation techniques are notoriously slow, due to the long range character of the Coulomb interactions. In addition, effects based on the fluctuation of dipoles, or the dielectric inhomogeneity in a medium, which could be important in the formation of the ordered lamellar phase, are collective effects that make the equilibration of the model system of interest very difficult. Using Maggs’s method [158] to simulate the electrostatics in a lattice-gas type model, we were able to circumvent these difficulties, allowing us to investigate the presence and behavior of mesophases in a model system resembling the experimental system of Sadakane *et al.* [144–146].

We first determined the phase diagram for the pure polar solvent mixture using the TMMC technique. For a fixed molar salt concentration,  $C = 51.89 \text{ mmol/L}$ , we performed a series of simulations within the two-phase coexistence region of the pure solvent mixture, finding, not only the experimentally observed lamellar phase, but also a multitude of other mesophases, such as a tubular and a droplet phase, which remind us of the phase behavior of block copolymers [169–172], or even surfactants [173, 174]. Considering the strong adsorption and electrostatic interactions, the system can be seen bound ion pairs at a distance set by the Bjerrum length with thick films of the corresponding preferred species adsorbed around each ion (see figure 4.9 for a schematic of this analogy). This view helps us relate our current system, to the diblock copolymer system.

The parallel drawn between the two systems is further supported when studying the structure and behavior of the lamellar phase. From density profiles of the lamellar phase at low temperatures, the ions and solvent seem to partition completely between the *A*-rich and *B*-rich lamella regions. This observation allowed us to build a simple mean-field model, from which we calculated an expression for the optimal lamella thickness,  $\delta$ . The expression predicts that the reduced lamella thickness,  $\tilde{\delta}$ , should scale with the power  $-2/3$  of the salt concentration. Coincidentally, the lamella thickness in block copolymers is found to scale with the copolymer molecular weight [169, 171] with the same power. From simulations of the lamellar phase for different salt concentrations and temperatures, we found that our mean-field model appears to predict the thickness of the lamellae very

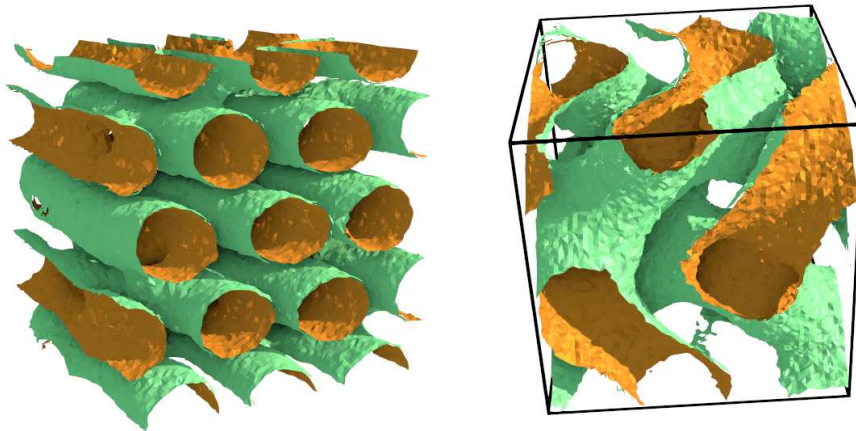


**Figure 4.10:** Representative isosurfaces at the interface between the  $A$  and  $B$  solvent micro-phases, of two observed mesophases at  $\varepsilon_B/\varepsilon_A = 9$ . Here, the orange color represents the side of the isosurface of the minority phase. We show a hexagonally ordered tubular phase in (a), and a gyroid phase in (b).

accurately, without the need of any fitting.

Given the large parameter space of our model system, we explored only a small fraction here. Preliminary results using e.g. a higher dielectric contrast  $\varepsilon_B/\varepsilon_A = 9$ , seem to confirm the existence of additional phases seen in diblock copolymer systems, such as the gyroid phase, and hexagonally ordered droplet and tubular phases. Representative isosurfaces of a gyroid phase and a hexagonally ordered tubular phase are shown in figure 4.10. Additionally, simulations closer to the critical point of the pure solvent mixture seem to exhibit a lamellar phase only at very low salt concentrations. This could be an indication that the lamellar phase in this region is the one predicted by Nabutovskii *et al.* [44], which is induced by the critical composition fluctuations in the system. Furthermore, keeping the salt concentration low, and lowering the temperature, leads to phase separation between an  $A$ -rich and a  $B$ -rich phase with inhomogeneities, which cause the effective shrinking of the two-phase region, as seen in experiments.

Finally, although we used our model to simulate antagonistic salt solutions, it is evident that it can be used to successfully simulate a multitude of systems and setups of interest.

## Acknowledgements

We thank S. Samin and R. van Roij, for discussions and help on developing our mean-field model.



# 5

---

## A Simulation Study on the Phase Behavior of Hard Rhombic Platelets

---

Using Monte Carlo simulations, we investigate the phase behavior of hard rhombic platelets as a function of the thickness of the platelets,  $T$ . The phase diagram displays a columnar phase and a crystal phase in which the platelets are stacked in columns that are arranged on a two-dimensional lattice. We find that the shape of the platelets determines the symmetry of the two-dimensional lattice, i.e., rhombic platelets form an oblique columnar phase and a simple monoclinic crystal phase. For sufficiently thick platelets, i.e., for a thickness-to-length ratio  $T/L > 0.17$ , we find only an isotropic fluid, an oblique columnar phase, and a monoclinic crystal phase. Surprisingly, for an intermediate plate thickness,  $0.083 < T/L < 0.17$ , we also find a region in between the isotropic (or nematic) phase and the columnar phase, where the smectic phase is stable. For sufficiently thin platelets,  $T/L < 0.13$ , the phase diagram displays a nematic phase. With the exception of the smectic phase, our results resemble the phase behavior of discotic particles. Our results may guide the synthesis and future experiments on rhombic nanoplates.

## 5.1 Introduction

With the advancement of technology and the prevalence of various display devices, liquid crystal displays (LCD) have played an increasingly important role in our everyday lives. LCDs use the light modulating properties of liquid crystals to display complex images, as such, the study of liquid crystals has never been more important and relevant than at the present age. Whereas normal periodic crystals exhibit long-range positional and orientational order in all spatial dimensions, liquid crystals exhibit long-range orientational and positional order in only two or less spatial dimensions.

Hard-particle models, i.e. models in which the particles interact only by their excluded volume, are particularly important in the study of liquid crystals because they can be used to test molecular theories for the properties of liquid crystals, and they provide a starting point for thermodynamic perturbation theories. The study of such models goes all the way back to 1949, when Onsager [49] predicted theoretically that a system of infinitely thin rods or a system of infinitely thin platelets exhibits a first-order phase transition from an isotropic phase to a nematic phase, which is driven purely by excluded-volume interactions. The first time a hard-particle model was used to simulate a liquid crystal was in 1972 by Vieillard-Baron [175] who investigated the phase behavior of a two-dimensional system of hard ellipses. Due to the computational restrictions of those times, it was not until 1985 that the phase behavior of the full three-dimensional system of ellipsoids was mapped out by Frenkel *et al.* [176], revealing isotropic, nematic, crystal, and plastic crystal phases. In 1997, the phase diagram of hard spherocylinders was determined by means of free-energy calculations using Monte Carlo simulations, and was found to exhibit an isotropic, nematic, (plastic) crystal, but also a smectic phase [177].

Frenkel *et al.* [178, 179] studied the limit of infinitely thin cylinders, or disks, in 1982, finding a first-order isotropic-nematic phase transition, and compared it with Onsager theory [49]. Later, in 1992, Veerman and Frenkel [180] studied a model for hard platelets, using a sphere truncated by two symmetrically opposite parallel planes, and observed a first-order phase transition from a nematic to a columnar phase which was later also confirmed for infinitely thin disks [181]. In addition, they found a so-called cubatic phase which turns out to be metastable with respect to the columnar phase in later studies [182–184]. The phase diagram of hard oblate spherocylinders, i.e. a model system of discotic-like particles, was determined as a function of the plate thickness by Marechal *et al.*, and exhibits isotropic, nematic, columnar, and two crystal phases. Marechal *et al.* also studied models of hard platelets with different degrees of roundness [183] focusing on the ‘devitrification’ process from a metastable cubatic to a columnar phase. More recently, a large class of polyhedral-shaped particles has been investigated, that exhibit plastic crystal and liquid crystal phases, but also intriguing crystal phases [7, 185–189]. Although plastic-crystal forming hard particles have been studied since 1985 [176, 190–192], the more ‘exotic’ states, such as quasi-crystals [185, 193], biaxial nematics [194–197], and even chiral phases [198], have only been studied very recently, which indicates [199] that the study of hard-particle systems is far from over.

There is an additional reason why hard-particle models have become important as of late, and that is because a wide variety of these systems are now experimentally available. Hard-sphere colloidal particles have been synthesized for over five decades now [200, 201],

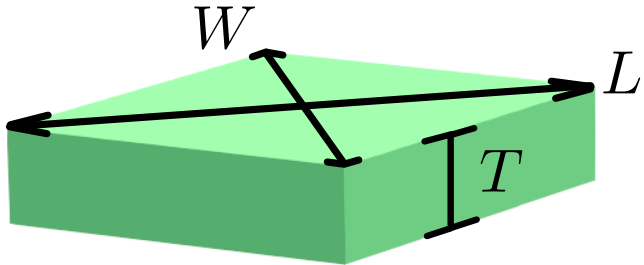


**Figure 5.1:** A rhombic platelet. The three lines, denote the characteristic dimensions of the platelet, with  $T$  being the thickness,  $W$  being the width or short axis length, and  $L$  the long axis length. In our simulations, we fix  $W/L = 2/3$ .

and various polyhedral-shaped particles have been synthesized recently [7–26].

In this work we focus on the phase behavior of particles of a specific polyhedral shape known as rhombohedron. The work is motivated by the recent synthesis of nano-platelets of this shape by Murray *et al.* [23, 26], and is focused on thin, or plate-like, shapes. For convenience, we refer to these particles as ‘rhombic platelets’. Current research on the self-assembly of these particles [26] has focused on two-dimensional planar geometries. Instead, we explore the self-assembly of the three-dimensional bulk system, which could prove useful for future experimental studies. We generally expect the phase behavior of platelets of different shapes to be qualitatively similar, i.e. we should at least find nematic, columnar, and crystal phases at the appropriate aspect ratios.

This chapter is organized as follows. In section 5.2 we discuss the hard-particle model, and in section 5.3 the computational methods used to simulate and characterize the different phases of the rhombic platelets. In section 5.4 we present our results, which are focused on the phase behavior of these flat particles. Finally, in section 5.5 we summarize the results, and discuss possible future ventures.

## 5.2 Model

We study the phase behavior and structure of a system consisting of hard rhombic platelets using Monte Carlo simulations. To this end, we model each particle as a rhombohedron which is basically a rhombus extruded in the third dimension. In figure 5.1 we show a typical rhombic platelet along with three lines, denoting the characteristic dimensions of the platelet, with  $T$  being the thickness,  $W$  being the short axis length, and  $L$  the long axis length. Two-dimensional rhombi can tile space, admitting either a tiling where all platelets are parallel, or a so-called rhombille tiling [202], with the former being the favorable one as shown in simulations [26]. Rhombic platelets can also tile the three-dimensional space by stacking different 2D tilings on top of each other.

Here, we simulate hard rhombic platelets, that interact solely through excluded volume interactions which means that platelets cannot overlap at any point in the simulation. In our simulations, we fix  $W/L = 2/3$ , which is close to the experimental value of recently synthesized  $\text{GdF}_3$  nanoplatelets [23], and investigate the phase behavior as a function of the reduced thickness,  $T/L$ .

## 5.3 Methods

### 5.3.1 NPT Cluster algorithm

Simulating hard particles using Monte Carlo simulations, is generally thought to be less efficient than using equivalent event-driven molecular dynamics (EDMD) simulations. On the other hand, implementing a fast and robust EDMD engine is very time consuming. One of the bigger problems with Monte Carlo simulations of hard particles in the *NPT* ensemble, is that volume moves become prohibitive as the number of particles is increased. This is because there is a higher probability to find an overlap between particles when compressing. A recent paper [203] introduces a new cluster algorithm which promises great speed-ups. The algorithm works by finding clusters of particles that are close to each other and treating them as one body when scaling the coordinates.

In more detail, we form clusters of particles that are close to each other. The probability to add a particle to a cluster,  $b(s_{ij})$ , depends on the minimum surface-to-surface distance  $s_{ij}$  between particles  $i$  and  $j$ . For calculating the shortest surface-to-surface distance,  $s$ , as well as overlaps between pairs of particles, we use the Gilbert Johnson Keerthi (GJK) algorithm [204], which can be employed for arbitrary convex particle shapes. The probability function  $b(s_{ij})$  can have any form, but we choose to use the one suggested in [203],

$$b(s_{ij}) = \begin{cases} 1 - \left(\frac{s_{ij}}{s_c}\right)^2, & 0 \leq s_{ij} < s_c \\ 0, & s_{ij} \geq s_c \end{cases} \quad (5.1)$$

where  $s_c$  is some appropriate cutoff, which affects the size of the clusters. To obey detailed balance, the algorithm replaces the standard *NPT* acceptance probability with,

$$\alpha(V \rightarrow V') = \frac{(V')^{N_c} \exp[-\beta PV' - \beta U(X_c, V')]}{V^{N_c} \exp[-\beta PV - \beta U(X_c, V)]} \frac{\omega(X_c|X')}{\omega(X_c|X)} \quad (5.2)$$

where  $X$  and  $X'$  denote the configurations before and after the volume move,  $X_c$  denotes a particular cluster realization, and  $\omega(X_c|X)$  is the probability of generating a cluster realization  $X_c$ , given the configuration  $X$ . The ratio of probabilities that appears in the right-hand side of equation (5.2) can be calculated as,

$$\frac{\omega(X_c|X')}{\omega(X_c|X)} = \prod_{[ij]} \frac{1 - b(s'_{ij})}{1 - b(s_{ij})} \quad (5.3)$$

where  $[ij]$  denotes pairs of particles belonging to the same cluster.

In pseudo-code, the algorithm for generating the clusters is shown in alg. 5.1. Because the surface-to-surface minimum distance calculation is an expensive procedure, we make some optimizations. Before calculating the distance, we first check if the center-to-center distance of the two particles is smaller than  $r_i^{out} + r_j^{out} + s_c$  (where  $r_i^{out}$  is the out-scribed sphere radius of particle  $i$ ), if it is, then we do an overlap check between the particles using their shapes dilated by a sphere of radius  $s_c/2$  (using GJK, this is a very simple overlap check). Only if the previous two tests succeed, we proceed, else, we skip the particle pair. It should also be noted that if a Cell List structure is used, it is generally faster to always rebuild it before calculating the acceptance weight, eq. (5.3).

**Algorithm 5.1** Cluster formation algorithm

---

```

 $n_c \leftarrow 0$ 
for all  $n \in N$  do
  if  $n$  not already in a cluster then
     $n_c \leftarrow n_c + 1$ 
     $n$  now belongs to cluster  $n_c$ 
     $push(stack, n)$ 
    while stack not empty do
       $i \leftarrow pop(stack)$ 
      for all  $j \in neighbour(i)$  do
        if  $j$  not already in a cluster then
          if  $rand[0, 1] < b(s_{ij})$  then
             $j$  now belongs to cluster  $n_c$ 
             $push(stack, j)$ 
          end if
        end if
      end for
    end while
  end if
end for

```

---

### 5.3.2 Order Parameters

To determine the isotropic-nematic (*I-N*), isotropic-columnar (*I-C*), isotropic-smectic (*I-Sm*), nematic-smectic (*N-Sm*), and smectic-columnar (*Sm-C*) coexistence packing fractions,  $\eta$ , we study the discontinuities in the equations of state. The equations of state are determined by expanding from the space-filling rhombic crystal phase. Furthermore, we calculate the nematic and smectic order parameters. The nematic order parameter,  $S$ , and nematic director,  $\hat{\mathbf{n}}_{\hat{u}}$ , along the particle symmetry axis,  $\hat{\mathbf{u}}$ , are identified as the largest eigenvalue, and corresponding eigenvector, of the nematic order parameter tensor [205],

$$Q_{\alpha\beta}^{\hat{u}} = \frac{1}{N} \sum_{i=1}^N \left[ \frac{3}{2} u_{i\alpha} \cdot u_{i\beta} - \frac{1}{2} \delta_{\alpha\beta} \right], \quad (5.4)$$

where  $u_{i\alpha}$  is the  $\alpha$ -th component of the symmetry axis,  $\hat{\mathbf{u}}$ , of particle  $i$ ,  $N$  is the number of particles, and  $\delta_{\alpha\beta}$  is the Kronecker delta. The smectic order parameter,  $\tau$ , is calculated along the nematic director,  $\mathbf{n}$ , and is given by [206–209]

$$\tau = \max_l \left| \sum_{j=1}^N e^{2\pi i \mathbf{r}_j \cdot \mathbf{n} / l} \right|, \quad (5.5)$$

where  $\mathbf{r}_j$  is the position of the  $j$ -th platelet, and the value of  $l \in R$  that maximizes the above expression is identified as the layer spacing. Additionally, we calculate the diffraction patterns along the nematic director corresponding to the long particle axis, i.e. the  $L$ -axis. This is done by projecting the particle positions on the plane defined by the

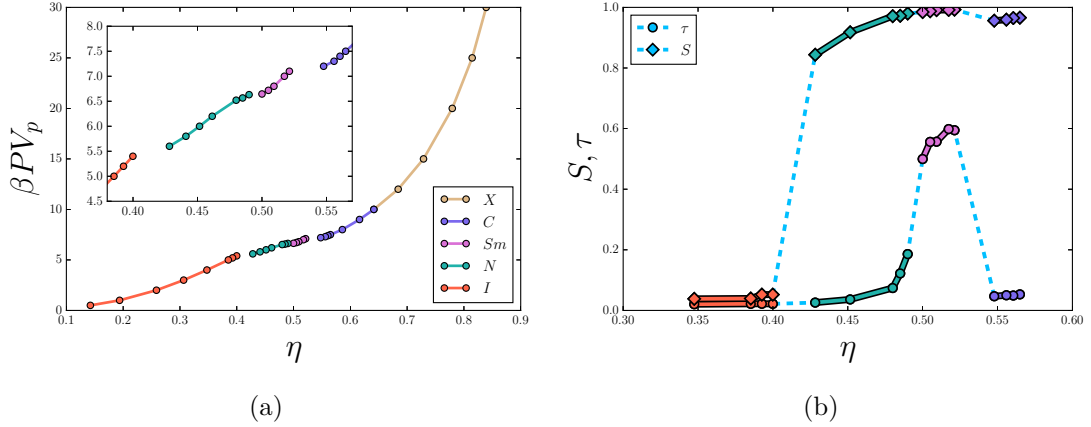


**Figure 5.2:** (a): Equation of state ( $\beta PV_p$  vs  $\eta$ ) for rhombic platelets with reduced width  $W/L = 2/3$  and thickness  $T/L = 1/9$ . The different points are colored according to the respective phase. Orange: isotropic phase ( $I$ ), Green: nematic phase ( $N$ ), Pink: smectic phase ( $Sm$ ), Purple: columnar phase ( $C$ ), Brown: rhombic crystal phase ( $X$ ). In the inset, a zoomed-in region of  $\eta \in (0.38, 0.57)$  is plotted showing more clearly the jumps associated with the three first-order phase transitions (namely  $I-N$ ,  $N-Sm$ , and  $Sm-C$ ). (b): Nematic,  $S$ , and smectic,  $\tau$ , order parameters for the same rhombic platelets as in (a). The nematic order parameter is plotted as circles, while the smectic order parameter is plotted as diamonds. The different points are colored according to the color-coding in (a).

nematic directors of the  $T$  and  $W$  particle axes, and subsequently calculating the Fourier transform of a two-dimensional histogram of the projected particle positions.

## 5.4 Results

We perform Monte Carlo (MC) simulations in the  $NPT$  ensemble, i.e. simulations where the number of particles,  $N$ , pressure  $P$ , and temperature  $T$  are fixed. We employ periodic boundary conditions along all three dimensions. We change the volume independently in each dimension so that the simulation box can accommodate the different phases, thereby avoiding severe finite size effects. We use the cluster algorithm described in section 5.3.1 for performing the volume change moves. Each Monte Carlo cycle consists of  $N$  attempts to translate a random particle,  $N$  attempts to rotate a random particle, and one attempt to change the volume of the simulation box. Configurations were initialized in an oblique crystal phase (an example of this phase is shown in figure 5.4), and simulated for  $\sim 10^7$  MC cycles. The equilibrium packing fraction,  $\eta$ , was calculated as an average over the last few million MC cycles.

### 5.4.1 Phase Behavior Characterization

In our Monte Carlo study, we find that hard rhombic platelets with a width-to-length ratio  $W/L = 2/3$  exhibit rich phase behavior; the platelets can transition through up to five different phases, depending on the reduced thickness,  $T/L$ . In figure 5.2(a), we have

plotted the equation of state ( $\beta PV_p$  vs  $\eta$ , where  $\beta = 1/(k_B T)$  with  $k_B$  the Boltzmann constant and  $T$  the temperature, and  $V_p$  the particle volume) for platelets with reduced thickness  $T/L = 1/9$ . The colors denote the thermodynamic phase of the respective state point. More specifically, the isotropic phase ( $I$ ) is represented by the orange color, the nematic phase ( $N$ ), by the green color, the smectic phase ( $Sm$ ), by the pink color, the columnar ( $C$ ), by the purple color, and the rhombic crystal phase is represented as the brown color. To appreciate the fine detail of the equation of state, we plot a magnified version for packing fractions  $\eta \in (0.38, 0.57)$ , in the inset, showing the jumps associated with the three first-order phase transitions ( $I-N$ ,  $N-Sm$ , and  $Sm-C$ ). This is further underpinned in figure 5.2(b), where we plot the nematic,  $S$ , and smectic,  $\tau$  order parameters, using once more the same color-coding. It can be clearly seen that the nematic order parameter,  $S$ , shows a jump at a packing fraction  $\eta \approx 0.4$ , clearly indicating the orientational alignment of the platelets along the nematic director. On the other hand, the smectic order parameter,  $\tau$ , clearly shows a jump at a packing fraction  $\eta \approx 0.5$ . The smectic order parameter jumps back to  $\sim 0$  in the columnar phase at a packing fraction  $\eta \approx 0.55$ .

### 5.4.2 Structure

We now turn our attention to the structure of these phases. To this end, we present configurations, along with the corresponding diffraction patterns, in figures 5.3, and 5.4, for platelets with reduced thickness  $T/L = 1/9$ . In the configurations, the particles are colored according to the absolute direction of the short axis – it is easily seen that with the exception of the isotropic phase, as shown in figure 5.3(a), all phases are orientationally ordered along the short particle axis, i.e. along the  $T$ -axis. From the configuration in figure 5.3(b) and the corresponding diffraction pattern, we observe that the nematic phase shows only weak positional order of the platelets along the nematic director, which is enhanced and clearly pronounced in the smectic phase. In the columnar phase, as shown in figure 5.4(b), we find that the particles form stacks which are arranged in a two-dimensional oblique lattice. We thus find a phase transition from the smectic phase, with one-dimensional positional order and strong orientational order along the nematic director, to a columnar phase with two-dimensional positional order and with additional weak orientational order in the direction perpendicular to the nematic director, as can be seen from the diffraction patterns and configurations.

### 5.4.3 Phase Diagram

Combining the information from the equations of state, the order parameters,  $S$  and  $\tau$ , and the diffraction patterns, we determine the phase diagram as a function of plate thickness,  $T/L$ , which is shown in figure 5.5. The hatched blue region denotes the region where the equation of state shows a jump, while the solid-colored regions represent the different phases according to the color-coding used in figure 5.2. From the phase diagram, we see that for sufficiently thick platelets,  $T/L > 0.17$ , only the isotropic, columnar, and rhombic crystal phases are present. For thinner platelets, we find a narrow regime where the smectic phase is stable, which is easy to miss. Upon decreasing  $T/L$  further,

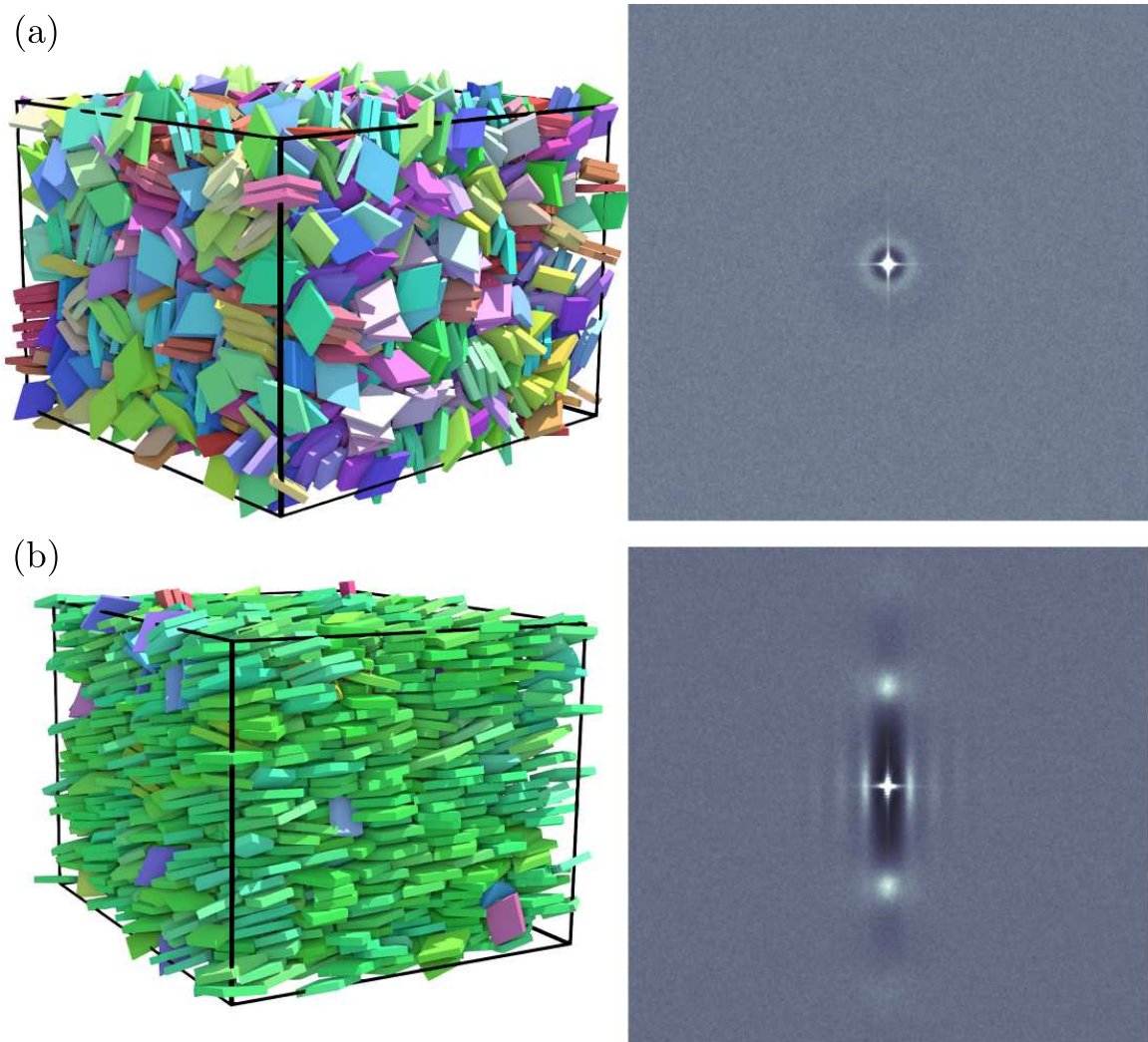


**Figure 5.3:** **Left:** Representative configurations of hard rhombic platelets with reduced width  $W/L = 2/3$  and thickness,  $T/L = 1/9$  for the isotropic (a) and nematic (b) phases. The particles are colored according to the direction of their short axis; the absolute value of the components of the particle direction is translated to normalized RGB values. **Right:** Diffraction patterns corresponding to the phases to the left, with the vertical axis being along the  $T$ -nematic director, and the horizontal axis, perpendicular to it.

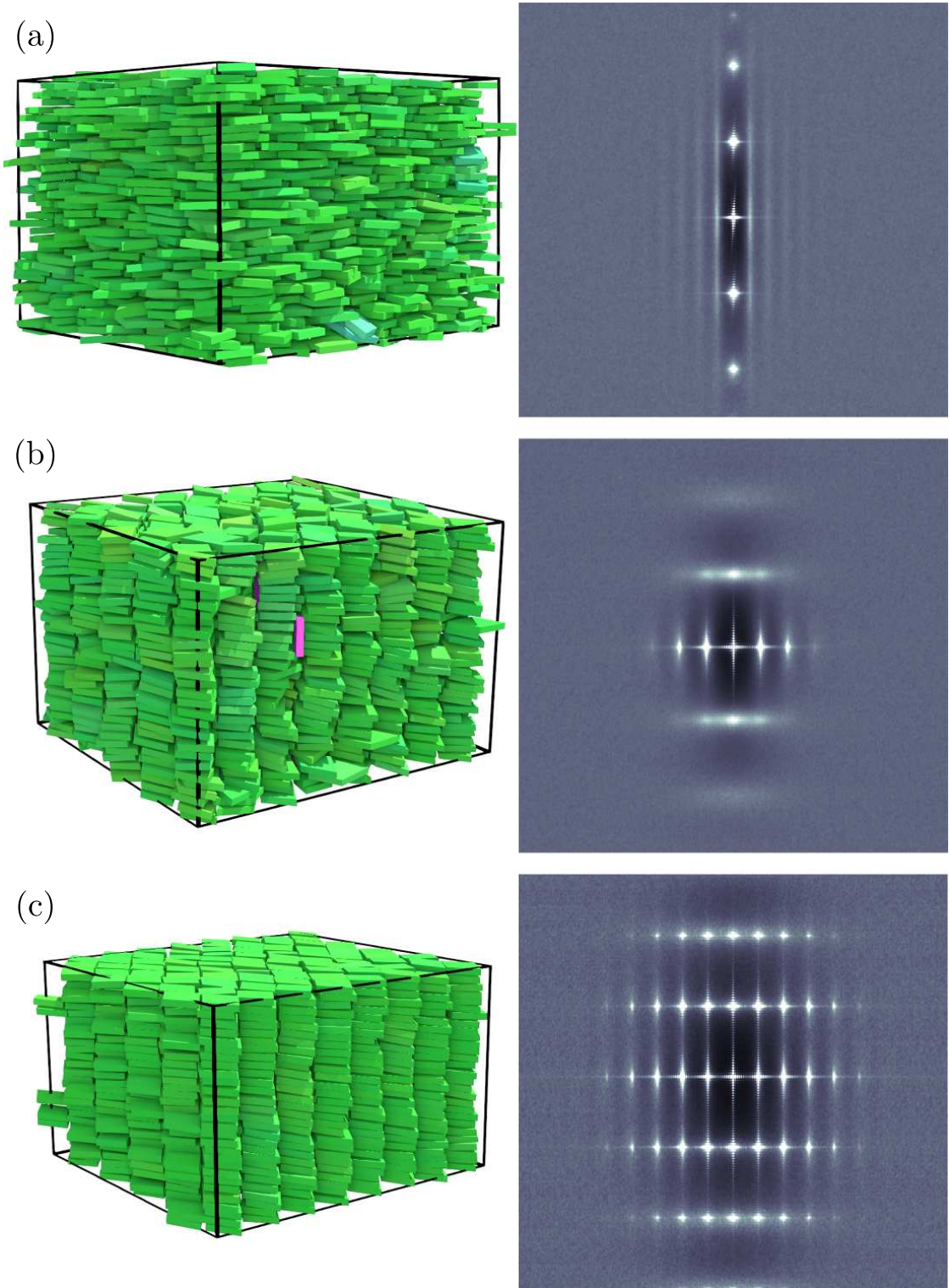


**Figure 5.4: Left:** Representative configurations of hard rhombic platelets with reduced width  $W/L = 2/3$  and thickness,  $T/L = 1/9$  for the smectic (a), columnar (b), and rhombic crystal (c) phases. The particles are colored according to the direction of their short axis; the absolute value of the components of the particle direction is translated to normalized RGB values. **Right:** Diffraction patterns corresponding to the phases to the left, with the vertical axis being along the  $T$ -nematic director, and the horizontal axis, perpendicular to it.

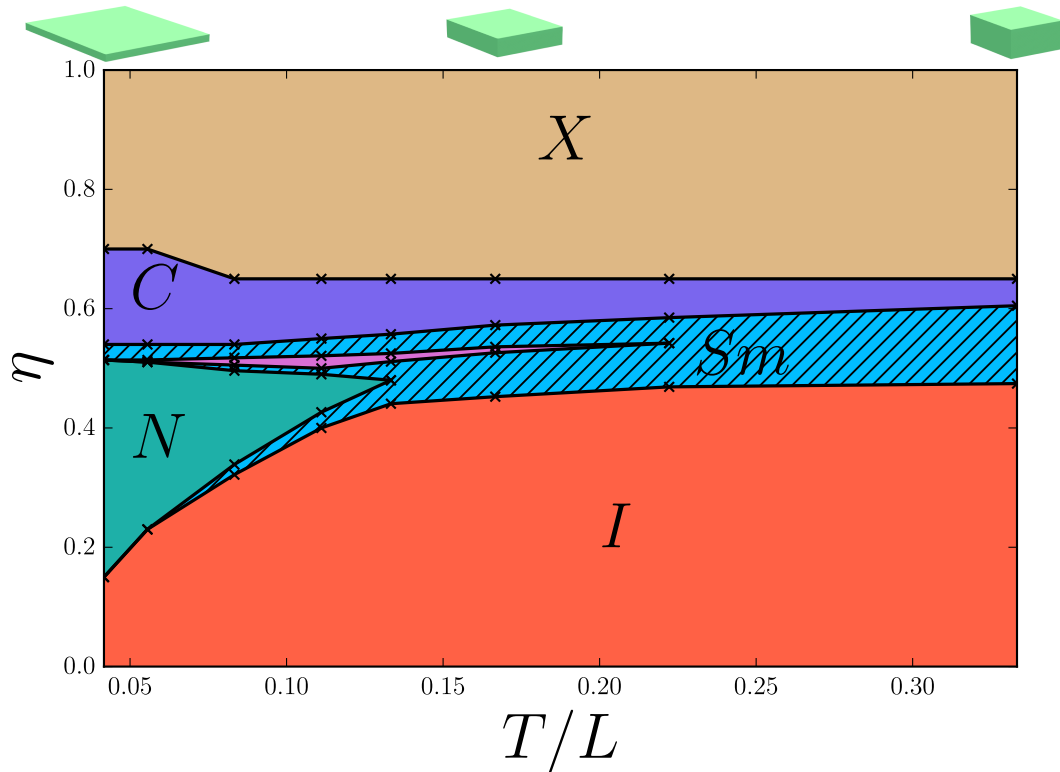


**Figure 5.5:** Phase diagram, of hard rhombic platelets with width-to-length ratio  $W/L = 2/3$ , in the packing fraction,  $\eta$  - reduced thickness,  $T/L$  representation, determined from  $NPT$  expansion runs. At the top of the diagram, and from left to right, the rhombic platelet is shown for increasing reduced thicknesses corresponding to the  $x$ -axis. The volume of the depicted platelets is fixed. The stable phases are coloured in the phase diagram as, Orange: isotropic phase ( $I$ ), Green: nematic phase ( $N$ ), Pink: smectic phase ( $Sm$ ), Purple: columnar phase ( $C$ ), Brown: crystal phase ( $X$ ), and Blue: two-phase coexistence regions.

the isotropic region becomes smaller, and the nematic phase takes over. For thickness  $0.083 < T/L < 0.133$ , the rhombic platelets experience, upon increasing the packing fraction, a (weakly) first-order phase transition from the isotropic to the nematic phase, followed by a (weakly) first-order phase transition to the smectic phase, and another one to the columnar phase, and a continuous transition to the crystal phase. For thickness  $T/L < 0.083$ , the smectic phase vanishes completely. It is also expected that the isotropic phase vanishes as  $T/L \rightarrow 0$ .

In addition, we investigated the possibility of the smectic phase being metastable. To this end, we carefully checked if the smectic phase spontaneously forms upon expanding the space-filling rhombic crystal phase, as well as upon compressing the isotropic fluid phase using MC simulations in the *NPT* ensemble for  $N \approx 2000$  rhombic platelets, with  $T/L = 1/9$ . Upon compressing the isotropic fluid phase, we indeed find that the smectic phase forms spontaneously, thereby lending strong support that the smectic phase is stable. Upon compression, long-lived columnar clusters are also formed. However, we were not able to recover a bulk columnar phase upon compressing the smectic phase further, at least within the simulation time that we considered.

Furthermore, we performed event-driven Molecular Dynamics (EDMD) simulations of rhombic particles with  $T/L = 1/9$ , in the *NVT* ensemble. Our EDMD implementation details can be found in chapter 6. For  $N \approx 2000$  particles, simulations close to the isotropic-nematic, and nematic-smectic coexistence, showed strong spinodal-like fluctuations in the local nematic, and smectic order parameters, respectively. This accompanied by the small ‘jumps’ in the equations of state, leads us to the conclusion that these transitions are weakly first order. We also find that the columnar phase melts into a smectic phase at a pressure  $\beta PV_p \approx 7.3$ , which is close to the coexistence pressure found from the MC expansion, but we find significant finite size effects for this transition, even for a columnar phase consisting of  $20 \times 52$  columns, i.e.,  $N = 52000$  particles.

Although the hard rhombic platelets have a fundamentally different shape from e.g. oblate hard spherocylinders (OHSC) of Ref. [183], preliminary simulations show striking agreement, at least quantitatively, in the phase behavior of the two particle shapes. Unlike the OHSC, though, we also find a smectic phase for reduced thickness  $0.083 < T/L < 0.17$ , and for packing fractions  $\eta \in (0.5, 0.52)$ . We speculate that the smectic phase is entropically stabilized by the non-circular shape of the rhombic platelets as well as the large flat facets.

## 5.5 Conclusion

Using Monte Carlo simulations, we determined the phase diagram of hard rhombic platelets with width-to-length ratio  $W/L = 2/3$ , as a function of the plate thickness,  $T/L$ . We measured the equations of state, diffraction patterns, as well as the nematic and smectic order parameters, and determined the phase boundaries from *NPT* expansion runs. We verified the type of the various phases by visual inspection of the particle configurations. In addition, we investigated the presence of metastability by performing compression runs, upon which a bulk smectic phase is formed, and EDMD simulations in the *NVT* ensemble. Our MC simulations as well as EDMD simulations, provide strong support

for a stable columnar and smectic phase in a system of hard-rhombic platelets, but it is hard to pinpoint exactly the phase transition due to severe finite-size effects and slow equilibration rates, as the free energies of the two phases are likely very close. This will also hamper the determination of the phase boundaries using free-energy calculations.

The phase behavior of rhombic platelets, presented here, is compatible with that of other platelet-like particles found in the literature, such as cylinders [179, 210], cut spheres [182, 184], and oblate hard spherocylinders [183]. Unlike the aforementioned particle shapes, the non-circular symmetry and flat facets of rhombic platelets leads to the presence of a stable smectic phase. The smectic phase is stable in a narrow density regime but could possibly be stabilized in a wider regime for different width-to-length ratios of  $W/L$ .

Generally, a biaxial phase is expected for anisotropic particles when the quantity  $\nu = T/W - W/L \approx 0$  [211], where  $T < W < L$  are the sizes of the three main particle axes. For the rhombic platelets presented here, we find from preliminary simulations that a biaxial nematic phase is present for extremely thin platelets,  $T/L < 0.05$ , corresponding to  $\nu \approx -0.6$ . Our preliminary results, as well as those found e.g. in Ref. [212] on brick-like particles, indicate that the stability of a biaxial phase also depends on an additional criterion for  $T/L$ , i.e. the platelets should be sufficiently thin. In the next chapter, we study the phase behavior of rhombic particles as a function of all parameters  $T$ ,  $W$ , and  $L$ . There, we focus on finding the combination of parameters that allow rhombic particles to form a biaxial phase.

Rhombic platelets of different aspect ratios can be synthesized and used in self-assembly experiments. In this work, we have investigated what the effect of a non-circularly symmetric particle shape is on the phase behavior of plate-like particles, and how the flat facets stabilize a layered structure such as the smectic phase.

# 6

---

## Investigating the Presence of a Biaxial Nematic Phase in Hard Rhombic Particles

---

We develop a highly efficient event-driven Molecular Dynamics (EDMD) algorithm that enables us to perform simulations on general convex particles. Using this algorithm we study the presence of a biaxial nematic phase for rhombic particles with  $T \leq W \leq L$ , where  $T$  is the thickness,  $W$  the width, and  $L$  the length of the particle, by simulating 68 different particle shapes. Upon expansion from the space-filling crystal structure, we find 10 different ordered phases, including a biaxial nematic phase. A biaxial smectic phase is also shown for the first time in a simulation study, which remarkably does not appear in the same particle shape parameter regime as the biaxial nematic phase. In addition, we map out a diagram of the different sequences of phases we find for increasing densities, as a function of the length and width of the rhombic particles. We find 9 regimes with different phase sequences, which conveys the complexity of the system. Our results show that due to the sharp-angled rhombic shape of the particles, the smectic phases are destabilized in favor of the biaxial nematic phase, making the area of the biaxial nematic phase in the phase diagram larger than in previously studied hard-particle systems.

## 6.1 Introduction

When discussing liquid crystals in the Introduction (section 1.6) we mentioned that, in a uniaxial nematic phase, particles which are anisotropic in shape, rod-like or plate-like, are oriented along a preferred direction, but their center of mass positions are randomly distributed as in a liquid. In cases where the particles are not uniaxial, they may also display orientational order along a second preferred axis [46] and form a so-called biaxial nematic liquid crystal. The biaxial nematic liquid crystal has two distinct optical axes along which the velocity of light is polarisation independent. This has important implications for next-generation liquid crystal applications.

Historically, systems consisting of biaxial particles were studied theoretically in the early 1970s [213–215], as a logical step up from particle models with uniaxial symmetry. These theoretical studies predicted the existence of a biaxial nematic phase in which the particles display orientational order in two directions. In addition, there was a need to explain discrepancies between theoretical predictions and experimental observations on the magnitude of the nematic order parameters and fractional density jumps during the isotropic-nematic transition [216]; the molecules studied in experiments were of course not perfectly uniaxial. In the following years, various theoretical hard-particle models were studied, including biaxial ellipsoids [216, 217], spheroplatelets [218], and board-like particles [219]. Theoretically studies by Straley [215] and Mulder [218], predicted that the biaxial nematic phase should appear in systems composed of particles that satisfy  $M^2 = LS$ , where  $L$ ,  $M$ ,  $S$  are the lengths of the long, medium, and short particle axes, respectively.

Although the biaxial nematic phase was identified for lyotropic liquid crystals since 1980, in a ternary potassium laurate-1-decanol-water mixture [220], early experimental evidence of a thermotropic biaxial nematic phase [221–224] was later refuted [225, 226]. The reason for the failure to observe thermotropic biaxial nematics is connected with the competition of this phase with other potential molecular organizations. It was not until 2004 when unambiguous and conclusive evidence of such a biaxial nematic phase was presented by Madsen *et al.* [227] and Acharya *et al.* [228]. These studies were received with considerable excitement, as it opens up new areas of both fundamental and applied research.

Simulation studies, although scarce, have also seen progress in the direction of biaxiality. Studies include hard-particle models of biaxial ellipsoids [217] and spheroplatelets [197, 229] as well as models with interactions such as systems of elongated attractive-repulsive biaxial Gay-Berne particles studied by Berardi *et al.* [230, 231], and model mixtures of rod-like and disk-like molecules interacting through inter-molecular potentials studied by Cuetos *et al.* [232]. Computer simulations of hard spheroplatelets by Peroukidis *et al.* [197, 229] showed, as predicted by theory [215, 218], that it is possible to obtain a biaxial nematic phase before the appearance of a smectic phase for a narrow shape regime,  $M^2 \approx LS$ , provided that also the ratio between the size of the long and short particle axis is large enough.

In this chapter, motivated by the simulation studies by Peroukidis *et al.* [197, 229] and experimental realization of colloidal dispersions of boardlike particles by van den Pol *et al.* [233], we use event-driven molecular dynamics (EDMD) simulations to study the presence

of a biaxial nematic phase in a model of hard rhombic particles like the ones introduced in the previous chapter. We investigate the phase behavior of rhombic particles as a function of particle shape, and find that they exhibit very rich phase behavior, including a biaxial nematic phase for a narrow packing fraction range but relatively wide shape parameter regime. This chapter is organized as follows: We describe our hard rhombic particle model and associated shape parameters in Sec. 6.2. In Sec. 6.3 we present the methods used, with the first part providing information and implementation details on the EDMD simulation techniques. This part is aimed at readers who are interested in the important but more technical details of our EDMD study and might be skipped by those interested only in the results, which we present in Sec. 6.4. Finally, in Sec. 6.5, we summarize and make some concluding remarks.

## 6.2 Model

We use the same model of hard rhombic particles as in chapter 5, which is shown in figure 5.1. Here, we extend our previous study, where we fixed the width-to-length ratio,  $W/L = 2/3$ , by looking at the phase behavior of rhombic particles with  $T \leq W \leq L$ , similar to the study by Peroukidis *et al.* [197]. It should be noted that the region  $T \geq L \geq W$  should also be very interesting, but is left for future work. We introduce the dimensionless length and width as  $\tilde{L} = L/T$  and  $\tilde{W} = W/T$  respectively, and study the phase behavior as a function of these two parameters. The rhombic particles become square when  $\tilde{W} = \tilde{L}$  and their phase behavior should be the same as that found by John *et al.* [234].

## 6.3 Methods

In order to study the phase behavior of the model described above, and due to the large number of particle shapes that we wish to investigate, the EDMD method seems better suited due to its fast equilibration times. Because of this choice, in contrast with the previous chapter where the *NPT* ensemble was employed, the simulations are necessarily restricted to the *NVT* ensemble. It should be noted that although EDMD is well-suited for systems with low dimensional symmetry, Monte Carlo *NPT* simulations might fair better in accurately determining the coexistence properties between highly ordered phases, because the dimensions of the periodic box are allowed to relax to the dimensions of the underlying ordered structure.

To investigate the structure and identify the various phases formed by rhombic particles, we use a combination of order parameters, diffraction patterns, visual inspection of typical configurations, and looking for ‘van der Waals loops’ in the equations of state. This is in the same spirit as chapter 5, where we restricted ourselves to rhombic particles with  $W/L = 2/3$  and  $\tilde{L} > 3$ .

### 6.3.1 Event-Driven Molecular Dynamics

In molecular dynamics (MD) simulations, the trajectories of atoms and molecules are determined by numerically integrating Newton's equations of motion for a system of interacting particles, where forces between the particles and their potential energies are calculated using interatomic potentials or molecular mechanics force fields. For hard particles whose interaction potential (see e.g. eq. 1.10) is discontinuous, the integration is ill-defined. Instead, one can numerically integrate the equations of motion to the next collision event, resolve the collision by modifying the velocities of the colliding particles, and rinse and repeat. Remarkably, such an EDMD simulation, was already performed in 1957 by Alder *et al.* [52] for a system of hard spheres, and actually preceded the first MD simulations with continuous potentials by Rahman [235].

Ever since the first EDMD simulation [52], the method has seen substantial improvements. In EDMD, the most resource intensive operation, is identifying the next collision event. In a naive implementation, one would identify only the next collision event by searching all possible collision events. Since only two particles participate in a collision event, and thus only those two particles are modified after the event, all other possible collision events that are calculated, are wasted. Instead, modern implementations use what is known as an event calendar [236]. The event calendar is responsible for storing and sorting possible events according to their time of occurrence. Events involving particles that have been modified also need to be easily invalidated. In our implementation, we use a very efficient event calendar, which shows a constant time,  $\mathcal{O}(1)$ , complexity in all operations [237]. The other important improvement comes from the realization that particles that are far apart are less likely to collide within a short period of time, than particles that are closer. There are various space partitioning algorithms that make it easy to find particles that are in close proximity, including the well known cell-linked list [157, 236, 238–240]. In case a space partition algorithm is used, the EDMD implementation also needs to keep track of the event where a particle traverses a partition, so that collision events are recalculated for the new neighboring particles [238]. In our EDMD implementation, we also use the *delayed states algorithm* [241], in which the particle state variables are not updated until an event involving the particle occurs.

Below we present, briefly, information pertinent to the implementation of our EDMD simulation of general hard convex particles.

### Rotation

To describe rotations, we use quaternions. A quaternion is composed of a scalar part and a vector part,  $q = (w, \mathbf{r})$ , or  $q = w + r_x i + r_y j + r_z k$ , in complex notation, where  $i^2 = j^2 = k^2 = -1$ . Quaternion multiplication is performed in an analogous way to complex numbers. A rotation by a given angle,  $\phi$ , about a fixed axis represented by an imaginary unit vector,  $\hat{\mathbf{n}} = n_x i + n_y j + n_z k$ , can be represented by the unit quaternion,

$$q = \cos \frac{\phi}{2} + \hat{\mathbf{n}} \sin \frac{\phi}{2}. \quad (6.1)$$

Application of this rotation to a vector,  $\mathbf{u}$ , is then given by the formula,

$$\mathbf{u}' = q\mathbf{u}q^{-1} = \mathbf{u} + 2\mathbf{r} \times (\mathbf{r} \times \mathbf{u} + w\mathbf{u}). \quad (6.2)$$

Being of unit length, the quaternion can be written as  $q = \exp\left(\frac{\phi}{2}\hat{\mathbf{n}}\right)$ . Applying a rotation,  $q$ ,  $i$  times, results in the quaternion  $q_i$ , which is simply given by,  $q_i = q^i$ , so that the evolution of a quaternion under constant angular velocity, is  $q_t = \exp\left(t\frac{\phi}{2}\hat{\mathbf{n}}\right)$ , which, cast in the form of eq. 6.1, reads,

$$q_t = \cos \frac{t\phi}{2} + \hat{\mathbf{n}} \sin \frac{t\phi}{2}. \quad (6.3)$$

We use the above formula to evolve the rotation of our particles between collisions, when the angular velocity remains constant. The time derivative,  $\dot{q}_t = dq_t/dt$ , is also easily derived and is given by,

$$\dot{q}_t = \frac{1}{2}\phi\hat{\mathbf{n}}q_t = \frac{1}{2}\boldsymbol{\omega}q_t, \quad (6.4)$$

where  $\boldsymbol{\omega} = \phi\hat{\mathbf{n}}$  is the imaginary angular velocity.

### Conservative Advancement

The most complex and time consuming operation in an EDMD simulation, is finding out if and when two particles are going to collide. To find the time of collision between two bodies, most commonly a distance function,  $d(t)$  is defined, which measures the closest distance between the two bodies as a function of time. This is usually solved iteratively using some root finding algorithm (e.g. Newton Raphson) [242], in a two-sided approach, meaning that the distance function is allowed to become negative (penetration). Our goal was to use the flexible GJK algorithm which is able to calculate the shortest distance between arbitrary convex shapes. However, GJK does not a priori provide a penetration depth, and although it can be extended to do so, the performance of this extension is poor. Luckily, a one-sided approach to finding the root of the distance function, called ‘conservative advancement’ (CA) was developed in 1996 by B. Mirtich [243] for exactly this reason.

CA exploits the fact that there exists an upper bound on the component of linear velocity parallel to the shortest distance between the two bodies. Consider two convex bodies moving at a constant linear and angular velocity, like in figure 6.1, and let  $\mathbf{c}_1$  be the point of body 1 closest to body 2, and  $\mathbf{c}_2$ , the point of body 2 closest to body 1. Since body 1 is convex it must lie entirely on one side of the plane passing through  $\mathbf{c}_1$  and perpendicular to the distance vector  $\mathbf{d} = \mathbf{c}_2 - \mathbf{c}_1$ . The same is true for body 2 and the corresponding plane through  $\mathbf{c}_2$ . Let  $\mathbf{x}_1$  and  $\mathbf{x}_2$  be the points at which the bodies will ultimately collide. No matter where on the convex bodies these points are situated, they will always have to cover a distance  $\|\mathbf{d}\|$  in the direction of  $\mathbf{d}$ . Based on this fact, it can be shown that the component of the velocity of a convex body with a circumscribed radius  $R$ , in the direction of  $\mathbf{d}$ , is bounded by,

$$v_d = \mathbf{v} \cdot \hat{\mathbf{d}} + \|\hat{\mathbf{d}} \times \boldsymbol{\omega}\|R, \quad (6.5)$$

where  $\mathbf{v}$  is the linear velocity,  $\boldsymbol{\omega}$  is the angular velocity, and  $\hat{\mathbf{d}}$  is the unit vector along  $\mathbf{d}$ . Using this bound, the time,  $t$ , before which it is ensured that no collision will take place, can be calculated as  $t = \|\mathbf{d}\|/v_d$ , and thus the simulation can be advanced to that point.

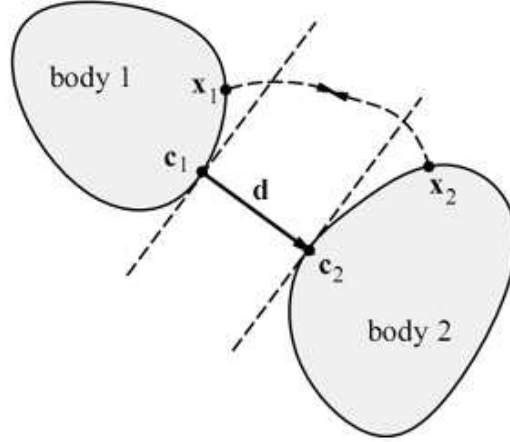


**Figure 6.1:** Two convex bodies approaching each other with constant linear and angular velocities.  $\mathbf{c}_1$  and  $\mathbf{c}_2$  are the two closest points of the two bodies, and  $\mathbf{d} = \mathbf{c}_2 - \mathbf{c}_1$ , is the distance vector, or ‘separating axis’.

The process is repeated until the two bodies are close enough, i.e. until the distance falls below some predetermined threshold.

Zhang et al. improved upon the conservative bound [244–247], for polyhedra and sphere swept volumes. We can make further improvements on the conservative bound on the velocity for general convex shapes. Consider a point  $\mathbf{r}$  on a convex particle, at time  $t_0 = 0$ . The projection of the velocity of this point on the minimum distance direction,  $\hat{\mathbf{d}}$ , reads,

$$v_d = \mathbf{v} \cdot \hat{\mathbf{d}} + (\boldsymbol{\omega} \times \mathbf{r}(t)) \cdot \hat{\mathbf{d}}, \quad (6.6)$$

where  $\mathbf{r}(t)$  is the position of the point  $\mathbf{r}$  at time  $t$ . Using Rodrigues’s rotation formula, this is written as,

$$\mathbf{r}(t) = \mathbf{r} \cos\|\boldsymbol{\omega}\|t + (\hat{\boldsymbol{\omega}} \times \mathbf{r}) \sin\|\boldsymbol{\omega}\|t + \hat{\boldsymbol{\omega}}(\hat{\boldsymbol{\omega}} \cdot \mathbf{r})(1 - \cos\|\boldsymbol{\omega}\|t). \quad (6.7)$$

We substitute the above formula into eq. 6.6, yielding,

$$v_d = \mathbf{v} \cdot \hat{\mathbf{d}} + (\boldsymbol{\omega} \times \mathbf{r}) \cdot \hat{\mathbf{d}} \cos\|\boldsymbol{\omega}\|t + \frac{1}{\|\boldsymbol{\omega}\|} (\boldsymbol{\omega} \times (\boldsymbol{\omega} \times \mathbf{r})) \cdot \hat{\mathbf{d}} \sin\|\boldsymbol{\omega}\|t. \quad (6.8)$$

Using properties of the triple product, we can rewrite the above expression as,

$$v_d = \mathbf{v} \cdot \hat{\mathbf{d}} + (\boldsymbol{\omega} \times \hat{\mathbf{d}}) \cdot \mathbf{r} \cos\|\boldsymbol{\omega}\|t + \frac{1}{\|\boldsymbol{\omega}\|} (\boldsymbol{\omega} \times (\boldsymbol{\omega} \times \hat{\mathbf{d}})) \cdot \mathbf{r} (\sin\|\boldsymbol{\omega}\|t). \quad (6.9)$$

We first maximize the above expression with respect to time. Substituting the solution to the maximization problem back in to the expression, and maximizing with respect to point  $\mathbf{r}$  on the convex particle, yields the final expression,

$$v_d = \mathbf{v} \cdot \hat{\mathbf{d}} + \sqrt{\max_r [(\boldsymbol{\omega} \times \hat{\mathbf{d}}) \cdot \mathbf{r}]^2 + \max_r [(\boldsymbol{\omega} \times (\boldsymbol{\omega} \times \hat{\mathbf{d}})) \cdot \mathbf{r} / \|\boldsymbol{\omega}\|]^2}. \quad (6.10)$$

The two ‘max’ expressions can be written in terms of the support function, of the convex shape:  $\max_r |\mathbf{x} \cdot \mathbf{r}| = \max[\pm \mathbf{x} \cdot s(\pm \hat{\mathbf{d}})]$ . The support function,  $s(\hat{\mathbf{d}})$ , returns the extreme

point of the shape in the direction  $\hat{\mathbf{d}}$ , and is also used extensively in the GJK algorithm. Note that for axisymmetric particles, it suffices to take the support function in either the positive or negative direction.

### Collision resolution

Collision resolution for non-spherical particles is slightly more involved due to the angular component of the momentum. To resolve the collision between two bodies, their common contact point,  $\mathbf{r}_C$ , as well as their common collision normal,  $\hat{\mathbf{n}}$ , at the time of collision, need to be known. The exchange of momentum between two colliding particles  $A$  and  $B$ , and assuming a spherically symmetric moment of inertia, is then given by,

$$\Delta\mathbf{p}_{AB} = 2(\hat{\mathbf{n}} \cdot (\mathbf{v}_B - \mathbf{v}_A)) \left( \frac{1}{m_A} + \frac{1}{m_B} + \frac{\|\mathbf{r}_{CA} \times \hat{\mathbf{n}}\|}{I_A} + \frac{\|\mathbf{r}_{CB} \times \hat{\mathbf{n}}\|}{I_B} \right)^{-1} \hat{\mathbf{n}}, \quad (6.11)$$

where  $\mathbf{r}_{CA} = \mathbf{r}_C - \mathbf{r}_A$ ,  $\mathbf{r}_A$  the position of particle  $A$ ,  $m_A$ ,  $m_B$  the mass of particles  $A$ , and  $B$ , and  $I_A$ ,  $I_B$ , the moments of inertia of the two bodies. The particle velocities are then updated immediately after the collision as,

$$\mathbf{v}_A \leftarrow \mathbf{v}_A - \frac{\Delta\mathbf{p}_{AB}}{m_A}, \quad (6.12)$$

$$\mathbf{v}_B \leftarrow \mathbf{v}_B + \frac{\Delta\mathbf{p}_{AB}}{m_B}, \quad (6.13)$$

and the angular velocities as,

$$\boldsymbol{\omega}_A \leftarrow \boldsymbol{\omega}_A - \frac{\mathbf{r}_{CA} \times \Delta\mathbf{p}_{AB}}{I_A}, \quad (6.14)$$

$$\boldsymbol{\omega}_B \leftarrow \boldsymbol{\omega}_B + \frac{\mathbf{r}_{CB} \times \Delta\mathbf{p}_{AB}}{I_B}. \quad (6.15)$$

It is evident that a way to calculate  $\mathbf{r}_C$ , and  $\hat{\mathbf{n}}$ , is necessary. In simulations, the surfaces of the particles will be at a small, finite distance apart, so it suffices to find the closest point of the two particles,  $\mathbf{r}_{CA}$ ,  $\mathbf{r}_{CB}$ , and the contact normal is then given by,  $\hat{\mathbf{n}} = (\mathbf{r}_{CB} - \mathbf{r}_{CA})/\|\mathbf{r}_{CB} - \mathbf{r}_{CA}\|$ . We explain how these points are calculated in the following subsection.

### GJK Closest Points Algorithm

To be able to calculate the closest points of two convex shapes, the GJK distance algorithm [204] needs to be adjusted. The distance algorithm builds a simplex out of the Minkowski sum of the two shapes,  $A$  and  $B$ , iteratively, by using the ‘support function’ of each shape,  $s(\hat{\mathbf{d}})$ . Every time a point is added to the simplex, it is reduced to its feature that is closest to the origin. This is repeated until the origin cannot be further approached, or until an overlap is found (this is the case if the origin is contained in the Minkowski sum). The simplex is built from points on the Minkowski hull,  $p = s_A(\hat{\mathbf{d}}) + s_B(-\hat{\mathbf{d}})$ , where  $s_A$  and  $s_B$  are the support functions of shape  $A$  and  $B$  respectively. For the distance algorithm,

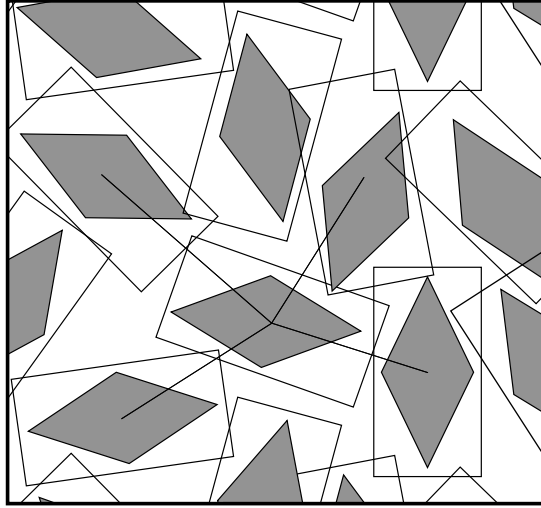


**Figure 6.2:** Example of a two-dimensional system of rhombic particles (gray) with surrounding bounding boxes (rectangles). The lines represent pairs of bounding regions that overlap each other and are part of the near-neighbour list of the particle in the middle.

we have to additionally store the points  $\mathbf{a} = s_A(\hat{\mathbf{d}})$ , and  $\mathbf{b} = s_B(-\hat{\mathbf{d}})$  along with  $p$ . To get the closest points, we project the origin on the closest feature of the Minkowski hull, to get a point  $q$ , and by calculating its barycentric coordinates  $u_i$ , the closest points are given by,

$$\mathbf{p}_A = \sum_{i=0}^{N-1} u_i \mathbf{a}_i \quad (6.16)$$

$$\mathbf{p}_B = \sum_{i=0}^{N-1} u_i \mathbf{b}_i, \quad (6.17)$$

where  $i$  runs over the  $N$  vertices of the closest feature. For the particular case of  $N = 3$ , i.e. for triangles, barycentric coordinates can be calculated using Cramer's rule. In practice, it is known that Cramer's rule is unstable, and this could also be seen in our simulations. Instead we used a numerically stable algorithm called Gaussian Elimination with Partial Pivoting (GEPP) [248]. Additionally, instead of using  $\hat{\mathbf{n}} = (\mathbf{p}_B - \mathbf{p}_A)/\|\mathbf{p}_B - \mathbf{p}_A\|$ , we use the distance vector,  $\mathbf{d}/\|\mathbf{d}\|$ , we get from the distance algorithm. This way, the calculations remain consistent.

### Near-Neighbour Lists

In a simulation where particles interact with each other, implementing an efficient neighbor search algorithm is very important. Donev *et al.* [239, 240] introduced the concept of *near-neighbor lists* (NNL) for the first time in EDMD simulations. The concept of NNLs is not new, and has been previously used in MD simulations [249], and shares many similarities with the well known *Verlet lists* [250]. Adoption of NNLs in EDMD have been hampered by the difficulty of updating these at the correct time.

For the NNL algorithm, at the start of the simulation, each particle,  $i$ , is enclosed by a *slightly enlarged* bounding region,  $\mathcal{B}_i$ . Subsequently, for each particle,  $i$ , a list of bounding

regions,  $\mathcal{B}_j$ , overlapping with  $\mathcal{B}_i$ , is stored as  $\mathcal{N}_i$ . In figure 6.2 we draw a schematic of a two-dimensional system of rhombic particles and surrounding bounding regions, where pairs of bounding regions that overlap each other are connected by lines. To efficiently find the overlapping bounding regions, a ‘cell list’ structure is used [239]. During the simulation, the bounding regions are immobile, but both  $\mathcal{B}_i$  and  $\mathcal{N}_i$  need to be updated when a particle comes in contact with its own bounding region,  $\mathcal{B}_i$ . Additionally, the current neighbours of particle  $i$ , need to update their neighbor lists accordingly, i.e. the  $\mathcal{N}_j \forall j \in \mathcal{N}_i$ . When a new neighbor,  $j$ , is added to a list  $\mathcal{N}_i$ , a collision event needs to be predicted between particles  $i$  and  $j$ . For the above update, a new type of event needs to be kept track of in the event calendar. This event keeps track of when a particle crosses its bounding region. Calculating this event is very hard for arbitrary shaped particles and bounding regions, and is the main reason why NNLs haven’t been adopted earlier in EDMD simulations. Moreover, the bounding region needs to wrap around the shape of the particle as closely as possible so that only the nearest neighbors are added to the NNLs.

Donev *et al.* implemented NNLs for ellipsoidal particles with the bounding regions being slightly enlarged ellipsoids of the same shape. Here, we implement NNLs for general convex shaped particles, and use bounding boxes as the bounding regions. For simplicity we assume the bounding boxes are centered at the centroid of the particle. The extent,  $l_i^\pm$  of the bounding box, along each dimension,  $\pm \hat{\mathbf{e}}_i$ , can be calculated for any convex shape by using its support function,

$$l_i^\pm = \hat{\mathbf{e}}_i \cdot s(\pm \hat{\mathbf{e}}_i). \quad (6.18)$$

The bounding box is enlarged by a fixed amount,  $c$ , in each direction,  $l'_i^\pm = l_i^\pm + c$ . When a particle crosses its bounding box, the box’s position and orientation are updated to those of the particle. The time at which a particle is going to cross its bounding box, can be easily calculated using the conservative advancement method introduced above. The velocity bound in eq. 6.10 is calculated for each dimension of the box, in both directions,  $\pm \hat{\mathbf{d}}_i$ . Using the support function to calculate the distance in that direction,  $d_i^\pm = l'_i^\pm \mp (s(\pm \hat{\mathbf{d}}_i) - \mathbf{r}_i^b)$ , where  $\mathbf{r}_i^b$  is the position of the box, the advancement time is determined as the minimum of the advancement times in each direction,  $t = \min d_i^\pm / u_{d_i^\pm}$ .

We should note that a different simple bounding shape exists which wraps better around convex shapes than the simple rectangular box. This type of shape is known as a discrete oriented polytope (DOP). While for the rectangular box introduced above, only three directions along the main Cartesian axes were used, in a  $k$ -DOP,  $k$  such directions are used instead. We have tried using a  $k$ -DOP instead of an oriented rectangular box. In this case, when updating the bounding region  $\mathcal{B}_j$  of particle  $j$ , the  $k$ -DOP is recalculated in a similar way to eq. 6.18,

$$l_i^\pm = \hat{\mathbf{n}}_i \cdot s(\pm \hat{\mathbf{n}}_i), \quad (6.19)$$

instead of updating its orientation. Calculating the time a particle crosses its bounding  $k$ -DOP the same as above, with the direction  $\hat{\mathbf{d}}_i$  replaced by the  $k$  predetermined directions,  $\hat{\mathbf{n}}_i$ . We found that even for particles such as the rhombic particle introduced here, there is no noticeable performance benefit of choosing this type of bounding shape. More anisotropic shapes, though, might see a bigger benefit.

### 6.3.2 Order Parameters

In addition to the order parameters introduced in section 5.3.2, we introduce two order parameter,  $\mathcal{B}$  and  $S_4$ , for quantifying the degree of biaxiality and cubatic order respectively. Given the three orthonormal symmetry axes,  $\hat{\mathbf{a}}$ ,  $\hat{\mathbf{b}}$ ,  $\hat{\mathbf{c}}$  of a particle, we use eq. 5.4 to calculate the three nematic order parameter tensors,  $Q^{\hat{a}}$ ,  $Q^{\hat{b}}$ , and  $Q^{\hat{c}}$ , respectively, and determine the largest eigenvalue,  $\lambda_{\hat{u}}^+$ , and corresponding eigenvector,  $\hat{\mathbf{n}}_{\hat{u}}$ , for each of them. The eigenvector corresponding to the largest of these eigenvalues, is identified as the principal laboratory axis,  $\hat{\mathbf{Z}}$ , and the corresponding particle symmetry axis, as the primary particle symmetry axis,  $\hat{\mathbf{z}}$ . The second largest eigenvalue is used to identify the secondary laboratory, and particle axes,  $\hat{\mathbf{Y}}$  and  $\hat{\mathbf{y}}$ , while the axes  $\hat{\mathbf{X}}$  and  $\hat{\mathbf{x}}$  are identified from the remaining eigenvalue and eigenvector. This can be easily implemented using a sorting procedure to sort sets of the type  $\{\lambda_{\hat{u}}^+, \hat{\mathbf{n}}_{\hat{u}}, \hat{\mathbf{u}}, Q^{\hat{u}}\}$  according to the value of the first element. Finally, the biaxial order parameter can be calculated as the following ensemble average,

$$\mathcal{B} = \frac{1}{3} \left\langle \hat{\mathbf{X}} \cdot Q^{\hat{x}} \cdot \hat{\mathbf{X}} + \hat{\mathbf{Y}} \cdot Q^{\hat{y}} \cdot \hat{\mathbf{Y}} - \hat{\mathbf{X}} \cdot Q^{\hat{y}} \cdot \hat{\mathbf{X}} - \hat{\mathbf{Y}} \cdot Q^{\hat{x}} \cdot \hat{\mathbf{Y}} \right\rangle. \quad (6.20)$$

The biaxial order parameter is normalized to unity, with low values of  $\mathcal{B}$  corresponding to an isotropic or uniaxial phase and values close to 1 corresponding to a phase with biaxial symmetry.

Similar to the biaxial phase, the cubatic phase exhibits no long-range positional order. While in both the biaxial nematic phase and the cubatic phase, the different particle symmetry axes align in three different orthogonal directions, in the cubatic phase, the direction along which particles choose to orient themselves, is chosen with equal probability. In this sense, the cubatic phase, is a special case of the biaxial nematic phase. A pertinent order parameter for measuring the cubatic order in a system exists, and is simply known as the cubatic order parameter, denoted as  $S_4$ . For this, a fourth-rank tensor is defined [182],

$$Q_{\alpha\beta\gamma\delta} = \frac{1}{24N} \sum_{\hat{u} \in \{\hat{\mathbf{a}}, \hat{\mathbf{b}}, \hat{\mathbf{c}}\}} \sum_{i=1}^N [ 35u_{i\alpha}u_{i\beta}u_{i\gamma}u_{i\delta} - 5(u_{i\alpha}u_{i\beta}\delta_{\gamma\delta} + u_{i\alpha}u_{i\gamma}\delta_{\beta\delta} + u_{i\alpha}u_{i\delta}\delta_{\beta\gamma} + u_{i\beta}u_{i\gamma}\delta_{\alpha\delta} + u_{i\beta}u_{i\delta}\delta_{\alpha\gamma} + u_{i\gamma}u_{i\delta}\delta_{\alpha\beta}) + (\delta_{\alpha\beta}\delta_{\gamma\delta}\delta_{\alpha\gamma}\delta_{\beta\delta}\delta_{\alpha\delta}\delta_{\beta\gamma}) ]. \quad (6.21)$$

As was the case for the second-rank tensor in eq. 5.4,  $u_{i\alpha}$ , here, is the  $\alpha$ -th component of the symmetry axis,  $\hat{\mathbf{u}}$ , of particle  $i$ ,  $N$  is the number of particles, and  $\delta_{\alpha\beta}$  is the Kronecker delta. This fourth-rank tensor is closely related to the set of fourth-rank spherical harmonics. It is highly symmetric and has the following property:

$$Q_{\alpha\beta\gamma\delta}\delta_{\gamma\delta} = 0. \quad (6.22)$$

The cubatic order parameter,  $S_4$ , is defined through the following tensor equation,

$$Q_{\alpha\beta\gamma\delta}Q_{\gamma\delta} = \frac{7S_4}{8}Q_{\alpha\beta}. \quad (6.23)$$

Since  $Q_{\alpha\beta}$  is symmetric and traceless, the above tensor equation reduces to only 5 coupled equations, for  $(\alpha, \beta) \in \{(x, x), (x, y), (x, z), (y, y), (y, z)\}$ . The equations can thus be cast in the following form,

$$T\mathbf{p} = \lambda\mathbf{p}, \quad (6.24)$$

where  $T$  is a  $5 \times 5$  square matrix, with each row given by,

$$\begin{bmatrix} Q_{\alpha\beta xx} - Q_{\alpha\beta zz} \\ 2Q_{\alpha\beta xy} \\ 2Q_{\alpha\beta xz} \\ Q_{\alpha\beta yy} - Q_{\alpha\beta zz} \\ 2Q_{\alpha\beta yz} \end{bmatrix}^T \quad (6.25)$$

for the 5 pairs  $(\alpha, \beta) \in \{(x, x), (x, y), (x, z), (y, y), (y, z)\}$ , and  $\mathbf{p}$  is the 5-dimensional vector. The cubatic order parameter can then be calculated from the largest absolute eigenvalue of equation 6.24,  $\lambda^+$ , as,

$$S_4 = \frac{8\lambda^+}{7}. \quad (6.26)$$

The parameter,  $Q$ , can be reconstructed from the eigenvector  $\mathbf{p}$  of equation 6.23. The cubatic order parameter takes the value of  $S_4 = 1$  for perfect cubatic ordering, with molecules pointing with probability 1/3 along each of the three axes. More generally, the cubatic order parameter is large for particle orientations that are either parallel or perpendicular to the eigenvectors of  $Q$ . This means that the cubatic order parameter is also large when there is uniaxial alignment (e.g. in nematic or smectic phases). In this case, the largest absolute eigenvalue of  $Q$ , should also be much larger than its other eigenvalues.

## 6.4 Results

Using the EDMD methods introduced above, we simulate  $N \sim 2 \cdot 10^3$  rhombic particles, in a box of fixed size, and with periodic boundary conditions. Configurations are initialized in an oblique crystal phase (an example of this phase is shown in figure 5.4). The particle velocities are initialized using uniform random unit vectors, while the angular velocities are set to 0. The average velocity of the system,  $\mathbf{u}^s = \sum_i^N \mathbf{u}_i / N$ , is subtracted from each particle's velocity to ensure that the system is not moving. The moment of inertia and mass of all particles is set to 1. The system is simulated for over  $t^* = tV_p^{1/3}/v_0 \sim 10^4$ , where  $V_p$  is the particle volume and  $v_0$  is the initial velocity of each particle, and the equilibrium pressure,  $P$ , is calculated as an average over the last time interval, i.e. where the system is equilibrated.

### 6.4.1 Phase Behavior and Structure

In chapter 5, we found that rhombic platelets with  $\tilde{W}/\tilde{L} = 2/3$ , and  $\tilde{L} \geq 9$  could transition through up to five different phases with increasing pressure, *I-N-Sm-C-X*. By removing the width-to-length ratio constraint, and adjusting  $\tilde{W}$  and  $\tilde{L}$  independently, we find that rhombic particles can exhibit 9 different phase sequences upon increasing density. In addition to the different phases found for rhombic platelets, i.e. isotropic (*I*), nematic (*N*), smectic (*Sm*), columnar (*C*), and crystal (*X*), we find 6 new phases: a prolate nematic phase with alignment along the  $L$  particle axis, a columnar phase with 4-fold rotational

symmetry in the plane perpendicular to the common columnar director, a cubatic phase, a smectic phase with cubatic intralayer ordering, the eluded biaxial nematic phase, and a biaxial smectic phase. Given the multitude of nematic phases, and to match the notation used in previous studies in biaxial phases, we denote the nematic phase with alignment along the  $L$ -axis as  $N_+$ , the nematic phase along the  $T$ -axis as  $N_-$ , and the biaxial phase as  $N_b$ . We denote the columnar phase with the 4-fold rotational symmetry as  $C^4$ , the cubatic phase simply as  $Cub$ , the smectic cubatic phase as  $Sm_{Cub}$ , and the biaxial smectic phase as  $Sm_b$ .

We first discuss the phase behavior of rhombic particles with a reduced width  $\tilde{W} = 4$  and length  $\tilde{L} = 11$ . In figure 6.3(a), we plot the equation of state, along with the nematic order parameter for the three particle symmetry axes,  $S^{\hat{W}}$ ,  $S^{\hat{T}}$ , and  $S^{\hat{L}}$ , as well as the biaxial nematic order parameter, as a function of the packing fraction,  $\eta$ . From the order parameters, we see that  $S^{\hat{L}}$  is large for  $\eta > 0.30$ , whereas the nematic order parameters in the other two directions,  $S^{\hat{W}}$  and  $S^{\hat{T}}$  have a small value of about 0.2, for  $0.3 \leq \eta \leq 0.43$ . We thus find a prolate nematic,  $N_+$ , phase for  $0.3 \leq \eta \leq 0.43$ . Upon increasing  $\eta$ ,  $S^{\hat{W}}$  and  $S^{\hat{T}}$  increase sharply, and the system transitions to a biaxial nematic phase,  $N_b$ . From the equation of state in figure 6.3(a), we see that the biaxial nematic region is small,  $\eta \in (0.43, 0.49)$ . Although this could indicate that the phase is metastable, we note that the biaxial nematic phase we found, was very stable for the length of our simulation runs, with no indication of phase separation. In figure 6.3(b-c), we show a typical configuration of rhombic particles in the biaxial phase, at a packing fraction  $\eta = 0.48$ . The coloring of the particles according to their orientation, nicely depicts the biaxial character of the phase. Note that the absolute value of the components of the particle orientational vector is translated to normalized RGB values. Increasing the packing fraction further, we also find a columnar and a crystal phase. We thus observe a  $I-N_+ - N_b - C - X$  phase sequence for rhombic particles with  $\tilde{W} = 4$  and  $\tilde{L} = 11$ .

We now investigate the phase behavior for rhombic particles with  $\tilde{W} = 7$  and  $\tilde{L} = 11$ . We plot the equations of state and the nematic order parameter for the three particle symmetry axes,  $S^{\hat{W}}$ ,  $S^{\hat{T}}$ , and  $S^{\hat{L}}$ , the biaxial nematic order parameter,  $\mathcal{B}$ , and the smectic order parameter,  $\tau$ , as a function of the packing fraction,  $\eta$ , in figure 6.4(a). From the order parameters, we see that  $S^{\hat{T}}$  increases sharply at  $\eta \approx 0.36$ , where we also see a ‘van der Waals loop’ in the equation of state, indicating that the transition from the isotropic ( $I$ ) phase to the  $N_-$  phase is (weakly) first order. The nematic order parameter increases slightly with packing fraction,  $\eta$ , until another (weakly) first order phase transition is encountered at  $\eta \approx 0.49$ . Here, the smectic order parameter,  $\tau$ , increases sharply, suggesting that the newly formed phase is smectic. Indeed, visual inspection of the particle configurations and respective diffraction pattern within this phase, confirm this. These are shown in figures 6.5(b), along with a particle configuration and the diffraction pattern of the  $N_-$  phase, in 6.5(a). In figure 6.4(a), at a packing fraction  $\eta \approx 0.54$ , we see another ‘van der Waals loop’ in the equation of state, where the smectic phase transitions to a columnar phase. Particles in the columnar phase are aligned, which is also recognized by the jump in the biaxial nematic order parameter,  $\mathcal{B}$ . For an example of how the columnar phase looks like, and its diffraction pattern, see figure 5.4(b) of chapter 5. Notice also the weird behavior of the biaxial nematic order parameter near the coexistence; due to the finite size effects, a system in the columnar region can spontaneously melt into a smectic phase

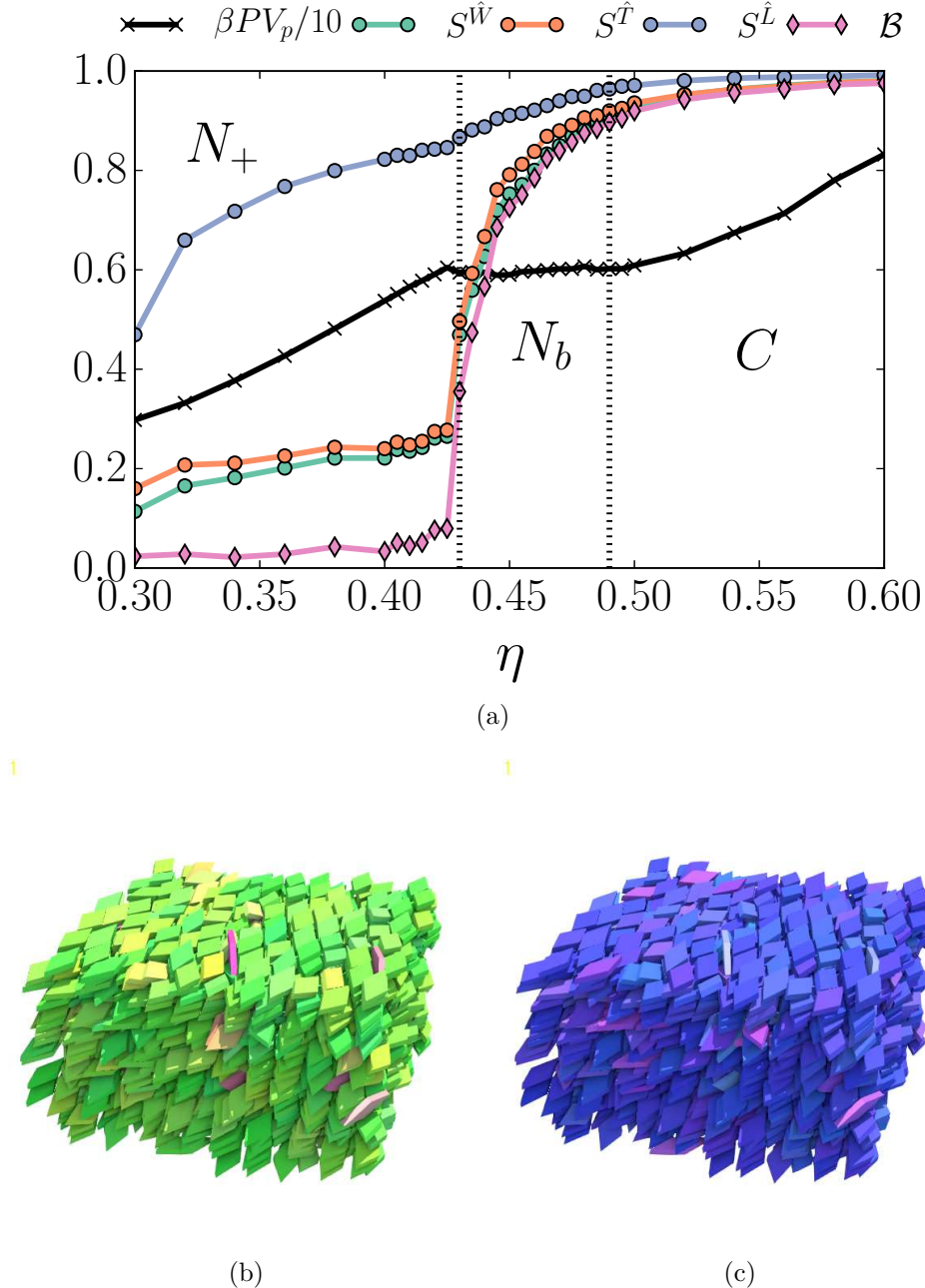


**Figure 6.3:** (a) Equation of state, and nematic and biaxial order parameters as a function of the packing fraction  $\eta = NV_p/V$ , for rhombic particles with  $\tilde{W} = 4$ , and  $\tilde{L} = 11$ . The equation of state is represented by the black line and is plotted as  $\beta PV_p/10$ . The  $S^{\hat{W}}$ ,  $S^{\hat{T}}$ , and  $S^{\hat{L}}$  order parameters are represented by the green, orange, and blue lines respectively. The pink line with rhombic markers represents the biaxial nematic order parameter,  $\mathcal{B}$ . The dotted lines denote approximate phase boundaries, where the different phases are labeled by their respective symbols. (b-c) Representative configurations of the biaxial phase for rhombic particles with  $\tilde{W} = 4$ , and  $\tilde{L} = 11$ , at packing fraction  $\eta = 0.48$ . The configuration (b) is colored according to the orientation of the  $\hat{T}$  axis, while the configuration (c) is colored according to the  $\hat{L}$  axis.

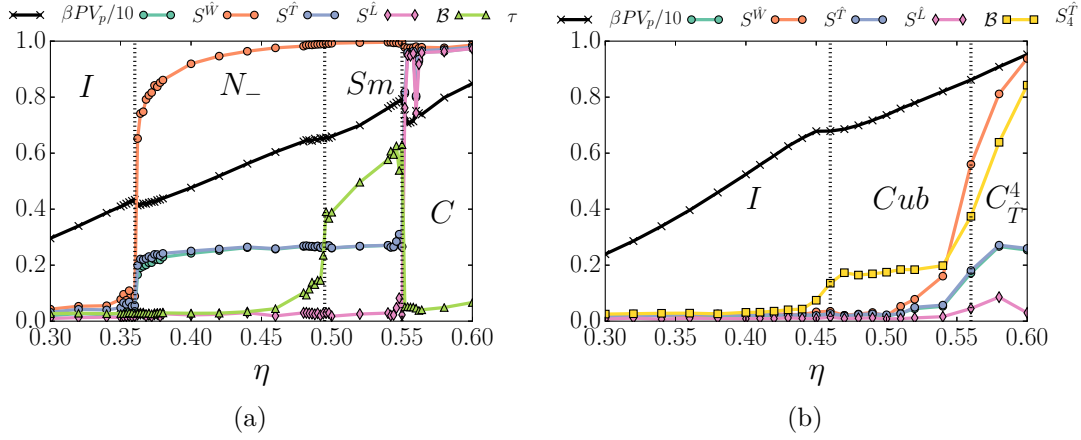


**Figure 6.4:** Equations of state, and nematic, biaxial, smectic, and cubatic order parameters as a function of the packing fraction  $\eta = NV_p/V$ , for rhombic particles with (a)  $\tilde{W} = 7$  and  $\tilde{L} = 11$ , and (b)  $\tilde{W} = 4$  and  $\tilde{L} = 5$ . The equations of state are represented by the black lines and are plotted as  $\beta PV_p/10$ . The  $S^{\tilde{W}}$ ,  $S^{\tilde{T}}$ , and  $S^{\tilde{L}}$  order parameters are represented by the green, orange, and blue lines respectively. The pink line with rhombic markers represents the biaxial nematic order parameter,  $B$ . In (a) we also plot the smectic order parameter,  $\tau$ , as a green line with triangular markers, while in (b) we also plot the cubatic order parameter,  $S_4^{\tilde{T}}$ , as a yellow line with square markers. The dotted lines denote approximate phase boundaries, where the different phases are labeled by their respective symbols.

which, as we discussed in the previous chapter, makes pinpointing the smectic-columnar transition rather troublesome. For rhombic particles with  $\tilde{W} = 7$  and  $\tilde{L} = 11$ , we thus find a  $I-N_- Sm-C-X$  phase sequence, similar to the rhombic platelets that we thoroughly investigated in the previous chapter.

In order to form a cubatic phase, the two particle dimensions of a rhombic particle,  $L$  and  $W$ , should be satisfy,  $L \approx W$ . For rhombic particles with  $\tilde{W} = 4$  and  $\tilde{L} = 5$ , we plot the equations of state, and the nematic order parameter for the three particle symmetry axes,  $S^{\tilde{W}}$ ,  $S^{\tilde{T}}$ , and  $S^{\tilde{L}}$ , the biaxial nematic order parameter,  $B$ , and the cubatic order parameter,  $S_4$ , as a function of the packing fraction,  $\eta$ , in figure 6.4(b). These rhombic particles show a phase sequence  $I-Cub-C^4-X$ . The different phase regions are indicated by their labels in figure 6.4(b). From the figure, we clearly see that the cubatic phase is entered from the isotropic phase through a first order phase transition, which is accompanied by a strong increase of the cubatic order parameter,  $S_4$ . The region where the cubatic phase is stable is not very large, i.e.  $\eta \in (0.45, 0.56)$ . An example of a particle configuration for the cubatic phase is shown in figure 6.6(a), together with its diffraction pattern shown on the right. From the diffraction pattern, we see that short range positional order is present. At  $\eta \approx 0.56$ , we see that the nematic order parameter in the direction of the  $\hat{T}$  axis,  $S^{\tilde{T}}$ , increases sharply. Here we find a columnar phase, but unlike the columnar phase found for particles with  $\tilde{W} = 7$  and  $\tilde{L} = 11$ , we do not find such a dramatic increase of the biaxial nematic order parameter,  $B$ , indicating that the particles in the columns can rotate freely around their  $\hat{T}$  axis. In figure 6.6(b) we show a configuration of the  $C^4$  phase, along with its diffraction pattern, which shows some medium range intracolumnar

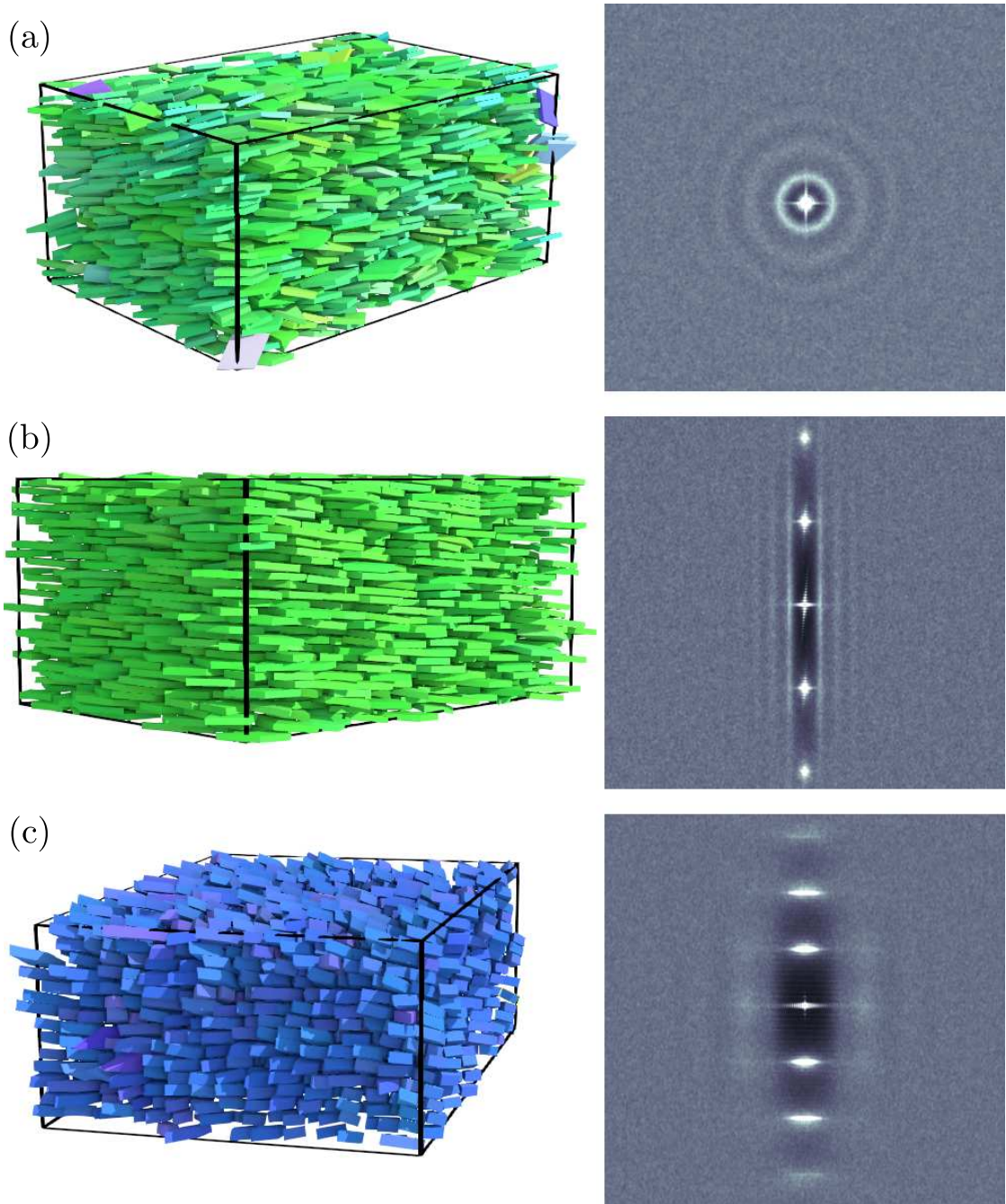


**Figure 6.5:** **Left:** Representative configurations of hard rhombic particles with reduced width  $\tilde{W} = 7$  and length  $\tilde{L} = 11$  for **(a)** a nematic phase at packing fraction  $\eta = 0.42$ , and **(b)** a smectic phase at packing fraction  $\eta = 0.52$ . **(c)** Representative configuration of hard rhombic particles with  $\tilde{W} = 2$  and  $\tilde{L} = 11$ , for a smectic biaxial  $Sm_b$  phase, at packing fraction  $\eta = 0.52$ . The particles in (a) and (b) are colored according to the orientation of their short axis,  $\hat{T}$ , while in (c) they are colored according to the orientation of their  $\hat{W}$  axis. **Right:** Diffraction patterns corresponding to the phases to the left, with (a) the vertical axis being along the  $\hat{L}$ -nematic director, and the horizontal axis along the  $\hat{W}$  director, and (b) and (c) the vertical axis being along the  $\hat{T}$ -nematic director, and the horizontal axis along the  $\hat{L}$  director.

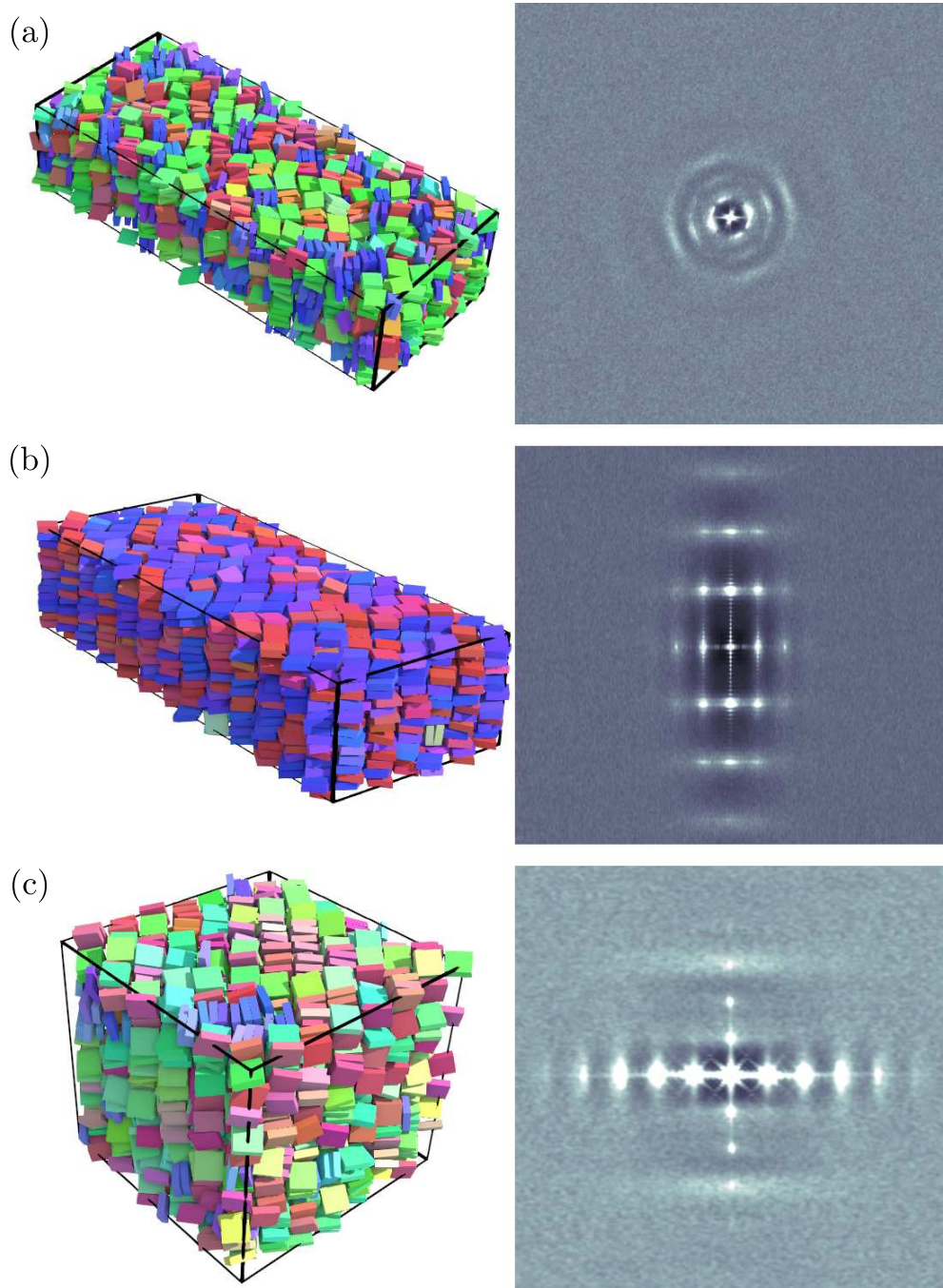


**Figure 6.6:** **Left:** Representative configurations of hard rhombic particles with  $\tilde{W} = 4$  and  $\tilde{L} = 5$ , for (a) a cubatic phase at packing fraction  $\eta = 0.52$ , and (b) for a plastic columnar  $C_4$  phase, at packing fraction  $\eta = 0.6$ . (c) Representative configurations of hard rhombic particles with  $\tilde{W} = 5$  and  $\tilde{L} = 5$ , for a smectic cubatic  $Sm_{Cub}$  phase, at packing fraction  $\eta = 0.5$ . The particles in (a) and (c) are colored according to the orientation of their short axis,  $\hat{T}$ , while in (b) they are colored according to the orientation of their  $\hat{W}$  axis. **Right:** Diffraction patterns corresponding to the phases to the left, with (a) the vertical axis being along the  $\hat{L}$ -nematic director, and the horizontal axis along the  $\hat{W}$  director, (b) the vertical axis being along the  $\hat{W}$ -nematic director, and the horizontal axis along the  $\hat{T}$  director, and (c) the vertical axis being along the  $\hat{T}$ -nematic director, and the horizontal axis along the  $\hat{L}$  director.

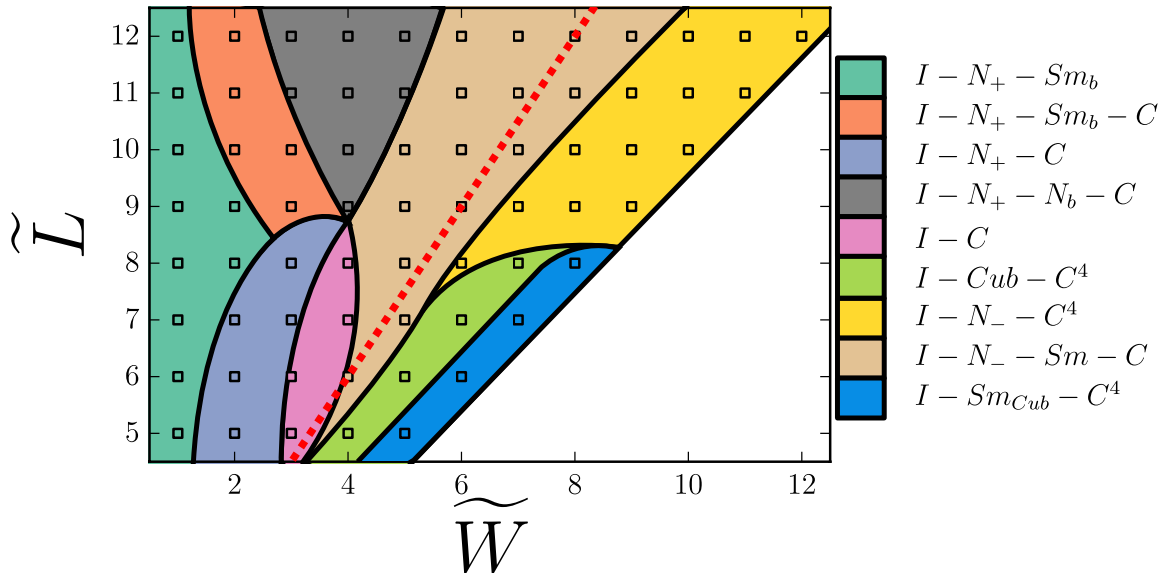


**Figure 6.7:** Phase diagram of rhombic particles, as a function of the particle shape parameters,  $\tilde{L}$  and  $\tilde{W}$ . Colored regions denote different phase sequences. The phase sequence corresponding to each color, is listed in the legend. The region boundaries are only guesstimates based on the sampled points, which are plotted as small squares. The red dashed line is the line of particle shapes with  $W/L = 2/3$  and for variable thickness  $T$ .

order. The coloring of the particle orientations clearly indicate the plastic nature of this phase. Stereographic projection of the particle orientations shows 4 peaks instead of a ring, indicating that the particles have two perpendicular preferred orientations. This can also be seen from the fact that there are two dominant colors present in figure 6.6(b), representing the two perpendicular directions. The cubic phase mentioned above, has been described as a parquet phase by John *et al.* [234] who studied hard perfect tetragonal parallelepipeds, and found a smectic phase with cubic-like intralayer ordering.

When  $L = W$ , the rhombic particles are equivalent to perfect tetragonal parallelepipeds with side-length  $\tilde{L}/\sqrt{2}$ . In this case, we find the same smectic phase as in Ref. [234], which is shown in figure 6.6(c), where the respective diffraction pattern clearly reveals the smectic ordering. Also note, that in this case, the  $C_4$  columnar phase becomes degenerate, as the two perpendicular orientations become equivalent. A  $I\text{-}Sm_{Cub}\text{-}C_4\text{-}X$  phase sequence is thus observed for rhombic particles with  $\tilde{L} = \tilde{W} = 5$ .

In certain cases where the ratio  $W/L$  is small enough, we find that prolate nematic  $N_+$  phase transition to a smectic phase with biaxial orientational order, which appears to be stable in only a small packing fraction range, even smaller than the smectic phase described above. A ‘snapshot’ of this phase is shown in figure 6.5(c) for particles with  $\tilde{W} = 2$  and  $\tilde{L} = 11$ . Due to the small range of stability of this phase, we were not able to pinpoint the exact phase boundaries. We thus find a  $I\text{-}N_+\text{-}Sm_b\text{-}C\text{-}X$  phase sequence for particles with  $\tilde{W} = 2$  and  $\tilde{L} = 11$ .

### 6.4.2 Phase Diagram

Following a similar procedure as above, we simulated and classified hard rhombic particles according to their phase sequences, as a function of their reduced width  $\tilde{W}$  and length  $\tilde{L}$ . In all cases, the particles crystallize at sufficiently high packing fractions. It is, thus, understood that all phase sequences end in the crystal,  $X$ , phase. We found 9 different phase sequences under which the different particle shapes are classified:  $I-N_+ Sm_b$ ,  $I-N_+ Sm_b-C$ ,  $I-N_+ -C$ ,  $I-N_+ -N_b -C$ ,  $I-C$ ,  $I-Cub-C^4$ ,  $I-Sm_{Cub}-C^4$ ,  $I-N_- -C^4$ ,  $I-N_- Sm-C$ . In figure 6.7, we summarize our results on the classification of the different particle shapes in a single phase sequence diagram, as a function of the particle shape parameters,  $\tilde{L}$  and  $\tilde{W}$ . Different colors are assigned to the various phase sequences listed above. The color coding is explained in the legend. Note that the boundaries of the different regions are estimates on the basis of the sample points which are depicted as small squares in the figure.

For comparison with the results of chapter 5 on rhombic platelets, we have also plotted a red dashed line corresponding to  $W/L = 2/3$ . We see that the results of that chapter are nicely confirmed here; at small values of  $L$  and  $W$ , i.e. for thick particles, we only find an isotropic to columnar,  $I-C$ , phase transition. For thinner particles, i.e. increasing  $\tilde{L}$  and  $\tilde{W}$ , the red line goes into the brown region, where we find a  $I-N_- Sm-C$  phase sequence.

Focusing on the grey region where a biaxial phase is observed in the phase diagram in figure 6.7, we see that the critical point lies at  $(\tilde{W}, \tilde{L}) \approx (4, 9)$ . Theoretical models of biaxial particles predict a critical point at  $W \approx \sqrt{LT}$ , or  $\nu = T/W - W/L \approx 0$  [215, 218]. The critical point we find for the rhombic particles, corresponds to  $\nu = -0.194$ , which deviates significantly from the predicted value. Simulations by Peroukidis *et al.* [197, 229] on hard spheroplatelets, exhibit, instead, a critical point at  $(w^*, l^*) \approx (3, 9)$ , which corresponds to  $\nu = 0$ , as predicted. Here,  $w^*$  and  $l^*$  are the reduced lengths of the spheroplatelet sides. Note, however, that in the limit where  $L = W$ , our  $L$  and  $W$  are equal to the length of the diagonal of square parallelepipeds, and thus a different choice of the particle size parameters could lead to a value of  $\nu$  closer to the one predicted. From the phase diagram we also see that the two nematic phases,  $N_+$  and  $N_-$ , are separated by the line at constant width,  $\tilde{W} \approx 4$ , which passes through the critical point of the biaxial region. A mysterious feature of the phase diagram, though, is the fact that the biaxial smectic phase,  $Sm_b$ , lies in the  $\tilde{W} < 4$  region.

It is interesting to further compare our results with the results of Peroukidis *et al.* [197, 229] for the spheroplatelets (or equivalently rounded parallelepipeds). Preliminary results by Dussi *et al.* [212] seem to suggest that ‘roundness’ increases the packing fraction range within which a stable biaxial phase is found. The rhombic particles we simulated here possess sharp edges, and indeed we find that the stable packing fraction range for the biaxial nematic phase is rather small. On the contrary, the region of biaxiality found by Peroukidis *et al.*, seems to cover a much smaller shape parameter regime than in our case. We speculate that the reason behind this is that the smectic phase is destabilized for these sharp-angled rhombic particles, allowing for a wider biaxial nematic region in the shape parameter space.

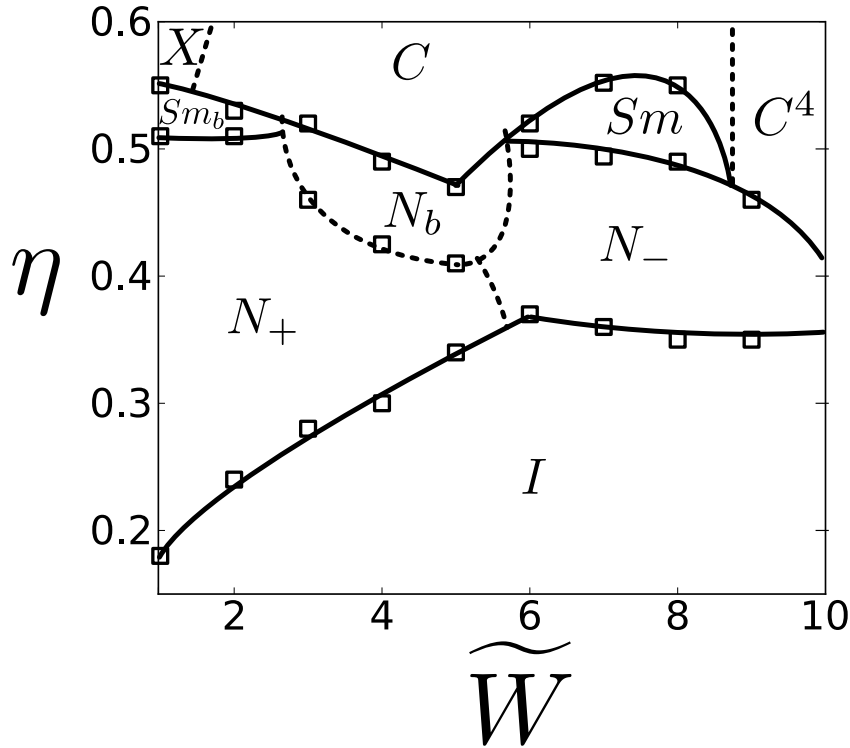


**Figure 6.8:** Slice of the phase diagram in figure 6.7 at  $\tilde{L} = 11$ , showing points of the approximate packing fractions at which the particles transition between different phases, for  $1 \leq \tilde{W} \leq 9$ . Solid lines represent the approximate location of first-order phase transitions. Dashed lines are used to represent continuous transitions, such as the transition between the different nematic phases. The different regions are labeled by their respective phase symbol.

#### 6.4.3 Phase Behavior as a Function of the Particle Width

To understand the transition of rhombic particles from oblate to a prolate alignment, we take a slice of the phase sequence diagram in figure 6.7 at  $\tilde{L} = 11$ . In figure 6.8 we plot points of the approximate packing fractions at which the particles transition between different phases, for  $1 \leq \tilde{W} \leq 9$ . In the state diagram of figure 6.8, we have drawn solid lines, to represent the approximate location of the first-order phase transitions. Dashed lines are used to represent continuous transitions, such as the transition between the different nematic phases. The topology of the state diagram, seems to suggest that for  $\tilde{W} \approx 5.5$ , the system might transition from a prolate nematic phase,  $N_+$ , to an oblate nematic phase,  $N_-$ , before reaching the biaxial nematic phase,  $N_b$ . This scenario has also been found for hard spheroplatelets [197, 229] and parallelepipeds [212]. It is also interesting to note that the prolate nematic phase,  $N_+$ , is significantly wider than the oblate nematic phase  $N_-$ , where the isotropic phase extends up to packing fractions of  $\eta \approx 0.35$ . Another interesting feature, is the disappearance of the smectic phase, and the appearance of the plastic columnar phase,  $C^4$ , at  $\tilde{W} \approx 8.5$ . In chapter 5, we speculated that the smectic phase was stabilized by the entropy gain that arises from the rotational degrees of freedom that are freed-up. Particles with  $L \approx W$  should gain less orientational entropy, than less symmetric ones. Finally, we clearly observe from figure 6.8, that the

two smectic phases are stable in a narrow packing fraction range.

## 6.5 Conclusion

We developed an efficient EDMD algorithm, which is based on the conservative advancement algorithm, with an improved conservative bound, in combination with the GJK distance algorithm [204], in order to perform simulations of hard convex particles. We also adapted the nearest-neighbor algorithm by Donev *et al.* [239, 240] for general convex shapes, using a box-shaped bounding neighborhood. We find that the algorithm allows us to simulate hard-particle systems very efficiently.

Motivated by the study of Peroukidis *et al.* [197, 229] on biaxial phases of hard spheroplatelets, we used the developed EDMD algorithms to investigate the stability of a biaxial phase in rhombic particles. The possibility of forming such a phase was first hinted in chapter 5, where rhombic platelets with large aspect ratios seemed to form a biaxial nematic phase. The efficiency of our EDMD algorithm allowed us to investigate the phase behavior of 68 different particle shapes, parametrized by the reduced width,  $\tilde{W}$  and length  $\tilde{L}$ , thus mapping the whole phase sequence diagram of rhombic particles with  $T \leq W \leq L$ . The different phases were identified using a combination of order parameters, equations of state, diffraction patterns, and visual inspection of the equilibrated particle configurations.

From the above analysis, we find that the rhombic particles exhibit up to 9 different phase sequences, depending on the particle shape. The 9 sequences we find are the following,  $I-N_+ Sm_b$ ,  $I-N_+ Sm_b-C$ ,  $I-N_+ C$ ,  $I-N_+ N_b-C$ ,  $I-C$ ,  $I-Cub-C^4$ ,  $I-Sm_{Cub}-C^4$ ,  $I-N_- C^4$ ,  $I-N_- Sm-C$ . The biaxial nematic phase has a lower critical point at  $(\tilde{W}, \tilde{L}) \approx (4, 9)$  which corresponds to  $\nu = -0.194$ . This deviates significantly from the predicted value of  $\nu = 0$ , although the exact definition of the three particle dimensions can greatly affect the value of the parameter,  $\nu$ . Additionally, we find, for the first time in computer simulations, a biaxial smectic phase,  $Sm_b$ , but remarkably, it is not present within the region where the biaxial nematic phase is stable. For plate-like particles, we suggested that the smectic phase is formed due to a gain in rotational entropy. In the case of the  $Sm_b$  phase, we think that the reason is a gain in ‘sliding’ entropy, i.e. the particles can slide more easily with respect to each other. The region of stability of the  $Sm_b$  phase is quite small and further simulations are needed to undeniably determine its stability. In the case of the spheroplatelets, a smectic-A phase is present. In order to form a smectic-A phase in the case of rhombic particles, the smectic layers should be formed perpendicular to the long,  $\hat{L}$ , axis, which would be highly unfavourable due to their sharp-angled shape. Comparing our results further with the results of Peroukidis *et al.* [197, 229], we find that the stable packing fraction range for the biaxial nematic phase is rather small. However, the region of biaxiality found by Peroukidis *et al.*, seems to cover a much smaller area than in our case. In addition, we plot in figure 6.8, the phase diagram for hard rhombic particles with  $\tilde{L}$ , in the packing fraction,  $\eta$ , reduced width,  $\tilde{W}$  representation, i.e. a slice of the phase sequence diagram of figure 6.7, at  $\tilde{L} = 11$ . We find that the tiny biaxial nematic region in between the prolate,  $N_+$ , and oblate,  $N_-$ , nematic phases, seems to be stabilized by the destabilization of the two smectic phases,  $Sm_b$  and  $Sm$ , at  $\tilde{W} \approx 2.5$  and  $\tilde{W} \approx 6$ ,

respectively. Preliminary results by Dussi *et al.* [212] on brick-like particles, show that the biaxial nematic phase is formed only for much higher particle aspect ratios. Previous simulation studies on hard uniaxial platelets [184] showed that the isotropic-to-columnar phase transition shifts to higher packing fractions by introducing some degree of particle roundness. If this argument is applied to the case of spheroplatelets, we expect that the roundness of the particle may increase the packing fraction range where the biaxial nematic phase is stable. Our results for rhombic particles with  $\tilde{L} = \tilde{W}$  agree well with the results by John *et al.* on hard perfect tetragonal parallelepipeds [234], where e.g. a smectic phase with cubatic intralayer orientational ordering is found. Moving to slightly asymmetric rhombic particles,  $\tilde{L} \approx \tilde{W}$ , we find that the  $Sm_{Cub}$  phase is replaced by the cubatic phase with short- to medium-ranged positional order.



## Spherical Confinement of Hard Convex-Shaped Particles

---

We investigate the behavior of two model systems of hard particles under spherical confinement, using Monte Carlo simulations, motivated by experiments on nanoparticles confined in emulsion droplets. The first system consists of hard cubic particles. From compression runs, we find that the surface layer crystallizes at a slower rate, while for big system sizes, the surface layers start crystallizing before the interior. We also find fluid-like regions between the surface layers and the interior, organized on the vertices of a cube. Lastly, we find a large number of differently oriented crystalline clusters, which might be indicative of the high vacancy concentration in the system. In the second system, we simulate round platelets (cylinders) with length-to-diameter ratio  $L/D = 1/2$  and discover a twisted columnar phase for system sizes  $N \geq 1005$ . We investigate the twist as a function of packing fraction,  $\eta$ , and system size,  $N$ .

## 7.1 Introduction

Many biological and colloidal systems consist of mesoscopic particles that are confined in space. Examples are, membrane proteins confined in a lipid membrane, or actin filaments confined in a biological cell [251]. Such systems have been studied extensively, due to the vast range of phenomena that are induced due to the confinement. A prime example of confinement-induced effects is the critical Casimir effect studied in chapters 2 and 3. In simple fluids (composed of small, neutral molecules) and well-characterized materials, the introduction of wall interactions, and the competition between fluid-wall and fluid-fluid forces, can lead to interesting surface-induced phase transitions. These include new types of phase transitions not found in the bulk, such as, layering, wetting transitions, as well as changes in the bulk phase behavior (of e.g. freezing, gas-liquid, liquid-liquid) [252]. The addition of salt in such fluids can even make like-charge colloids attract [253, 254]. In block copolymers, confinement has been found to induce a range of novel morphologies [255]. Hard particle models have also been studied under confinement, finding similar effects, such as e.g. the existence of different layered solid phases in hard spheres confined between parallel hard plates [134, 256] and a reentrant freezing of a two-dimensional colloidal crystal [257].

Confinement of liquid crystals in droplets can have interesting applications, due to their liquid-like behavior and crystal-like optical properties. In 1925, Zocher reported the observation, of small birefringent domains in colloidal suspensions of vanadium pentoxide, by polarized light microscopy [258]. He called these domains *tactoids* from the Greek “to assemble”, and correctly inferred that they must be made of small rod-like particles aligned in the same direction. If an isotropic suspension of nematogens is brought under conditions where it coexists with a nematic liquid-crystalline phase, the shape of the formed nematic tactoids resembles a spindle-like shape due to the anisotropy of the surface tension of the isotropic-nematic interface [258–267]. In 1985, it was surprisingly demonstrated by Williams [268], using theory, that the director field in spherical bipolar tactoids of achiral nematogens, exhibited a parity breaking transition to a twisted configuration. In figure 7.1 we show a schematic representation of the director field on the surface of a spherical bipolar tactoid. Prinsen *et al.* [269] extended this study to non-spherical and non-bipolar tactoids, finding that if the bend and twist elastic constants are small enough in comparison to the splay elastic constant, the twisted (parity-broken) structure is energetically more favourable. Prinsen *et al.* also found that the transition to a twisted structure happens sharply at some critical volume. This twisting was experimentally detected for thermotropic liquid crystals already in 1968, by Williams [270] and in several other studies thereafter [271–273]. A twisted structure was detected in lyotropic liquid crystals only recently [274–277].

In this chapter, we investigate the behavior of hard cubes and hard cylinders under spherical confinement. Our study is motivated by experiments, on cubic  $\text{Fe}_3\text{O}_4$  nanoparticles and  $\text{EuF}_3$  nanoplates confined in emulsion droplets. In these experiments, the nanoparticles are dispersed in a suitable (apolar) solvent. This dispersion is emulsified into an oil-in-water emulsion, and subsequently, the oil phase is evaporated from the suspended emulsion droplets, causing the packing fraction of the nanoparticles in the droplets to increase slowly, which eventually leads to crystallization. De Nijs and Dussi

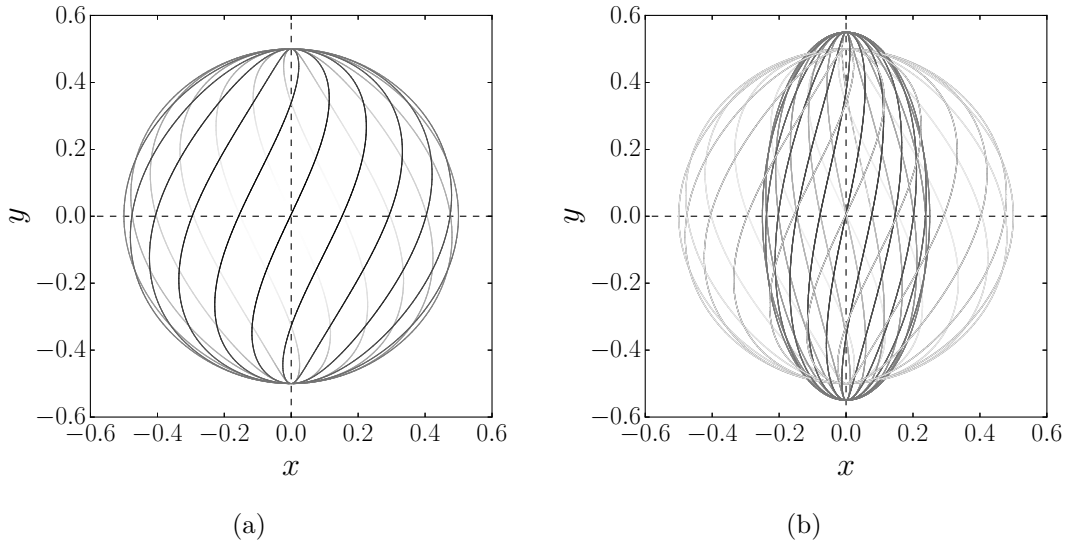


**Figure 7.1:** Plot of director field, generated using the equation of a helix with variable radius, equal to the radius of the spherical cap in the direction of the helix (eqs. (7.8-7.10)) **(a)**: Director field on the surface of a spherical bipolar tactoid with radius  $R = 1/2$ . **(b)**: Director field at a distance  $r = R/2$  from the center of the tactoid, modelled as a prolate ellipsoid with height  $2R' = 2.2R$ .

*et al.* had previously investigated the crystallization of hard spheres under spherical confinement, using emulsion droplets of cobalt iron oxide nanoparticles and core-shell silica colloids using, and also with event-driven molecular dynamics (EDMD) simulations [278]. In their study, they reported the formation of icosahedral clusters consisting of up to 100,000 particles, which are entropically favored over the bulk face-centered cubic crystal structure.

We investigate the crystallization of hard cubes under spherical confinement in the first part of this chapter. The phase behavior of hard cubes has been the subject of several recent simulation studies [279–282]. Jagla found that freely rotating cubes melt through a first-order transition, and subsequently, Agarwal and Escobedo found a first-order phase transition between a fluid and an ordered phase. Agarwal *et al.* [281] identified the ordered phase at coexistence as a cubatic phase, which is characterized by the presence of long-range orientational order along three perpendicular axes, but a lack of long-range positional order. In addition, the authors found appreciable diffusion in the ordered phase, which led them to the conclusion that the phase is a cubatic liquid crystal, instead of a crystal phase. However, the authors noted that the size of their simulations made it difficult to determine the extent of the positional order in their system. The work by Smallenburg *et al.*, later showed that the stable ordered phase is a simple cubic crystal phase that contains many vacancies (over two orders of magnitude larger than typically seen in colloidal systems). Hence, the diffusion as found by Agarwal *et al.* [281] is attributed to the vacancy diffusion in the vacancy-rich simple cubic crystal phase.

In the second part of this chapter, we investigate the effects of spherical confinement on hard round platelets, which are modeled as cylinders. Various models of round platelets

have been studied extensively, including hard ‘cut spheres’ [180, 182, 184], and hard oblate spherocylinders [183, 283]. In all cases, an oblate nematic and a columnar phase was found among the isotropic and crystal phases, while the cubatic phase was determined to be metastable with respect to the isotropic-columnar transition[184]. In the limit of infinitely thin platelets, it was shown that they transition from an isotropic to a nematic phase through a weakly first order transition [179], followed by a first-order transition to a columnar phase [181]. Unfortunately, hard cylinders were only studied in simulations by Blaak *et al.* [210], where it was found that cylinders with length-to-diameter ratio,  $L/D = 0.9$ , do not form a cubatic phase, but instead a plastic crystal-like phase was found in between the nematic and crystal phases. Nonetheless, the results for hard ‘cut spheres’ and oblate spherocylinders [180, 182–184, 283] are relevant for the study of hard cylinders.

As we mentioned, our study of the spherical confinement of hard cubes and cylinders is motivated by experiments on synthesized cubic  $\text{Fe}_3\text{O}_4$  nanoparticles and  $\text{EuF}_3$  nanoplatelets confined in emulsion droplets. Employing *NPT* Monte Carlo simulations we slowly compress a spherically confined system of hard cubes, and investigate the crystallization of different surface layers and the interior. Compression of hard cylinders with a width-to-diameter ratio of  $L/D = 0.5$ , which is close to the aspect ratio of the round platelets in the experiments, leads to confinement induced chiral symmetry breaking of the columnar, even though the platelets themselves are achiral. We investigate the behavior of the twisted tactoid further, by studying the twist angle as a function of the tactoid packing fraction, and the amount of confined cylinders.

In section 7.2 we introduce our two models, i.e. hard cubes and hard cylinders. In section 7.3, we describe our simulation techniques, including the method used to detect particle overlaps with a spherical boundary, and the algorithms involved in identifying crystalline clusters and particle surface layers in a spherically confined system of particles. Finally, we present our results on the spherical confinement of cubes and cylinders in section 7.4.

## 7.2 Models

Due to the high surface tension between the oil and water phase, we expect that the shape of emulsion droplets will not deviate significantly from a perfect sphere, and we thus model the interface between the two phases as a hard (impenetrable) spherical boundary.

The two hard-particle models studied in the current chapter are depicted in figure 7.2. We denote the length of the side of the cube as  $\sigma$ , as is shown in the figure. The support function for cubes,  $s(\hat{\mathbf{d}})$ , in the direction given by the unit vector  $\hat{\mathbf{d}}$ , can be calculated using the following expression,

$$s(\hat{\mathbf{d}}) = \frac{\sigma}{2} \text{sgn}(\hat{\mathbf{d}}). \quad (7.1)$$

Note that in the particular case of cubes (or rectangular parallelepipeds) using the separating-axis theorem algorithm [284] instead of GJK to detect overlaps might be slightly more efficient.

For the cylinders we denote the length, or height, of the cylinders as  $L$ , and its diameter,  $D$ , as shown in figure 7.2. The support function we use for cylinders with their main

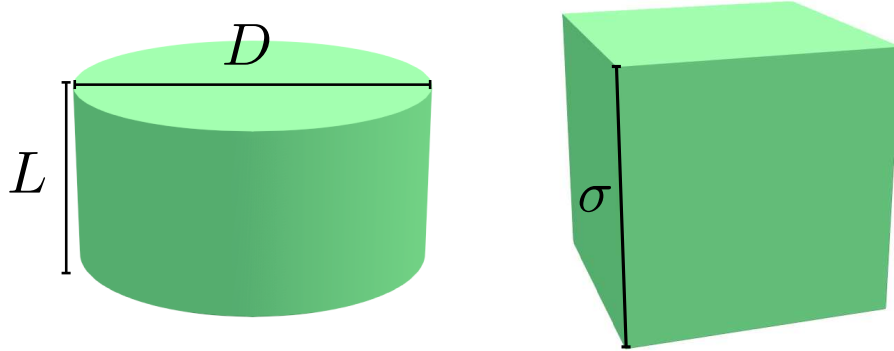


**Figure 7.2:** **Left:** Hard cylinder with length  $L$  and diameter  $D$ . **Right:** Hard cube of side length  $\sigma$ .

axis aligned along the unit vector,  $\hat{\mathbf{u}}$ , is given by,

$$s(\hat{\mathbf{d}}) = \begin{cases} \text{sgn}(\hat{\mathbf{d}} \cdot \hat{\mathbf{u}}) \frac{L}{2} \hat{\mathbf{u}} + \frac{D}{2} \frac{\mathbf{w}}{\|\mathbf{w}\|}, & \text{if } \mathbf{w} \neq 0 \\ \text{sgn}(\hat{\mathbf{d}} \cdot \hat{\mathbf{u}}) \frac{L}{2} \hat{\mathbf{u}}, & \text{otherwise} \end{cases} \quad (7.2)$$

where  $\mathbf{w} = \hat{\mathbf{d}} - (\hat{\mathbf{d}} \cdot \hat{\mathbf{u}})\hat{\mathbf{u}}$ , is the component  $\hat{\mathbf{d}}$  perpendicular to  $\hat{\mathbf{u}}$ .

## 7.3 Methods

We use Monte Carlo simulations, to simulate cubes and cylinders in the *NVT* and *NPT* ensembles. In addition to overlap checks when translating or rotating a particle, we need to check if the particle remains in the confines of the hard spherical boundary. This check is also performed when reducing the size of the spherical boundary during a volume change attempt. The algorithms used to detect particle overlaps with a spherical boundary are described below.

### 7.3.1 Detecting Particle Overlap with a Spherical Boundary

For simplicity, we assume that the spherical boundary of radius,  $R$ , lies at the origin. For a convex particle at position  $\mathbf{r}$ , we first check if its inscribed sphere of radius  $\rho_{\text{in}}$  lies completely outside the boundary, i.e.  $\mathbf{r}^2 \geq (R - \rho_{\text{in}})^2$ , if it does, the particle lies definitely on, or outside the spherical boundary. If, on the other hand, the circumscribed sphere with radius  $\rho_{\text{out}}$  lies completely inside the boundary,  $\mathbf{r}^2 < (R - \rho_{\text{out}})^2$ , then the particle lies definitely inside the spherical boundary. If none of the above checks hold we have to further check if the particle overlaps the boundary. For polyhedral-shaped particles, it suffices to check if any of its vertices,  $\mathbf{r}_i$ , lie outside the boundary, i.e.  $\mathbf{r}_i^2 \geq R^2$ . For cylinders and other convex particles, we could not come up with a general expression for the containment inside a spherical boundary. Instead, we use an approximate algorithm; we predefine a set of directions,  $\hat{\mathbf{d}}_i$ , and, using the support function, test the corresponding support points,  $\mathbf{r}_i = s(\hat{\mathbf{d}}'_i)$ , for containment, where  $\hat{\mathbf{d}}'_i$  is the direction  $\hat{\mathbf{d}}_i$  rotated to the particle's frame. In our simulations, we predefine a set of 26 different directions. For

cylinders, this means that they effectively behave as octagonal platelets with respect to the spherical boundary.

In retrospect, we can come up with an exact algorithm for cylinders, which we describe for future reference. At first, we determine the circular face that should be checked for intersection with the spherical boundary. Its position,  $\mathbf{r}$ , is given by,

$$\mathbf{r} = \mathbf{r}_0 + \frac{L}{2} \text{sgn}(\hat{\mathbf{u}} \cdot \mathbf{r}_0) \hat{\mathbf{u}} \quad (7.3)$$

where  $\mathbf{r}_0$  is the position of the cylinder, and  $\hat{\mathbf{u}}$  is the unit vector along the main axis of the cylinder. We then simply check if the circle at  $\mathbf{r}$  is contained in the circle created by the intersection of a plane with normal  $\hat{\mathbf{u}}$  and containing the point  $\mathbf{r}$ , with the spherical boundary. The center of the circular section is given by,  $\mathbf{c} = (\hat{\mathbf{u}} \cdot \mathbf{r}) \hat{\mathbf{u}}$  and its radius by  $\rho = \sqrt{R^2 - (\mathbf{r} \cdot \hat{\mathbf{u}})^2}$ , so that finally  $\|\mathbf{r} - \mathbf{c}\|^2 < (\rho - D/2)^2$  should hold for the cylinder to be contained inside the boundary.

### 7.3.2 Monte Carlo Stack Rotation Move

To speed up the equilibration of Monte Carlo simulations of round platelets, we implement a Monte Carlo move that is designed to rotate short stacks [184, 210]. We select a particle,  $i$ , randomly and define a stack, by the particles,  $j$ , with a center-to-center distance,  $\|\mathbf{r}_j - \mathbf{r}_i\| < D/2$ . We subsequently generate a random vector in the plane perpendicular to the main axis of particle  $i$ , and rotate the stack around this axis by  $\pi/2$ . Finally, the move is accepted if no overlaps are generated, and rejected otherwise. This move can easily be seen to obey detailed balance. Furthermore, the simulation is ergodic since regular rotation and translation moves are also performed. Although the acceptance ratio of these moves is tiny ( $\sim 10^{-6}$ ), the small number of moves that are accepted during the simulation do significantly speed up the equilibration. We perform this move once every 10 Monte Carlo cycles.

### 7.3.3 Cluster and Surface Layer Identification

To identify crystalline clusters in our simulated configurations, we follow the same procedure as in Ref. [285]. We first calculate the bond orientational order parameter,  $q_{lm}$  for each particle,  $i$ ,

$$q_{lm}(i) = \frac{1}{N_b(i)} \sum_{j=1}^{N_b(i)} Y_{lm}(\mathbf{r}_{ij}), \quad (7.4)$$

over the  $N_b(i)$  neighbors that are found within a cutoff distance,  $r_c$ , from particle  $i$ . Here,  $Y_{lm}(\mathbf{r}_{ij})$  are the spherical harmonics, with  $m \in [-l, l]$ , and  $\mathbf{r}_{ij} = \mathbf{r}_j - \mathbf{r}_i$  is the relative position of particles  $i$  and  $j$ . Subsequently, the correlation between two neighboring particles,  $i$  and  $j$ , is calculated using the following expression,

$$d_l(i, j) = \frac{\sum_{m=-l}^l q_{lm}(i) \bar{q}_{lm}(j)}{\left( \sum_{m=-l}^l |q_{lm}(i)|^2 \right)^{1/2} \left( \sum_{m=-l}^l |q_{lm}(j)|^2 \right)^{1/2}}, \quad (7.5)$$

and solid particles are then defined as those having more than  $n_c$  neighbors for which  $d_l(i, j) > d_c$ . The crystalline clusters are built from the list of solid particles using the cluster algorithm 5.1, where the condition becomes  $d_l(n, j) > d'_c$ , for some  $d'_c > d_c$ , and where  $n$  is the first particle added to the cluster, and  $j$  is the candidate particle.

For identifying columns of round platelets, we use algorithm 5.1 again, with the condition  $\|\mathbf{r}_{ij} - (\hat{\mathbf{u}}_i \cdot \mathbf{r}_{ij})\hat{\mathbf{u}}_i\| < D/2$ , i.e. that their distance projected on the plane perpendicular to the orientation,  $\hat{\mathbf{u}}_i$ , of particle  $i$  is smaller than  $D/2$ . The neighbors of a particle,  $i$ , are defined as those within a distance  $D$ .

Furthermore, in our analysis, we identify different surface layers. Unfortunately, there is no unique way to identify a concave hull of a set of points. The authors of Ref. [278], used a so-called cone algorithm [286], where for a given particle, its associated cone region is defined as the region inside a cone of a certain side length and angle, whose apex resides on the particle. A hollow cone is a cone region with no other particles inside it. A particle is identified as being on the surface if at least one associated hollow cone exists. Here, we instead use the concept of the  $\alpha$ -shape [287], which is a generalization of the convex hull. As mentioned in Edelsbrunner's and Mücke's paper [288], one can intuitively think of an  $\alpha$ -shape as the following. Imagine a huge mass of ice-cream making up the space and containing the points as 'hard' chocolate pieces. Using a sphere-shaped ice-cream spoon with radius  $\alpha$  we carve out all parts of the ice-cream block we can reach without bumping into chocolate pieces, thereby even carving out holes in the inside (e.g. parts not reachable by simply moving the spoon from the outside). The algorithm itself, is quite complex to implement. Instead, we use the computational geometry algorithms library, CGAL [289] for the  $\alpha$ -shape algorithm. Different surface layers can be identified by applying the algorithm repeatedly to the set of points left after removing the surface points.

### 7.3.4 Calculating the Twist

In twisted tactoids of round platelets, the director field is defined by the tangent of the curve passing through the center of mass of the particles in a column. Given such a curve with coordinates  $\mathbf{r}(t)$ , parameterized by  $t \in [-1, 1]$ , i.e. the normalized position along the nematic director,  $\hat{\mathbf{n}}$ , we determine the degree of twist in configurations of round platelets by calculating the slope of the director field with the meridian at  $t = 0$ ,

$$\chi(r) = \frac{1}{\|\mathbf{r}(0)\|} \left. \frac{\partial [(\hat{\mathbf{n}} \times \mathbf{r}(0)) \cdot \mathbf{r}(t)] / \partial t}{\partial [\hat{\mathbf{n}} \cdot \mathbf{r}(t)] / \partial t} \right|_{t=0}, \quad (7.6)$$

where  $r = \|\mathbf{r}(0)\|$ .

In implementing the above analysis, we first identify individual columns in a configuration, as described in the previous section, and the nematic director,  $\hat{\mathbf{n}}$ . We subsequently calculate the column's center of mass,  $\mathbf{r}_{cm}$ , and approximate  $\mathbf{r}(0) \approx \mathbf{r}_{cm} - (\hat{\mathbf{n}} \cdot \mathbf{r}_{cm})\hat{\mathbf{n}}$ , i.e. the projection of  $\mathbf{r}_{cm}$  on the plane defined by  $\hat{\mathbf{n}}$ , and fit a straight line through the centroids of the column's particles, to get its 'tangent' at the position of the center of mass,  $\hat{\mathbf{d}}$ . The slope with the meridian is then calculated from the expression below,

$$\chi(r) = \frac{1}{\|\mathbf{r}(0)\|} \frac{(\hat{\mathbf{n}} \times \mathbf{r}(0)) \cdot \hat{\mathbf{d}}}{\hat{\mathbf{n}} \cdot \hat{\mathbf{d}}}. \quad (7.7)$$

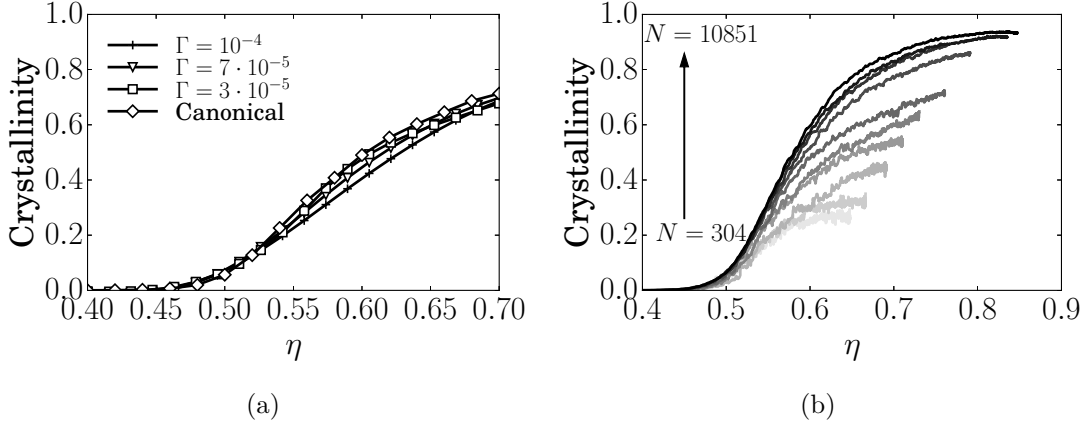


**Figure 7.3:** (a): Fraction of crystalline particles as a function of the packing fraction,  $\eta$ , for a system of  $N = 1911$  hard cubes in spherical confinement, using different compression rates,  $\Gamma$ , as obtained from MC simulations. For comparison, we also plot the crystallinity as obtained from MC simulations in the  $NVT$  ensemble. The compression plots are smoothed-out using a 3rd order B-spline interpolation. (b): Fraction of crystalline particles as a function of the packing fraction,  $\eta$ , for a system of  $N \in \{304, 437, 624, 751, 1016, 1911, 3839, 5904, 7664, 10851\}$  cubes in spherical confinement, using a compression rate  $\Gamma = 3 \cdot 10^{-5}$ . The data, here, have been smoothed-out using a Savitzky-Golay filter.

## 7.4 Results

### 7.4.1 Crystallization of Hard Cubes Under Spherical Confinement

We perform Monte Carlo simulations of hard cubes in spherical confinement in the  $NPT$  ensemble. We compress the system by exponentially incrementing the system pressure,  $\beta P \sigma^3$ , at a rate  $\Gamma$ , starting from some pressure  $\beta P_0 \sigma^3$ , so that the pressure after  $t$  MC steps have elapsed, is given by  $\beta P \sigma^3 = \beta P_0 \sigma^3 (1 + \Gamma)^t$ .

We need to determine a sufficiently slow compression rate, such that jamming and defects in the resulting crystalline structure is avoided. To this end, we performed compression runs of  $N = 1911$  hard cubes for different compression rates, and measured the fraction of crystalline particles in the system, using the cluster criterion in section 7.3.3, where we set the cutoff distance,  $r_c$  to the first minimum of the radial distribution function,  $g(r)$ ,  $r_c = 1.4$ , the symmetry index,  $l = 4$ , the threshold value for the minimum number of neighbours,  $n_c = 5$ , and the minimum threshold value for a solid bond,  $d_c = 0.6$ , and addition to a cluster,  $d'_c = 0.9$ . In addition, we performed simulations in the  $NVT$  ensemble for various packing fractions, to determine the equilibrium crystallinity — since we are expanding from a dense configuration, some degree of hysteresis could be present. In figure 7.3(a), we plot the degree of crystallinity of the system for  $\Gamma = 10^{-4}$ ,  $7 \cdot 10^{-5}$ , and  $3 \cdot 10^{-5}$ , along with the results from the canonical ( $NVT$ ) simulations. Note that the curves for the compression runs have been smoothed out using a 3rd order B-spline. Hard cubes are known to show coexistence between the cubic crystal phase and the

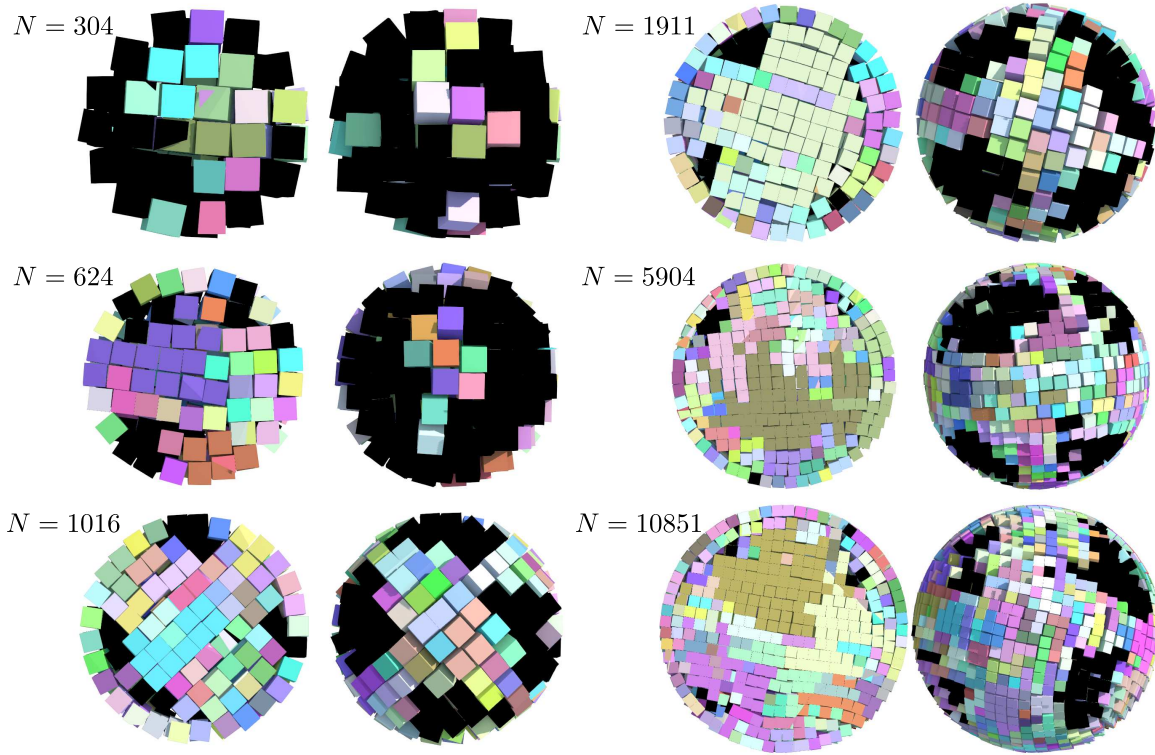


**Figure 7.4:** Final configurations of compression runs for different system sizes,  $N$ . The left figure of each pair, shows a cut through the middle. Particles are colored according to the cluster they belong to. Fluid-like particles are colored black.

isotropic phase for packing fractions  $\eta \in [0.45, 0.5]$ . From the figure, we see that indeed, crystallization is initiated at  $\eta \approx 0.45$ , but reaches 50% crystallinity only at a packing fraction,  $\eta \approx 0.6$ , due to the effects of confinement. We also note that with the exception of  $\Gamma = 10^{-4}$ , the crystallinity for the other compression rates are quite close to the equilibrium value. This is also confirmed from visual inspection of the final configurations, which show larger crystalline domains, i.e. with less defects.

For the remainder of our simulations, we choose a compression rate  $\Gamma = 3 \cdot 10^{-5}$ . Additionally, we perform compression runs for different system sizes, of  $N \in [304, 10851]$  particles. In figure 7.3(b), we plot the fraction of crystalline particles for systems of  $N \in [304, 10851]$  particles, as a function of the packing fraction. The plots have been smoothed-out with a Savitzky-Golay filter [290], to remove the large noise of the smaller system sizes. We notice that up to  $\eta \approx 0.5$ , there are no significant differences in the crystallinity between the different system sizes. The system size appears to also play an increasingly less significant role on the crystallinity, indicating that the bulk limit is already approached for  $N > 5904$ , where the crystallinity reaches 95%, although confinement could play an important role on the presence of vacancies, and should be further studied.

We now focus on the formation of crystalline clusters. In figure 7.4 we present snapshots of the final configuration of the compression runs, for different system sizes,  $N \in [304, 10851]$ . In the figure, we have colored particles according to the cluster they belong to. Fluid-like particles are colored black. The first thing we observe, is that in all

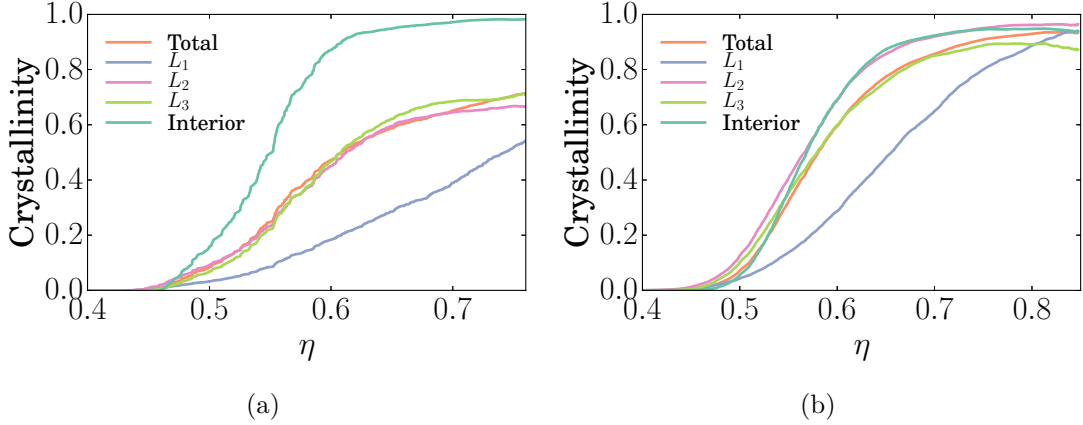


**Figure 7.5:** Fraction of crystalline particles as a function of packing fraction,  $\eta$ , for the whole system, the three first surface layers, and the interior of a spherically confined system consisting of (a):  $N = 1911$  particles, and (b):  $N = 10851$  particles. The data, has been smoothed-out using a Savitzky-Golay filter.

cases, we find a large number of differently oriented crystalline clusters, indicating that there are many defects in the crystal structure. This could also be caused by the high vacancy concentration. From visual inspection of the configurations, we find that the cubic layers in the crystal twist with respect to each other, for system sizes as small as  $N = 751$  particles, which could also potentially contribute to the observation of a large number of clusters. Another significant feature, is that for  $N \geq 1016$ , we find clusters of fluid-like particles, which are organized on the vertices of a cube. These regions of the spherically confined system have the highest frustration because they are not compatible with the orientation of the crystal structure.

To further get a grasp on the way the spherically confined system of hard cubes crystallizes, we plot the fraction of crystalline particles as a function of packing fraction,  $\eta$ , for the whole system, the three first surface layers, and the interior of a spherically confined system consisting of  $N = 1911$ , and  $N = 10851$  particles, in figure 7.5. In figure 7.5(a), we see for  $N = 1911$  particles, that the interior crystallizes at a faster rate compared to the surface layers. Here, the outermost surface layer,  $L_1$ , is the least crystalline, while the second and third layers,  $L_2$ , and  $L_3$ , have about the same crystallinity. The crystallinity of the surface layers, here, is lower due to the fluid-like patches described above. For  $N = 10851$ , we observe a significantly different picture; the surface layers now crystallize with a rate close to that of the interior, with layers  $L_2$ , and  $L_3$ , even starting to crystallize earlier than the interior, in the region  $\eta < 0.55$ . The outermost surface layer also shows a much higher crystal fraction, as the effects of sphere's curvature are less pronounced. Curiously, the third surface layer, as well as the interior, exhibit a maximum at  $\eta \approx 0.74$ , and decrease slightly for large packing fractions. This subtle effect was also seen in Ref. [212], for hard spheres, although it was not discussed.

Finally, we compare the structure of our configurations to Scanning Electron Microscope (SEM) images of so-called ‘supraparticles’ of synthesized  $\text{Fe}_3\text{O}_4$  cubic nanoparticles, in figure 7.6, where for comparison, we show the final configuration of  $N = 3839$  hard

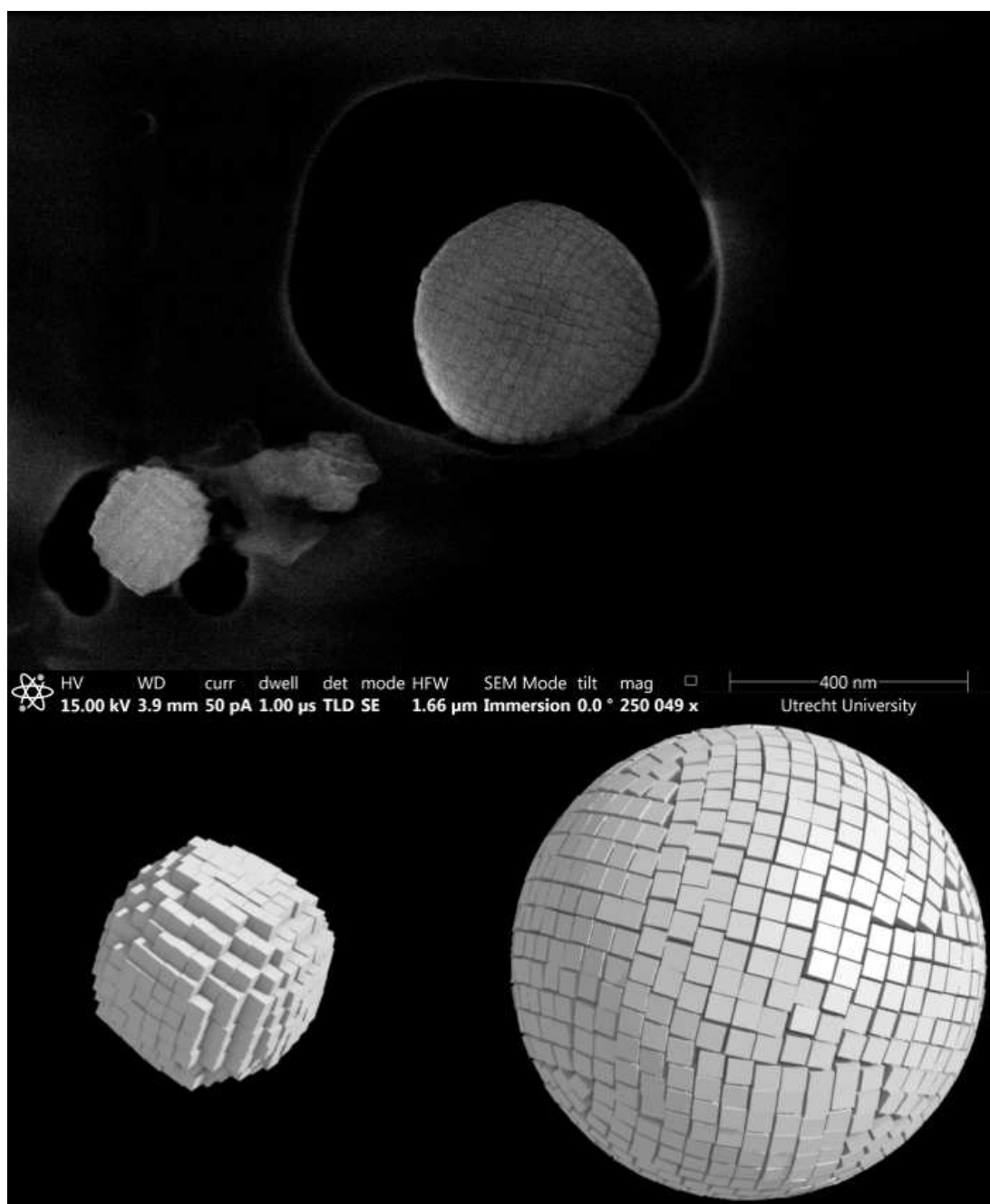


**Figure 7.6:** **Top:** Scanning electron microscopy (SEM) image of supraparticles of synthesized  $\text{Fe}_3\text{O}_4$  cubic nanoparticles. **Bottom:** Final configuration of  $N = 3839$  hard cubes, as obtained from MC simulations in spherical confinement, with the left image showing the inner core of the system, after removing the surface layers.

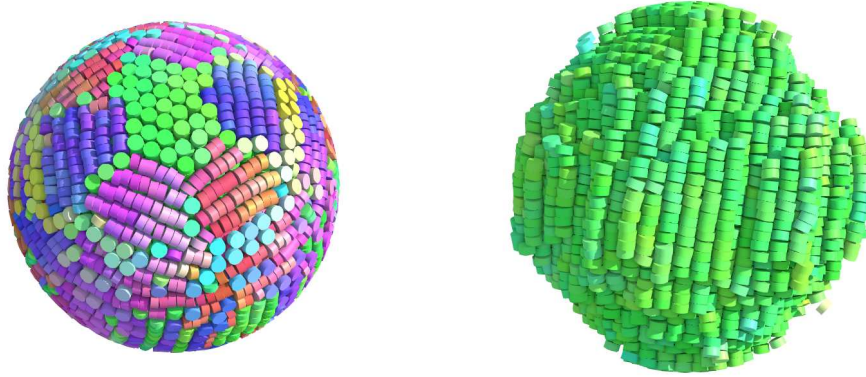


**Figure 7.7:** **Left:** Typical configuration of  $N = 10656$  round platelets in spherical confinement, at a packing  $\eta = 0.65$ , obtained from MC simulations. **Right:** The same configuration showing only the columns consisting of particles with orientation close to the nematic director.

cubes, which is close to the number of cubes in the supraparticle. The  $\text{Fe}_3\text{O}_4$  nanocubes have an edge length of  $\sigma = 22$  nm, and were prepared by thermal decomposition of iron (III) oleate, by modifying previous literature methods [291]. The resemblance of the structures is striking. Moreover, in experiments, there is evidence that the surface layers of the supraparticle get easily detached. In our simulations, we observed 8 fluid-like clusters between the interior and the surface layer(s), which could reduce the contact between the surface layers and the interior, leading to a weaker binding and perhaps detachment (in an experimental setup).

#### 7.4.2 Chiral Twist in Spherically Confined Hard Round Platelets

We next investigate the spherical confinement of hard round platelets of length-to-diameter ratio  $L/D = 0.5$ . We first expand a system consisting of  $N = 10656$  cylinders, and equilibrate it at different pressures. We find a discontinuity in the equation of state at packing fractions  $\eta \in (0.52, 0.56)$ , where the system transitions from an isotropic to a columnar phase. We also perform a compression run from the dilute isotropic fluid phase, consisting of  $N = 2581$  particles, and find that indeed the system transitions to a columnar phase.

In figure 7.7, we show snapshots of a configuration consisting of  $N = 10656$  round platelets, at a packing  $\eta = 0.65$ . The columns at the surface are organized in hexagonal patches close to where the ‘bulk’ hexagonally ordered columns meet the boundary surface. From our simulations, we find that the columnar phase shows a chiral twist, which can be observed in figure 7.7 (**Right**), where only the columns consisting of particles with orientation close to the nematic director are visible.

To further support the claim that we indeed see a twist in our system, we apply the analysis introduced in section 7.3.4, to calculate the ‘direction’ of each column,  $\hat{\mathbf{d}}(r)$ , for the configuration presented in figure 7.7. In figure 7.8(a), we plot the director field, projected on the plane perpendicular to the nematic director. From this figure, we can clearly see that the director field shows a left-handed chiral twist. Notice also the hexagonal shape of the columnar cluster. In figure 7.8(b), we plot the twist  $\chi(r)$ , as a function of the reduced distance,  $r/R$ , where  $R$  is the radius of the spherical boundary. The twist,

$\chi(r)$ , shows linear behavior, as can be seen by the linear fit.

To make sense of this linear behavior of  $\chi(r)$ , we build an ‘empirical’ model, based on our observations. We model the director field line, at center of mass coordinates  $(r, \theta)$  (in polar coordinates), inside a twisted tactoid of radius  $R$ , as a helix whose radius follows the surface of a prolate ellipsoid with radius  $r$  and height  $2R'$ , consisting of  $k$  coils (within the confines of the ellipsoid). An example of this, for  $r = R/2$ , is shown in figure 7.1(b), where we also draw the director field lines at the boundary. The parametric equations for a right-handed director field are presented below,

$$x(t) = r\sqrt{1-t^2} \sin(\pi kt + \theta) \quad (7.8)$$

$$y(t) = R't \quad (7.9)$$

$$z(t) = r\sqrt{1-t^2} \cos(\pi kt + \theta) \quad (7.10)$$

with  $t \in [-1, 1]$ , so that the position of the director field line as a function of the variable  $t$ , is given by  $\mathbf{r}(t) = [x(t), y(t), z(t)]^T$ . The projection of the line on the plane perpendicular to the vector  $\mathbf{r}(0)$ , i.e. on the plane spanned by the vectors  $\hat{\mathbf{e}}_u = [z(0)/r, 0, -x(0)/r]^T$  and  $\hat{\mathbf{e}}_w = [0, 1, 0]^T$ , is given by,

$$u(t) = r\sqrt{1-t^2} [\cos(\theta) \sin(\pi kt + \theta) - \sin(\theta) \cos(\pi kt + \theta)] \quad (7.11)$$

$$w(t) = R't \quad (7.12)$$

The tangent of this projected line is,

$$\frac{\partial u(t)}{\partial t} = 2\pi rk\sqrt{1-t^2} \cos(\pi kt) \quad (7.13)$$

$$\frac{\partial w(t)}{\partial t} = R' \quad (7.14)$$

Setting  $t = 0$ , we get,

$$\chi(r) = \left. \frac{\partial u(t)/\partial t}{\partial w(t)/\partial t} \right|_{t=0} = \frac{2\pi kr}{R'}, \quad (7.15)$$

which reproduces the behavior we observed in figure 7.8(b). We unfortunately need information on the curvature of the columns,  $R'$  to calculate the number of twists,  $k$  in eq. (7.15). We can calculate the maximum angle of the director field with a meridian at the surface of the tactoid, as  $\alpha = \arctan[\chi(R)]$ .

Having established the presence of a twisted phase, and a model describing its geometry, we further investigate the dependence of the twist on the packing fraction of the system. To this end, we perform MC simulations of  $N = 10656$  platelets in the *NVT* ensemble, for different packing fractions  $\eta \in [0.56, 0.7]$ . We find that the twist evolves slowly, so we run the simulations for up to  $2 \cdot 10^7$  MC cycles. In figure 7.9(a) we plot the equilibrium twist angle  $\alpha$  as a function of the packing fraction,  $\eta$ . For  $\eta < 0.6$ , the twist angle fluctuates too much and even changes handedness, and thus the data is not reliable. From figure 7.9(a) we see that the twist angle,  $\alpha$ , increases with packing fraction, up to  $\eta \approx 0.67$ . For  $\eta > 0.67$ , the twist angle,  $\alpha$ , seems to decrease with  $\eta$ , but as we show next, even  $2 \cdot 10^7$  MC cycles might have not been enough to equilibrate the system sufficiently.

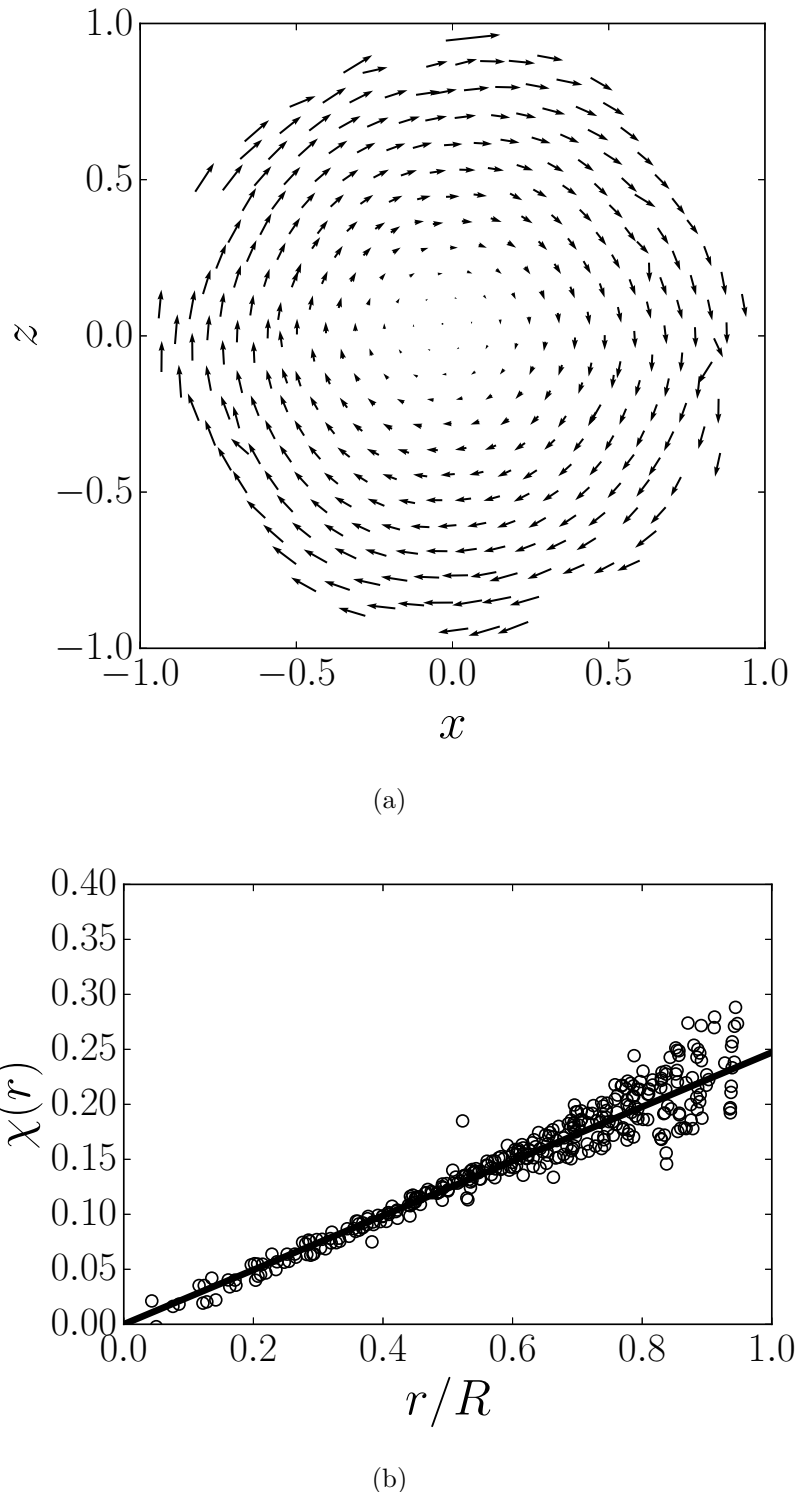


**Figure 7.8:** (a) Plot of the calculated director field for  $N = 10656$  particles, and packing fraction  $\eta = 0.65$ , projected on the plane perpendicular to the nematic director. (b) Twist,  $\chi(r)$ , as a function of the reduced column distance,  $r/R$ , from the center of the tactoid. The line seen in the figure is a linear fit.

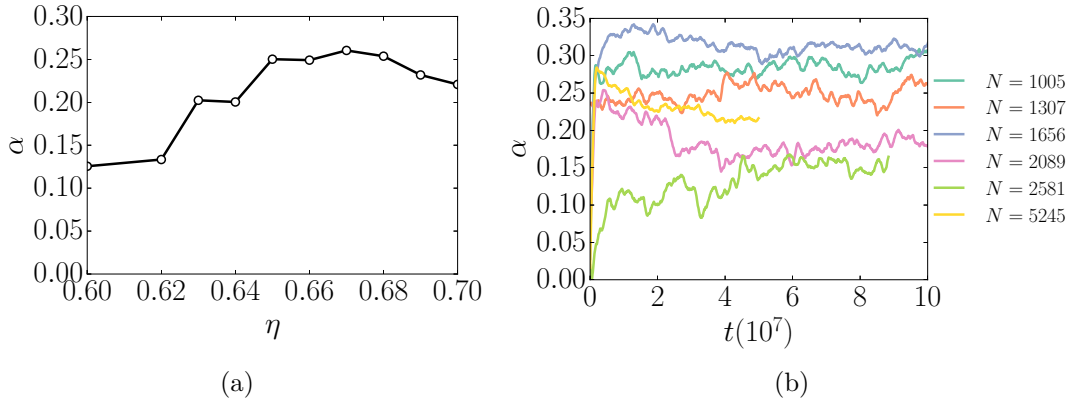


**Figure 7.9:** (a) Plot of the equilibrium twist angle,  $\alpha$ , as a function of the packing fraction,  $\eta$  for a system consisting of  $N = 10656$  hard cylinders in spherical confinement. (b) Equilibrium twist angle,  $\alpha$ , of a system of hard cylinders in spherical confinement, at packing fraction  $\eta = 0.65$ , as a function of the MC cycles,  $t$ , for different system sizes,  $N$ , shown in the legend. The plots are smoothed-out using a Savitzky-Golay filter.

In figure 7.9(b) we plot the twist angle,  $\alpha$ , as a function of the number of MC cycles, for different system sizes,  $N \in [1005, 5245]$ . For system sizes  $N < 1005$ , we do not observe a chiral configuration, due to the strong confinement effect. From figure 7.9(b), we see that the twist angle,  $\alpha$ , equilibrates extremely slowly; even  $10^8$  MC cycles seem not to be enough in some cases. Furthermore, from the current plots of the twist angle,  $\alpha$ , we are unable to find possible relations of the twist angle with system size. In Ref. [269], it is found that the twist angle remains 0 up to some critical system volume  $v_0$ , at which the system shows a sharp transition to a twisted phase, and then increases as a function of the volume of the system. Our results indeed confirm that the twist angle is zero up to a critical system size,  $N < 1005$ , and becomes non-zero for sufficiently large systems sizes. However, our simulations do not show that  $\alpha$  increases with system size.

## 7.5 Conclusion

In conclusion, motivated by experiments, on cubic  $\text{Fe}_3\text{O}_4$  nanoparticles and round  $\text{EuF}_3$  nanoplatelets confined in emulsion droplets, we implemented a Monte Carlo algorithm in order to perform simulations of spherically confined systems of hard convex-shaped particles.

Hard cubes are known to show coexistence between an isotropic fluid phase and a simple cubic crystal phase in the bulk, at packing fraction  $\eta \in (0.45, 0.5)$  [282]. From compression runs, we find that, indeed, the fraction of crystalline particles starts to increase at  $\eta \approx 0.45$ , although strong boundary effects persist for system sizes up to the largest investigated, i.e.  $N = 10851$ . We additionally found that the first surface layer crystallizes at a slower rate, while for big system sizes, the surface layers start crystallizing before the interior. For system sizes  $N \geq 1016$ , we find fluid-like regions between the first couple of layers and the interior, which are positioned on the vertices of a cube. This

last observation could potentially explain why the surface layers detach in experiments. Lastly, we find a large number of clusters, which might be indicative of the high vacancy concentration in the system [282].

For the system of hard cylinders, we observed chiral configurations, where the columns twist around a common axis, upon compression. We devised various methods to analyse the degree of twist in the system. We find that the slope of the tangent of a director field line (column), follows a linear dependence as a function of the column distance from the center of the ‘twist’. We subsequently built an empirical model to successfully explain the reason why this dependence is observed. Unfortunately, the twisted system evolves very slowly, especially, at these high packing fractions, and thus a relationship between the twist angle,  $\alpha$ , and packing fraction,  $\eta$ , or system size,  $N$ , could not be established, although we were able to find that system sizes with  $N < 1005$  particles, did not exhibit chiral phases, mainly due to the strong boundary effects. Note that in our analysis we assumed that the director field is centered at the middle of the tactoid, but from the curvature of the columns, we believe it might be possible for the center of the director field to drift around the tactoid. We expect that the shape of the particle should also play an important role in the twisting transition, as the elastic constants of the system are also dependent on the particle shape. To this end, careful calculation of the elastic constants [292, 293], could give further insight on the formation of chiral phases in entropic systems. We mention here that a twist is not seen in emulsion droplets of round  $\text{EuF}_3$  nanoplatelets, but these are rounded unlike the cylindrical particles simulated here. Moreover, the attraction between the (oleic acid) ligands present on the surface of the nanoplatelets may affect the elastic constants of the system significantly.

## Acknowledgements

We thank Da Wang for discussions and for sharing experimental results and SEM images.

# References

- [1] M. Karplus, *Development of multiscale models for complex chemical systems: from h+ h2 to biomolecules (nobel lecture)*, Angewandte Chemie International Edition **53**, 9992 (2014).
- [2] M. Planck, *On the law of distribution of energy in the normal spectrum*, Annalen der Physik **4**, 1 (1901).
- [3] P. Kollman, *Free energy calculations: applications to chemical and biochemical phenomena*, Chemical reviews **93**, 2395 (1993).
- [4] S. G. Moustafa, A. J. Schultz, and D. a. Kofke, *A comparative study of methods to compute the free energy of an ordered assembly by molecular simulation*, The Journal of Chemical Physics **139**, 084105 (2013).
- [5] L. Onsager, *Crystal statistics. I. A two-dimensional model with an order-disorder transition*, Phys. Rev. **65**, 117 (1944).
- [6] R. Lipowsky, *Surface critical phenomena at first-order phase transitions*, Ferroelectrics **73**, 69 (1987).
- [7] J. Henzie, M. Grünwald, A. Widmer-Cooper, P. L. Geissler, and P. Yang, *Self-assembly of uniform polyhedral silver nanocrystals into densest packings and exotic superlattices.*, Nat. Mater. **11**, 131 (2012).
- [8] J. Zhang, Z. Luo, B. Martens, Z. Quan, A. Kumbhar, N. Porter, Y. Wang, D.-M. Smilgies, and J. Fang, *Reversible Kirkwood-Alder transition observed in Pt3Cu2 nanooctahedron assemblies under controlled solvent annealing/drying conditions.*, J. Am. Chem. Soc. **134**, 14043 (2012).
- [9] J. J. Choi, K. Bian, W. J. Baumgardner, D.-M. Smilgies, and T. Hanrath, *Interface-induced nucleation, orientational alignment and symmetry transformations in nanocube superlattices.*, Nano Lett. **12**, 4791 (2012).
- [10] Z. Quan, W. S. Loc, C. Lin, Z. Luo, K. Yang, Y. Wang, H. Wang, Z. Wang, and J. Fang, *Tilted face-centered-cubic supercrystals of PbS nanocubes.*, Nano Lett. **12**, 4409 (2012).
- [11] M. Eguchi, D. Mitsui, H.-L. Wu, R. Sato, and T. Teranishi, *Simple reductant concentration-dependent shape control of polyhedral gold nanoparticles and their plasmonic properties.*, Langmuir **28**, 9021 (2012).
- [12] X. Xia and Y. Xia, *Symmetry breaking during seeded growth of nanocrystals.*, Nano Lett. **12**, 6038 (2012).
- [13] L. Rossi, S. Sacanna, W. T. M. Irvine, P. M. Chaikin, D. J. Pine, and A. P. Philipse, *Cubic crystals from cubic colloids*, Soft Matter **7**, 4139 (2011).
- [14] H.-L. Wu, C.-H. Kuo, and M. H. Huang, *Seed-mediated synthesis of gold nanocrystals with systematic shape evolution from cubic to trisoctahedral and rhombic dodecahedral structures.*, Langmuir **26**, 12307 (2010).
- [15] X. Zhang, C. Dong, J. A. Zapien, S. Ismathullah Khan, Z. Kang, J. Jie, X. Zhang, J. C. Chang, C.-S. Lee, and S.-T. Lee, *Polyhedral organic microcrystals: from cubes to rhombic dodecahedra.*, Angew. Chem. Int. Edit. **48**, 9121 (2009).

- [16] A. R. Tao, D. P. Ceperley, P. Sinsermsuksakul, A. R. Neureuther, and P. Yang, *Self-organized silver nanoparticles for three-dimensional plasmonic crystals.*, Nano Lett. **8**, 4033 (2008).
- [17] S. C. Glotzer and M. J. Solomon, *Anisotropy of building blocks and their assembly into complex structures.*, Nat. Mater. **6**, 557 (2007).
- [18] A. R. Tao, P. Sinsermsuksakul, and P. Yang, *Polyhedral silver nanocrystals with distinct scattering signatures.*, Angew. Chem. Int. Edit. **45**, 4597 (2006).
- [19] A. S. Barnard, X. M. Lin, and L. A. Curtiss, *Equilibrium morphology of face-centered cubic gold nanoparticles >3 nm and the shape changes induced by temperature.*, J. Phys. Chem. B **109**, 24465 (2005).
- [20] B. Wiley, T. Herricks, Y. Sun, and Y. Xia, *Polyol Synthesis of Silver Nanoparticles: Use of Chloride and Oxygen to Promote the Formation of Single-Crystal, Truncated Cubes and Tetrahedrons*, Nano Lett. **4**, 1733 (2004).
- [21] Y. Sun and Y. Xia, *Shape-controlled synthesis of gold and silver nanoparticles.*, Science (New York, N.Y.) **298**, 2176 (2002).
- [22] E. Matijevic, *Monodispersed metal (hydrous) oxides - a fascinating field of colloid science*, Accounts Chem. Res. **14**, 22 (1981).
- [23] T. Paik, D.-K. Ko, T. R. Gordon, V. Doan-Nguyen, and C. B. Murray, *Studies of Liquid Crystalline Self-Assembly of GdF<sub>3</sub> Nanoplates by In-Plane, Out-of-Plane SAXS*, ACS Nano **5**, 8322 (2011).
- [24] T. Paik, T. R. Gordon, A. M. Prantner, H. Yun, and C. B. Murray, *Designing Tripodal and Triangular Gadolinium Oxide Nanoplates and Self-Assembled Nanofibrils as Potential Multimodal Bioimaging Probes*, ACS Nano **7**, 2850 (2013).
- [25] T. Paik, B. T. Diroll, C. R. Kagan, and C. B. Murray, *Binary and Ternary Superlattices Self-Assembled from Colloidal Nanodisks and Nanorods*, J. Am. Chem. Soc. **137**, 6662 (2015).
- [26] X. Ye, J. Chen, M. Engel, J. A. Millan, W. Li, L. Qi, G. Xing, J. E. Collins, C. R. Kagan, J. Li, S. C. Glotzer, and C. B. Murray, *Competition of shape and interaction patchiness for self-assembling nanoplates*, Nat. Chem. **5**, 466 (2013).
- [27] M. E. Fisher and P.-G. de Gennes, *Phenomenes aux parois dans un melange binaire critique*, C. R. Hebd. Seances Acad. Sci. **287**, 207 (1978).
- [28] G. Flöter and S. Dietrich, *Universal amplitudes and profiles for critical adsorption*, Zeitschrift für Physik B Condensed Matter **97**, 213 (1995).
- [29] C. Bauer, T. Bieker, and S. Dietrich, *Wetting-induced effective interaction potential between spherical particles*, Phys. Rev. E **62**, 5324 (2000).
- [30] A. J. Archer and R. Evans, *Solvent-mediated interactions and solvation close to fluid-fluid phase separation: A density functional treatment*, J. Chem. Phys. **118**, 9726 (2003).
- [31] A. J. Archer, R. Evans, R. Roth, and M. Oettel, *Solvent mediated interactions close to fluid-fluid phase separation: Microscopic treatment of bridging in a soft-core fluid*, J. Chem. Phys. **122**, (2005).
- [32] D. Beysens and D. Estève, *Adsorption phenomena at the surface of silica spheres in a binary liquid mixture*, Phys. Rev. Lett. **54**, 2123 (1985).

- [33] R. Brown, *Xvii. a brief account of microscopical observations made in the months of june, july and august 1827, on the particles contained in the pollen of plants; and on the general existence of active molecules in organic and inorganic bodies*, Philos. Mag. **4**, 161 (1828).
- [34] J. Dalton. *Memoirs at manchester lit.* in Phil. Soc., volume 5, page 550, (1803).
- [35] J. Perrin, *L'agitation moléculaire et le mouvement brownien*, C. R. Hebd. Seances Acad. Sci. **146**, 967 (1908).
- [36] D. Bonn, J. Otwinowski, S. Sacanna, H. Guo, G. Wegdam, and P. Schall, *Direct observation of colloidal aggregation by critical casimir forces*, Phys. Rev. Lett. **103**, 156101 (2009).
- [37] C. Hertlein, L. Helden, A. Gambassi, S. Dietrich, and C. Bechinger, *Direct measurement of critical casimir forces.*, Nature **451**, 172 (2008).
- [38] R. R. Netz and H. Orland, *Beyond Poisson-Boltzmann: Fluctuation effects and correlation functions*, The European Physical Journal E **1**, 203 (2000).
- [39] R. R. Netz, *Electrostatistics of counter-ions at and between planar charged walls: From Poisson-Boltzmann to the strong-coupling theory*, The European Physical Journal E **5**, 557 (2001).
- [40] A. Onuki, *Ginzburg-Landau theory of solvation in polar fluids: Ion distribution around an interface*, Physical Review E **73**, 021506 (2006).
- [41] B. Derjaguin, *A theory of interaction of particles in presence of electric double layers and the stability of lyophobe colloids and disperse systems*, Progress in Surface Science **43**, 1 (1993).
- [42] B. Derjaguin and L. Landau, *Theory of the stability of strongly charged lyophobic sols and of the adhesion of strongly charged particles in solutions of electrolytes*, Acta physicochim. URSS **14**, 633 (1941).
- [43] E. J. W. Verwey, J. T. G. Overbeek, and K. Van Nes. *Theory of the stability of lyophobic colloids: the interaction of sol particles having an electric double layer*, (1948).
- [44] V. Nabutovskii, N. Nemov, and Y. Peisakhovich, *Charge-density and order-parameter waves in liquid and solid electrolytes in the vicinity of the critical point*, Physics Letters A **79**, 98 (1980).
- [45] P. G. de Gennes and J. Prost, *The Physics of Liquid Crystals (International Series of Monographs on Physics)* (Clarendon Press, 1995).
- [46] G. R. Luckhurst and T. J. Sluckin, *Biaxial Nematic Liquid Crystals, Theory, Simulation, and Experiment* (John Wiley & Sons, Ltd, Chichester, UK, 2015).
- [47] H. Stegemeyer, L. Pohl, D. Demus, G. Pelzl, H. Finkelmann, K. Hiltrop, and M. Schadt, *Liquid Crystals* (Steinkopff, 1994).
- [48] J. E. Jones. *On the determination of molecular fields. ii. from the equation of state of a gas.* in *Proceedings of the Royal Society of London A: Mathematical, Physical and Engineering Sciences*, volume 106, pages 463–477. The Royal Society, (1924).
- [49] L. Onsager, *The effects of shape on the interaction of colloidal particles*, Ann. NY Acad. Sci. **51**, 627 (1949).
- [50] J. G. Kirkwood and F. P. Buff, *The statistical mechanical theory of solutions. i*, J. Chem. Phys. **19**, 774 (1951).

- [51] M. N. Rosenbluth and A. W. Rosenbluth, *Further results on monte carlo equations of state*, The Journal of Chemical Physics **22**, 881 (1954).
- [52] B. Alder and T. Wainwright, *Phase transition for a hard sphere system*, J. Chem. Phys. **27**, 1208 (1957).
- [53] W. Krauth, *Statistical mechanics: algorithms and computations* (OUP Oxford, 2006).
- [54] L. Tonks, *The Complete Equation of State of One, Two and Three-Dimensional Gases of Hard Elastic Spheres*, Phys. Rev. **50**, 955 (1936).
- [55] W. W. Wood and J. Jacobson, *Preliminary results from a recalculation of the monte carlo equation of state of hard spheres*, The Journal of Chemical Physics **27**, 1207 (1957).
- [56] M. E. J. Newman and G. T. Barkema, *Monte Carlo methods in statistical physics* (Clarendon Press; Oxford University Press, New York, 1999).
- [57] M. Michel, S. C. Kapfer, and W. Krauth, *Generalized event-chain monte carlo: Constructing rejection-free global-balance algorithms from infinitesimal steps*, The Journal of chemical physics **140**, 054116 (2014).
- [58] M. Krich and S. Dietrich, *Finite-size scaling for critical films.*, Phys. Rev. Lett. **66**, 345 (1991).
- [59] M. Krich and S. Dietrich, *Specific heat of critical films, the casimir force, and wetting films near critical end points*, Phys. Rev. A **46**, 1922 (1992).
- [60] M. Krich, *The Casimir effect in critical systems* (World Scientific, 1994).
- [61] H. B. G. Casimir, *On the attraction between two perfectly conducting plates.*, Kon. Ned. Akad. Wetensch. Proc. **51**, 793 (1948).
- [62] A. Hanke, F. Schlesener, E. Eisenriegler, and S. Dietrich, *Critical casimir forces between spherical particles in fluids.*, Phys. Rev. Lett. **81**, 1885 (1998).
- [63] O. Vasilyev, A. Gambassi, A. Maciołek, and S. Dietrich, *Universal scaling functions of critical casimir forces obtained by monte carlo simulations.*, Phys. Rev. E **79**, 041142 (2009).
- [64] B. Derjaguin, *Untersuchungen über die reibung und adhäsion, iv*, Kolloid-Zeitschrift **69**, 155 (1934).
- [65] T. F. Mohry, S. Kondrat, A. Maciołek, and S. Dietrich, *Critical casimir interactions around the consolute point of a binary solvent*, Soft matter **10**, 5510 (2014).
- [66] T. F. Mohry, A. Maciołek, and S. Dietrich, *Phase behavior of colloidal suspensions with critical solvents in terms of effective interactions*, J. Chem. Phys. **136**, 224902 (2012).
- [67] T. F. Mohry, A. Maciołek, and S. Dietrich, *Structure and aggregation of colloids immersed in critical solvents*, J. Chem. Phys. **136**, 224903 (2012).
- [68] A. Gambassi, A. Maciołek, C. Hertlein, U. Nellen, L. Helden, C. Bechinger, and S. Dietrich, *Critical Casimir effect in classical binary liquid mixtures*, Physical Review E **80**, 061143 (2009).
- [69] A. Maciołek and S. Dietrich, *Review* (2016). (to be published).
- [70] P. Gallagher, M. Kurnaz, and J. Maher, *Aggregation in polystyrene-sphere suspensions in near-critical binary liquid mixtures*, Phys. Rev. A **46**, 7750 (1992).
- [71] P. Gallagher and J. Maher, *Partitioning of polystyrene latex spheres in immiscible critical liquid mixtures*, Phys. Rev. A **46**, 2012 (1992).

- [72] T. Narayanan, A. Kumar, E. Gopal, D. Beysens, P. Guenoun, and G. Zalczer, *Reversible flocculation of silica colloids in liquid mixtures*, Physical Review E **48**, 1989 (1993).
- [73] S. R. Kline and E. W. Kaler, *Colloidal interactions in water/2-butoxyethanol solvents*, Langmuir **10**, 412 (1994).
- [74] Y. Jayalakshmi and E. W. Kaler, *Phase behavior of colloids in binary liquid mixtures*, Phys. Rev. Lett. **78**, 1379 (1997).
- [75] B. Rathke, H. Grüll, and D. Woermann, *Stability of dilute colloidal silica suspensions in the vicinity of the binodal curve of the system 2-butoxyethanol/water*, Journal of colloid and interface science **192**, 334 (1997).
- [76] R. D. Koehler and E. W. Kaler, *Colloidal phase transitions in aqueous nonionic surfactant solutions*, Langmuir **13**, 2463 (1997).
- [77] J. S. van Duijneveldt and D. Beysens, *Adsorption on colloids and flocculation: The influence of salt*, J. Chem. Phys. **94**, 5222 (1991).
- [78] D. Beysens and T. Narayanan, *Wetting-induced aggregation of colloids*, Journal of statistical physics **95**, 997 (1999).
- [79] A. Drzewiński, A. Maciołek, and R. Evans, *Influence of capillary condensation on the near-critical solvation force.*, Phys. Rev. Lett. **85**, 3079 (2000).
- [80] R. Okamoto and A. Onuki, *Casimir amplitudes and capillary condensation of near-critical fluids between parallel plates: renormalized local functional theory.*, J. Chem. Phys. **136**, 114704 (2012).
- [81] T. J. Sluckin, *Wetting phenomena and colloidal aggregation in binary mixtures*, Phys. Rev. A **41**, 960 (1990).
- [82] H. Löwen, *Solvent-induced phase separation in colloidal fluids*, Phys. Rev. Lett. **74**, 1028 (1995).
- [83] R. R. Netz, *Colloidal flocculation in near-critical binary mixtures*, Phys. Rev. Lett. **76**, 3646 (1996).
- [84] T. Gil, J. H. Ipsen, and C. F. Tejero, *Wetting controlled phase transitions in two-dimensional systems of colloids*, Physical Review E **57**, 3123 (1998).
- [85] H. Guo, T. Narayanan, M. Sztuchi, P. Schall, and G. H. Wegdam, *Reversible phase transition of colloids in a binary liquid solvent*, Phys. Rev. Lett. **100**, 188303 (2008).
- [86] V. D. Nguyen, S. Faber, Z. Hu, G. H. Wegdam, and P. Schall, *Controlling colloidal phase transitions with critical casimir forces*, Nat. Commun **4**, 1584 (2013).
- [87] M. T. Dang, A. V. Verde, P. G. Bolhuis, P. Schall, et al., *Temperature-sensitive colloidal phase behavior induced by critical casimir forces*, J. Chem. Phys. **139**, 094903 (2013).
- [88] V. D. Nguyen, M. T. Dang, T. A. Nguyen, and P. Schall, *Critical casimir forces for colloidal assembly*, J. Phys. Condens. Matter **28**, 043001 (2016).
- [89] J. R. Edison, S. Belli, R. Evans, R. van Roij, and M. Dijkstra, *Phase behaviour of colloids suspended in a near-critical solvent: a mean-field approach*, Mol. Phys. **113**, 2546 (2015).
- [90] J. R. Edison, N. Tasios, S. Belli, R. Evans, R. van Roij, and M. Dijkstra, *Critical Casimir Forces and Colloidal Phase Transitions in a Near-Critical Solvent: A Simple Model Reveals a Rich Phase Diagram*, Phys. Rev. Lett. **114**, 038301 (2015).

- [91] K. Binder, A. M. Ferrenberg, and D. P. Landau, *Wetting in fluid systems. wetting and capillary condensation of lattice gases in thin film geometry*, Ber. Bunsen Phys. Chem. **98**, 340 (1994).
- [92] D. Nicolaides and R. Evans, *Monte-carlo study of phase-transitions in a confined lattice gas*, Phys. Rev. B **39**, 9336 (1989).
- [93] R. Evans and U. M. B. Marconi, *Phase equilibria and solvation forces for fluids confined between parallel walls*, J Chem Phys **86**, 7138 (1987).
- [94] J. R. Heringa and H. W. J. Blöte, *Geometric cluster monte carlo simulation*, Phys. Rev. E **57**, 4976 (1998).
- [95] H. Hobrecht and A. Hucht, *Many-body critical casimir interactions in colloidal suspensions*, Physical Review E **92**, 042315 (2015).
- [96] E. Rabani, D. R. Reichman, P. L. Geissler, and L. E. Brus, *Drying-mediated self-assembly of nanoparticles*, Nature **213901**, 2 (2003).
- [97] A. Z. Panagiotopoulos, *On the equivalence of continuum and lattice models for fluids*, J Chem Phys **112**, 7132 (2000).
- [98] A. Z. Panagiotopoulos, *Thermodynamic properties of lattice hard-sphere models*, J. Chem. Phys. **123**, (2005).
- [99] K. E. Gubbins, *The role of computer simulation in studying fluid phase equilibria*, Molecular Simulation **2**, 223 (1989).
- [100] D. J. Ashton and N. B. Wilding, *Grand canonical simulation of phase behaviour in highly size-asymmetrical binary fluids*, Mol. Phys. **109**, 999 (2011).
- [101] F. A. Escobedo and F. J. Martínez-Veracoechea, *Optimized expanded ensembles for simulations involving molecular insertions and deletions. i. closed systems*, J. Chem. Phys. **127**, 174103 (2007).
- [102] F. A. Escobedo, *Optimized expanded ensembles for simulations involving molecular insertions and deletions. ii. open systems.*, J Chem Phys **127**, 174104 (2007).
- [103] A. Z. Panagiotopoulos, *Monte carlo methods for phase equilibria of fluids*, J. Phys. Condens. Matter **12**, R25 (2000).
- [104] G. Latouche, *Level-Independent Quasi-Birth-and-Death Processes* (John Wiley & Sons, Inc., 2010).
- [105] G. Bolch, S. Greiner, H. de Meer, and K. Trivedi, *Queueing Networks and Markov Chains: Modeling and Performance Evaluation with Computer Science Applications* (Wiley, 2006).
- [106] J. Hansen and I. McDonald, *Theory of Simple Liquids* (Elsevier Science, 2006).
- [107] R. Pandit, M. Schick, and M. Wortis, *Systematics of multilayer adsorption phenomena on attractive substrates*, Physical Review B **26**, 5112 (1982).
- [108] R. Evans, *Fluids adsorbed in narrow pores: Phase-equilibria and structure*, J. Phys. Condens. Matter **2**, 8989 (1990).
- [109] P. Pieranski, *Two-dimensional interfacial colloidal crystals*, Phys. Rev. Lett. **45**, 569 (1980).
- [110] K. A. Maerzke, L. Gai, P. T. Cummings, and C. McCabe. *Simulating phase equilibria using wang-landau-transition matrix monte carlo.* in *J. Phys. Conf. Ser.*, volume 487, page 012002. IOP Publishing, (2014).

- [111] F. Del Rio, E. Avalos, R. Espindola, L. F. Rull, G. Jackson, and S. Lago, *Vapour-liquid equilibrium of the square-well fluid of variable range via a hybrid simulation approach*, Mol. Phys. **100**, 2531 (2002).
- [112] L. Vega, E. de Miguel, L. F. Rull, G. Jackson, and I. A. McLure, *Phase equilibria and critical behavior of square-well fluids of variable width by gibbs ensemble monte carlo simulation*, J. Chem. Phys. **96**, 2296 (1992).
- [113] D. L. Pagan and J. D. Gunton, *Phase behavior of short-range square-well model*, J. Chem. Phys. **122**, 184515 (2005).
- [114] R. Evans, R. J. F. Leote de Carvalho, J. R. Henderson, and D. C. Hoyle, *Asymptotic decay of correlations in liquids and their mixtures*, J. Chem. Phys. **100**, 591 (1994).
- [115] J. Hansen and I. McDonald, *Theory of Simple Liquids* (Academic Press, 2006).
- [116] O. A. Vasilyev, *Critical casimir interactions between spherical particles in the presence of bulk ordering fields*, Phys. Rev. E **90**, 012138 (2014).
- [117] M. G. Noro and D. Frenkel, *Extended corresponding-states behavior for particles with variable range attractions*, The Journal of Chemical Physics **113**, 2941 (2000).
- [118] G. Vliegenthart and H. N. Lekkerkerker, *Predicting the gas-liquid critical point from the second virial coefficient*, The Journal of Chemical Physics **112**, 5364 (2000).
- [119] H. T. Dobbs, G. A. Darbellay, and J. M. Yeomans, *Capillary condensation between spheres*, EPL (Europhysics Letters) **18**, 439 (1992).
- [120] P. Hopkins, A. J. Archer, and R. Evans, *Solvent mediated interactions between model colloids and interfaces: A microscopic approach*, J. Chem. Phys. **131**, (2009).
- [121] R. Okamoto and A. Onuki, *Attractive interaction and bridging transition between neutral colloidal particles due to preferential adsorption in a near-critical binary mixture*, Phys. Rev. E **88**, 022309 (2013).
- [122] P. J. Upton, J. O. Indekeu, and J. M. Yeomans, *Wetting on spherical and cylindrical substrates: Global phase diagrams*, Phys. Rev. B **40**, 666 (1989).
- [123] S. L. Veatch, P. Cicuta, P. Sengupta, A. Honerkamp-Smith, D. Holowka, and B. Baird, *Critical fluctuations in plasma membrane vesicles*, ACS Chemical Biology **3**, 287 (2008).
- [124] B. B. Machta, S. L. Veatch, and J. P. Sethna, *Critical casimir forces in cellular membranes*, Phys. Rev. Lett. **109**, 138101 (2012).
- [125] M. Zubaszewska, A. Maciołek, and A. Drzewiński, *Critical casimir forces along the isofields*, Physical Review E **88**, 052129 (2013).
- [126] N. Tasios, J. R. Edison, R. van Roij, R. Evans, and M. Dijkstra, *Critical Casimir interactions and colloidal self-assembly in near-critical solvents.*, J. Chem. Phys. **145**, 084902 (2016).
- [127] J. Heringa and H. Blöte, *Geometric symmetries and cluster simulations*, Physica A **254**, 156 (1998).
- [128] D. J. Ashton, J. Liu, E. Luijten, and N. B. Wilding, *Monte carlo cluster algorithm for fluid phase transitions in highly size-asymmetrical binary mixtures*, J. Chem. Phys. **133**, 194102 (2010).
- [129] D. Ashton, N. Wilding, R. Roth, and R. Evans, *Depletion potentials in highly size-asymmetric binary hard-sphere mixtures: Comparison of simulation results with theory*, Phys. Rev. E **84**, 061136 (2011).

- [130] H. B. Tarko and M. E. Fisher, *Theory of critical point scattering and correlations. iii. the ising model below  $T_c$  and in a field*, Phys. Rev. B **11**, 1217 (1975).
- [131] A. Drzewiński, A. Maciołek, and A. Ciach, *Effect of bulk magnetic field on critical ising films*, Phys. Rev. E **61**, 5009 (2000).
- [132] T. W. Burkhardt and E. Eisenriegler, *Casimir interaction of spheres in a fluid at the critical point*, Phys. Rev. Lett. **74**, 3189 (1995).
- [133] R. Guida and J. Zinn-Justin, *Critical exponents of the n-vector model*, J. Phys. A-Math. Gen. **31**, 8103 (1998).
- [134] A. Fortini and M. Dijkstra, *Phase behaviour of hard spheres confined between parallel hard plates: manipulation of colloidal crystal structures by confinement*, J. Phys. Condens. Mat. **18**, L371 (2006).
- [135] E. L. Eckfeldt and W. W. Lucasse, *The Liquid–Liquid Phase Equilibria of the System Cyclohexane–Methyl Alcohol in the Presence of Various Salts as Third Components.*, The Journal of Physical Chemistry **47**, 164 (1943).
- [136] B. J. Hales, G. L. Bertrand, and L. G. Hepler, *Effects of Third Components on Critical Mixing in the Water-Triethylamine System*, The Journal of Physical Chemistry **70**, 3970 (1966).
- [137] J. Jacob, M. a. Anisimov, J. V. Sengers, A. Oleinikova, H. Weingärtner, and A. Kumar, *Novel phase-transition behavior near liquid/liquid critical points of aqueous solutions: Formation of a third phase at the interface*, Physical Chemistry Chemical Physics **3**, 829 (2001).
- [138] A. F. Kostko, M. A. Anisimov, and J. V. Sengers, *Criticality in aqueous solutions of 3-methylpyridine and sodium bromide*, Physical Review E **70**, 1 (2004).
- [139] M. Wagner, O. Stanga, and W. Schröer, *Tricriticality in the ternary system 3-methylpyridine/water/NaBr? Measurements of the viscosity*, Physical Chemistry Chemical Physics **4**, 5300 (2002).
- [140] D. Subramanian, D. A. Ivanov, I. K. Yudin, M. A. Anisimov, and J. V. Sengers, *Mesoscale Inhomogeneities in Aqueous Solutions of 3-Methylpyridine and Tertiary Butyl Alcohol*, Journal of Chemical & Engineering Data **56**, 1238 (2011).
- [141] D. Subramanian and M. A. Anisimov, *Resolving the mystery of aqueous solutions of tertiary butyl alcohol.*, The journal of physical chemistry. B **115**, 9179 (2011).
- [142] J. Leys, D. Subramanian, E. Rodezno, B. Hammouda, and M. a. Anisimov, *Mesoscale phenomena in solutions of 3-methylpyridine, heavy water, and an antagonistic salt*, Soft Matter **9**, 9326 (2013).
- [143] K. Sadakane, H. Seto, H. Endo, and M. Shibayama, *A periodic structure in a mixture of D<sub>2</sub>O/3-methylpyridine/ NaBPh<sub>4</sub> induced by solvation effect*, Journal of the Physical Society of Japan **76**, 4 (2007).
- [144] K. Sadakane, A. Onuki, K. Nishida, S. Koizumi, and H. Seto, *Multilamellar Structures Induced by Hydrophilic and Hydrophobic Ions Added to a Binary Mixture of D<sub>2</sub>O and 3-Methylpyridine*, Physical Review Letters **103**, 167803 (2009).
- [145] K. Sadakane, N. Iguchi, M. Nagao, H. Endo, Y. B. Melnichenko, and H. Seto, *2D-Ising-like critical behavior in mixtures of water and 3-methylpyridine including antagonistic salt or ionic surfactant*, Soft Matter **7**, 1334 (2011).

- [146] K. Sadakane, M. Nagao, H. Endo, and H. Seto, *Membrane formation by preferential solvation of ions in mixture of water, 3-methylpyridine, and sodium tetraphenylborate.*, The Journal of chemical physics **139**, 234905 (2013).
- [147] T. Araki and A. Onuki, *Dynamics of binary mixtures with ions: dynamic structure factor and mesophase formation.*, Journal of physics. Condensed matter : an Institute of Physics journal **21**, 424116 (2009).
- [148] A. Onuki, T. Araki, and R. Okamoto, *Solvation effects in phase transitions in soft matter.*, Journal of physics. Condensed matter : an Institute of Physics journal **23**, 284113 (2011).
- [149] A. Onuki, R. Okamoto, and T. Araki, *Phase Transitions in Soft Matter Induced by Selective Solvation*, Journal of The Chemical Society of Japan **84**, 569 (2011).
- [150] A. Onuki and R. Okamoto, *Selective solvation effects in phase separation in aqueous mixtures*, Current Opinion in Colloid & Interface Science **16**, 525 (2011).
- [151] R. Okamoto and A. Onuki, *Charged colloids in an aqueous mixture with a salt*, Physical Review E **84**, 051401 (2011).
- [152] F. Pousaneh and A. Ciach, *The effect of antagonistic salt on a confined near-critical mixture*.Soft matter (2014).
- [153] M. Engel and H.-R. Trebin, *Self-assembly of monatomic complex crystals and quasicrystals with a double-well interaction potential*, Physical review letters **98**, 225505 (2007).
- [154] M. Engel, P. F. Damasceno, C. L. Phillips, and S. C. Glotzer, *Computational self-assembly of a one-component icosahedral quasicrystal*, Nature materials **14**, 109 (2015).
- [155] M. Krajčí and J. Hafner, *Structure and stability of quasicrystals: Modulated tiling models*, Physical Review B **46**, 10669 (1992).
- [156] V. Dmitrienko and S. Astaf'ev, *Oscillating interatomic potentials and growth of icosahedral quasicrystals*, Physical review letters **75**, 1538 (1995).
- [157] D. Frenkel and B. Smit, *Understanding Molecular Simulation: From Algorithms to Applications* (Elsevier Science, 2001).
- [158] A. C. Maggs and V. Rossetto, *Local Simulation Algorithms for Coulomb Interactions*, Physical Review Letters **88**, 196402 (2002).
- [159] K. S. Yee et al., *Numerical solution of initial boundary value problems involving maxwell's equations in isotropic media*, IEEE Trans. Antennas Propag **14**, 302 (1966).
- [160] L. Levrel and A. C. Maggs, *Monte Carlo algorithms for charged lattice gases*, Physical Review E **72**, 016715 (2005).
- [161] T. Hirono, Y. Shibata, W. Lui, S. Seki, and Y. Yoshikuni, *The second-order condition for the dielectric interface orthogonal to the yee-lattice axis in the fDTD scheme*, IEEE microwave and guided wave letters **10**, 359 (2000).
- [162] A. Duncan, R. Sedgewick, and R. Coalson, *Improved local lattice approach for Coulombic simulations*, Physical Review E **71**, 046702 (2005).
- [163] A. C. Maggs, *Auxiliary field Monte Carlo for charged particles.*, The Journal of chemical physics **120**, 3108 (2004).
- [164] L. Levrel and A. C. Maggs, *Boundary conditions in local electrostatics algorithms.*, The Journal of chemical physics **128**, 214103 (2008).

- [165] C. Kalidas, G. Hefter, and Y. Marcus, *Gibbs energies of transfer of cations from water to mixed aqueous organic solvents*, Chemical reviews **100**, 819 (2000).
- [166] Y. Marcus, *Gibbs energies of transfer of anions from water to mixed aqueous organic solvents*, Chemical reviews **107**, 3880 (2007).
- [167] A. Onuki, S. Yabunaka, T. Araki, and R. Okamoto, *Structure formation due to antagonistic salts*, Current Opinion in Colloid & Interface Science **22**, 59 (2016).
- [168] J. R. Errington, *Evaluating surface tension using grand canonical transition matrix monte carlo simulation and finite size scaling*, Phys. Rev. E **67**, 012102 (2003).
- [169] F. S. Bates and G. H. Fredrickson, *Block Copolymer Thermodynamics: Theory and Experiment*, Annu. Rev. Phys. Chem. **41**, 525 (1990).
- [170] M. W. Matsen, *The standard Gaussian model for block copolymer melts*, Journal of Physics: Condensed Matter **14**, R21 (2002).
- [171] F. S. Bates and G. H. Fredrickson, *Block Copolymers—Designer Soft Materials*, Phys. Today **52**, 32 (1999).
- [172] R. D. Groot and T. J. Madden, *Dynamic simulation of diblock copolymer microphase separation*, The Journal of Chemical Physics **108**, 8713 (1998).
- [173] J. M. Seddon and R. H. Templer, *Cubic Phases of Self-Assembled Amphiphilic Aggregates*, Philos. Trans. R. Soc. A Math. Phys. Eng. Sci. **344**, 377 (1993).
- [174] J. Seddon and R. Templer, in *Handb. Biol. Phys.* (1995).
- [175] J. Vieillard-Baron, *Phase transitions of the classical hard-ellipse system*, J. Chem. Phys. **56**, 4729 (1972).
- [176] D. Frenkel and B. Mulder, *The hard ellipsoid-of-revolution fluid*, Mol. Phys. **55**, 1171 (1985).
- [177] P. Bolhuis and D. Frenkel, *Tracing the phase boundaries of hard spherocylinders*, J. Chem. Phys. **106**, 666 (1997).
- [178] D. Frenkel and R. Eppenga, *Monte Carlo study of the isotropic-nematic transition in a fluid of thin hard disks*, Phys. Rev. Lett. **49**, 1089 (1982).
- [179] R. Eppenga and D. Frenkel, *Monte carlo study of the isotropic and nematic phases of infinitely thin hard platelets*, Molecular physics **52**, 1303 (1984).
- [180] J. A. C. Veerman and D. Frenkel, *Phase behavior of disklike hard-core mesogens*, Phys. Rev. A **45**, 5632 (1992).
- [181] M. A. Bates and D. Frenkel, *Infinitely thin disks exhibit a first order nematic-columnar phase transition*, Phys. Rev. E **57**, 4824 (1998).
- [182] P. D. Duncan, M. Dennison, A. J. Masters, and M. R. Wilson, *Theory and computer simulation for the cubatic phase of cut spheres*, Phys. Rev. E **79**, 031702 (2009).
- [183] M. Marechal, A. Cuetos, B. Martínez-Haya, and M. Dijkstra, *Phase behavior of hard colloidal platelets using free energy calculations*, J. Chem. Phys. **134**, 094501 (2011).
- [184] M. Marechal, A. Patti, M. Dennison, and M. Dijkstra, *Frustration of the Isotropic-columnar phase transition of colloidal hard platelets by a transient Cubatic phase*, Phys. Rev. Lett. **108**, 206101 (2012).
- [185] P. F. Damasceno, M. Engel, and S. C. Glotzer, *Predictive self-assembly of polyhedra into complex structures*, Science **337**, 453 (2012).

- [186] A. P. Gantapara, J. de Graaf, R. van Roij, and M. Dijkstra, *Phase diagram and structural diversity of a family of truncated cubes: Degenerate close-packed structures and vacancy-rich states*, Phys. Rev. Lett. **111**, 015501 (2013).
- [187] A. P. Gantapara, J. de Graaf, R. van Roij, and M. Dijkstra, *Phase behavior of a family of truncated hard cubes*, J. Chem. Phys. **142**, 054904 (2015).
- [188] J. de Graaf, R. van Roij, and M. Dijkstra, *Dense regular packings of irregular nonconvex particles*, Phys. Rev. Lett. **107**, 155501 (2011).
- [189] J. de Graaf, L. Filion, M. Marechal, R. van Roij, and M. Dijkstra, *Crystal-structure prediction via the floppy-box monte carlo algorithm: Method and application to hard (non) convex particles*, J. Chem. Phys. **137**, 214101 (2012).
- [190] S. J. Singer and R. Mumaugh, *Monte carlo study of fluid–plastic crystal coexistence in hard dumbbells*, J. Chem. Phys. **93**, 1278 (1990).
- [191] C. Vega and P. A. Monson, *Plastic crystal phases of hard dumbbells and hard spherocylinders*, J. Chem. Phys. **107**, 2696 (1997).
- [192] H. Graf and H. Löwen, *Density functional theory for hard spherocylinders: phase transitions in the bulk and in the presence of external fields*, J. Phys. Cond. Mat. **11**, 1435 (1999).
- [193] A. Haji-Akbari, M. Engel, A. S. Keys, X. Zheng, R. G. Petschek, P. Palffy-Muhoray, and S. C. Glotzer, *Disordered, quasicrystalline and crystalline phases of densely packed tetrahedra*, Nature **462**, 773 (2009).
- [194] P. I. C. Teixeira, A. Masters, and B. Mulder, *Biaxial nematic order in the hard-boomerang fluid*, Mol. Cryst. Liq. Cryst. **323**, 167 (1998).
- [195] Y. Martinez-Raton, S. Varga, and E. Velasco, *Biaxial nematic phases in fluids of hard board-like particles*, Phys. Chem. Chem. Phys. **13**, 13247 (2011).
- [196] A. B. L. op Reinink, S. Belli, R. Van Roij, M. Dijkstra, A. V. Petukhov, and G. J. Vroege, *Tuning biaxiality of nematic phases of board-like colloids by an external magnetic field*, Soft Matter **10**, 446 (2014).
- [197] S. D. Peroukidis and A. G. Vanakaras, *Phase diagram of hard board-like colloids from computer simulations*, Soft Matter **9**, 7419 (2013).
- [198] S. Dussi and M. Dijkstra, *Entropy-driven formation of chiral nematic phases by computer simulations*, Nat. Commun. **7**, (2016).
- [199] M. Dijkstra, *Entropy-driven phase transitions in colloids: From spheres to anisotropic particles*, Adv. Chem. Phys. **156**, 35 (2014).
- [200] G. Kolbe, The complex chemical behavior of silica, Ph.D. thesis, University of Jena, 1956.
- [201] W. Stöber, A. Fink, and E. Bohn, *Controlled growth of monodisperse silica spheres in the micron size range*, J. Colloid Interf. Sci. **26**, 62 (1968).
- [202] J. H. Conway, H. Burgiel, and C. Goodman-Strauss, *Naming Archimedean and Catalan polyhedra and tilings*, chapter 21. CRC Press, (2016).
- [203] N. G. Almarza, *A cluster algorithm for Monte Carlo simulation at constant pressure*, J. Chem. Phys. **130**, 184106 (2009).
- [204] E. G. Gilbert, D. W. Johnson, and S. S. Keerthi, *A fast procedure for computing the distance between complex objects in three-dimensional space*, IEEE Journal on Robotics and Automation **4**, 193 (1988).

- [205] P. de Gennes, *Short range order effects in the isotropic phase of nematics and cholesterics*, Mol. Cryst. Liq. Cryst. **12**, 193 (1971).
- [206] P. de Gennes and J. Prost, *The physics of liquid crystals* (Oxford University Press, 1993).
- [207] K. Kobayashi, *On the theory of translational and orientational melting with application to liquid crystals*, Phys. Lett. A **31**, 125 (1970).
- [208] W. L. McMillan, *Simple molecular model for the smectic a phase of liquid crystals*, Phys. Rev. A **4**, 1238 (1971).
- [209] M. Cifelli, G. Cinacchi, and L. DeGaetani, *Smectic order parameters from diffusion data*, J. Chem. Phys. **125**, 164912 (2006).
- [210] R. Blaak, D. Frenkel, and B. M. Mulder, *Do cylinders exhibit a cubatic phase?*, J. Chem. Phys. **110**, 11652 (1999).
- [211] B. Mulder, *Isotropic-symmetry-breaking bifurcations in a class of liquid-crystal models*, Phys. Rev. A **39**, 360 (1989).
- [212] S. Dussi, When shape is enough: from colloidal spheres to twisted polyhedra, from icosahedral to chiral order, Ph.D. thesis, University of Utrecht, 2016.
- [213] M. J. Freiser, *Ordered States of a Nematic Liquid*, Physical Review Letters **24**, 1041 (1970).
- [214] R. Alben, *Phase Transitions in a Fluid of Biaxial Particles*, Physical Review Letters **30**, 778 (1973).
- [215] J. P. Straley, *Ordered phases of a liquid of biaxial particles*, Physical Review A **10**, 1881 (1974).
- [216] P. J. Camp, C. P. Mason, M. P. Allen, A. A. Khare, and D. A. Kofke, *The isotropic-nematic phase transition in uniaxial hard ellipsoid fluids: Coexistence data and the approach to the Onsager limit*, The Journal of Chemical Physics **105**, 2837 (1996).
- [217] P. J. Camp and M. Allen, *Phase diagram of the hard biaxial ellipsoid fluid*, The Journal of Chemical Physics **106**, 6681 (1997).
- [218] B. Mulder, *Isotropic-symmetry-breaking bifurcations in a class of liquid-crystal models*, Physical Review A **39**, 360 (1989).
- [219] S. Belli, A. Patti, M. Dijkstra, and R. van Roij, *Polydispersity Stabilizes Biaxial Nematic Liquid Crystals*, Physical Review Letters **107**, 148303 (2011).
- [220] L. J. Yu and A. Saupe, *Observation of a Biaxial Nematic Phase in Potassium Laurate-1-Decanol-Water Mixtures*, Physical Review Letters **45**, 1000 (1980).
- [221] J. Malthête, N. H. Tinh, and A. M. Levelut, *New mesogens with six, four, or three parafinic chains* J. Chem. Soc., Chem. Commun. 1548 (1986).
- [222] S. Chandrasekhar, B. R. Ratna, B. K. Sadashiva, and V. N. Raja, *A Thermotropic Biaxial Nematic Liquid Crystal*, Molecular Crystals and Liquid Crystals Incorporating Nonlinear Optics **165**, 123 (1988).
- [223] K. Praefcke, B. Kohne, D. Singer, D. Demus, G. Pelzl, and S. Diele, *Thermotropic biaxial nematic phases with negative optical character [1]*, Liquid Crystals **7**, 589 (1990).
- [224] K. Praefcke, B. Kohne, B. Gündogan, D. Singer, D. Demus, S. Diele, G. Pelzl, and U. Bakowsky, *News on Nematic-Biaxial Liquid Crystals 1*, Molecular Crystals and Liquid Crystals **198**, 393 (1991).

- [225] I. G. Shenouda, Y. Shl, and M. E. Neubert, *Mesomorphic Properties of 4-[3',4',5'-tri(*p*-*n*-Dodecyloxybenzylxy)]-Benzoyloxy-4''- *p*-*n*-Dodecyloxybenzylxybiphenyl*, Molecular Crystals and Liquid Crystals Science and Technology. Section A. Molecular Crystals and Liquid Crystals **257**, 209 (1994).
- [226] J. R. Hughes, G. Kothe, G. R. Luckhurst, J. Malthête, M. E. Neubert, I. Shenouda, B. A. Timimi, and M. Tittelbach, *A deuterium nuclear magnetic resonance investigation of the symmetry and orientational order of the nematic phase of 4-[3,4,5-tris(4-dodecyloxybenzylxy)benzoyloxy]-4'-(4-dodecyloxybenzoyloxy)-1,1'-biphenyl. A biaxial nematic?*, The Journal of Chemical Physics **107**, 9252 (1997).
- [227] L. A. Madsen, T. J. Dingemans, M. Nakata, and E. T. Samulski, *Thermotropic Biaxial Nematic Liquid Crystals*, Physical Review Letters **92**, 145505 (2004).
- [228] B. R. Acharya, A. Primak, and S. Kumar, *Biaxial Nematic Phase in Bent-Core Thermotropic Mesogens*, Physical Review Letters **92**, 145506 (2004).
- [229] S. D. Peroukidis, A. G. Vanakaras, and D. J. Photinos, *Supramolecular nature of the nematic-nematic phase transitions of hard boardlike molecules*, Physical Review E **88**, 062508 (2013).
- [230] R. Berardi and C. Zannoni, *Do thermotropic biaxial nematics exist? A Monte Carlo study of biaxial Gay-Berne particles*, The Journal of Chemical Physics **113**, 5971 (2000).
- [231] R. Berardi, L. Muccioli, S. Orlandi, M. Ricci, and C. Zannoni, *Computer simulations of biaxial nematics*, Journal of Physics: Condensed Matter **20**, 463101 (2008).
- [232] A. Cuetos, A. Galindo, and G. Jackson, *Thermotropic Biaxial Liquid Crystalline Phases in a Mixture of Attractive Uniaxial Rod and Disk Particles*, Physical Review Letters **101**, 237802 (2008).
- [233] E. Van den Pol, A. Petukhov, D. Thies-Weesie, D. Byelov, and G. Vroege, *Experimental realization of biaxial liquid crystal phases in colloidal dispersions of boardlike particles*, Physical review letters **103**, 258301 (2009).
- [234] B. S. John, C. Juhlin, and F. A. Escobedo, *Phase behavior of colloidal hard perfect tetragonal parallelepipeds*, J. Chem. Phys. **128**, 044909 (2008).
- [235] A. Rahman, *Correlations in the motion of atoms in liquid argon*, Physical Review **136**, A405 (1964).
- [236] D. Rapaport, *The Art of Molecular Dynamics Simulation* (Cambridge University Press, 2004).
- [237] G. Paul, *A Complexity O(1) priority queue for event driven molecular dynamics simulations*, Journal of Computational Physics **221**, 615 (2007).
- [238] H. Sigurgeirsson, A. Stuart, and W.-L. Wan, *Algorithms for Particle-Field Simulations with Collisions*, Journal of Computational Physics **172**, 766 (2001).
- [239] A. Donev, S. Torquato, and F. H. Stillinger, *Neighbor list collision-driven molecular dynamics simulation for nonspherical hard particles. I. Algorithmic details*, Journal of Computational Physics **202**, 737 (2005).
- [240] A. Donev, S. Torquato, and F. H. Stillinger, *Neighbor list collision-driven molecular dynamics simulation for nonspherical hard particles.*, Journal of Computational Physics **202**, 765 (2005).

- [241] M. Marín, D. Risso, and P. Cordero, *Efficient Algorithms for Many-Body Hard Particle Molecular Dynamics*, J. Comput. Phys. **109**, 306 (1993).
- [242] L. H. de la Peña, R. van Zon, J. Schofield, and S. B. Opps, *Discontinuous molecular dynamics for semiflexible and rigid bodies*, The Journal of chemical physics **126**, 074105 (2007).
- [243] B. V. Mirtich, Impulse-based dynamic simulation of rigid body systems, Ph.D. thesis, University of California at Berkeley, 1996.
- [244] X. Zhang, M. Lee, and Y. Kim, *Interactive continuous collision detection for non-convex polyhedra*, The Visual Computer **22**, 749 (2006).
- [245] M. Tang, Y. J. Kim, and D. Manocha. *C2A: Controlled Conservative Advancement for Continuous Collision Detection of Polygonal Models*. in *Robotics and Automation, 2009. ICRA'09. IEEE International Conference on*, pages 849–854. IEEE, (2009).
- [246] M. Tang, D. Manocha, and Y. J. Kim, *Hierarchical and Controlled Advancement for Continuous Collision Detection of Rigid and Articulated Models*, IEEE Transactions on Visualization and Computer Graphics **20**, 755 (2014).
- [247] X. Zhang, in *Simulations, Serious Games and Their Applications* (Springer, 2014).
- [248] N. J. Higham, *Accuracy and stability of numerical algorithms* (Siam, 2002).
- [249] M. Allen and D. Tildesley, *Computer simulation of liquids* (Clarendon Press, 1987).
- [250] L. Verlet, *Computer “experiments” on Classical Fluids. I. Thermodynamical Properties of Lennard-Jones Molecules*, Physical review **159**, 98 (1967).
- [251] E. Chow and J. Skolnick, *Effects of confinement on models of intracellular macromolecular dynamics*, Proceedings of the National Academy of Sciences **112**, 14846 (2015).
- [252] L. D. Gelb, K. E. Gubbins, R. Radhakrishnan, and M. Sliwinska-Bartkowiak, *Phase separation in confined systems*, Rep. Prog. Phys. **62**, 1573 (1999).
- [253] J. C. Crocker and D. G. Grier, *When like charges attract: The effects of geometrical confinement on long-range colloidal interactions*, Phys. Rev. Lett. **77**, 1897 (1996).
- [254] U. Nellen, J. Dietrich, L. Helden, S. Chodankar, K. Nygård, J. Friso van der Veen, and C. Bechinger, *Salt-induced changes of colloidal interactions in critical mixtures*, Soft Matter **7**, 5360 (2011).
- [255] B. Yu, P. Sun, T. Chen, Q. Jin, D. Ding, B. Li, and A.-C. Shi, *Confinement-induced novel morphologies of block copolymers*, Phys. Rev. Lett. **96**, 138306 (2006).
- [256] M. Schmidt and H. Löwen, *Phase diagram of hard spheres confined between two parallel plates*, Phys. Rev. E **55**, 7228 (1997).
- [257] R. Bubeck, C. Bechinger, S. Neser, and P. Leiderer, *Melting and reentrant freezing of two-dimensional colloidal crystals in confined geometry*, Phys. Rev. Lett. **82**, 3364 (1999).
- [258] H. Zocher, *Über freiwillige strukturbildung in solen. (eine neue art anisotrop flüssiger medien.)*, Zeitschrift für anorganische und allgemeine Chemie **147**, 91 (1925).
- [259] K. Coper and H. Freundlich, *The formation of tactoids in iron oxide sols*, Transactions of the Faraday Society **33**, 348 (1937).
- [260] I. Langmuir, *The role of attractive and repulsive forces in the formation of tactoids, thixotropic gels, protein crystals and coacervates*, The Journal of Chemical Physics **6**, 873 (1938).

- [261] M. A. Bates, *Computer simulation studies of nematic liquid crystal tactoids*, Chem. Phys. Lett. **368**, 87 (2003).
- [262] P. Prinsen and P. van der Schoot, *Continuous director-field transformation of nematic tactoids*, Eur. Phys. J. E **13**, 35 (2004).
- [263] A. Cuetos, R. van Roij, and M. Dijkstra, *Isotropic-to-nematic nucleation in suspensions of colloidal rods*, Soft Matter **4**, 757 (2008).
- [264] A. Cuetos and M. Dijkstra, *Kinetic pathways for the isotropic-nematic phase transition in a system of colloidal hard rods: a simulation study*, Physical review letters **98**, 095701 (2007).
- [265] P. Prinsen and P. van der Schoot, *Shape and director-field transformation of tactoids*, Physical Review E **68**, 021701 (2003).
- [266] A. Verhoeff, R. Otten, P. van der Schoot, and H. Lekkerkerker, *Magnetic field effects on tactoids of plate-like colloids*, The Journal of chemical physics **134**, 044904 (2011).
- [267] A. Verhoeff, I. Bakelaar, R. Otten, P. van der Schoot, and H. Lekkerkerker, *Tactoids of plate-like particles: Size, shape, and director field*, Langmuir **27**, 116 (2010).
- [268] R. Williams, *Two transitions in tangentially anchored nematic droplets*, Journal of physics A: mathematical and general **19**, 3211 (1986).
- [269] P. Prinsen and P. van der Schoot, *Parity Breaking in Nematic Tactoids*, J. Phys. Condens. Matter **16**, 8835 (2004).
- [270] R. Williams, *Optical rotatory effect in the nematic liquid phase of p-azoxyanisole*, Phys. Rev. Lett. **21**, 342 (1968).
- [271] G. Volovik and O. Lavrentovich, *Topological dynamics of defects: boojums in nematic drops*, Zh Eksp Teor Fiz **85**, 1997 (1983).
- [272] O. Lavrentovich and V. Sergan, *Parity-breaking phase transition in tangentially anchored nematic drops*, Il Nuovo Cimento D **12**, 1219 (1990).
- [273] D.-K. Yang, K.-U. Jeong, and S. Z. D. Cheng, *Structure of Liquid Crystal Droplets with Chiral Propeller Texture*, J. Phys. Chem. B **112**, 1358 (2008).
- [274] L. Tortora and O. D. Lavrentovich, *Chiral symmetry breaking by spatial confinement in tactoidal droplets of lyotropic chromonic liquid crystals*, Proc. Natl. Acad. Sci. **108**, 5163 (2011).
- [275] J. Jeong, Z. S. Davidson, P. J. Collings, T. C. Lubensky, and A. G. Yodh, *Chiral symmetry breaking and surface faceting in chromonic liquid crystal droplets with giant elastic anisotropy*, Proc. Natl. Acad. Sci. **111**, 1742 (2014).
- [276] J. Jeong, L. Kang, Z. S. Davidson, P. J. Collings, T. C. Lubensky, and A. G. Yodh, *Chiral structures from achiral liquid crystals in cylindrical capillaries*, Proc. Natl. Acad. Sci. **112**, E1837 (2015).
- [277] C. Peng and O. D. Lavrentovich, *Chirality amplification and detection by tactoids of lyotropic chromonic liquid crystals*, Soft Matter **11**, 7257 (2015).
- [278] B. de Nijs, S. Dussi, F. Smallenburg, J. D. Meeldijk, D. J. Groenendijk, L. Filion, A. Imhof, A. van Blaaderen, and M. Dijkstra, *Entropy-driven formation of large icosahedral colloidal clusters by spherical confinement*, Nat. Mater. **14**, 56 (2015).
- [279] E. A. Jagla, *Melting of hard cubes*, Phys. Rev. E **58**, 4701 (1998).

- [280] B. S. John, C. Juhlin, and F. A. Escobedo, *Phase behavior of colloidal hard perfect tetragonal parallelepipeds*, J. Chem. Phys. **128**, 0 (2008).
- [281] U. Agarwal and F. A. Escobedo, *Mesophase behaviour of polyhedral particles*, Nat. Mater. **10**, 230 (2011).
- [282] F. Smallenburg, L. Filion, M. Marechal, and M. Dijkstra, *Vacancy-stabilized crystalline order in hard cubes*, Proc. Natl. Acad. Sci. **109**, 17886 (2012).
- [283] A. Cuetos and B. Martínez-Haya, *Columnar phases of discotic spherocylinders.*, J. Chem. Phys. **129**, 214706 (2008).
- [284] S. Gottschalk, M. C. Lin, and D. Manocha. *Obbtree: A hierarchical structure for rapid interference detection.* in *Proceedings of the 23rd annual conference on Computer graphics and interactive techniques*, pages 171–180. ACM, (1996).
- [285] P. Rein ten Wolde, M. J. Ruiz-Montero, and D. Frenkel, *Numerical calculation of the rate of crystal nucleation in a lennard-jones system at moderate undercooling*, The Journal of chemical physics **104**, 9932 (1996).
- [286] Y. Wang, S. Teitel, and C. Dellago, *Melting of icosahedral gold nanoclusters from molecular dynamics simulations*, The Journal of chemical physics **122**, 214722 (2005).
- [287] H. Edelsbrunner, D. Kirkpatrick, and R. Seidel, *On the shape of a set of points in the plane*, IEEE Transactions on information theory **29**, 551 (1983).
- [288] H. Edelsbrunner and E. P. Mücke, *Three-dimensional alpha shapes*, ACM Transactions on Graphics (TOG) **13**, 43 (1994).
- [289] The CGAL Project, *CGAL User and Reference Manual* (CGAL Editorial Board, 2016).
- [290] A. Savitzky and M. J. Golay, *Smoothing and differentiation of data by simplified least squares procedures.*, Analytical chemistry **36**, 1627 (1964).
- [291] J. Park, K. An, Y. Hwang, J.-G. Park, H.-J. Noh, J.-Y. Kim, J.-H. Park, N.-M. Hwang, and T. Hyeon, *Ultra-large-scale syntheses of monodisperse nanocrystals*, Nature materials **3**, 891 (2004).
- [292] M. P. Allen and D. Frenkel, *Calculation of liquid-crystal frank constants by computer simulation*, Physical Review A **37**, 1813 (1988).
- [293] P. A. O'Brien, M. P. Allen, D. L. Cheung, M. Dennison, and A. Masters, *Elastic constants of hard thin platelets by Monte Carlo simulation and virial expansion*, Physical Review E **78**, 051705 (2008).



# Summary

Colloidal particles, i.e. particles at the nanometer scale, experience random motion (**Disorder**) generated by collisions with smaller solvent particles. This random motion is known as *Brownian motion*, and it allows colloidal particles to explore the space of possible configurations. As a consequence, they are able to reach the most (thermodynamically) favorable structure (**Order**). This process is known as *self-assembly*. The title of this thesis, *Order from Disorder*, is referring to the self-assembly process, which is extensively studied here. More specifically, we use computers to simulate models of several colloidal systems. Computer simulations can reveal aspects of a physical process which are otherwise difficult or impossible to solve analytically, or measure experimentally. The thesis is divided in two main themes; in chapters 2, 3, and 4, we study colloidal systems where the various particles interact with each other either directly or indirectly, and in chapters 5, 6, and 7, we study systems of *hard* particles i.e. particles that cannot overlap but that also do not further interact with each other.

Colloids dispersed in a binary solvent mixture experience long-ranged solvent-mediated (SM) interactions (critical Casimir forces) upon approaching the critical demixing point of the solvent mixture. The range of the interaction is set by the bulk correlation length of the solvent mixture, which diverges upon approaching the critical point. It is generally poorly understood how a (dense) suspension of colloids will self-assemble under these conditions. In chapter 2, we use a two-dimensional lattice model of a binary solvent mixture and hard disks (as a model for the colloids), and perform extensive Monte Carlo simulations investigating the phase behaviour of this model colloidal suspension as a function of colloid size and wettability under conditions where the solvent reservoir is supercritical. We find broad colloidal gas-liquid (G-L), and gas-crystal (G-X) coexistence. The critical point of the mixture shifts significantly from that of the colloid-free solvent upon adding a small volume fraction of colloids. Upon increasing the preference of the colloids for one of the solvent species, at a fixed temperature and radius, the G-L binodals broaden and the G-L critical point shifts towards the critical point of the solvent. However, we find a saturation point above which the phase coexistence is unchanged. The phase behaviour with respect to the size of the colloid is arguably more important than that with respect to the adsorption strength. Upon increasing the colloid size, the G-L binodal becomes much flatter, and the critical point shifts to larger colloid fraction.

Due to the large difference in length scales between the colloid and solvent, and the critical slowing down as the ternary mixture critical point is approached, studying a three-dimensional system using Monte Carlo simulations was deemed computationally unfeasible when starting out our study presented in chapter 2. In chapter 3, we overcome these problems by developing a rejection-free geometric cluster algorithm that enables us to study the scaling of the critical Casimir potentials in a two-dimensional system, and more importantly, the full ternary mixture of colloidal hard spheres suspended in an explicit three-dimensional solvent mixture. The effective potentials seem to scale according to the limit known as the *small-sphere* limit, suggesting that the colloids in our simulations are closer in size to e.g. proteins. The phase diagram of the three-dimensional

system displays stable colloidal gas, liquid, and crystal phases, as well as broad gas-liquid and gas-crystal phase coexistence, and pronounced fractionation of the solvent in the coexisting colloid phases. The topology of the phase diagram in our three-dimensional study shows striking resemblance to that of the previous chapter.

Motivated by recent experiments where a lamellar mesophase was observed when adding a certain concentration of an organic salt in a binary solvent mixture, we develop an efficient lattice model, and present the first simulation study of an antagonistic salt suspended in a polar binary solvent mixture in chapter 4. Although theoretical models have been able to describe the experimental results to a certain extent, the degrees of freedom of the solvent mixture are integrated out, and treated on a mean-field level, thereby ignoring fluctuations. Moreover, simulation techniques involving electrostatics are computationally expensive, due to the long range of the Coulomb interaction. In our lattice model, similarly to previous chapters, the solvent mixture and electrostatics are treated explicitly, by combining the simplicity of a lattice gas model and the efficiency of the Maggs' auxiliary field method for treating the electrostatics. In our study of an antagonistic salt solution, we find rich mesophase behavior, including a lamellar phase, for a wide range of temperatures, and solvent and salt compositions. The phase behavior of the system resembles that of diblock copolymers. We argue that because of the strong adsorption and electrostatic interactions, the system can be viewed as consisting of bound ion pairs at a distance set by the Bjerrum length and a thick film of the corresponding preferred species adsorbed around each ion. This picture, underlines the similarities shared between the two different systems. We further analyze the ion distribution, and behavior of the lamellar phase as a function of the salt concentration and temperature and build a simple mean-field theory which is capable of describing our observations. The mean-field model predicts that the lamella thickness, should scale with the power  $-2/3$  of the salt concentration.

In chapter 5, we investigate the phase behavior of hard rhombic platelets as a function of the thickness of the platelets. Hard plate-like particles are known to exhibit nematic and columnar phases. Using the equations of state, diffraction patterns, as well as the nematic and smectic order parameters we determine the phase diagram of the rhombic platelets. The phase diagram displays a columnar phase and a crystal phase in which the platelets are stacked in columns that are arranged on a two-dimensional lattice. We find that the shape of the platelets determines the symmetry of the two-dimensional lattice, i.e., rhombic platelets form an oblique columnar phase and a simple monoclinic crystal phase. For sufficiently thick platelets, we find only an isotropic fluid, an oblique columnar phase, and a monoclinic crystal phase. Surprisingly, for an intermediate plate thickness, we also find a region in between the isotropic (or nematic) phase and the columnar phase, where the smectic phase is stable. For sufficiently thin platelets, the phase diagram displays a nematic phase, and we find hints of a possible biaxial nematic phase. With the exception of the smectic phase, our results resemble the phase behavior of discotic particles.

Given the possibility of a biaxial nematic phase in chapter 5, we further investigate the phase behavior of rhombic particles, for a broader range of parameters, in chapter 6. We develop a highly efficient event-driven molecular dynamics (EDMD) algorithm that enables us to perform simulations on general convex particles. Using this algorithm we study the presence of a biaxial nematic phase for rhombic particles, by simulating 68

different particle shapes. Upon expansion from the space-filling crystal structure, we find 10 different ordered phases, including a biaxial nematic phase. A biaxial *smectic* phase is shown for the first time in a simulation study, which remarkably does not appear in the same particle shape parameter regime as the biaxial nematic phase. In addition, we map out a diagram of the different sequences of phases we find for increasing densities, as a function of the length and width of the rhombic particles. We find 9 regimes with different phase sequences, which conveys the complexity of the system. Our results show that due to the sharp-angled rhombic shape of the particles, the smectic phases are destabilized in favor of the biaxial nematic phase, making the area of the biaxial nematic phase in the phase diagram larger than in previously studied hard-particle systems.

Many biological and colloidal systems consist of mesoscopic particles that are confined in space. Examples are, membrane proteins confined in a lipid membrane, or actin filaments confined in a biological cell. Confinement of liquid crystals in droplets can have interesting applications, due to their liquid-like behavior and crystal-like optical properties. Motivated by experiments, on cubic  $\text{Fe}_3\text{O}_4$  nanoparticles and  $\text{EuF}_3$  nanoplatelets confined in emulsion droplets, in chapter 7 we investigate the behavior of two model systems of hard particles under spherical confinement using Monte Carlo simulations. The first system consists of hard cubic particles. From compression runs, we find that the surface layer crystallizes at a slower rate, while for big system sizes, the surface layers start crystallizing before the interior. We also find fluid-like regions between the surface layers and the interior, organized on the vertices of a cube. Remarkably, we find that the crystallized core shows some twisting. Lastly, we find a large number of clusters, which might be indicative of the high vacancy concentration in the system. In the second system, we simulate round platelets (cylinders) and discover a twisted columnar phase for large-enough systems, while smaller systems do not exhibit such a phase, due to the strong boundary effects. We devise various methods to analyse the degree of twist in the system. We find that the slope of the tangent of a director field line (column), follows a linear dependence as a function of the column distance from the center of the ‘twist’. We subsequently built an empirical model to successfully explain the reason why this dependence is observed. Unfortunately, the twisted system evolves very slowly, especially, at the very high packing fractions this twisted phase is observed, and thus a relationship between the twist angle, and packing fraction, or system size, can not be established.

# Samenvatting

Colloïdale deeltjes, dat wil zeggen deeltjes met een grootte in de orde van nanometers, ervaren een willekeurige beweging (**Wanorde**), die gegenereerd wordt door botsingen met de kleinere moleculen van het oplosmiddel. Deze willekeurige beweging staat bekend als *Brownse beweging*, en maakt het voor colloïdale deeltjes mogelijk om verschillende configuraties te verkennen. Ten gevolge hiervan kunnen ze de meest (thermodynamisch) gunstige structuur bereiken (**Orde**). Dit proces staat bekend als *zelforganisatie*. De titel van dit proefschrift, *Orde uit Wanorde*, verwijst naar het zelforganisatie proces dat in deze thesis uitvoerig wordt bestudeerd. Om specifieker te zijn, gebruiken we computers om verschillende colloïdale modelsystemen te simuleren. Computersimulaties kunnen aspecten van een fysisch proces ophelderden welke analytisch of experimenteel moeilijk of onmogelijk op te lossen zijn. Het proefschrift is verdeeld in twee hoofdthema's; In hoofdstukken 2, 3 en 4 worden colloïdale systemen bestudeerd waarin de verschillende deeltjes direct of indirect met elkaar interacteren, en in hoofdstukken 5, 6 en 7, bestuderen we systemen van harde deeltjes, namelijk deeltjes die niet kunnen overlappen, maar verder geen interactie met elkaar hebben.

Bij het naderen van het kritische ontmengingspunt van een binair vloeistof mengsel, ervaren de colloïden in zo'n mengsel langedracht vloeistof-gemedieerde interacties (kritische Casimir-krachten). Het bereik van de interactie wordt bepaald door de correlatielengte van het bulk vloeistof mengsel, welke divergeert naar mate het kritisch punt nadert. Het was nog niet duidelijk hoe een (dichte) suspensie van colloïden zou zelforganiseren onder deze condities. In hoofdstuk 2 gebruiken we een tweedimensionaal roostermodel van een binair vloeistofmengsel en harde schijven (een representatie van de colloïden). Op dit systeem voeren we uitgebreide Monte Carlo simulaties uit. We onderzoeken het fasegedrag van deze colloïdale suspensie model als functie van de colloïdale grootte en adsorptie, waarbij het vloeistofreservoir superkritisch is. We vinden een brede colloïdale gas-vloeistof (G-L) en gas-kristal (G-X) coëxistentie. Bij het toevoegen van een kleine volumefractie van colloïden verschuift het kritische punt van de mengsel aanzienlijk ten opzicht van die van een colloïd-vrije vloeistof. Gegeven dat de temperatuur en de grootte van colloïden constant blijft, vinden we dat de G-L binodaal platter wordt en dat het kritische punt naar een hogere colloïdf fractie verschuift wanneer de voorkeur van de colloïden voor een van de oplosmiddelen versterkt wordt. We vinden echter een verzadigingspunt waarvoor de fase-coëxistentie ongewijzigd blijft. Het fasegedrag met betrekking tot de grootte van het colloïden is blijkbaar belangrijker dan dat ten opzichte van de adsorptiesterkte. Bij het vergroten van de colloïden wordt de G-L binodaal veel platter, en het kritische punt verschuift naar een hogere colloïdf fractie.

Aan het begin van onze studie in hoofdstuk 2, werd het bestuderen van een driedimensionaal systeem met behulp van Monte Carlo-simulaties computationeel onmogelijk geacht. Dit was wijten aan het grote verschil in lengteschalen tussen de colloïden en de vloeistof, en aan de kritische vertraging wanneer het kritische punt van het ternaire mengsel wordt benaderd. In hoofdstuk 3 overwinnen we deze problemen door een afstotingsvrij geometrisch cluster-algoritme te ontwikkelen. Met dit algoritme bestuderen we

zowel de schaling van de kritieke Casimir-potentialen in een tweedimensionaal systeem als een volledig ternair mengsel van colloïdale harde bollen gedispergeerd in een expliciet driedimensionaal vloeistofmengsel. De effectieve potentialen lijken te schalen volgens een limiet die bekend staat als de *small-sphere*-limiet, wat suggereert dat de grootte van de colloïden in onze simulaties dichter bij die van b.v. eiwitten ligt. Het fasediagram van het driedimensionale systeem toont stabiele colloïdale gas-, vloeistof- en kristal fasen, evenals brede gas-vloeistof- en gas-kristal fase-coëxistentie, en fractionering van de vloeistof in de coëxistente colloïdale fasen. De topologie van het fasediagram in onze driedimensionale studie toont een opvallende gelijkenis met die in het vorige hoofdstuk.

Geïnspireerd door recente experimenten waarin na het toevoegen van een bepaalde concentratie van een organisch zout in een binair vloeistofmengsel een lamellaire mesofase werd geobserveerd, ontwikkelen we een efficiënt roostermodel en presenteren we in Hoofdstuk 4 de eerste simulatiestudie van een antagonistische zout opgelost in een polair binair oplosmiddelmengsel. Alhoewel theoretische modellen tot op zekere hoogte de experimentele resultaten kunnen beschrijven, worden de vrijheidsgraden van het vloeistofmengsel uitgemiddeld en worden ze op mean-field theorie niveau behandeld, waardoor fluctuaties worden genegeerd. Daarnaast zijn simulatietechnieken die elektrostatica betreffende computationeel kostbaar in verband met het lange bereik van de Coulomb-interactie. In vergelijking met vorige hoofdstukken worden in ons roostermodel het vloeistofmengsel en de elektrostatica explicet behandeld door een combinatie van een eenvoudig roostergasmodel en de efficiëntie van de ‘auxiliary field’ methode, welke ontwikkeld is door Maggs voor de behandeling van de elektrostatica. In ons onderzoek vinden we rijk mesofase gedrag, waaronder een lamellaire fase, voor een breed scala van temperaturen en vloeistof- en zout- samenstellingen. Het fasegedrag van de antagonistische zoutoplossing lijkt op die van diblokcopolymeren. We redeneren dat door de sterke adsorptie- en elektrostaticche interacties het systeem kan worden gezien als gebonden ionparen op een afstand die door de Bjerrumlengte is vastgesteld, en een dikke film van de bijbehorende geprefereerde vloeistof die om elke ionen wordt geadsorbeerd. Dit beeld legt de nadruk op de overeenkomsten die tussen de twee verschillende systemen bestaan. We analyseren de ionenverdeling en het gedrag van de lamellaire fase verder als functie van de zoutconcentratie en temperatuur, en bouwen een eenvoudige mean-field theorie die in staat is om onze waarnemingen te beschrijven. Het mean-field model voorspelt dat de lamella-dikte met de zoutconcentratie tot de macht  $-2/3$  schaalt.

In hoofdstuk 5 onderzoeken we het fasegedrag van harde rhombische plaat-achtige deeltjes als functie van hun dikte. Harde plaatachtige deeltjes staan bekend om het vormen nematische en kolom fasen. Met behulp van de toestandsvergelijkingen, diffractionpatronen, evenals de nematische en smectische orderparameters bepalen we het fasediagram van de rhombische plaat-achtige deeltjes. Het fasediagram laat een kolomfase en een kristalfase zien waarin de deeltjes gestapeld zijn in kolommen die op een tweedimensionaal rooster zijn geplaatst. We laten zien dat de vorm van de deeltjes de symmetrie van het tweedimensionale rooster bepaalt, dat wil zeggen dat rhombische plaatachtige deeltjes een schuine kolomfase vormen en een eenvoudige monoklinische kristalfase. Voor voldoende dikke deeltjes vinden we alleen een isotropische vloeistof, een schuine kolomfase en een monoklinische kristalfase. Tot onze verbazing, vinden we in een gebied tussen de isotropische (of nematische) fase en de kolom fase ook een stabiele smectische fase.

Voldoende dunne deeltjes vormen een nematische fase, en we vinden aanwijzingen voor een mogelijke biaxiale nematische fase. Met uitzondering van de smectische fase zijn onze resultaten vergelijkbaar met het fased gedrag van discotische deeltjes.

Gezien de mogelijkheid tot het vormen van een biaxiale nematische fase in hoofdstuk 5, onderzoeken we in hoofdstuk 6 het fased gedrag van rhombische deeltjes voor een breder scala van parameters. We ontwikkelen een zeer efficiënt zogenaamd event-driven molecular dynamics algoritme waarmee we simulaties van algemene convexe deeltjes kunnen uitvoeren. Met behulp van dit algoritme bestuderen we de aanwezigheid van een biaxiale nematische fase bij rhombische deeltjes door 68 verschillende deeltjesvormen te simuleren. Bij expansie vanuit de ruimtevullende kristalstructuur vinden we 10 verschillende geordend fasen, waaronder een biaxiale nematische fase. We laten voor het eerste een biaxiale *smectische* fase in een simulatie studie zien. Opmerkelijk genoeg wordt deze niet in hetzelfde deeltjesvormregime als de biaxiale nematische fase geobserveerd. Daarnaast stellen we een diagram uit de verschillende fase-sequenties samen, die we voor toenemende dichtheden vinden, als een functie van de lengte en de breedte van de rhombische deeltjes. We vinden 9 regimes met verschillende fase sequenties, wat de complexiteit van het systeem overbrengt. Uit onze resultaten blijkt dat de smectische fasen door de scherphoekige rhombische vorm van de deeltjes gedestabiliseerd worden ten gunste van de biaxiale nematische fase, waardoor het gebied van de biaxiale nematische fase in het fasediagram groter is dan in eerder bestudeerde systemen van harde deeltjes.

Veel biologische en colloïdale systemen bestaan uit mesoscopische deeltjes die begrensd zijn in ruimte. Voorbeelden zijn membraanewitten, die in een lipidmembraan opgesloten zijn, of actinfilamenten, die in een biologische cel zitten. Het beperken van vloeibare kristallen binnen druppels kan interessante toepassingen hebben, door het vloeibaarachtig gedrag en de kristalachtige optische eigenschappen. Geïnspireerd door experimenten van kubische  $\text{Fe}_3\text{O}_4$  en plaatachtige  $\text{EuF}_3$  nanodeeltjes die opgesloten zitten in emulsiedruppels, onderzoeken we in hoofdstuk 7 het gedrag van twee modelsystemen van harde deeltjes in een bol met behulp van Monte Carlo simulaties. Het eerste systeem bestaat uit harde kubische deeltjes. Door het systeem te comprimeren vinden we dat de laag die het dichtst bij het oppervlak van de bol ligt, langzamer kristalliseert, terwijl we voor grote systemen juist zien dat de kern van de bol langzamer kristalliseert dan de lagen aan het oppervlak. Bovendien vinden we vloeistofachtige gebieden tussen de oppervlaktelagen en de kern die op de hoekpunten van de kubus liggen. Opmerkelijk genoeg, vinden we dat de gekristalliseerde kern een beetje gedraaid is. Tenslotte vinden we een groot aantal clusters, wat mogelijk kan wijzen op een hoge concentratie van lege plekken in het systeem. In het tweede systeem simuleren we ronde plaatachtige deeltjes (cilinders) en ontdekken we voor groot genoeg systemen, een gedraaide kolomfase, terwijl door de sterke grenseffecten zulke fasen niet aanwezig zijn in kleinere systemen. Wij bedenken verschillende methoden om de mate van draaiing in het systeem te analyseren. We vinden dat de helling van de tangent van een richtingsveldlijn (kolom) een lineaire afhankelijkheid heeft als functie van de afstand van de kolom ten opzichte van het centrum van de 'draai'. Vervolgens hebben we een empirische model gebouwd om deze afhankelijkheid succesvol uit te leggen. Helaas evolueert bij de zeer hoge pakingsfracties waar deze gedraaide fase waargenomen wordt, het gedraaide systeem heel langzaam waardoor een relatie tussen de draaihoek en de pakingsfractie of systeemgrootte niet kan worden vastgesteld.

# Acknowledgements

Dutch historian and cultural theorist Johan Huizinga, in his book titled ‘Homo Ludens’, discusses the importance of play, saying the following,

*“Play is distinct from ‘ordinary’ life both as to locality and duration. This is the third main characteristic of play; its secludedness, its limitedness. It is ‘played out’ within certain limits of time and place. It contains its own course and meaning. Play begins, and then at a certain moment it is ‘over’ ”.*

A PhD is also a kind of play, as defined above, and as every play eventually comes to an end, so has my PhD. Although some types of ‘play’ are conducted by a single individual, this was certainly not the case during my PhD, as many people supported me and made the journey extremely enjoyable. This section is dedicated to, the best of my ability, thanking these people and acknowledging their support.

A PhD supervisor is supposed to be a mentor, transferring knowledge and challenging the PhD candidate. Beyond that, a good supervisor is also expected to be supportive and understanding, and share the excitement of discovery with the student. Unfortunately that is not always the case, but I’m glad to say that my supervisor, Prof. Dr. Ir. Marjolein Dijkstra, has been excellent. I was always amazed by the number students and respective research topics she could juggle every single day. Thus, I would like to thank Marjolein, for her professional support, for always asking ‘what if’ questions, and for not pressuring me to perform free energy calculations. It was also fun when we had the ‘Beers with Peers’, and dinner at your place with everyone!

Furthermore, I would like to thank all the people who have somehow contributed to this Thesis, with the most important contributor after my supervisor being John R. Edison, who acted somewhat as my cosupervisor during my first year. John was a good friend (and a great Bobsitter) from whom I learned a lot. I would also like to thank the infamous Prof. Bob Evans not only for his input on my and John’s research, but also for the desperate times inside the ‘Ornstein fridge’, the fun (non) alcoholic conversations, and for learning from him more about scientific writing than any course I *should have* followed. I thank Sela Samin for discussions and his collaboration on my work on antagonistic salts, and René van Roij for his input on the theoretical aspects of my research. I’m also grateful for my collaboration with Da Wang, who allowed me to peek inside the experimental (i.e. the real) world. Thanks also goes to Florian Fahrenberger and the team of Prof. Dr. Christian Holm for constructive discussions on possible computational models of electrolyte solutions. I also learned a lot from supervising Marjolein, Joep, and Alexander together with Simone, so thank you for the long and interesting meetings. Lastly, I thank, Simone Belli, Anna Maciołek, Nigel Wilding, and Douglas Ashton, for their discussions. I also acknowledge the support of Hera and Thor. No I’m not a paganist, these are the names of our computer clusters.

I am deeply grateful to Prof. Dr. George Floudas, who first introduced me to scientific research, and Christos Grigoriadis who taught me the experimental techniques needed for my research during my Bachelor’s thesis. During my Master’s, Prof. Dr. Gerard T.

Barkema's simulation course was very motivating in my career as a simulator. During my Master's thesis under the supervision of Marjolein, Anjan P. Gantapara was very helpful, even though I could occasionally become imposing.

I would also like to extend my acknowledgements to the staff members of the Soft-Condensed Matter (SCM) group, Prof. Dr. Alfons van Blaaderen, Prof. Dr. Ir. Marjolein Dijkstra, Dr. Arnout Imhof, Prof. Dr. René van Roij, Dr. Laura Filion, Dr. Ir. Marijn van Huis, Dr. Patrick Baesjou, Dr. Krassimir Velikov, who have created an amazing group where theory, simulations, and experiments meet, as well as the technical staff Peter Helfferich, Relinde Moes-van Dijk, Chris Schneijdenberg, and Dr. Judith Wijnhoven for the support.

The two most important 'playmates' have of course been my officemates, Guido Avvisati, and Harini Pattabhiraman. I remember when I first met Guido in our office, OL020, he somehow reminded me of a mafioso. I wasn't far off, as he terrorised everyone with his pranks; it has now become a habit of mine to lock my computer before leaving the room so that Guido doesn't mess with it. Our various trips and conferences wouldn't have been as enjoyable without Guido around. I also remember when I met Harini for the first time. She used to whisper at all times making her barely audible. As time went on, the volume of her voice increased, especially when Guido was misbehaving. I'm also thankful of Harini for often reminding us of our various responsibilities, and for watering the plants. I can't stress enough how uplifting it was to always have someone to share your troubles with instead of silently focusing on the computer monitor the whole day — although there certainly were such days.

I remember Marjolein once mentioned that the people of the current group were closest to each other than any of the previous groups. It certainly felt like having friends instead of just 'colleagues'. Not only would we often go out for beers and have fun at conferences, but we even organized trips with each other. I had tons of fun drinking beers with everyone and especially Zdenek Preisler who often accompanied me to my favorite late night bar, the 'Boothill Saloon', and would always somehow convince me stay up drinking beers till the early morning. Thanks to Ernest for being there for Zdenek all the other days I was not around! Thanks to Wiebke, Wessel, Simone, Zdenek, Vasilakis, Jessi, and John for an amazing road trip! Special thanks to Simone and Guido for making our conference in Rome amazing. I got so excited I wanted to trace back to my Italian roots by learning Italian. Thanks to Tonnishtha for just being fun to be around, and for being the second coolest Indian in OL. Thanks to Giulia for (nearly) always making criticizing remarks! I would also like to thank all the people that would express their amazement when I would attend a Friday morning meeting. Moreover, I would like to thank Jessi for polishing my bad Dutch translationn of the *Summary* section.

The ancient Greek/Romans used to say that 'a healthy mind in a healthy body', which underlies the fact that we should perform some form of workout for our brains to function properly. Thus, I would like to thank all the people with which I played fussball, which helped me keep my mind 'healthy'.

Finally, I would like to thank all my colleagues through the four years of my PhD, thank you very much Anjan, John, Simone, Guido, Nina, Henriëtte, Thijs, Jissy, Tian-Song, Marjolein, Joost, Marlous, Rao, Murphy, Xiaobin, Djamel, Belli, Thomas, Andreas, Weikai, Chris, Giulia, Ernest, Tonnishtha, Sid, Da, Vats, Harini, Berend, Vasilis, Rik,

Rama, Fabian, Doug, Bart, Ran, Wessel, Zdenek, Somil, Sina, Naveed, Anna, Frankje, Ravi, Ajoy, Federico, Sela, Bram, Mathijs, Jeffrey, Giuseppe, Massimiliano, Carmine, Robin, Stijn, and Tara. If I have somehow forgotten to mention someone, you probably already know that I am really bad with names, sorry!

Love and support has not only come from colleagues, but also from my housemates, and friends, Panos Moraitis, Stavros Ouzounis, Petros Theodorou, Stathis Grigoropoulos, Eugenios Tsolakis, and Alex Papadopoulos. Thank you guys for all the discussions, the partying, and for just being there.

But most importantly, I would like to thank my family. My parents, Sylvana and Vasilis, have always supported me, and gave me enough freedom to study what I wanted. They never pushed me to study for school, which, I think, allowed me to reach this far in my studies. They also always showed great interest in my work, despite it being difficult to grasp. Thus, dankjewel mama, ευχαριστώ μπαμπά. I also thank my grandmother Stavroula, ευχαριστώ Γιαγιά. And of course I thank Lydia, my little sister (who's not little any more), for always putting up with me, and for the long discussions on mathematics, and whatnot. Lastly I want to thank Charlotte Kiekebos, the person I've spent the most time on after work and sleep for the past two years. Thank you for making me challenge the simple things in life, for your support, and for making it so obvious to my colleagues that I got a girlfriend! Dankjewel Charlotje!

Thank you all for playing along!

— Nikos Tasios, May 2017

# List of Publications

The following publications have been made, or are being prepared, as part of the author's PhD:

- John R. Edison, Nikos Tasios, Simone Belli, Robert Evans, René van Roij, and Marjolein Dijkstra. *Critical Casimir forces and colloidal phase transitions in a near-critical solvent: A simple model reveals a rich phase diagram.* Physical review letters 114.3 (2015): 038301.
- Nikos Tasios, John R. Edison, René van Roij, Robert Evans, and Marjolein Dijkstra. *Critical Casimir interactions and colloidal self-assembly in near-critical solvents.* The Journal of Chemical Physics 145.8 (2016): 084902.
- Nikos Tasios, and Marjolein Dijkstra. *From 2D to 3D: Critical Casimir interactions and phase behavior of colloidal hard spheres in a near-critical solvent.* The Journal of Chemical Physics 146.13 (2017): 134903.
- Nikos Tasios, and Marjolein Dijkstra. *A simulation study on the phase behavior of hard rhombic platelets.* The Journal of Chemical Physics 146.14 (2017): 144901.
- Nikos Tasios, Sela Samin, René van Roij, and Marjolein Dijkstra. *Microphase separation in mixtures containing hydrophilic and hydrophobic ions* manuscript in preparation (based on chapter 4).
- Nikos Tasios/Simone Dussi, and Marjolein Dijkstra. *Recipes for biaxial phases with hard particles.* manuscript in preparation (based on chapter 6 and work by S. Dussi).
- Civan Avci, Inhar Imaz, Jose Angel Pariente, Nikos Tasios, Javier Pérez-Carvajal, Maria Isabel Alonso, Alvaro Blanco, Marjolein Dijkstra, Cefe Lopez, and Daniel Maspoch. *Three-Dimensional Photonic Crystals Self-Assembled from Polyhedral Metal-Organic Framework Particles.* manuscript submitted.

Other publications by the author:

- Nikos Tasios, Anjan Prasad Gantapara, and Marjolein Dijkstra. *Glassy dynamics of convex polyhedra.* The Journal of chemical physics 141.22 (2014): 224502.
- Nikos Tasios, Christos Grigoriadis, Michael Ryan Hansen, Henrike Wonneberger, Chen Li, Hans W. Spiess, Klaus Müllen, and George Floudas. *Self-Assembly, Dynamics, and Phase Transformation Kinetics of Donor Acceptor Substituted Perylene Derivatives.* Journal of the American Chemical Society 132.21 (2010): 7478-7487.

## About the Author

Nikos Tasios was born in the Greek island, Rodos. His father, Vasilis is Greek and his mother, Sylvana is half Dutch, half Italian. Nikos started his studies in physics in Leiden University in 2005, but returned soon after to Greece, to study physics at the University of Ioannina, where he also obtained his bachelors degree in 2009. During his bachelor thesis, he performed experiments under the supervision of Prof. George Floudas and Christos Grigoriadis, leading to his first publication, in JACS. During his bachelors thesis, he came in contact with simulations for the first time, which would lead him to Utrecht. There, Nikos studied for his masters degree in ‘theoretical physics’ and completed his masters thesis on simulations of the *Glassy Dynamics of Convex Polyhedra* under the supervision of Prof. Marjolein Dijkstra. Nikos received his masters degree in 2013, and soon after started looking for a job in the industry. In a turn of events, even though he was about to work for a certain company, Prof. Marjolein Dijkstra offered him a PhD position which he accepted in 2013 making him an official member of the Soft Condensed Matter group of the physics department in Utrecht. Aside work, Nikos enjoys programming, watching Japanese anime, and playing and collecting *retro* video games and consoles.